UNIVERSITY
of
GLASGOW

3D Non-Linear and Multi-Region Boundary Element Stress Analysis

Xiao-Wei Gao

A thesis submitted for the degree of
Doctor of Philosophy at the University of Glasgow

Department of Civil Engineering
University of Glasgow
March 1999

To my family

Acknowledgements

My deepest thanks and sincere appreciation goes to my supervisor Dr. Trevor G. Davies for his invaluable guidance and advice throughout this study.

I would like to thank Regius Professor N. Bicanic, the Head of the Department, and Cormack Professor S. J. Wheeler for their encouragement and support.

I would also like to thank Mr. K. McColl, Mr. S. McLean and Ms. J. McCulloch for assistance with the computing facilities, and Mrs. E. Davies, Ms B. Grant and Mrs. T. Bryden for their help.

I am grateful to my friends Dr. B. S. Zhang, Dr. H. P. Chen and Dr. C. J. Pearce for the valuable suggestion and technical discussion.

Further thanks are given to my friends Mr. Ali Alnuaimi, Ms X. Y. Tao, Ms Z. H. Liao, Mr. F. Basile, Mr. L. Cunningham, Y. P. Lee and Mr. D. Gallipoli for their friendship and support.

I am grateful to the Vice-Chancellors and Principales of the Universities of the United Kingdom for their financial support through an ORS award, and the Faculty of Engineering, Glasgow University, for funding this work through a Faculty of Engineering Research Scholarship.

Finally, I give my thanks to my wife Fang Wang and my daughter Lingjie Li for their endless understanding and encouragement. Without their support, this work could not have been completed.

Abstract

This thesis is concerned with resolving some important issues existing in nonlinear three-dimensional boundary element analysis. The new findings can be outlined as follows:

- Two new simple auxiliary equations which are required to supplement the fundamental boundary integral equations in solving traction-discontinuity problems using multiple-node technique are derived from the symmetric property and the equilibrium equations of the stress tensor. These equations have been used to deal with the corners and edges of single region and multi-region problems.
- A sub-structure algorithm is developed for solving multi-region problems with corners and edges, using the derived auxiliary equations. This algorithm can deal with nodes where more than two materials intersect.
- A novel infinite element formulation suitable for multi-layered media was developed. In particular, a set of useful analytical expressions was derived for evaluating strongly singular surface integrals over the infinite surface.
- A set of unified elastoplastic constitutive relationships dealing with hardening, softening and ideal plasticity behaviour is derived from the Il'iushin postulate in strain space. These relationships are suitable for both small and finite deformation rate-independent elastoplastic problems.
- Some new identities are derived for the initial stress and strain kernels. Based on these, a new transformation technique from domain integrals to cell boundary integrals is developed, for accurate evaluation of the strongly singular domain integrals pertaining to interior stresses.
- Two new iterative schemes are introduced for the first time in the incremental variable stiffness method for solving the non-linear system of equations. In particular, in the second one, a novel assembly process was proposed, in which the system equations are expressed in terms of the *plastic multiplier*.
- These formulations have been implemented within a Fortran computer code and illustrative numerical examples have been solved to demonstrate its practical utility.

Notation

An attempt has been made throughout this thesis to keep the notation as consistent as possible. Each symbol is defined as it is introduced. Some of the more commonly used symbols are described below:

$\mathbf{t}$ (or t_i)	Surface traction verctor
$\mathbf{u}$ (or u_i)	Displacement vector
b_i	Body force
$\mathbf{D}^e$ (or D^e_{ijkl})	Elastic constitutive tensor
$\mathbf{D}^{ep}$ (or D^{ep}_{ijkl})	Elastoplastic constitutive tensor
$\mathbf{D}^t$ (or D^t_{ijkl})	Consistent tangent operator
f	Loading function (yield function)
h^α	Internal variables
N_α	Shape functions
N'_α	Shape functions in sub-elements (or cells)
$\mathbf{n}$ (or n_i)	Outward normal vector of a surface
$J(\xi,\eta,\zeta)$	Jacobian of transformation
U_{ij}, T_{ij}	Kelvin's fundamental solutions for displacements and tractions
G	Shear modulus of elasticity
E	Young's modulus
E_{ijk} and E_{ijkl}	Fundamental solutions of initial stresses for displacement and stresses, respectively
[E]	Coefficient matrix of initial stresses for system equations
{X}	Boundary unknown vector

$\{Y\}$	Vector on the right-hand side of an equation
P, p	Source points at boundary and interior, respectively
Q, q	Field points at boundary and interior, respectively
σ (or σ_{ij})	Cauchy stress tensor
σ^e (or σ^e_{ij})	Elastic stress tensor
σ^p (or σ^p_{ij})	Plastic (initial) stress tensor
ε (or ε_{ij})	Strain tensor
ε^p (or ε^p_{ij})	Plastic strain tensor
$\bar{\varepsilon}^p$	Equivalent plastic strain
λ	Plastic multiplier
ξ, η, ζ	Intrinsic co-ordinates
ξ', η', ζ'	Intrinsic co-ordinates in sub-elements (or cells)
ν	Poisson's ratio
Ω	Domain of a body
Γ	Boundary of a body

The subscripts

ijkl	Cartesian co-ordinate system
α	Shape function
comma	Differentiation with respect to a co-ordinate at the field point

Chapter 1

Introduction

1.1 General

In general, it is not possible to obtain analytical solutions for stress analysis of practical engineering structures. Therefore, various numerical methods for the solution of such problems have been developed for this purpose. The principal numerical methods applied to the solution of boundary value problems in continuum mechanics are approximate discretisation methods such as the finite difference, finite element and boundary element methods.

The finite difference method (Southwell, 1946) is carried out by directly discretising the governing differential equation at a series of points in the domain of the problem and results in an narrow-banded set of system equations. The drawbacks of this method are that a large number of points is required in order to obtain accurate solutions and boundary conditions are often difficult to deal with.

The finite element method (FEM) (Zienkiewicz, 1977; Owen and Hinton, 1980) has been outstandingly successful in applications to a very wide range of problems. In this method, the domain of the body is divided into elements and distributions of the physical variables (e.g. displacements, potentials) in an element are entirely determined in terms of their local (nodal) values, via interpolation (shape) functions. The resulting system equations, involving the nodal values as unknowns, are banded and often symmetric. Since material properties are specified at element level, the FEM can deal with inhomogeneous materials as easily as single-material problems. This feature makes the FEM very versatile and consequently it has become the dominant numerical method.

There are, however, many classes of problems (principally, infinite or semi-infinite problems, fracture analysis and dynamics) for which FEM is not ideally suited and more efficient techniques, such as those based on integral equations, are available.

The boundary element method (BEM) has emerged only in the last two decades as a powerful numerical method of analysis of continuum problems, although its roots lie much deeper in the mathematical theory of integral equations, largely associated with the work of Fredholm. In this technique, the governing differential equation is transformed into boundary integral equation by means of Betti's reciprocal work theorem (Cruse, 1969) or more generally by weighted residual techniques (Brebbia, 1978) with particular solutions (fundamental solutions). Since the resulting system equations only involve the variables defined over the boundary of the body, the dimensionality of the problem can be reduced by one. Moreover, the use of fundamental solutions implicitly incorporates the infinite boundary conditions, and allows greater resolution of stress concentrations. These advantages have spurred the use of BEM in a wide range of applications.

1.2 Boundary Element Method in Solid Mechanics

BEM can be classified into two groups: indirect and direct. In the indirect formulation, the integral equations are expressed in terms of density functions.

Once the density functions are solved, the actual displacements and stresses can be easily computed. This method is particularly useful for displacement discontinuity problems (Crouch and Starfield, 1983).

In the direct formulation, the integral equations are expressed in terms of the actual physical variables, such as tractions and displacements. Once the boundary unknowns are obtained, the displacements and stresses at selected internal points can then be calculated from these boundary values. The direct method is the far more common approach and in the sequel, only this method is addressed. Only a brief survey of the relevant literature is given in this chapter. More detailed citations are deferred to the relevant chapters.

1.2.1 Boundary Element Method in Linear Elasticity

The direct formulation of the BEM for linear elasticity was presented by Rizzo (1967). Cruse and Rizzo (1968) and Cruse (1968) extended the formulation to elastodynamics. Snyder and Cruse (1975), Stern et al (1976) and Cruse (1978) applied it to fracture mechanics.

The fundamental solution used by Rizzo (1967) and Cruse (1969) is Kelvin's solution for a unit point load applied within the infinite medium. The Mindlin's singular solution (1936) was applied by Nakaguma (1979) to half-space problems and a special Green's function was employed by Cruse (1978) for cracked plates.

Since the book by Brebbia (1978), the BEM has developed rapidly. Lachat and Watson (1975, 1976) and Watson (1979) contributed important work on higher order boundary elements in three dimensional (3D) problems. More recent notable advances focus on the treatment of the singularities during integration of the fundamental solutions (Banerjee and Butterfield, 1981; Mukherjee, 1982; Cruse, 1988; Hartmann, 1989; Sladek et al., 1986; Bonnet, 1989; Gray et al., 1990; Aliabadi, 1997).

A general method for the evaluation of strongly singular and hypersingular integrals was reported by Guiggiani and Gigante (1990), using Taylor series expansions in a local coordinate system. Further applications were reported by Huber et al. (1993) and Mi & Aliabadi (1996). Their formulations can also be used for evaluation of singular surface integrals. Regularization of hypersingular boundary integral equations is described by Krishnasamy et al. (1992), Lutz et al. (1992) and Cruse and Richardson (1996).

Perhaps the most successful applications of BEM are to *fracture mechanics,* as exemplified by the works of Cruse and co-workers (Cruse, 1988; Cruse and Novati, 1992; Polch et al., 1987; Richardson and Cruse, 1998), Aliabadi and co-workers (Aliabadi and Rooke, 1991; Aliabadi, 1997; Mi and Aliabadi, 1992) and Rudolphi et al. (1988).

The singular quarter-point boundary element proposed by Blandford et al. (1981) and Martinez and Dominguez (1985) is reported to give accurate and stable results (Brebbia and Dominguez, 1992). Also, applications to *dynamic analysis,* e.g. Dominguez and Alarcon (1981), Nardini and Brebbia (1982) and Banerjee and co-workers (Banerjee et al, 1986, 1992; Wilson et al., 1990); and to *infinite and semi-infinite region* problems (Crouch and Starfield, 1983; Zheng and Gao, 1986; Wang and Gao, 1998). In semi-infinite

problems, infinite boundary element techniques have been described by Watson (1979), Beer and Watson (1989), Davies and Bu (1996), Gao and Davies (1998a).

1.2.2 Boundary Element Method in Elasto-plasticity

In non-linear BEM, the initial work was done by Swedlow and Cruse (1971) and developed further by Riccardella (1973) and Mendelson and Albers (1975). Corrected formulations were published by Mukherjee (1977), Bui (1978) and Telles and Brebbia (1979).

To avoid the strong singularity of the domain integrals arising in the direct evaluation of interior stresses, the stresses may be calculated from the nodal displacements by differentiating the shape functions, using methods similar to those employed in FEM (Banerjee and Cathie, 1980; Cathie, 1980; Wearing and Dimagiba, 1998). The singularity can also be circumvented by employing indirect approaches based on the application of known reference solutions (Telles and Brebbia, 1979; Brebbia et al., 1984; Banerjee et al., 1989). To avoid discretising the whole body, multi-region BEM technique can be employed (Banerjee et al. 1989) or a second boundary may be defined (Lee and Fenner, 1986).

It is preferable to evaluate the interior stresses directly. For constant (or linear) cells, the singularities of the initial stress (strain) kernels can be eliminated analytically or semi-analytically (Riccardella, 1973; Mendelson and Albers, 1975; Zheng and Gao, 1986; Gao and Lu, 1992; Telles, 1983; Chandra and Saigal, 1991). For arbitrary cells of more complex geometry and higher order shape functions, however, more general techniques have to be used. To make the strongly singular domain integrals bounded, Banerjee and Davies (1984) and Banerjee and Raveendra (1986) excluded a small sphere around the singular point and employed the volume sub-division technique, proposed by Lachat and Watson (1975) and coded by Mustoe (1984), to accurately calculate the weakly singular integrals.

A different approach for direct evaluation of principal value integrals was developed by Huber et al. (1996) and Cisilino et al. (1998), based on work by Guiggiani and Gigante (1990) and Guiggiani et al. (1992).

Another strategy for evaluation of the strongly singular domain integrals is to isolate the singularity by subtracting the singular term from the principal value integrals, and then

transforming the domain integrals, via Gauss theorem, into surface integrals (Huang and Du, 1988; Zhang et al., 1992; Chen et al., 1996). To circumvent calculation of the transformed integrals over the whole surface of the problem, Dallner and Kuhn (1993) transformed the domain integrals into boundary integrals over the volume cells around the singular point. This improvement saves much computational effort, although, as for other transformation techniques, it has only been implemented with initial strain approaches.

To solve the non-linear system equations, the iterative procedure described by Telles and Brebbia (1979, 1980) based on an initial strain approach is commonly used. On account of the unconditional stability and to speed up the iterative convergence, implicit solution schemes have been developed recently (Telles and Carrer, 1991; Bonnet and Mukherjee, 1996; Poon et al., 1998b; Burghardt and Van, 1998). Among these works, Bonnet and Mukherjee (1996) first applied the *consistent tangent operator* method to the boundary element method. This method, which was first proposed by Simo and Taylor (1985) in the finite element method context, exploits the quadratic rate of convergence in the Newton-Raphson iterative process.

A different type of solution strategy (incremental variable stiffness) was proposed by Banerjee and co-workers (Banerjee et al., 1989; Banerjee, 1994). In this scheme, the internal variables are eliminated, by expressing them in terms of boundary variables, and consequently no iteration is needed.

1.2.3 Boundary Element Method for Multi-Region Problems

In many practical situations, it is necessary to solve problems containing piece-wise homogeneous regions. To solve such problems, multi-region algorithms have been described (Lachat and Watson, 1975; Brebbia and Walker, 1980; Brebbia et al., 1984; Banerjee and Butterfield, 1981; Crotty, 1982; Kane and Saigal, 1990). In these algorithms, the system equations are obtained by assembling each zonal set, by invoking the equilibrium and compatibility conditions at the interface nodes.

The coefficient matrices in BEM, even for a single region, are non-symmetric and fully populated. Hence, it is practically impossible to establish the system equations in core, particularly for large 3D engineering problems. In consequence, a significant application of the multi-region BEM algorithm is to single-zone problems (Butenschon et al., 1989) and

also for eigenvalue extraction in free-vibration analysis (Wilson et al, 1990; and Raveendra and Banerjee, 1992). The rationale here is that if the region of interest is (artificially) partitioned into a number of sub-domains, the resulting system equations become sparse and banded. The gain in computational efficiency more than compensates for the increase in the number of degrees of freedom (Gao and Davies, 1999a).

1.3 Scope of Thesis

Although much excellent work has been done on BEM techniques, many important issues still need to be resolved, such as the corner problem and related multi-region problems; the evaluation of strongly singular domain integrals as well as the solution techniques in non-linear BEM. The following is a short description of the work contained within this thesis.

In Chapter Two, the basic formulation of the BEM in linear elasticity is introduced. Some numerical results demonstrate the application of BEM to half-space problems. In Chapter Three, the key element is the treatment of corners and edges arising in stress-discontinuity problems. A multiple-node technique is employed to solve the corner problem, where displacements are uniquely defined but tractions are multi-valued. Two simple auxiliary equations, which are required to supplement the fundamental boundary integral equations, are derived from the symmetric property and the equilibrium equations of the stress tensor. The numerical implementation of these equations is illustrated for two- and three-dimensional problems.

Chapter Four is on the application of the BEM to multi-region problems, where the emphasis is on the use of the auxiliary equations for the nodes where zones intersect, particular for nodes where more than two zones intersect. Some distinct features for the latter case are demonstrated in applications to a three-zoned cube and a four-zoned thick-wall cylinder. A sub-structure technique is used to establish the system equations, which is also used in Chapter Five to solve the multi-layered half-space problems with inclusions. A novel infinite element formulation suitable for multi-layered media is described in that Chapter and a set of useful analytical expressions is also presented there. Applications to the analysis of the interaction between a pier and the surrounding soil (a two-layered infinite medium) is presented to demonstrate the potential of the technique.

In Chapter Six, general rate-independent elastoplastic constitutive relations used for the non-linear BEM are derived in strain space from Il'iushin's postulate (Il'iushin, 1961; Naghdi and Trapp, 1975b). These relations are valid for hardening, perfect plasticity and softening materials. Consistent tangent operator and Stress-return mapping algorithm for drawing stresses back to yield surface are also derived in this chapter. Formulations for four commonly used criteria with kinematic hardening are given in the final section of this Chapter.

Chapters Seven and Eight are concerned with the further development of the non-linear BEM. An efficient method for evaluation of the strongly singular domain integrals is presented in Chapter Seven. In this method, the strong singularities appearing in the domain integrals are removed by transforming the domain integrals into cell boundary integrals, based on two identities for initial stress and initial strain kernels which are derived in the same Chapter. The formulations derived in the Chapter are fully numerical and have the same simple forms for both 2D and 3D problems. The internal stresses can be accurately calculated using these formulations.

Solution techniques for the non-linear system equations are described in Chapter Eight. Two different techniques are presented there, i.e., a Newton-Raphson iteration scheme and an incremental variable-stiffness algorithm. The former incorporates the consistent tangent operator in the Newton-Raphson iterative process, so a quadratic rate of convergence can be achieved. In the latter, a new variable stiffness solution scheme is proposed, in which the system equations are expressed in terms of *plastic multipliers*. Moreover, iterative processes are presented for both variable stiffness methods. These iterative schemes allow the use of larger load increments. In both solution techniques, since strain space constitutive relations are used, hardening, perfect plasticity and softening behaviour are treated in a unified way. Stress-return mapping algorithms are used in both processes.

A brief description of the computer programs developed using the methods described in this thesis can be found in Chapter Nine, following which several benchmark tests are explored. Finally, some general conclusions and proposals for future work are drawn in Chapter Ten.

Chapter 2

Boundary Element Method for 3D Elasticity

2.1 Introduction

The pioneering work on boundary elements can be dated back to the 1960s to Jaswon and Ponter (1963) and Symm (1964) for torsion problems of shafts with regular cross-sections. Cruse (1969) first used the direct integral equation approach to solve three-dimensional problems employing flat triangular elements, with the displacements and tractions assumed constant over each element, analogous to Rizzo's work (1967) for two-dimensional problems.

Although Cruse (1974) extended his work to linear elements, the substantial improvement to higher-order elements, as used in the finite element method, was first made by Lachat (1975) and subsequently published by Lachat and Watson (1976).

Increasing activity in boundary element research followed the BEM conference held at Southampton University in 1978.

In this chapter, the direct formulation of the BEM for three-dimensional elasticity is presented. The strongly singular integrals of the traction kernel are avoided by making use of the rigid body motion condition and the weakly singular integrals of the displacement kernel are treated by utilizing the property of the degenerated element (Lachat, 1975).

2.2 Governing Equations of Elasticity

The governing differential equations for elasticity are derived from the equilibrium condition:

$$\frac{\partial \sigma_{ij}}{\partial x_i} + b_j = 0 \tag{2.1}$$

in which, b_i and $\ddot{u}_i$ are the components of the body force and acceleration vectors respectively, ρ is the mass density, and σ_{ij} is the symmetrical stress tensor. If the stress tensor at a boundary point is known, the tractions at this point are given via Cauchy's formula as:

$$t_i = \sigma_{ij} n_j \tag{2.2}$$

where n_j are the direction cosines of the outward normal.

Hooke's law, relating the stress and strain tensors in an isotropic elastic solid, can be written as:

$$\sigma_{ij} = \lambda \delta_{ij} \varepsilon_{kk} + 2G\varepsilon_{ij} \tag{2.3a}$$

or

$$\sigma_{ij} = D^e_{ijkl} \varepsilon_{ij} \tag{2.3b}$$

where, the fourth-order elastic constitutive tensor D^e_{ijkl} can be expressed as:

$$D^e_{ijkl} = \lambda \delta_{ij} \delta_{kl} + G(\delta_{ik}\delta_{jl} + \delta_{il}\delta_{jk}) \tag{2.4}$$

in which, G is the shear modulus and λ is the *Lame coefficient,* which can be written as:

$$\lambda = \frac{2G\nu}{1-2\nu} \tag{2.5}$$

The strains can be expressed in terms of displacements as:

$$\varepsilon_{ij} = \frac{1}{2}\left(\frac{\partial u_i}{\partial x_j} + \frac{\partial u_j}{\partial x_i}\right) \tag{2.6}$$

Substituting (2.3a) in (2.1) and using (2.6), it follows that:

$$\frac{G}{1-2\nu}\frac{\partial^2 u_j}{\partial x_i \partial x_j}+G\frac{\partial^2 u_i}{\partial x_j \partial x_j}+b_i=0 \tag{2.7}$$

Equation (2.7) is the well-known Navier's equations for elastostatic problems. After substitution of boundary conditions, the displacements can be solved from (2.7). The fundamental solution (particular solution) of equation (2.7), for a unit point force in an infinite medium, plays a central role in BEM algorithms.

2.3 The Kelvin Fundamental Solution for 3D Elasticity

Assuming that a unit point force P_i is applied at a source point p, a body force b_i^* at a field point q can be written as:

$$b_i^*(p,q)=\delta(x(q)-x(p))P_i \tag{2.8}$$

where $\delta(x(q)-x(p))$ is the Dirac delta function which has the following property for any continuous function f(x), $x\in\Omega$:

$$\int_\Omega \delta(x(q)-x(p))f(q)d\Omega(q)=f(p) \tag{2.9}$$

Substituting (2.8) into (2.7), and noting (2.9), a set of fundamental solutions U_{ij} for displacements can be obtained (Love, 1944). Since the components of the unit force P_i are independent, these solutions can be written as (Brebbia, 1978, for example)

$$U_{ij}(p,q)=\frac{1}{16\pi(1-\nu)Gr}\{(3-4\nu)\delta_{ij}+r_{,i}r_{,j}\} \tag{2.10}$$

where

$$r=\sqrt{r_i r_i} \tag{2.11}$$

$$r_i=x_i(q)-x_i(p) \tag{2.12}$$

$$r_{,i}=\frac{\partial r}{\partial x(q)}=\frac{r_i}{r} \tag{2.13}$$

From (2.6), (2.3) and (2.2), the fundamental solutions for tractions corresponding to (2.10) are given by:

$$T_{ij}(p,q) = \frac{-1}{8\pi(1-\nu)r^2}\{[(1-2\nu)\delta_{ij} + 3r_{,i}r_{,j}]r_{,k}n_k - (1-2\nu)(n_j r_{,i} - n_i r_j)\} \tag{2.14}$$

The solutions $U_{ij}(p,q)$ and $T_{ij}(p,q)$ are the well-known Kelvin fundamental solutions of 3D elasticity. They have the following properties:

- Vanishing at infinity

  $U_{ij} = T_{ij} = 0$ as $r \to \infty$
- Singularity

  U_{ij} and T_{ij} have singularities of orders $O(r^{-1})$ and $O(r^{-2})$, respectively.
- Symmetry of U_{ij}

  $U_{ij}(p,q) = U_{ij}(q,p)$
- Anti-symmetry of T_{ij}

  $T_{ij}(p,q) = -T_{ij}(q,p)$

These properties are of considerable importance in BEM algorithms. The first property enables BEM to automatically model boundary conditions at infinity. On the other hand, they cause difficulties in the numerical evaluation of the relevant integrals. Fortunately, these singularities can be treated by employing various transformation (and other) techniques.

2.4 Betti's Reciprocal Theorem

We assume that a body with domain Ω and boundary Γ is in two equilibrium states. The stresses and strains are denoted by $(\sigma_{ij}, \varepsilon_{ij})$ and $(\sigma^*_{ij}, \varepsilon^*_{ij})$ for the two states, respectively. Using (2.3a), we can see that:

$$\begin{aligned}\sigma_{ij}\varepsilon^*_{ij} &= \lambda\delta_{ij}\varepsilon_{kk}\varepsilon^*_{ij} + 2G\varepsilon_{ij}\varepsilon^*_{ij} \\ &= \lambda\varepsilon_{kk}\varepsilon^*_{ll} + 2G\varepsilon_{ij}\varepsilon^*_{ij} \\ &= (\lambda\delta_{ij}\varepsilon^*_{ll} + 2G\varepsilon^*_{ij})\varepsilon_{ij} \\ &= \sigma^*_{ij}\varepsilon_{ij}\end{aligned} \tag{2.15}$$

So the following integral statement holds:

$$\int_\Omega \sigma_{ij}\varepsilon^*_{ij}d\Omega = \int_\Omega \sigma^*_{ij}\varepsilon_{ij}d\Omega \tag{2.16}$$

Integrating by parts both sides of (2.16) and using (2.1) and (2.6), leads to

$$\int_\Omega b^*_i u_i d\Omega + \int_\Gamma t^*_i u_i d\Gamma = \int_\Omega b_i u^*_i d\Omega + \int_\Gamma t_i u^*_i d\Gamma \tag{2.17}$$

Equation (2.17) is Betti's "Reciprocal Theorem" which will be used to establish boundary integral equations, based on Kelvin's fundamental solutions.

2.5 Boundary Integral Equation

If the first (un-starred) set of quantities in (2.17) correspond to the problem under consideration and the second set of quantities are taken to be Kelvin's fundamental solution, then Betti's reciprocal theorem (2.17) becomes:

$$\begin{aligned} u_i(p) = &\int_\Gamma U_{ij}(p,Q)t_j(Q)d\Gamma(Q) - \int_\Gamma T_{ij}(p,Q)u_j(Q)d\Gamma(Q) \\ &+ \int_\Omega U_{ij}(p,q)b_j(q)d\Omega(q) \end{aligned} \tag{2.18}$$

in which, the lower case letters p and q represent the points taking values in the domain, while the upper case letters Q (and subsequently P) denotes the points on the boundary of the body.

Equation (2.18) is only suitable for evaluation of the interior displacements. To obtain boundary integral equations, a limiting process needs to be taken, in which the interior point p is allowed to approach the boundary point P. The resulting formulation can be expressed (e.g., Brebbia, 1978) as:

$$\begin{aligned} &c_{ij}(P)u_j(P) + \int_\Gamma T_{ij}(P,Q)u_j(Q)d\Gamma(Q) \\ &= \int_\Gamma U_{ij}(P,Q)t_j(Q)d\Gamma(Q) + \int_\Omega U_{ij}(P,q)b_j(q)d\Omega(q) \end{aligned} \tag{2.19}$$

where $c_{ij}(P)$ is a constant depending on the geometric conditions of boundary point P, which can be resolved using either the analytical method proposed by Hartmann (1983) or the rigid body displacement method as described in the sequel. However, for a smooth

boundary point there is a simple form, $c_{ij}(P)=1/2\delta_{ij}$. Comparing (2.19) with (2.18), we can see that the latter is a special case, with $c_{ij}=\delta_{ij}$.

2.6 Numerical Implementation

In principle, the boundary unknowns (displacements and/or tractions) can be obtained from equation (2.19) after imposing the specified boundary conditions. However, it is not possible to obtain closed form solutions in general. So recourse must be had to numerical techniques. The boundary element method (BEM) can be summarized as:

- The boundary is discretised into elements, over which geometry and field variables are approximated by nodal values via shape functions.
- Source point P in (2.19) is collocated at each boundary node, resulting in a system of linear equations.
- The system of equations is solved for the unknown displacements and tractions.

The details of this procedure are described below.

2.6.1 Boundary Discretisation

We assume that the boundary Γ is sub-divided into N elements, each of which forms a piecewise continuous approximation to the boundary. On each element, the positional co-ordinates are calculated by:

$$x_i(\xi,\eta)=\sum_{\alpha=1}^{M} N_\alpha(\xi,\eta)\, x_i^\alpha \qquad (2.20)$$

where, M is number of element nodes, x_i^α is the i-th component of the co-ordinates at node α and $N_\alpha(\xi,\eta)$ are termed "shape functions" which map the global co-ordinate system x_i ,i=1, 2,3, into an intrinsic co-ordinate system (ξ,η). In this work, 8-noded quadratic quadrilateral elements are employed. The shape functions take the form:

$$N_1(\xi,\eta)=\frac{1}{4}(1-\xi)(\eta-1)(\xi+\eta+1)$$

$$
\begin{aligned}
N_2(\xi,\eta) &= \frac{1}{4}(1+\xi)(1-\eta)(\xi-\eta-1) \\
N_3(\xi,\eta) &= \frac{1}{4}(1+\xi)(1+\eta)(\xi+\eta-1) \\
N_4(\xi,\eta) &= \frac{1}{4}(1-\xi)(1+\eta)(\eta-\xi-1) \\
N_5(\xi,\eta) &= \frac{1}{2}(1-\xi^2)(1-\eta) \\
N_6(\xi,\eta) &= \frac{1}{2}(1+\xi)(1-\eta^2) \\
N_7(\xi,\eta) &= \frac{1}{2}(1-\xi^2)(1+\eta) \\
N_8(\xi,\eta) &= \frac{1}{2}(1-\xi)(1-\eta^2)
\end{aligned}
\tag{2.21}
$$

Fig.2.1 shows a typical transformation from global to intrinsic co-ordinate systems.

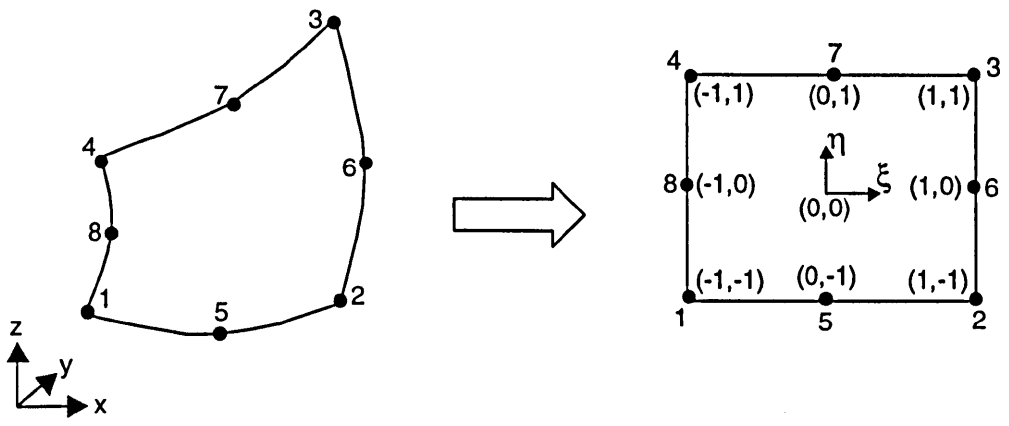

Fig.2.1 Transformation from global to intrinsic co-ordinate systems

The displacements and tractions can also be represented using these same shape functions by:

$$
\begin{aligned}
u_i(\xi,\eta) &= \sum_{\alpha=1}^{8} N_\alpha(\xi,\eta)\, u_i^\alpha \\
t_i(\xi,\eta) &= \sum_{\alpha=1}^{8} N_\alpha(\xi,\eta)\, t_i^\alpha
\end{aligned}
\tag{2.22}
$$

Discretizing the boundary into N_e elements and substituting (2.22) into (2.19) for a collocation point P leads to (without consideration of body forces):

$$c_{ij}(x^P)u_j^P + \sum_{n=1}^{N_e}\sum_{\alpha=1}^{8} u_j^\alpha \int_{-1}^{1}\int_{-1}^{1} T_{ij}(x^P, x(\xi,\eta))N_\alpha(\xi,\eta)J(\xi,\eta)d\xi d\eta$$
$$= \sum_{n=1}^{N_e}\sum_{\alpha=1}^{8} t_j^\alpha \int_{-1}^{1}\int_{-1}^{1} U_{ij}(x^P, x(\xi,\eta))N_\alpha(\xi,\eta)J(\xi,\eta)d\xi d\eta \qquad (2.23)$$

In (2.23), the nodal displacements u_j^α and tractions t_j^α have been taken out of the integrals as they are constants over an element. The Jacobian of the transformation from the global to the intrinsic co-ordinate system is given by:

$$J(\xi,\eta) = |\mathbf{r}_\xi \times \mathbf{r}_\eta| \qquad (2.24)$$

where

$$\mathbf{r}_\xi = \frac{\partial x_1(\xi,\eta)}{\partial \xi}\mathbf{e}_1 + \frac{\partial x_2(\xi,\eta)}{\partial \xi}\mathbf{e}_2 + \frac{\partial x_3(\xi,\eta)}{\partial \xi}\mathbf{e}_3$$
$$\mathbf{r}_\eta = \frac{\partial x_1(\xi,\eta)}{\partial \eta}\mathbf{e}_1 + \frac{\partial x_2(\xi,\eta)}{\partial \eta}\mathbf{e}_2 + \frac{\partial x_3(\xi,\eta)}{\partial \eta}\mathbf{e}_3 \qquad (2.25)$$

in which, $\mathbf{e}_1$, $\mathbf{e}_2$, $\mathbf{e}_3$ are the unit vectors of the global co-ordinate axes.

The integral functions (containing the kernels) can be assembled as follows:

$$c_{ij}(x^P)u_j^P + \sum_{n=1}^{N_e}\sum_{\alpha=1}^{8} H_{ij}^{n\alpha}u_j^\alpha = \sum_{n=1}^{N_e}\sum_{\alpha=1}^{8} G_{ij}^{n\alpha}t_j^\alpha \qquad (2.26)$$

where

$$H_{ij}^{n\alpha} = \int_{-1}^{1}\int_{-1}^{1} T_{ij}(x^P, x(\xi,\eta))N_\alpha(\xi,\eta)J(\xi,\eta)d\xi d\eta$$
$$G_{ij}^{n\alpha} = \int_{-1}^{1}\int_{-1}^{1} U_{ij}(x^P, x(\xi,\eta))N_\alpha(\xi,\eta)J(\xi,\eta)d\xi d\eta \qquad (2.27)$$

Taking each node in turn as the collocation point P and performing the integrations indicated in (2.27), a system of linear algebraic equations is formed by assembling all element contributions, which can be written in matrix form as

$$[H]\{u\}=[G]\{t\} \qquad (2.28)$$

where {u} and {t} are 3N nodal displacement and traction vectors, respectively, and [H] and [G] are 3N×3N coefficient matrices, with N being the total number of nodes.

For a discretized boundary, all nodal degrees of freedom must have a prescribed value of some kind (displacements or tractions). To be able to use standard solvers (such as the

Gaussian elimination technique), the matrices [H] and [G] in (2.28) must be rearranged according to the boundary conditions in such a way that all the unknowns are placed on the left-hand side and the prescribed values are multiplied by relevant coefficients and transferred to the right-hand side. This yields:

$$[A]\{x\}=\{y\} \tag{2.29}$$

The matrix [A] is un-symmetric and fully populated. In general, the unknowns can be obtained from (2.29) by standard matrix reduction methods.

2.6.2 Weakly Singular Integrals—Element Subdivision

Now let us examine the details of the integrals appearing in (2.27). From (2.10) and (2.14) it is observed that these integrals involve singularities as r tends to zero. Hence, special integration schemes become necessary. When the source point P and field point Q are located in different elements, standard Gaussian quadrature may be applied to the U_{ij} and T_{ij} kernels (no singularity). Thus:

$$\int_{-1}^{1}\int_{-1}^{1} f(\xi,\eta)d\xi d\eta = \sum_{m=1}^{G_\xi}\sum_{n=1}^{G_\eta} f(\xi_m,\eta_n)w_m w_n \tag{2.30}$$

where G_m and G_n are the numbers of Gaussian integration points and ξ_m and ξ_m are the Gaussian co-ordinates with associated weighting functions w_m and w_n.

When P and Q are located in the same element, the U_{ij} and T_{ij} kernels are singular because they contain terms of the orders 1/r and $1/r^2$, respectively. In this case, the direct application of Gaussian quadrature is inadequate. However, element sub-division techniques (Lachat, 1975; Lachat and Watson, 1976) can be used to reduce the order of these singularities. For weakly singular integrals, this technique is sufficient.

In the element sub-division technique, an element containing the source node P is further divided into two (for a corner node) or three (for a mid-side node) triangular elements, with P located at a vertex of the triangle. In numerical implementations, two strategies can be used to achieve this purpose. The first is to sub-divide the original element (Mustoe, 1984) by re-determining the global co-ordinates for each sub-element (Fig.2.2). The alternative strategy is to sub-divide the intrinsic element (e.g., Becker, 1992) by determining intrinsic co-ordinates for each sub-element (Fig.2.3).

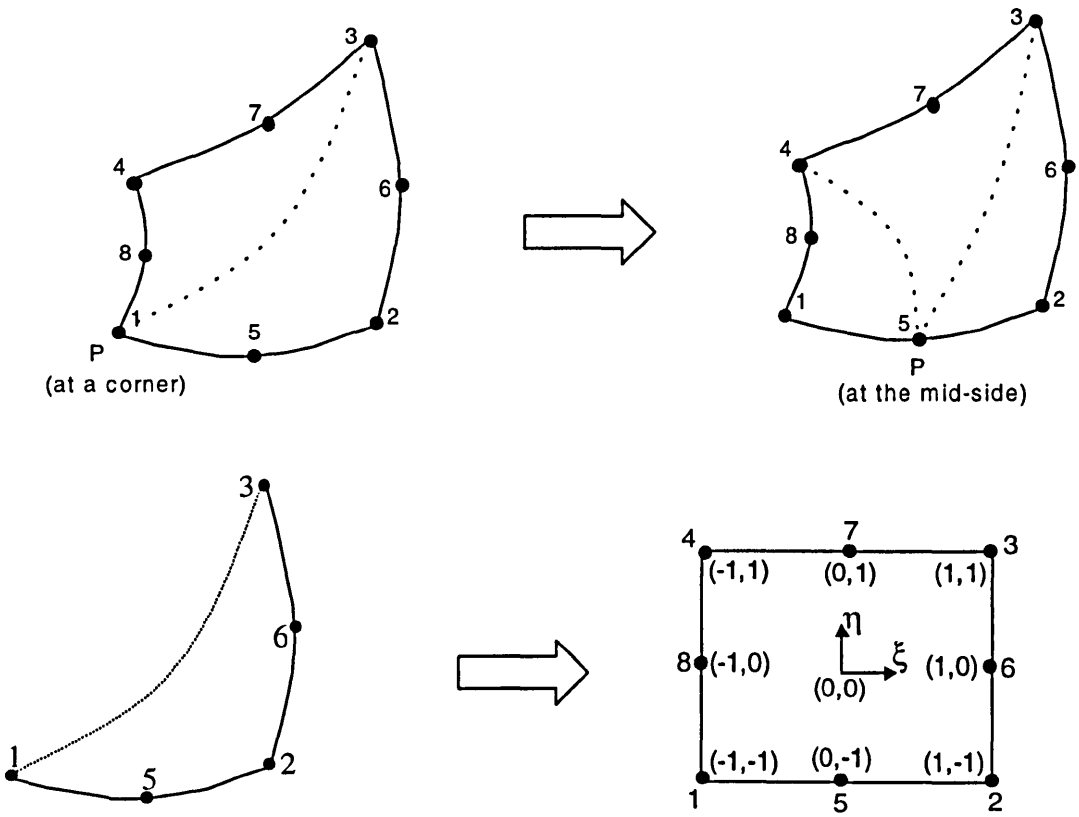

Fig.2.2 Element subdivision and triangle-to-square transformation in global co-ordinate system

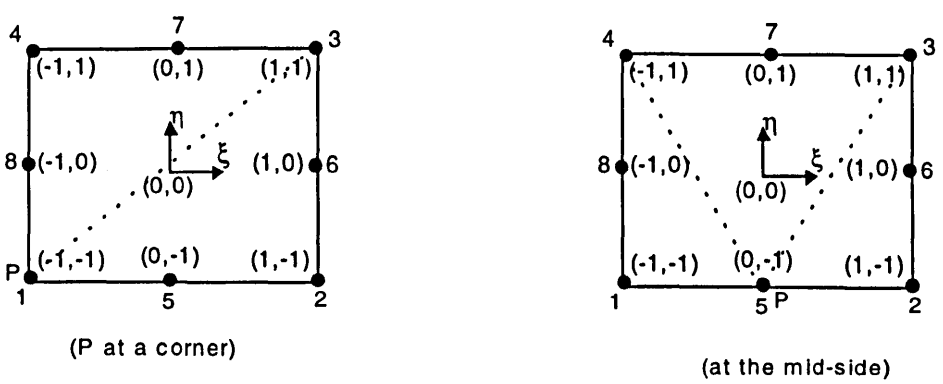

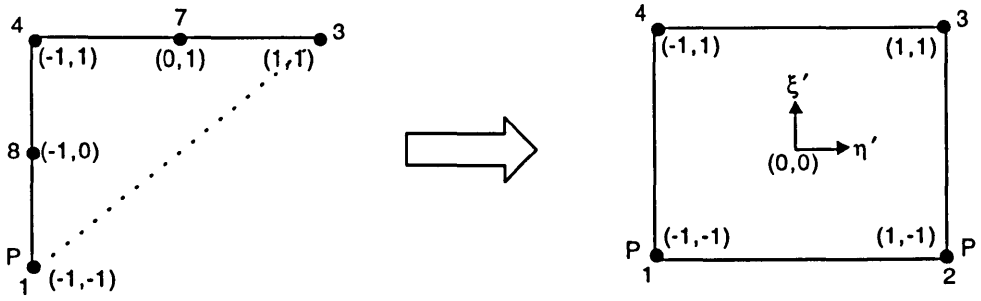

Fig.2.3 Element subdivision and triangle-to-square transformation in intrinsic co-ordinate system

In the first strategy, the Gaussian quadrature formulation (2.30) can be directly applied to all sub-elements. The Jacobian in (2.27) tends to zero as $O(r)$ as $r \to 0$, i.e.,

$$d\Gamma = J\,d\xi d\eta, \qquad J \to O(r) \tag{2.31}$$

as a result of the degeneracy of the nodes coincident with P (Lachat and Watson, 1976). For instance, nodes 1, 8 and 4 in Fig.2.2 have the same co-ordinates as point P. The zero Jacobian effectively reduces the order of singularity of the kernels by one.

In the second strategy, a new set of intrinsic co-ordinates ξ' and η' with their origin at the centre of the element needs to be defined for each sub-element (see Fig.2.3). Linear shape functions are used to determine the original intrinsic co-ordinates for a point in the new intrinsic co-ordinate system, as follows:

$$\begin{aligned} \xi(\xi',\eta') &= \sum_{\alpha=1}^{4} N'_\alpha(\xi',\eta')\,\xi^\alpha \\ \eta(\xi',\eta') &= \sum_{\alpha=1}^{4} N'_\alpha(\xi',\eta')\,\eta^\alpha \end{aligned} \tag{2.32}$$

where the linear rectangular shape functions are defined as:

$$N'_1(\xi',\eta') = \frac{1}{4}(1-\xi')(1-\eta')$$

$$N'_2(\xi',\eta') = \frac{1}{4}(1+\xi')(1-\eta')$$

$$N'_3(\xi',\eta') = \frac{1}{4}(1+\xi')(1+\eta')$$

$$N'_4(\xi',\eta') = \frac{1}{4}(1-\xi')(1+\eta')$$

ξ^α and η^α in (2.32) are the nodal values of the original intrinsic co-ordinates. Now the integrals for boundary element Γ_e can be transformed as follows:

$$\begin{aligned}\int_{\Gamma_e} f(P,Q)d\Gamma &= \int_{-1}^{1}\int_{-1}^{1} f(\xi,\eta)J(\xi,\eta)d\xi d\eta \\ &= \sum_{s=1}^{N_s}\int_{-1}^{1}\int_{-1}^{1} f(\xi(\xi',\eta'),\eta(\xi',\eta'))J(\xi(\xi',\eta'),\eta(\xi',\eta'))J_s(\xi',\eta')d\xi' d\eta'\end{aligned} \tag{2.33}$$

in which N_s is the number of the sub-elements on the boundary element Γ_e and $J_s(\xi',\eta')$ is the Jacobian of the transformation from the original to the new intrinsic co-ordinate system:

$$\begin{aligned}J_s(\xi',\eta') &= \frac{\partial(\xi,\eta)}{\partial(\xi',\eta')} = \begin{bmatrix} \dfrac{\partial\xi^1(\xi',\eta')}{\partial\xi'} & \dfrac{\partial\xi^2(\xi',\eta')}{\partial\xi'} \\ \dfrac{\partial\xi^1(\xi',\eta')}{\partial\eta'} & \dfrac{\partial\xi^2(\xi',\eta')}{\partial\eta'} \end{bmatrix} \\ &= \frac{\partial\xi^1(\xi',\eta')}{\partial\xi'}\frac{\partial\xi^2(\xi',\eta')}{\partial\eta'} - \frac{\partial\xi^2(\xi',\eta')}{\partial\xi'}\frac{\partial\xi^1(\xi',\eta')}{\partial\eta'}\end{aligned} \tag{2.34}$$

The Jacobian $J_s(\xi',\eta')$ tends to zero as $O(r)$ as $r \to 0$, since the original intrinsic co-ordinates of the two nodes associated with P take the same values in the transformed sub-element (Becker, 1992). For instance, the nodes 1 and 2 in the transformed sub-element in Fig.2.3 are made coincident by setting

$$\xi^2 = \xi^1 = -1; \quad \eta^2 = \eta^1 = -1$$

Again the zero Jacobian reduces the singularity of the boundary integrals by one.

From (2.10) it can be seen that the kernel U_{ij} are singular with order $O(r^{-1})$, so the integrals in (2.27a) are weakly singular. After using the element sub-division technique, these singularities are eliminated. However, from (2.14) it is observed that the integrals involved in the integrals of (2.27b) are strongly singular. After using the element sub-division technique, one order of singularity still remains. Other techniques must be employed in this case.

2.6.3 Strongly Singular Integrals—Rigid Body Considerations

The strongly singular integration in (2.27b), together with the constant c_{ij}, yields the diagonal terms of the matrix [H] in (2.28). Accurate evaluation of these terms is critically important. Although direct evaluation of these integrals is possible by utilizing certain co-ordinate transformations (Guiggiani and Gigante, 1990), by far the most popular method is to use the rigid body motion constraint. Three cases need to be consided:

- **Closed region problems**

Assuming a unit rigid body displacement in the n-th direction of the cartesian co-ordinates, the tractions must all be zero, i.e.,

$$\begin{aligned} u_j &= \delta_{jn} \\ t_j &= 0 \end{aligned} \tag{2.35}$$

and hence from (2.28):

$$[H]\{I\}^n = 0 \tag{2.36}$$

where $\{I\}^n$ contains unit displacements for all nodes in the n direction and zero in any other direction. From (2.36) it is apparent that:

$$[H]_{ii} = -\sum_{\substack{j=1 \\ j\neq i}}^{N} [H]_{ij} \tag{2.37}$$

which implies that the diagonal terms of the matrix [H] can be determined from the sum of the corresponding off-diagonal terms.

- **Infinite region problems**

The boundary of infinite region problems can be divided into a finite part Γ and an infinite part Γ_∞. Assuming rigid body displacement and substituting (2.35) into (2.19), it follows that:

$$c_{in}(P) + \int_{\Gamma} T_{in}(P,Q)d\Gamma(Q) + \int_{\Gamma_\infty} T_{in}(P,Q)d\Gamma(Q) = 0$$

The last integral on the left-hand side can be integrated analytically, thus:

$$\int_{\Gamma_\infty} T_{in}(P,Q)d\Gamma(Q) = -\delta_{in} \tag{2.38}$$

Consequently, the diagonal terms consisting of the free terms and singular components can be calculated from:

$$[H]_{ii} = [I] - \sum_{\substack{j=1 \\ j\neq i}}^{N} [H]_{ij} \tag{2.39}$$

where [I] is the 3×3 identity matrix.

- **Semi-infinite region problems**

As for infinite region problems, the boundary of semi-infinite regions can be divided into a finite part Γ, including the half-space surface, and the infinite half-spherical boundary $\Gamma_{H\infty}$ (Fig.2.4).

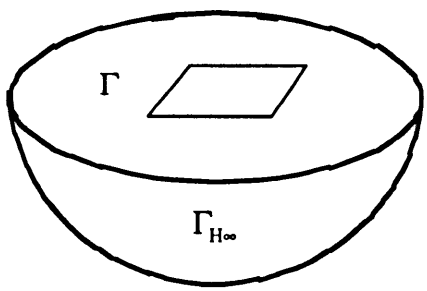

Fig.2.4 Boundary division of semi-infinite region

Using (2.35) in (2.19) it follows that

$$c_{in}(P) + \int_{\Gamma} T_{in}(P,Q)d\Gamma(Q) + \int_{\Gamma_{H\infty}} T_{in}(P,Q)d\Gamma(Q) = 0 \tag{2.40}$$

The last integral on the left-hand side can be integrated (Gao and Davies, 1998a) as

$$\int_{\Gamma_{H\infty}} T_{in}(P,Q)d\Gamma(Q) = -\frac{1}{2}\delta_{in} \tag{2.41}$$

Hence, the diagonal terms can be determined from:

$$[H]_{ii} = \frac{1}{2}[I] - \sum_{\substack{j=1 \\ j\neq i}}^{N} [H]_{ij} \tag{2.42}$$

Application and verification of (2.37) and (2.39) to closed and infinite regions can be found throughout the literature. However, few workers (Liu and Farris, 1993; Davies and Bu,1996; Gao and Davies, 1997, 1998a) have described the application of (2.42) to semi-infinite problems. In the next section, this formulation will be applied to flexible and rigid foundations embedded in semi-infinite media.

2.7 Application to Foundation Problems

The utility of the BEM algorithm described above is demonstrated by analyzing flexible and rigid foundations embedded in an half-space. Equation (2.42) is used to determine the strong singularity. The infinite (free) surface is truncated at a radius of 50 times the foundation dimensions. The region so enclosed is discretized using five (only) elements (excluding the foundation) in the radial direction. The exterior boundary is free, since the surface is assumed infinite.

2.7.1 Square Flexible Foundation on a Semi-Infinite Medium

The vertical displacements u_z on the surface of the elastic half-space due to uniformly distributed vertical pressure P acting on a square foundation (Fig.2.5a) are calculated. Fig.2.5b shows the BEM mesh of the foundation. Due to symmetry, only a quarter of the foundation is considered. The discretisation required (giving a total of 320 nodes) 95 quadratic elements, including 25 elements for the foundation. Analytical solutions for points beneath the foundation by Giroud (1968) were used to verify the results. Tables 2.1-2.3 show the computed vertical displacements beneath the foundation.

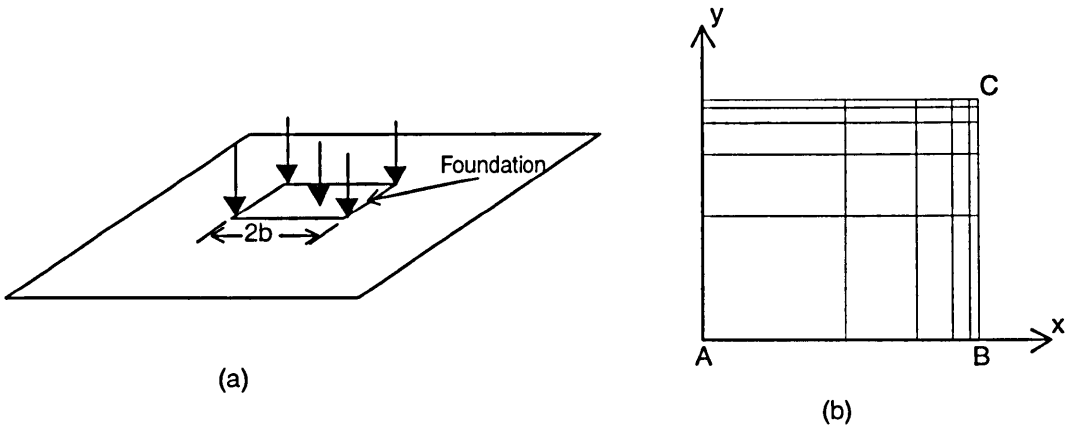

Fig.2.5 Square foundation embedded in semi-infinite space
(a) Schematic model; (b) BEM mesh (quadrant)

Table 2.1 Dimensionless displacement (Gu_z/Pb) beneath *corner* of foundation (point C)

ν	Current	Analytical	Error (%)
0	0.5623	0.5611	0.21
0.3	0.3931	0.3928	0.08
0.5	0.2809	0.2806	0.11

Table 2.2 Dimensionless displacement (Gu_z/Pb) beneath *centre of a side* (point B)

ν	Current	Analytical	Error (%)
0	0.7637	0.7660	0.30
0.3	0.5351	0.5362	0.20
0.5	0.3834	0.3830	0.11

Table 2.3 Dimensionless displacement (Gu_z/Pb) beneath *centre of* the foundation (point A)

ν	Current	Analytical	Error (%)
0	1.1184	1.1222	0.34
0.3	0.7846	0.7855	0.11
0.5	0.5618	0.5611	0.12

The agreement between the numerical results and the analytical solution is excellent. In this example, 25 elements were used for the foundation. However, it was found that if only one quadratic element was used over a quadrant of the foundation, the errors were still less than 1%. The reason for using so many elements is that the same mesh was employed for the rigid foundation: in that case, the tractions at the edge of the foundation are infinite. Of course, a mesh containing elements of greatly differing sizes requires careful integration of the kernel functions. An adaptive algorithm for this purpose is necessary (Gao and Davies, 1999b).

2.7.2 Square Rigid Foundation on a Semi-Infinite Medium

A smooth rigid square foundation, with the same geometry as in Example 2.7.1 is now considered. The BEM mesh used in above example is also adopted. The boundary condition is now vertical displacement rather than distributed force. The Poisson's ratio ν takes the value of 0.3. Since, in theory, the traction t_z at the edges of the foundation are infinite, the results are sensitive to the sizes of the element at the edges. Five different mesh schemes were employed, differing in the ratios adopted between the dimensions of adjacent elements. Fig.2.6 shows the variation of the traction t_z along the central line AB for the case in which the edge element width is 0.41% of the half-foundation width b. The tractions rise monotonically towards the edge and the edge singularity is clearly resolved. Numerical trials show that if one uses a coarse mesh, the singularity can contaminate the (traction) solutions towards the interior of the foundation. Nevertheless, the vertical compliance is determined satisfactorily even with a coarse mesh. Fig. 2.7 is a convergence study which depicts the results for various edge element sizes, where the total force F is calculated by integrating the vertical tractions.

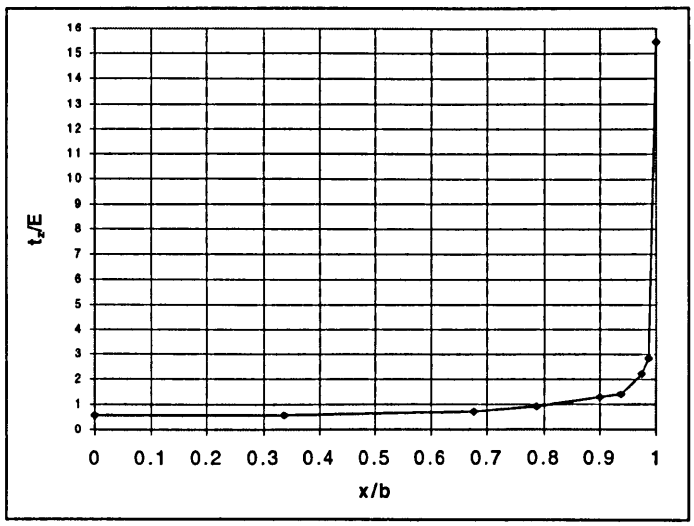

Fig.2.6 Vertical traction along central axis (u_z=1)

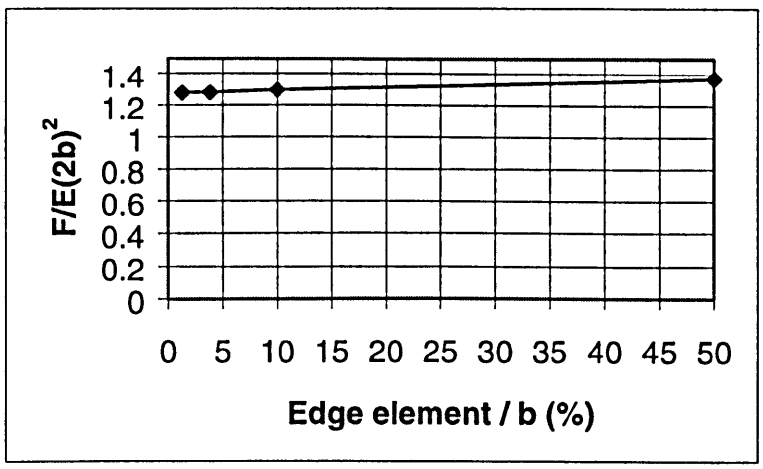

Fig.2.7 Convergence study (edge element width)

The approximate analytical solution (Whitman and Richart, 1967) relating vertical displacement to vertical load can be written as:

$$u_z = \frac{F(1-\nu^2)}{2\beta_z Eb}$$

They obtained the value 1.087 for the coefficient β_z. However, the value for β_z determined from the numerical results is 1.156 (approximately 7% higher). Since our numerical results converge to this latter value, we are reasonably confident that the approximate analytical solution is in error.

2.7.3 Circular Rigid Foundation on Semi-Infinite Medium

This example concerns a smooth circular rigid foundation (with radius a=1) subjected to unit vertical displacement. The problem is discretized using 75 quadratic elements, including 45 foundation elements, with a total of 260 nodes. Fig.2.8 shows the schematic model and the BEM mesh for one quadrant of the foundation. Table 2.4 gives the computed values of the reaction F, for three valuesof Poisson's ratio, and for unit Young's modulus.

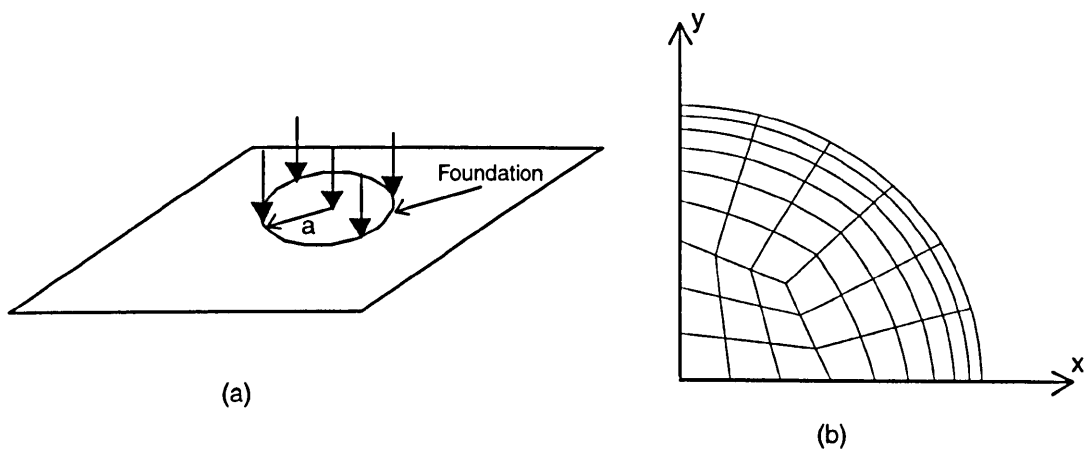

Fig.2.8 Circular rigid foundation on semi-infinite space
(a) Schematic model; (b) BEM mesh

Table 2.4 Reaction F to rigid disk displacement (a=1, E=1)

ν	Current	Analytical	Error (%)
0.0	2.015	2.	0.7
0.3	2.207	2.198	0.45
0.5	2.671	2.663	0.3

From the comparison between the numerical and the analytical solutions (Poulos and Davis, 1974), it can be seen that although the vertical tractions are singular at the edge of the rigid foundation, the computational results are still in very good agreement with the analytical solutions. This lends weight to the earlier conjecture that the analytical solution for the square rigid foundation is inaccurate.

2.7.4 Discussion

From above examples, it is clear that excellent results can be obtained simply by truncating the infinite free surface sufficiently far from the region of interest. Moreover, the unloaded region can be modelled using only a coarse mesh, provided that diagonal terms are computed using (2.42). This treatment can save a great deal of computer memory and computational effort. One needs only contrast this with the demands of an equivalent finite element analysis to see how effective this BEM approach is.

2.8 Summary

In this Chapter, the basic boundary integral equations for elasticity are reviewed. The numerical implementation of these integral equations using the boundary element technique are described, with the focus on the treatment of the singularities. The weakly singular surface integrals are accurately evaluated by means of an element sub-division technique, while the strongly singular integrals are treated using the rigid body motion constraint. In addition to the well-known formulations (2.37) and (2.39) for closed and infinite problems, a formulation (2.42) is presented for semi-infinite problems. Applications to some simple foundation problems illustrate the effectiveness of the algorithm.

Chapter 3

Corners and Edges in Discontinuous Traction Problems

3.1 Introduction

Boundary element method solutions are now available for many problems in applied mechanics and the method has substantial advantages over other numerical techniques, in some respects. However, in order to develop efficient numerical algorithms of general validity, a number of issues require special attention.

One of these issues is the treatment of discontinuities in the geometry and in the boundary conditions. It is well known that at corner nodes, the displacements are uniquely defined but the surface tractions are multi-valued, due to the different outward normal vectors. One obvious way to tackle such problems is to "round-off" corners and edges (Jaswon and Symm, 1977). Alternatively, one can simply assume that the tractions are equal for each of the surfaces meeting at the corner node (Cruse, 1974). Lachat and Watson (1976) suggested that the errors incurred by this treatment were mainly confined to the corner and were not significant at distant points. But Alarcon et al. (1979) pointed out that this can lead to significant errors in the evaluation of the solution at interior points.

Although it is not always necessary to obtain detailed results at or near a boundary discontinuity, these simple procedures can not be satisfactory since the results, even at some distance away from the rounded edges or corners, must be affected (Banerjee and Butterfield, 1981). Moreover, there is a large class of problems involving re-entrant corners, etc., where results at (or near to) the geometric discontinuity form the most important part of the solution. On the other hand, in multi-zone problems it is evidently

impossible to round-off the interface corners and edges. Particularly, for corners where more than two zones meet, the assumption of "equal tractions" usually leads to unacceptable results.

In order to resolve the corner problem, Riccardella (1973) introduced the "double-node" concept for two-dimensional (2D) problems, whereby nodes were placed close to both sides of each corner. This technique requires a sufficiently large gap between the corner nodes, so that the equations written for each node are well-conditioned. Brebbia and Dominguez (1977) later elaborated the use of this technique (which they term 'binodes') for linear elements. Determining the optimal gap width is problematic.

A popular method to treat the corner problems is the use of discontinuous elements (Patterson and Sheikh, 1984; Brebbia and Dominguez, 1992). In this method, the multiple nodes defined over different elements intersecting at a corner are moved inside their corresponding elements. This method can avoid the problems incurred at the corner but results in discontinuous boundary displacements and tractions. Although this method is very flexible, it does present some drawbacks:

- The total number of degrees of freedom is greatly increased.
- The interpolation functions depend on the position of the node inside the elements.
- More refined numerical integration procedures are generally required due to the need to evaluate nearly singular integrals when integrating over neighbouring elements.
- Some cases require the introduction of transitional semi-discontinuous elements.
- It is difficult to resolve the stress concentration at corners or edges.

On the basis of the symmetry of the stress tensor and the invariance of the trace of the strain tensor, Chaudonneret (1978) derived two auxiliary relationships among the traction components, consistent with 2D linear elasticity. A simpler approach using basically the same principle was developed by Yan and Lin (1994) and Mustoe (1980) who used a polynomial interpolation (within a local triangular region) to establish a relationship between tractions and displacements. Wardle and Crotty (1978) described a formulation of this type for linear elements while Rudolphi (1983) described an implementation using quadratic elements for zoned problems, including discontinuous stress components. In a different way, Zhang and Mukherjee (1991) generated auxiliary equations, for plane strain,

by expressing the stresses at a corner surface point as a linear combination of tractions and tangential displacement derivatives.

Numerous other methods also have been suggested to treat corner problems. For example, Alarcon et al. (1979) related the displacements to the principal stresses at the corners, and used these principal stresses as the primary unknowns. Gray & Luts (1990) used multiple nodes to represent the geometry, and the auxiliary equations are obtained by differentiating the usual boundary integral equation.

Most of the existing auxiliary equations are based on Hooke's law, and therefore rely on isotropic elastic material properties. It is difficult to establish unified equations for linear, non-linear, 2D and 3D problems. Besides, some auxiliary equations were derived from the "unique stress" assumption at a corner. This assumption does not hold true for some situations (Zhang and Mukherjee, 1991).

In this Chapter, a novel set of auxiliary equations is derived from the symmetry property and the equilibrium equations of the stress tensors. These equations have been applied to multi-region 3D problems. Detailed numerical implementation formulations are given and are followed by some numerical examples. For the purpose of further development, some 2D situations are also discussed in the chapter.

3.2 Multiple Node Concept for Corners and Edges

At a corner node, the displacements are uniquely defined but the tractions are multi-valued. We define a node for each of the elements (surfaces) which meet at the same corner (or edge) point, but have different outward normals. Thus, for N original boundary nodes, including corner nodes, and $\tilde{N}$ additional corner and edge nodes, the resulting BEM equations will be

$$[H]\{u\} = [\tilde{G}]\{t\} \tag{3.1}$$

where, [H] is a 3N×3N matrix and $[\tilde{G}]$ is a 3N×3(N+$\tilde{N}$) matrix.

We can see that the fundamental BEM formulation (2.26) can provide only 3N equations for displacements and tractions through collocation of points. The number of unknowns in the final system equations, after assembling the prescribed boundary conditions, depends on the situations at the corners.

Assuming that two elements share a common node at a corner, we can identify six possible scenarios, as shown in Fig.3.1. In this Figure, the notations **u, t, u/t** denote the boundary conditions; displacements specified, tractions specified, and mixed conditions specified, respectively.

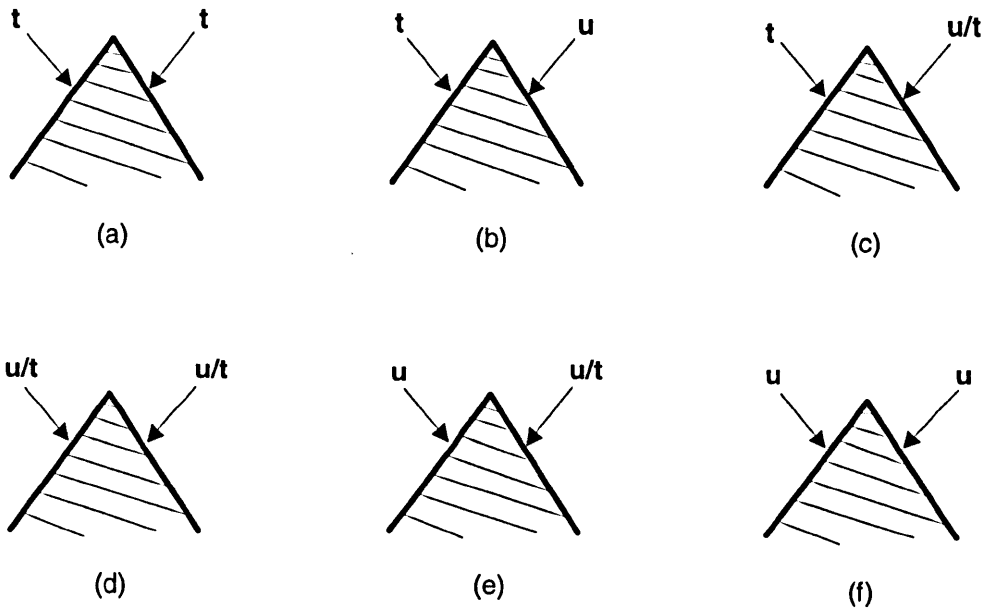

Fig.3.1. Boundary conditions at a corner

For scenarios (a), (b) and (c), the solution of equation (3.1) presents no difficulty, because after assembling the boundary conditions, only 3N unknowns remain. However, for scenarios (d) and (e) (mixed boundary conditions) and (f) (all the components of the displacements are prescribed), the tractions at the corner nodes can not be condensed, so that more unknowns than equations remain. Auxiliary equations must be established in these cases.

3.3 Auxiliary Equations for Corners and Edges

In this section, two sets of auxiliary equation are derived to supplement those from the boundary integral equations. The first of these sets of equations is novel and has been published (Gao and Davies, 1999a). Much of this Chapter is based on that paper.

3.3.1 First Auxiliary Equation based on the Stress Equilibrium Equation

Differentiating (2.2), we obtain:

$$\frac{\partial t_i}{\partial x_i} = \frac{\partial(\sigma_{ij} n_j)}{\partial x_i} = n_j \frac{\partial \sigma_{ij}}{\partial x_i} \tag{3.2}$$

and using the equilibrium equations (2.1) to eliminate the stress tensor, the following relationship can be derived, after replacing the index j by i in the final result:

$$\frac{\partial t_i}{\partial x_i} = 0 \tag{3.3}$$

in which, the convention that the repeated subscript (i) implies summation is adopted, as elsewhere in this thesis.

Although the traction vector has three components, it should be noted that the derivatives in (3.3) are only meaningful on a surface since the tractions are surface fields. As shown in the sequel, this means that we must operate on (3.3) over a boundary element. Although this yields only one auxiliary equation for each of the intersecting surfaces, they are linearly independent since they are derived from the geometry of different surfaces. Further, they are valid whether the stress field is continuous or discontinuous around a corner or edge, because the derivation is based only on the equilibrium equations of the stress tensors, which always hold true.

For 2D corner problems, equation (3.3) provides exactly the right number of equations. However, in some 3D problems (e.g. edge in Fig.3.2 and corner in Fig.3.3), more equations are required.

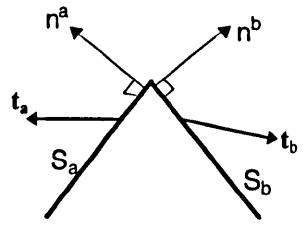

Fig.3.2 Two surfaces meeting at an edge

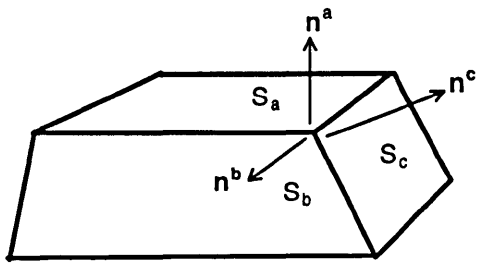

Fig.3.3 Three surfaces meeting at a corner

3.3.2 Second Auxiliary Equation based on Stress Symmetry

In order to obtain enough auxiliary equations, we assume that the stress tensor is continuous around a corner or edge. Referring to Fig.3.2, the unit outward normals $\mathbf{n}^a$ and $\mathbf{n}^b$ relate to surfaces S_a and S_b, respectively. Application of (2.2) to surfaces S_a and S_b, yields:

$$t_i^a = \sigma_{ij} n_j^a \tag{3.4}$$

$$t_i^b = \sigma_{ij} n_j^b \tag{3.5}$$

Multiplying both sides of (3.4) and (3.5) by n_i^b and n_i^a, respectively, yields:

$$n_i^b t_i^a = n_i^b \sigma_{ij} n_j^a \tag{3.6}$$

$$n_i^a t_i^b = n_i^a \sigma_{ij} n_j^b \tag{3.7}$$

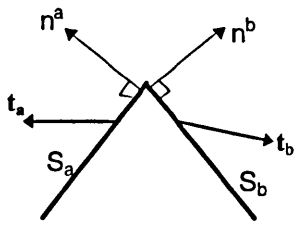

Fig.3.2 Two surfaces meeting at an edge

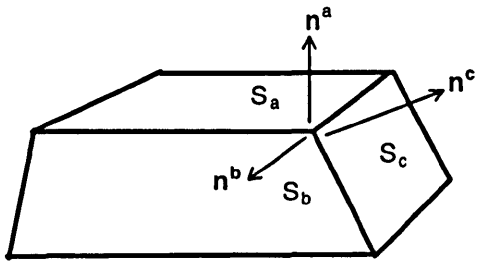

Fig.3.3 Three surfaces meeting at a corner

3.3.2 Second Auxiliary Equation based on Stress Symmetry

In order to obtain enough auxiliary equations, we assume that the stress tensor is continuous around a corner or edge. Referring to Fig.3.2, the unit outward normals $\mathbf{n}^a$ and $\mathbf{n}^b$ relate to surfaces S_a and S_b, respectively. Application of (2.2) to surfaces S_a and S_b, yields:

$$t_i^a = \sigma_{ij} n_j^a \tag{3.4}$$

$$t_i^b = \sigma_{ij} n_j^b \tag{3.5}$$

Multiplying both sides of (3.4) and (3.5) by n_i^b and n_i^a, respectively, yields:

$$n_i^b t_i^a = n_i^b \sigma_{ij} n_j^a \tag{3.6}$$

$$n_i^a t_i^b = n_i^a \sigma_{ij} n_j^b \tag{3.7}$$

Using the symmetry property of the stress tensor, $\sigma_{ij} = \sigma_{ji}$, (3.7) becomes

$$n_i^a t_i^b = n_i^a \sigma_{ji} n_j^b = n_j^b \sigma_{ji} n_i^a = n_i^b \sigma_{ij} n_j^a \tag{3.8}$$

On contrasting (3.8) with (3.6), it follows that:

$$n_i^b t_i^a = n_i^a t_i^b \qquad \text{or} \qquad \mathbf{n}^b \cdot \mathbf{t}^a = \mathbf{n}^a \cdot \mathbf{t}^b \tag{3.9}$$

Equation (3.9) states that the projection of traction vector $\mathbf{t}^a$ on the normal direction $\mathbf{n}^b$ is equal to the projection of traction vector $\mathbf{t}^b$ on the normal direction $\mathbf{n}^a$. Obviously this is one of the basic results of the property of reciprocity (Saada, 1974). In the 2D case, it reduces to:

$$n_1^b t_1^a - n_1^a t_1^b = n^a t_2^b - n_2^b t_2^a \tag{3.10}$$

This is the result obtained by Chaudonneret (1978) by considering the symmetry of the stress tensor, $\sigma_{12}=\sigma_{21}$. From the derivation of (3.9), it can be see that the property of the stress tensor, $\sigma_{ij}=\sigma_{ji}$, only provides one additional equation for both 2D and 3D problems, notwithstanding published statements to the contrary (Chaudonneret, 1978).

Equations (3.9) and (3.3) together generate enough supplemental equations for a 3D corner or edge. In the sequel, further details of the application of these results to specific problems are given for clarity.

3.3.3 Remarks on the Application of the Auxiliary Equations

Some remarks on the application of the auxiliary equations (3.3) and (3.9) is given in the following for 2D and 3D problems.

- 3D single-region problems

For the edge node, as shown in Fig.3.2, nine quantities are involved (three displacement components, u_i, and six traction components, t_i^a and t_i^b, i=1,2,3). We have also nine equations (three from BEM equation (3.1), one from (3.9), two from (3.3) for surfaces S_a

and S_b respectively, and three from the prescribed boundary conditions: displacements/tractions or mixed). For three surfaces meeting at a corner node (see Fig.3.3), twelve quantities are involved (three displacement components, u_i, and nine traction components, t_i^a, t_i^b and t_i^c, i=1,2,3). For this case, we can establish twelve equations (three from (3.1), three from (3.9) for S_a-S_b, S_b-S_c and S_c-S_a respectively, three from (3.3) for surfaces S_a, S_b and S_c respectively, and three from the prescribed boundary conditions). So, for 3D single-region problems, the corner problem is resolved.

- 2D single-region problems

For 2D problems, there may be more equations than quantities, so we only need to choose some of equations obtained from (3.3) and (3.9) to assemble into the global system of equations. For example, for the corner shown in Fig.3.2, six quantities are involved (two displacement components, u_i, and four traction components, t_i^a and t_i^b, i=1,2), but we can establish seven equations (two from (3.1), one from (3.9), two from (3.3), and two from the prescribed boundary conditions). Only two of the auxiliary equations from Eq.(3.3) for the edges S_a and S_b are required.

- Multi-zone problems

Strictly speaking, for the corners on common boundaries shared by three or more regions, the use of (3.9) may lead to invalid results. As a example, we consider a point at which three regions intersect in a plane (Fig.3.4). For convenience of analysis, we separate the body along the common boundaries and analyze the normal tractions.

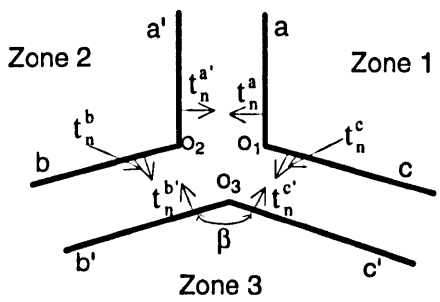

Fig.3.4. Separated corner of three-zone intersection

According to (3.9), we can establish the following equation for corner $\angle b'o_3c'$:

$$n^{b'}t_n^{c'} = n^{c'}t_n^{b'}$$

and using the interface equilibrium condition:

$$t_n^b + t_n^{b'} = 0$$
$$t_n^c + t_n^{c'} = 0$$

we see that when $\beta \rightarrow 180^0$, i.e., $n^{b'} = n^{c'}$, the following result may be obtained:

$$t_n^b = t_n^c$$

But this is false in general when the elastic moduli of zones 1 and 2 are different.

On the other hand, (3.3) is valid for multi-zone problems. However, it should be noted that after using the interface equilibrium conditions, only one equation is independent for a common boundary, although two equations can be established using (3.3) for two surfaces in contact. Even so, we can still obtain enough equations to deal with problems involving the interaction of several zones. For example, after consideration of the interface equilibrium conditions, there are twelve unknowns for the 3D three-zone problem shown in Fig.3.4 (three displacement components and nine traction components associated with the three common surfaces). We can establish twelve equations (nine from (3.1) for the three zones and three from (3.3) for the three common surfaces). For more than three-zones, there may be more auxiliary equations available than unknowns. In such cases, the redundant equations may be discarded.

3.4 Numerical Implementation of Auxiliary Equations

No particular difficulties arise in incorporating (3.9) into the BEM code. But (3.3) is expressed in differential form, so this must be recast into a more convenient form. Further, as mentioned earlier, since tractions are surface fields, (3.3) must be expressed in terms of boundary quantities, i.e., nodal tractions and nodal coordinates.

Using the interpolation function N_α, the co-ordinates and tractions at a point can be expressed as:

$$x_i = N_\alpha(\xi)x_i^\alpha \tag{3.11}$$

$$t_i = N_\alpha(\xi)t_i^\alpha \tag{3.12}$$

where x_i^α and t_i^α (with i=1-2(3) for 2D (3D) problems) are the nodal co-ordinates and tractions and ξ is the intrinsic co-ordinate ((ξ,η) if for 3D problems).

Differentiating (3.12):

$$\frac{\partial t_i}{\partial x_j} = \frac{\partial t_i}{\partial \xi_k}\frac{\partial \xi_k}{\partial x_j} \text{ or } \qquad \left[\frac{\partial t}{\partial X}\right] = \left[\frac{\partial t}{\partial \xi}\right]\left[\frac{\partial \xi}{\partial X}\right] \tag{3.13}$$

In order to evaluate matrix $\left[\frac{\partial \xi}{\partial X}\right]$, differentiating (3.11) yields

$$dx_i = \frac{\partial x_i}{\partial \xi_k}d\xi_k \quad \text{or} \quad [dX] = \left[\frac{\partial X}{\partial \xi}\right][d\xi] \tag{3.14}$$

Multiplying both sides of (3.14) by the transpose of the matrix $\left[\frac{\partial X}{\partial \xi}\right]$, we obtain:

$$[L]^T[dX] = [L]^T[L][d\xi] \tag{3.15}$$

where

$$[L] = \left[\frac{\partial X}{\partial \xi}\right] \quad \text{or} \quad [L]_{ik} = \frac{\partial x_i}{\partial \xi_k} = \frac{\partial N_\alpha}{\partial \xi_k}x_i^\alpha \tag{3.16}$$

in which $[L]_{ik}$ represents the (i, k)th element of the matrix [L].

Now $[L]^T[L]$ on the right-hand side of (15) is a square matrix, thus:

$$[d\xi] = \left([L]^T[L]\right)^{-1}[L]^T[dX] \tag{3.17}$$

This process projects the spatial vector d**x** on to the ξ plane.

Obviously, (3.17) results in:

$$\left[\frac{\partial \xi}{\partial X}\right] = \left([L]^T[L]\right)^{-1}[L]^T \tag{3.18}$$

Similar to (3.16), the following equations can be written:

$$\left[\frac{\partial t}{\partial \xi}\right]_{ik} = \frac{\partial N_\alpha}{\partial \xi_k} t_i^\alpha \text{ or } \left[\frac{\partial t}{\partial \xi}\right] = [t][N'] \tag{3.19}$$

where the elements of the matrices [t] and [N'} are:

$$[t]_{i\alpha} = t_i^\alpha, \qquad [N']_{\alpha k} = \frac{\partial N_\alpha}{\partial \xi_k} \tag{3.20}$$

Finally, substituting (3.19) into (3.13) and the result into (3.3), the following equation can be derived:

$$\mathrm{Tr}\left([t][N']\left[\frac{\partial \xi}{\partial X}\right]\right) = n_i(\rho \ddot{u}_i - f_i) \tag{3.21}$$

in which Tr denotes the trace of a matrix and $\left[\frac{\partial \xi}{\partial X}\right]$ is obtained from (3.18).

In the sequel, this result (equation (3.21)) is elaborated for 2D and 3D problems.

3.4.1 Formulation for two-dimensional problems

Fig.3.5 shows a quadratic isoparametric boundary element for 2D problems. It is assumed that one of the nodes is at a corner or at an edge.

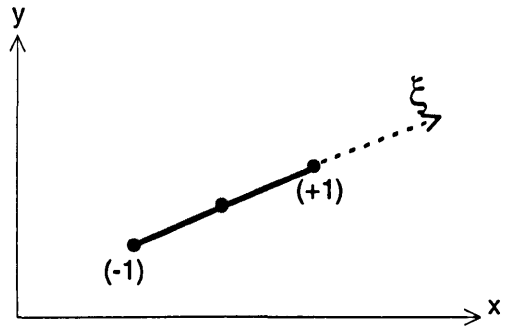

Fig.3.5 A quadratic boundary element for 2D problems

For this 2D case, equation (3.16) becomes:

$$[L]=\begin{bmatrix}\dfrac{\partial x}{\partial \xi}\\ \dfrac{\partial y}{\partial \xi}\end{bmatrix} \tag{3.22}$$

Substituting the above equation into (3.18), it follows that:

$$\left[\frac{\partial \xi}{\partial X}\right]=\frac{1}{|J|}[\ell_1,\ \ell_2] \tag{3.23}$$

where

$$\ell_1=\frac{\partial x}{\partial \xi}\Big/\sqrt{\left(\frac{\partial x}{\partial \xi}\right)^2+\left(\frac{\partial y}{\partial \xi}\right)^2}$$

$$\ell_2=\frac{\partial y}{\partial \xi}\Big/\sqrt{\left(\frac{\partial x}{\partial \xi}\right)^2+\left(\frac{\partial y}{\partial \xi}\right)^2} \tag{3.24}$$

$$|J|=\sqrt{\left(\frac{\partial x}{\partial \xi}\right)^2+\left(\frac{\partial y}{\partial \xi}\right)^2} \tag{3.25}$$

and the terms $\dfrac{\partial x}{\partial \xi}$ and $\dfrac{\partial y}{\partial \xi}$ are evaluated using (3.16).

It is evident that the terms ℓ_1 and ℓ_2 shown by (3.24) are the direction cosines of the local axis ξ with respect to the global axes, and $|J|$ is the Jacobian of the transformation. In the light of (3.20) and (3.23), and noticing that the index k is unity here, we obtain:

$$\left([t][N']\left[\frac{\partial \xi}{\partial X}\right]\right)_{ij}=[t]_{i\alpha}[N']_{\alpha k}\left[\frac{\partial \xi}{\partial X}\right]_{kj}=\frac{1}{|J|}t_i^{\alpha}\frac{\partial N_{\alpha}}{\partial \xi}\ell_j \tag{3.26}$$

Finally, substituting the above equation into (3.21), it follows that:

$$\frac{\partial N_{\alpha}}{\partial \xi}\ell_i t_i^{\alpha}=|J|n_i(\rho \ddot{u}_i-b_i) \tag{3.27}$$

Equation (3.27) is suitable for use with linear, quadratic and higher order boundary elements (corresponding to α=2,3 etc.).

3.4.2 Formulation for three-dimensional problems

Fig.3.6 shows a quadratic isoparametric boundary element for 3D problems, with the assumption that one of the element nodes is on a corner.

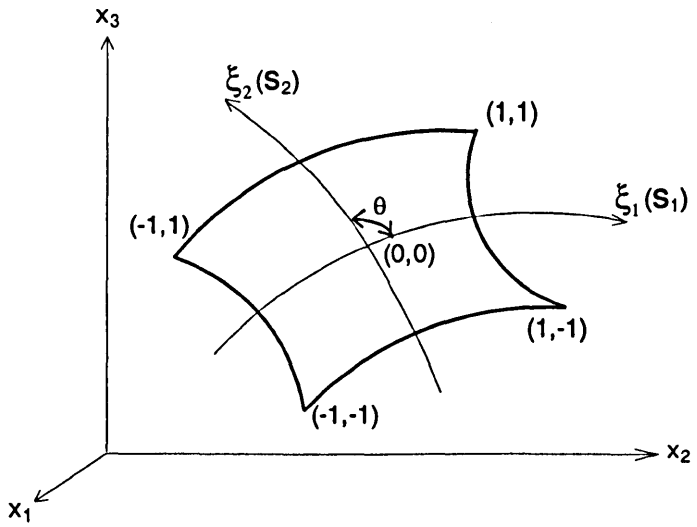

Fig.3.6 An isoparametric element for 3D problems

According to (3.16):

$$[L]=\begin{bmatrix} \frac{\partial x_1}{\partial \xi_1} & \frac{\partial x_1}{\partial \xi_2} \\ \frac{\partial x_2}{\partial \xi_1} & \frac{\partial x_2}{\partial \xi_2} \\ \frac{\partial x_3}{\partial \xi_1} & \frac{\partial x_3}{\partial \xi_2} \end{bmatrix} \tag{3.28}$$

in which $\frac{\partial x_i}{\partial \xi_k}$ are calculated using (3.16).

Substituting (3.28) into (3.18) and after some matrix manipulation, we obtain:

$$\left[\frac{\partial \xi}{\partial X}\right]=\frac{1}{|J|}\begin{bmatrix} \ell_{11} & \ell_{12} & \ell_{13} \\ \ell_{21} & \ell_{22} & \ell_{23} \end{bmatrix} \tag{3.29}$$

where

$$|J| = |S_1 \times S_2| = \sqrt{|S_1|^2 |S_2|^2 - (S_1 \cdot S_2)^2} \tag{3.30}$$

$$\ell_{1i} = c\left(\frac{|S_2|}{|S_1|}\frac{\partial x_i}{\partial \xi_1} - \cos\theta \frac{\partial x_i}{\partial \xi_2}\right) \tag{3.31}$$

$$\ell_{2i} = c\left(\frac{|S_1|}{|S_2|}\frac{\partial x_i}{\partial \xi_2} - \cos\theta \frac{\partial x_i}{\partial \xi_1}\right) \tag{3.32}$$

and

$$|S_k| = \sqrt{\left(\frac{\partial x_1}{\partial \xi_k}\right)^2 + \left(\frac{\partial x_2}{\partial \xi_k}\right)^2 + \left(\frac{\partial x_3}{\partial \xi_k}\right)^2} \tag{3.33}$$

$$S_1 \cdot S_2 = \frac{\partial x_1}{\partial \xi_1}\frac{\partial x_1}{\partial \xi_2} + \frac{\partial x_2}{\partial \xi_1}\frac{\partial x_2}{\partial \xi_2} + \frac{\partial x_3}{\partial \xi_1}\frac{\partial x_3}{\partial \xi_2} \tag{3.34}$$

$$\cos\theta = \frac{S_1 \cdot S_2}{|S_1||S_2|} \tag{3.35}$$

$$c = \frac{1}{\sqrt{1 - \cos^2\theta}} \tag{3.36}$$

In (3.29), ℓ_{11}, ℓ_{12} and ℓ_{13}, and ℓ_{21}, ℓ_{22} and ℓ_{23} are the components of the direction vectors $\mathbf{S}_1$ and $\mathbf{S}_2$ (see Fig.3.6) which are aligned along the intrinsic co-ordinate axes ξ_1 and ξ_2 respectively, and $|J|$ is the Jacobian of the transformation.

Substituting (3.29) into (3.21), a formulation similar to (3.27) is obtained:

$$\frac{\partial N_\alpha}{\partial \xi_k}\ell_{ki} t_i^\alpha = |J| n_i (\rho \ddot{u}_i - b_i) \tag{3.37}$$

in which, indices k=1,2; i=1,2,3 and α=1,..., L, with L being the number of element nodes.

3.5 Numerical Example

A three dimensional BEM computer code to treat the corner and edge problems using the formulations derived in this paper has been written. To demonstrate the validity of this method, several benchmark cases have been examined. One of these is presented here. More complicated applications can be found in Chapter 4.

Fig. 3.7 shows a cube subjected to a uniformly distributed force of P_1=1 on the top surface (z^+) and P_2=2 on the right surface (x^+), subjected to the constraint boundary condition that the front (y^-), back (y^+) and left (x^-) surfaces are roller supports and that the bottom surface (z^-) is fixed. This 3D computational model is actually equivalent to a plane strain problem, as shown in Fig.3.8.

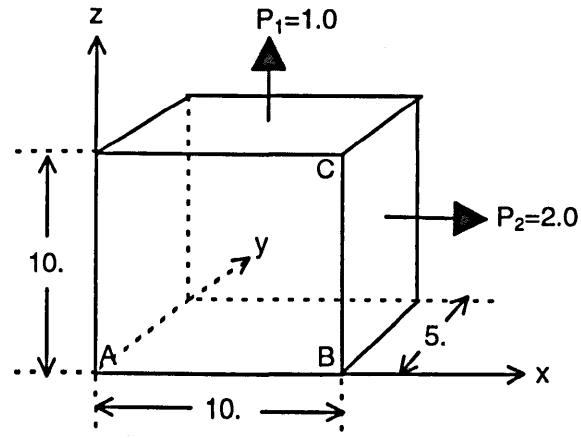

Fig.3.7 A cube under tension

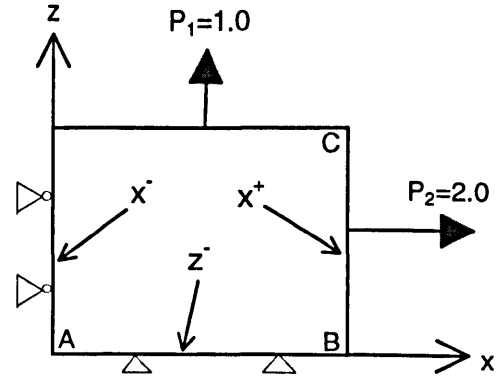

Fig.3.8. Front surface (y^-) of the cube

In Fig.3.7, points A and B are the corner nodes of the three intersecting surfaces, associated with three nodes (defined on the surfaces z^-, x^- and y^- for point A, and z^-, x^+ and y^- for point B).

In the computation, the surfaces of the cube were discretized into eight-noded quadratic isoparametric boundary elements (with three elements in the y-direction and five elements in the x- and z-directions). The Young's modulus E and Poisson's ratio ν were assumed to be unity and 0.3, respectively. For comparison purposes, the same problem was also analyzed using an elementary 3D-BEM program (BEM3D) and a standard plane-strain finite element (FE) program (OASYS). The plane-strain FE discretisation involved the use of one hundred quadratic elements. Tables 3.1 and 3.2 show the calculated tractions and the displacements for some selected points. Table 3.3 shows the stresses at the Gauss points computed by the FE program along the line z=0.1057, and Figs.3.9 and 3.10 show the distributions of the shear and normal tractions on the bottom surface along the line of intersection of the front and bottom surfaces (the x axis).

Table 3.1 Calculated tractions

		Point A			Point B		
	Program	Face z^-	Face x^-	Face y^-	Face z^-	Face x^+	Face y^-
t_x	Current	-0.002	-0.619	0^*	-1.712	2.0^*	0^*
	FEM	-0.007	-0.612	0^*	-1.696	2.010	0^*
	BEM3D	-0.217			-3.149		
t_y	Current	-0.003	0^*	-0.642	-0.005	0^*	0.457
	FEM	0^*	0^*	-0.632	0^*	0^*	0.515
	BEM3D	-0.229			0.351		
t_z	Current	-1.385	0^*	0^*	3.830	0^*	0^*
	FEM	-1.432	-0.007	0^*	3.396	0^*	0^*
	BEM3D	-1.399			3.831		

Note: The superscript '*' indicates a prescribed value.

Table 3.2 Calculated displacements

Point	Program	u_x	u_y	u_z
C	Current	15.3302	0.0000*	0.0078
	FEM	15.3800	0.0000*	-0.0699
	BEM3D	15.3338	0.0000*	0.0102

Table 3.3 Stresses at Gauss points (FE), along the line z=0.1057

No.	x-coordinate	σ_{xx}	σ_{zz}	σ_{xz}	σ_{yy}
1	0.1057	-0.6115	-1.375	-0.0078	-0.5959
2	1.289	-0.6093	-1.3682	-0.0961	-0.5932
3	3.289	-0.5962	-1.3302	-0.2564	-0.5779
4	6.289	-0.5430	-1.1737	-0.5711	-0.5150
5	8.817	-0.5624	-0.9437	-1.0716	-0.4518
6	9.683	0.1900	1.5280	-1.6957	0.5154

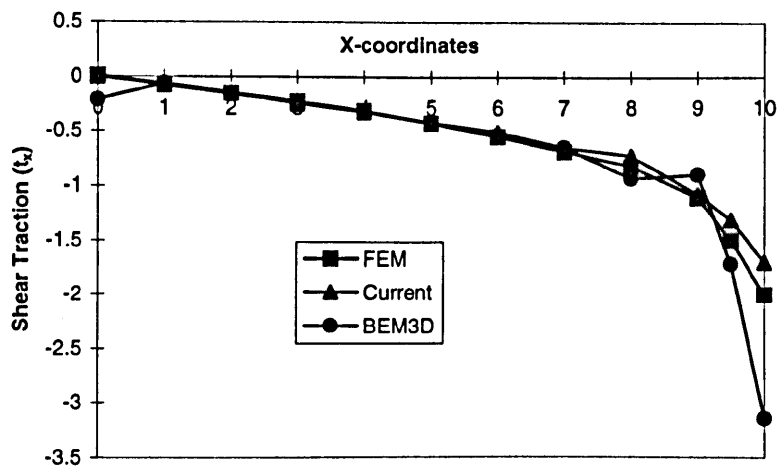

Fig.3.9 Shear tractions along bottom of the cube

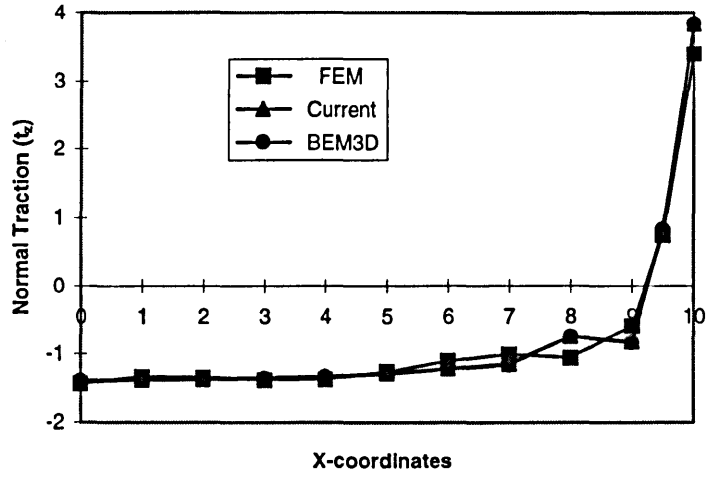

Fig.3.10 Normal tractions along bottom of the cube

The results shown in Table 3.1 illustrate the very good agreement between the results obtained using the current program and those from the finite element program. The discrepancies are believed to be due to discretisation effects and, particularly, the calculation and interpolation of the (FE) tractions from the stresses (given in Table 3.3) at the Gauss points (since stresses are not computed on the surfaces).

By contrast, the elementary boundary element program (BEM3D) often yields misleading results. These appear in some instances to be (approximately) the 'average' value of the independent tractions at each of the intersecting surfaces, although this is not always the case. It should be noted that this program does return the correct traction value when only one value is unspecified.

By contrast, in this particular case, the results recorded in Table 3.2 show that displacements are largely unaffected by the treatment of the corners. This is not a result which can be relied upon in general.

Further detailed information on the distribution of tractions along the bottom of the cube is depicted in Figs.3.9 and 3.10. Particularly evident in Fig.3.9 is the improvement obtained by properly modelling the corner problem.

3.6 Summary

Novel auxiliary equations, which are required to supplement the fundamental boundary integral equations in discontinuous boundary traction problems, are derived for 2D and 3D problems from the equilibrium equations and the symmetric property of the stress tensor. These equations can be used to deal with the corners and edges of single region and multi-region problems in elastostatics, plasticity and dynamics. For 2D problems, these auxiliary equations do not invoke the assumption of a continuous stress field, but this more restrictive assumption may be required for some 3D problems.

Chapter 4

Boundary Element Method for Multi-Region Problems

4.1 Introduction

The boundary element method has developed rapidly for problems involving homogeneous regions. However, in many practical situations, it is necessary to solve problems containing piece-wise homogeneous regions. Consequently, several multi-region BEM algorithms have been developed (Lachat and Watson, 1975; Brebbia and Walker, 1980; Brebbia et al., 1984; Banerjee and Butterfield, 1981; Crotty, 1982; Kane and Saigal, 1990). In these algorithms, the system equations are obtained by assembling each zonal set, by invoking the equilibrium and compatibility conditions at the interface nodes.

The coefficient matrices in BEM, even for a single region, are non-symmetric and fully populated. Hence, it is practically impossible to establish the system equations in core, particularly for large 3D engineering problems. However, the use of multi-region BEM can significantly increase computational efficiency (Butenschon et al., 1989). The rationale here is that if the region of interest is (artificially) partitioned into a number of sub-domains, the resulting system equations become sparse and banded. The gain in computational efficiency more than compensates for the increase in the number of degrees of freedom. Other significant applications of the multi-region BEM algorithm are to fracture mechanics (Cruse and Myers, 1977; Perucchio and Ingraffea, 1985; Crotty and Wardle, 1985; Raveendra and Cruse, 1989; Beer, 1993) and eigenvalue extraction in free-vibration analysis (Wilson et al, 1990; and Raveendra and Banerjee, 1992).

In multi-region BEM algorithms, two important issues must be paid particular attention. The first and most important issue is the treatment of corners and edges. It is well known that at corners or edges, the displacements are uniquely defined but the surface tractions are multi-valued. Although rounding-off corners and edges can indeed give good results for some single region problems, it is evidently impossible to round-off interface corners and edges in multi-zone problems. In the sequel, it is also demonstrated using numerical examples that the unique traction assumption at a two-zone intersecting corner (or edge) can provide reasonable approximate solutions, but for corners where more than two zones meet, the unique traction assumption usually leads to unacceptable results.

The commonly accepted method for the treatment of corners and edges where several regions intersect is to introduce additional nodes at the corners and edges, and then develop auxiliary equations to determine the additional unknowns (Gao and Davies, 1999a). For example, Banerjee (1994) introduced a resistance relationship, for potential problems, at each node of each interface element to eliminate the additional unknowns. Rudolphi (1983) described an implementation using quadratic elements for zoned problems, including discontinuous stress components.

The second issue in multi-region BEM is the equation solution technique. The system equations, as noted above, are generally sparse, block-banded and nonsymmetric. They are also often not positive-definite nor diagonally dominant, and often ill-conditioned. Numerous solution strategies have been proposed for solving such equations. A direct matrix block factorization process has been described by Banerjee and Butterfield (1981), Brebbia and Walker (1980), Lachat and Watson (1975, 1977), and Crotty (1982) which exploits the substantial (block) sparsity. Tomlin (1972), Butterfield and Tomlin (1971), Bailecki and Nahlik (1987) and Bailecki (1987) have described unsymmetric sparse block-banded frontal equation solving algorithms. Kane et al. (1990) described a zone condensation technique to save computer storage space.

Iterative solution techniques have recently begun to receive significant favourable attention from boundary element researchers (Kane et al., 1991; Prasad et al., 1994 and Leung and Walker, 1997); the advantages of the GMRES algorithm described by Saad and Schultz (1986) are increasingly recognized. This algorithm operates directly on the original set of unsymmetric matrix equations and therefore requires only one matrix-vector multiplication in each iteration.

Singular value decomposition (SVD) (Press et al., 1992) deals with equation sets that are singular or nearly so. Although this technique is relatively slow, it is reliable. Consequently, it has been adopted in this study, whenever the need has arisen.

In this Chapter, the multi-region problem is addressed using the multiple node concept and the auxiliary equations derived in the previous chapter are used to close the equation set. In addition, two assembly processes, which have some novel aspects, are also presented to establish the system equations.

4.2 Multi-Region BEM Algorithms

Various assembly methods can be used to establish the multi-region system equations (e.g. Banerjee and Butterfield, 1981; Brebbia et al., 1980, 1984; Kane et al., 1990). In the present study, we employ a different (substructure) technique. The discretized BEM equation (3.1) for the i-th zone can be expressed as:

$$[H^i]\{u^i\}=[G^i]\{t^i\} \tag{4.1}$$

$[H^i]$ and $[G^i]$ are square and rectangular coefficient matrices, respectively, and $\{u^i\}$ and $\{t^i\}$ are column vectors of nodal displacements and tractions.

We collect the nodes for each zone into two sets. The first set includes the nodes solely associated with a single region. This set of nodes are called 'external nodes' and will be eliminated at the zonal level. The remaining nodes reside on region-to-region interfaces. For convenience, all the nodes associated with corner and edge points are classified into the latter set. Equation (4.1) can then be written in the form:

$$\begin{bmatrix} [H^i_{EE}] & [H^i_{EI}] \\ [H^i_{IE}] & [H^i_{II}] \end{bmatrix} \begin{Bmatrix} \{u^i_E\} \\ \{u^i_I\} \end{Bmatrix} = \begin{bmatrix} [G^i_{EE}] & [G^i_{ES}] \\ [G^i_{IE}] & [G^i_{IS}] \end{bmatrix} \begin{Bmatrix} \{t^i_E\} \\ \{t^i_S\} \end{Bmatrix} \tag{4.2}$$

in which, the subscript I denotes displacements at the region-to-region interface nodes (Fig.4.1); the subscript S denotes tractions at the system nodes (interface and additional nodes), and the subscript E denotes the quantities at the remaining external nodes associated with a single region, and which will be eliminated at the zonal level.

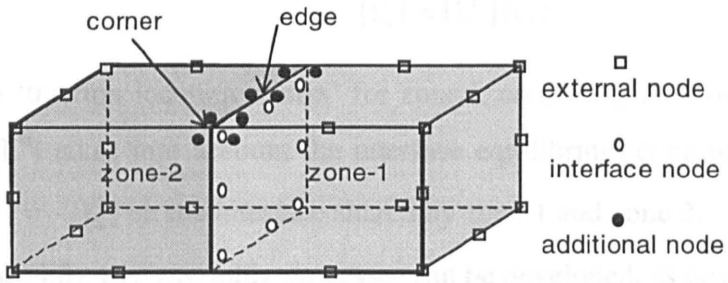

Fig.4.1 A two-zone problem

The boundary conditions are applied at the zonal level and, after shifting the unknowns to the left-hand side, then the block-banded matrix (4.2) gives:

$$[A^i_{EE}]\{X^i_E\}+[H^i_{EI}]\{u^i_I\}=[G^i_{ES}]\{t^i_S\}+\{B^i_E\} \tag{4.3}$$

and:

$$[A^i_{IE}]\{X^i_E\}+[H^i_{II}]\{u^i_I\}=[G^i_{IS}]\{t^i_S\}+\{B^i_I\} \tag{4.4}$$

From (4.3):

$$\{X^i_E\}=[A^i_{EE}]^{-1}\left(-[H^i_{EI}]\{u^i_I\}+[G^i_{ES}]\{t^i_S\}+\{B^i_E\}\right) \tag{4.5}$$

Substituting the above equation into (4.4) yields:

$$[C^i_{II}]\{u^i_I\}=[D^i_{IS}]\{t^i_S\}+\{Y^i_I\} \tag{4.6}$$

where

$$[C^i_{II}]=[H^i_{II}]-[A^i_{IE}][A^i_{EE}]^{-1}[H^i_{EI}]$$

$$[D^i_{IS}]=[G^i_{IS}]-[A^i_{IE}][A^i_{EE}]^{-1}[G^i_{ES}] \tag{4.7}$$

$$\{Y^i_I\}=\{B^i_I\}-[A^i_{IE}][A^i_{EE}]^{-1}\{B^i_E\}$$

It is convenient to define a global traction vector $\{t_S\}$ for all the interface nodes and all the additional nodes, such that the local traction vector $\{t^i_S\}$ can be expressed in terms of $\{t_S\}$ by the equation:

$$\{t_S^i\} = [L^{ti}]\{t_S\} \tag{4.8}$$

where $[L^{ti}]$ is the 'traction location matrix' for zone i, consisting only of 0, 1 and -1. The construction of $[L^{ti}]$ takes into account the interface equilibrium conditions; for example, the condition $\{t_S^1\} = -\{t_S^2\}$ on the interface shared by zone 1 and zone 2.

From (4.6) and (4.8), two assembly processes can be developed, as described below.

4.2.1 Mixture Representation of System Equations

In the similar way to the treatment of tractions, we define a global displacement vector $[u_I]$ for all the interface and additional nodes and introduce a displacement location matrix $[L^{ui}]$ for zone i, consisting of 0, 1, namely:

$$\{u_I^i\} = [L^{ui}]\{u_I\} \tag{4.9}$$

The construction of $[L^{ui}]$ takes into account the displacement compatibility conditions, for example, the condition $\{u_I^1\} = \{u_I^2\}$ on the interface shared by zone 1 and zone 2

Applying (4.6), (4.8) and (4.9) to each zone and assembling all the zonal equations, together with the auxiliary equations (3.37) and (3.9), yields the final system equations. For problems containing m zones, we obtain:

$$\begin{bmatrix} -[D_{IS}^1][L^{t1}] & [C_{II}^1][L^{u1}] \\ -[D_{IS}^2][L^{t2}] & [C_{II}^2][L^{u2}] \\ \cdots & \cdots \\ -[D_{IS}^m][L^{tm}] & [C_{II}^m][L^{um}] \\ [E_A] & [0] \end{bmatrix} \begin{Bmatrix} \{t_S\} \\ \{u_I\} \end{Bmatrix} = \begin{Bmatrix} \{Y_I^1\} \\ \{Y_I^2\} \\ \cdots \\ \{Y_I^m\} \\ \{Y_A\} \end{Bmatrix} \tag{4.10}$$

in which, $[E_A]$ and $\{Y_A\}$ are generated using (3.37) and (3.9), after considering the traction boundary conditions. On solving the system of equations, we obtain the values of the displacements and tractions at the interface nodes and at the additional nodes. Then, through backward substitution, we find all the remaining unknowns.

The advantage of the above assembly process is that we can solve (4.10) simultaneously for both displacements and tractions. The drawback is that it requires relatively large computer memory, although (4.10) only includes the displacements and tractions at

interface and additional nodes. Alternatively, we can employ the following assembly process which needs less storage space.

4.2.2 Traction Representation of System Equations

Since the matrix $[D^i_{IS}]$ in (4.6) is generally not square, no inverse matrix can be found. However, $[C^i_{II}]$ is always square, so from (4.6) and (4.8), it follows that:

$$\{u^i_I\} = [\hat{D}^i_{IS}]\{t_S\} + \{\hat{Y}^i_I\} \tag{4.11}$$

Here:

$$[\hat{D}^i_{IS}] = [C^i_{II}]^{-1}[D^i_{IS}][L^{ii}] \tag{4.12}$$

$$\{\hat{Y}^i_I\} = [C^i_{II}]^{-1}\{Y^i_I\} \tag{4.13}$$

Applying (4.11) to each zone and assembling all the zonal contributions, together with the auxiliary equations (3.37) and (3.9), we obtain the final system equations. The assembly process is performed node-by-node and employs a cyclic rule for the displacement compatibility conditions, i.e.

$$\begin{aligned} &\{u^i_I\} = \{u^j_I\}; \\ &i = 1, 2, ..., m-1; \\ &j = i+1, i+2, ..., m \end{aligned} \tag{4.14}$$

for a node at the intersection of m zones. For example, for a point where three zones intersect, as shown as in Fig.4.2(b), compatibility yields:

$$\{u^1_I\} = \{u^2_I\} \tag{4.15}$$

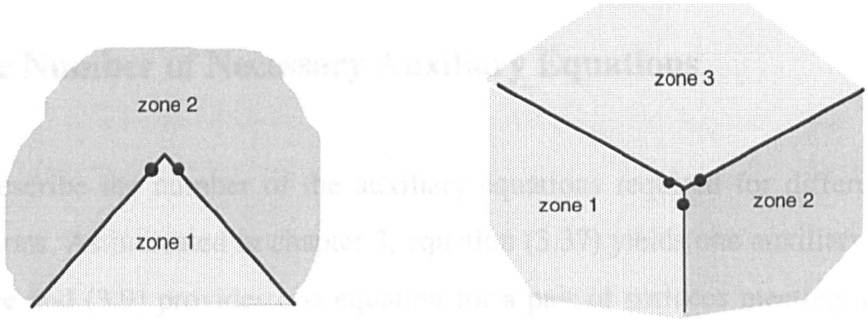

Fig.4.2 (a) Corners of two intersecting zones and (b) three intersecting zones

Also, from (4.11):

$$\left([\hat{D}^1_{IS}]+[\hat{D}^2_{IS}]\right)\{t_S\} = \{\hat{Y}^2_I\} - \{\hat{Y}^1_I\} \tag{4.16}$$

Similarly, we can write two other equations ($\{u^1_I\} = \{u^3_I\}$ and $\{u^2_I\} = \{u^3_I\}$) which, together with the auxiliary equations from (3.37) and (3.9), leads to the system equations:

$$\begin{bmatrix} [\hat{D}^1_{IS}]+[\hat{D}^2_{IS}] \\ [\hat{D}^1_{IS}]+[\hat{D}^3_{IS}] \\ [\hat{D}^2_{IS}]+[\hat{D}^3_{IS}] \\ [E_A] \end{bmatrix} \{t_C\} = \begin{Bmatrix} \{\hat{Y}^2_I\} - \{\hat{Y}^1_I\} \\ \{\hat{Y}^3_I\} - \{\hat{Y}^1_I\} \\ \{\hat{Y}^3_I\} - \{\hat{Y}^2_I\} \\ \{Y_A\} \end{Bmatrix} \tag{4.17}$$

This system set of equations is compact and the unknowns involved are only the tractions at the system nodes (interface and additional nodes), and hence less computer storage space is required. A problem which often occurs in practical problems is that displacements are specified over some of the system nodes. In that case, the corresponding columns of the square matrix $[C^i_{II}]$ in (4.6) are zero after assembling the boundary conditions, which prevents its inversion. In such cases, we set the diagonal elements of these columns to unity and add the specified displacements to the corresponding positions of $\{Y^i_I\}$ in (4.6). The subsequent process is the same as described above.

4.2.3 The Number of Necessary Auxiliary Equations

Now we describe the number of the auxiliary equations required for different corner or edge situations. As indicated in chapter 3, equation (3.37) yields one auxiliary equation for each surface and (3.9) provides one equation for a pair of surfaces meeting at a corner or edge. It is noted that although an interface is shared by two zones, after taking into account the interface equilibrium conditions, the interface equations ((3.37) and (3.9)) for one zone only can be used.

For the 3D two-zone edge intersection shown in Fig.4.2(a) (with two nodes associated with the point), and after consideration of the interface equilibrium conditions, there are nine unknowns (three displacement components and six traction components). Accordingly, nine equations are required. Six equations are provided by the fundamental BEM equation (4.1) and two auxiliary equations can be obtained from (3.37) and one from (3.9).

For the 3D three-zone edge intersection shown in Fig.4.2(b) (with three nodes associated with the point), there are twelve unknowns (three displacement components and nine traction components). So, twelve equations are needed. The fundamental BEM equation (4.1) provides nine equations and hence three auxiliary equations are required. However, we can generate six auxiliary equations (three from (3.37) and another three from (3.9)). In this case, we need to select three from these six. Our experience indicates that selection of equations from (3.37) is superior to those from (3.9).

This analysis is also suitable for 2D corner or edge problems. The following expression can be used to calculate the number (m) of necessary auxiliary equations required for corner or edge points:

$$m = d * (n - z + 1) \tag{4.18}$$

where, d=2 (3) for 2D (3D) problems, n is the number of the nodes associated with the corner or edge point, and z is the number of the zones meeting at the corner or edge point.

4.2.4 Solution Technique for Multi-Region System Equations

In most cases, we can use Gaussian elimination to solve the system equations (4.10) or (4.17). However, if a region is not explicitly prevented from undergoing rigid body displacements, then the solution technique described by (4.10) and inversion of $[C_{II}^{i}]$ in (4.11) fails. For this situation, the singular value decomposition technique (SVD) (Press et al. 1992) provides a convenient means of overcoming the problem, albeit at the expense of greater computational time.

Numerical problems may occur if the ratio of the values of the coefficient matrices of $\{t_S\}$ and $\{u_I\}$ become unduly large. This problem can be circumvented by normalising the coefficients by a representative value of shear modulus. Evidently, the same representative value must be used for all zones.

4.3 Numerical Examples

A 3-D elastostatic multi-region BEM computer code (ESMI-3D) based on the mixture representation (4.10) has been written in FORTRAN 77 using the algorithm presented in this chapter. This code can deal with arbitrarily many zones using 4-node linear and 8-node quadratic elements. As infinite boundary element technique (Davies and Bu, 1996; Gao and Davies, 1997) also has been incorporated into the code so that semi-infinite problems can be solved very efficiently. Two representative examples used to validate the code are described below; these were run on a 486DX/66 microcomputer, using single precision arithmetic. For any interface node, the tractions are referred to the surface of the lower numbered zone. The SVD technique was used for solving these problems, although no singularities were detected in these particular examples (which indicates the auxiliary equations generated using Eqs.(3.9) and (3.37) are linearly independent).

4.3.1 Three-zoned Cube Problem

The first example is a cube, consisting of three zones, subjected to uniform extension, i.e., u=10 (Fig.4.3). Both the central point B and the bottom central point C are represented by three independent nodes, one for each of the faces. The cube is discretized into 88 eight-noded elements (40, 24 and 24 for zones 1, 2 and 3, respectively) with 212 original nodes and 20 additional nodes. All the elements have the same dimension (2.5×2.5).

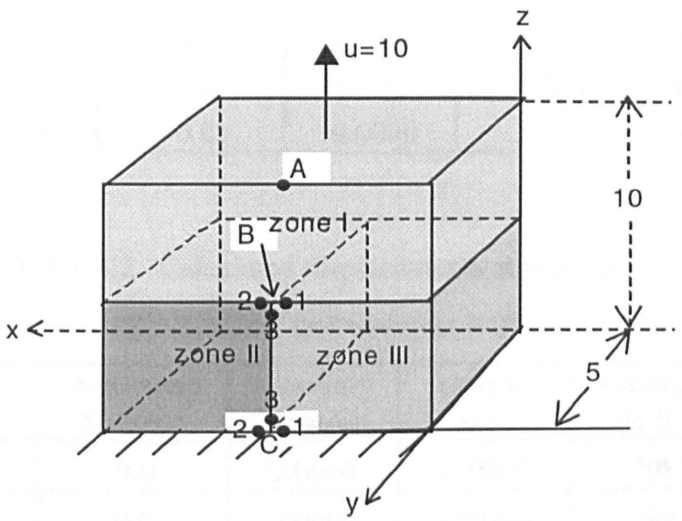

Fig.4.3 A cube undergoing a displacement u=10

To compare with the analytical solution, firstly, we take the mechanical properties of the three zones to be same, i.e., $E_1=E_2=E_3=1$ and $\nu_1=\nu_2=\nu_3=0$. Table 4.1 shows the computed tractions t_z for the nodes associated with points A, B and C. Table 4.2 shows the displacements at the point B, where the column headed by the title 'Auxiliary equation' indicates the results computed using the auxiliary equations presented in this thesis, and the columns headed by the titles 'Unique at C' and 'Unique at B' denote the results obtained by defining only one node at points C and B, respectively. It is evident that these simplified methods fail to capture the correct solution.

Table 4.1 Calculated tractions t_z for interface nodes

($E_1=E_2=E_3=1$ and $\nu_1=\nu_2=\nu_3=0$)

Point	Node	Analytical Solution	Auxiliary equation	Unique at C	Unique At B
A		1.0	1.0000	0.9995	0.4857
B	1	-1.0	-1.0000	-1.0089	-7.6385
	2	-1.0	-1.0000	-0.9994	
	3	0.0	0.0000	0.0030	
C	1	-1.0	-1.0000	-0.0021	-24.0765
	2	-1.0	-1.0000		24.1647
	3	0.0	0.0000		-27.6547

Table 4.2 Calculated displacements at point B

($E_1=E_2=E_3=1$ and $\nu_1=\nu_2=\nu_3=0$)

	Analytical Solution	Auxiliary equation	Unique at C	Unique At B
u_x	0.0	0.0000	-0.0005	-3.7981
u_y	0.0	0.0000	-0.0006	-1.7823
u_z	5.0	5.0000	4.9929	-0.8397

Inspection of these Tables shows that the auxiliary equation algorithm presented in this thesis gives results in excellent agreement with the analytical solutions. The unique (single) node method can only provide approximate results for two zone intersections at corners or edges but for three zones intersecting at corners or edges, the computed results are unacceptable.

Secondly, we take the mechanical properties of the three zones to be $E_1=5$, $E_2=3$ & $E_3=1$, and $\nu_1=\nu_2=\nu_3=0.2$. The tractions at points B and C computed using the present algorithm are given in Table 4.3.

Table 4.3 Traction values

(E_1=5., E_2=3., E_3=1., and $\nu_1=\nu_2=\nu_3$= 0.2)

Point	Node	t_x	t_y	t_z
B	1	1.5749	3.3347	-0.6671
	2	0.8857	-2.4120	-6.1122
	3	-0.8602	-3.2954	1.1881
C	1	-2.4271	-5.6103	-0.4534
	2	-0.4655	3.2384	-6.6272
	3	-1.9077	-5.1288	2.1881

From Table 4.3, we can see that the stress-discontinuity phenomenon due to the different stiffnesses of the materials can be clearly distinguished. This is impossible to discern using the unique node method. Moreover, the application of the unique node method in this case yields even worse results than before.

4.3.2 Four-zoned Thick-Wall Cylinder Problem

The second (three-dimensional) example is a thick circular cylinder subjected to internal pressure, p=1. Fig.4.4 shows the mesh employed which is composed of 4 zones with 48 eight-noded elements (12 elements for each zone), with 131 original nodes and 63 additional nodes. A quarter of the cylinder is analysed. The x-y plane (at z=20) is subjected to 'roller' boundary conditions (u_z=0) and symmetry is assumed about the z=0 plane to simulate a state of plane strain. The vertical (x=0) and horizontal (y=0) boundaries are also 'roller' supports (i.e., u_x=0 and u_y=0, respectively).

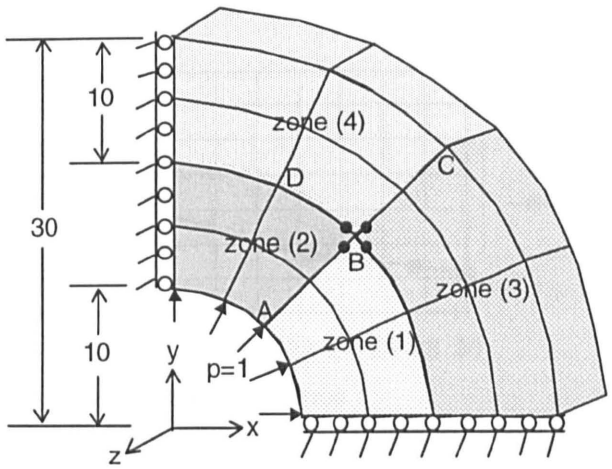

Fig.4.4 Cylinder subjected to internal pressure

To compare with analytical solutions, we assume $E_1=E_2=E_3=E_4=1$ and $\nu_1=\nu_2=\nu_3=\nu_4=0.3$. Figs.4.5 and 4.6 show the variations of the radial displacements and circumferential stresses along the radial (r) direction.

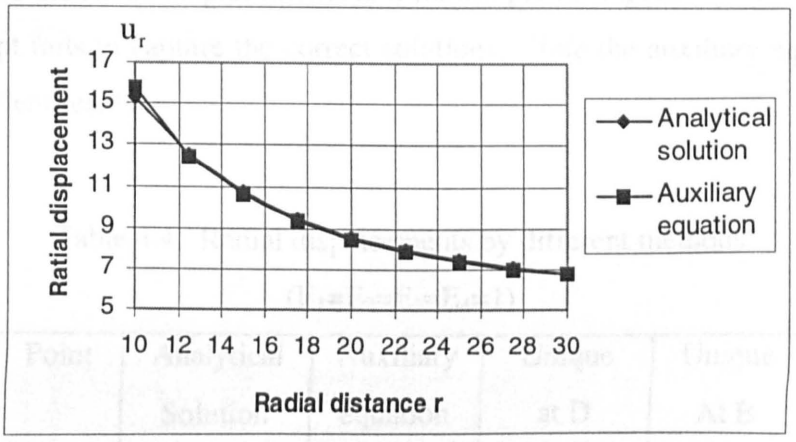

Fig.4.5 Variation of radial displacement vs. radial distance ($E_1=E_2=E_3=E_4=1$)

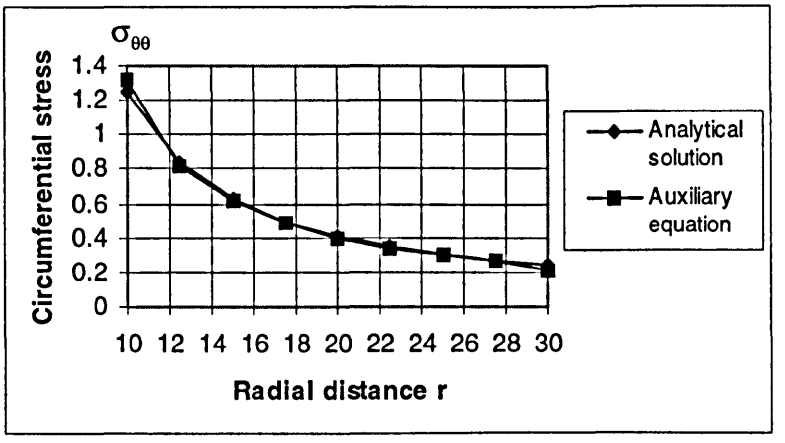

Fig.4.6 Variation of circumferential stress vs. radial distance
($E_1=E_2=E_3=E_4=1$)

From Figs. 4.5 and 4.6, we observe that the auxiliary equation algorithm gives results which are in excellent agreement with the analytical solutions. The small discrepancies at the inner and outer surfaces may be due to the rather coarse mesh adopted.

To compare the results obtained by analytical, auxiliary, and unique node methods, Table 4.4 shows the radial displacements at different points. Again, we see that the unique traction concept fails to capture the correct solutions, while the auxiliary equation method produces excellent results.

Table 4.4 Radial displacements by different methods
($E_1=E_2=E_3=E_4=1$)

Point	Analytical Solution	Auxiliary equation	Unique at D	Unique At B
A	15.275	15.124	14.691	14.540
B	8.613	8.587	8.107	7.731
C	6.825	6.796	6.334	5.928

To examine the effect of piece-wise (zonal) inhomogeneity, analyses have been carried out for $E_1=E_2=1$, $E_3=E_4=3$ and $E_1=E_3=3$, $E_2=E_4=1$. In these analyses, $\nu_1=\nu_2=\nu_3=\nu_4=0.3$. Fig.4.7 shows the circumferential stress variation along the radius ABC (see Fig. 4.4) for these two cases.

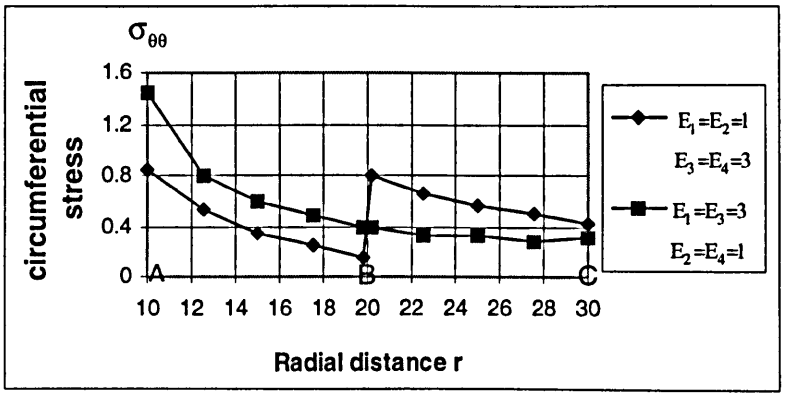

Fig.4.7. Variation of circumferential stress along line ABC

From Fig.4.7, one can observe that the circumferential stress is discontinuous at the point B (more starkly for the first case) because of the non-homogeneous material properties at this interface. This phenomenon can not be captured using the conventional multi-region BEM program.

Radial displacements, also along ABC, are plotted in Fig. 4.8. Naturally, displacements are continuous and, as expected, in the case when the outer region is stiffened, there is a pronounced change in the gradient of the radial displacement.

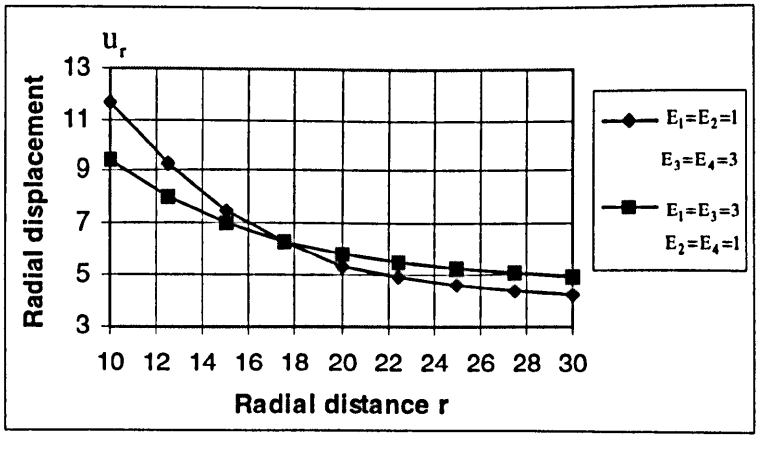

Fig.4.8 Variation of radial displacement along line ABC

4.4 Summary

Two approaches to the solution of the multi-region BEM system equations have been presented, which can deal with arbitrarily many zones. One of these (traction representation method) is particularly advantageous, if computer memory resources are limited. To the author's best knowledge, the multi-region corner/edge problem for more than two intersecting zones is dealt with here for the first time. Some representative numerical results are presented which demonstrate the validity and scope of the algorithm.

Chapter 5

Infinite Boundary Element Technique for Multi-Layered Media

5.1 Introduction

In numerous practical engineering problems, the region of interest extends to infinity. The boundary element method (BEM) is ideally suited for the analysis of such problems because often only a finite region of the surface has to be discretized and the conditions at infinity are automatically satisfied by the fundamental solution. However, for half-space problems, the surface to be discretized also extends to infinity. Although such problems can sometimes be solved by using fundamental solutions for the half-space (Telles and Brebbia, 1981; Jiang, 1986) such as the Mindlin's solution (or Melan's solution) instead of Kelvin's solution, there are some limitations to their use (Beer and Watson, 1989). As demonstrated in Chapter 2, some half-space problems can be satisfactorily solved by simply employing large elements to discretize the far-field of the infinite surface. However, the discretization of the far-field may require the introduction of many more degrees of freedom. A much more effective method is to incorporate infinite elements into the conventional boundary element analysis. Infinite boundary elements were first proposed by Watson (Watson, 1979) and later employed by Beer, Watson and Swoboda (1987) to model a small region of a long tunnel. Zhang et al. (1989) described the application of infinite elements to dam foundations. Beer and Watson (1989) introduced 'ghost' elements in their infinite element formulation in order to exploit the anti-symmetry of the traction kernel. Davies and Bu (1996) developed a semi-analytical approach based on a circular

region of exclusion in the far-field region. The approach is efficient for many problems, but requires the construction of an additional set of elements for each source point.

In this Chapter, the algorithm described by Davies and Bu (1996) is significantly improved (Gao and Davies, 1998a) and extended to multi-layered problems (Gao and Davies, 1998c). Here, the integrals over the infinite surfaces are transformed into line integrals which form a closed contour and are evaluated analytically. Using this formulation, we obviate the need to perform numerical integrations over the entire region. The illustrative example of a deep foundation demonstrates the applicability and accuracy of this novel approach.

5.2 Asymptotic Behaviour of the Far-Field

In this thesis, the multi-layered problem is modelled by subdividing the continuum into sub-regions, each consisting of a single material. All of the infinite surfaces (including the ground surface and the interfaces) bounding the layers are assumed to be parallel. All the layered-regions are composed of two (upper and lower) infinite surfaces and an edge (bounding) surface (S_H), except for the base region which is composed of one infinite surface and an hemisphere. Each infinite surface consists of a finite core region S_F (near-field) and an infinite surface S_I (far-field). Fig.5.1 shows a three-layered infinite model, where the contour Γ_I of the infinite surface S_I extends to infinity.

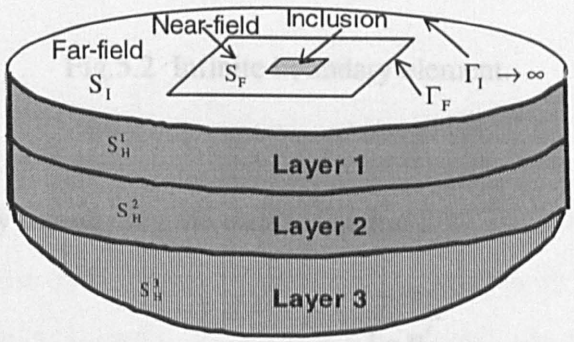

Fig.5.1 Model of the three-layered half-space problem

The traction and displacement conditions at infinity are automatically satisfied by the fundamental solution and we only need to discretise the layer interfaces (including the surface) into elements. For each of these surfaces, the near-field S_F and the boundaries of any inclusions are modelled with (finite) boundary elements and the far-field S_I is modelled by infinite elements, over which the tractions are assumed to be zero and the displacements and co-ordinates are mapped through co-ordinate transformation and decay functions, respectively.

5.2.1 Mapping and discretisation of the Infinite Surfaces

For the infinite boundary elements, the same standard shape functions (2.21) are employed, but we allow one of the intrinsic functions (η) to take the limits -1 to ∞ instead of -1 to +1 (see Fig.5.2)

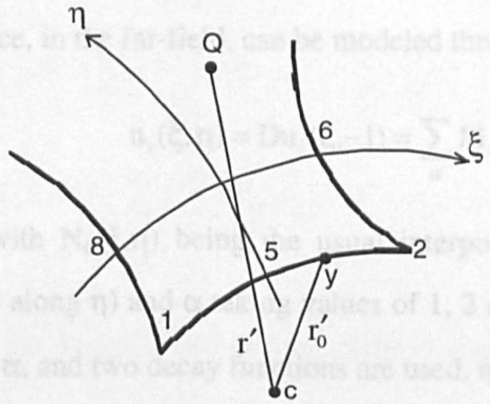

Fig.5.2 Infinite boundary element.

This is accomplished by introducing the transformation :

$$\xi = \xi', \quad \eta = \frac{1+3\eta'}{1-\eta'} \tag{5.1}$$

where both ξ' and η' take values from -1 to +1. Accordingly

$$x_i = N_\alpha(\xi,\eta)x_i^\alpha = N_\alpha\left(\xi_1(\xi',\eta'),\xi_2(\xi',\eta')\right)x_i^\alpha \tag{5.2}$$

Thus, the integrals over infinite elements become:

$$\int_{-1}^{\infty}\int_{-1}^{+1} f(P,Q)d\xi d\eta = \int_{-1}^{+1}\int_{-1}^{+1} f(P,Q)J(\xi',\eta')d\xi' d\eta' \tag{5.3}$$

where the Jacobian of the transformation is given by

$$J(\xi',\eta') = \frac{\partial(\xi,\eta)}{\partial\xi'\partial\eta'} = \frac{\partial\xi}{\partial\xi'}\frac{\partial\eta}{\partial\eta'} - \frac{\partial\eta}{\partial\xi'}\frac{\partial\xi}{\partial\eta'} = \frac{\partial\eta}{\partial\eta'} = \frac{4}{(1-\eta')^2} \tag{5.4}$$

5.2.2 Displacement decay functions

In general, for the analysis of linear half-space problems, boundary elements need to be specified on the surface of the semi-infinite domain. However, the displacement behaviour over this unbounded surface, in the far-field, can be modeled through decay functions as:

$$u_i(\xi,\eta) = Du_i(\xi,-1) = \sum_\alpha M_\alpha Du_i^\alpha \tag{5.5}$$

in which, $M_\alpha=N_\alpha(\xi,-1)$ with $N_\alpha(\xi,\eta)$ being the usual interpolation function (the radial direction is assumed to be along η) and α taking values of 1, 2 and 5, u_i^α are the values of the displacements at node α, and two decay functions are used, namely:

$$D = \frac{r_0'}{r'} \tag{5,6}$$

$$D = e^{1-r'/r_0'} \tag{5.7}$$

where r_0' is the distance from the point y (on the line η=-1) to an arbitrary reference point c, while r' is the distance to the corresponding field point Q (with the same value of ξ as shown in Fig.5.2). Points y, Q and c are co-planar. In general, the reference point c will be located at the centre of the loaded area. The effectiveness of these two different decay functions is demonstrated by some numerical examples, in the sequel.

5.3 Infinite Boundary Element Formulations

In the infinite boundary element approach, only the near-field needs to be discretized into elements and the outer elements bounding the near-field are served by the infinite elements.

5.3.1 Discretisation of the Boundary Integral Equations Involving the Infinite Boundary

With the aid of equation (5.5) and taking into account the traction-free and zero displacement conditions on the infinite surface, the discretised boundary element formulation of (2.19) for an infinite surface (see Fig.5.1) can be written as:

$$
\begin{aligned}
c_{ij}u_j = &\sum_{M'}\sum_{\alpha=1}^{8} t_j^{\alpha}\int_{\Delta S_F} U_{ij}N_{\alpha}d\Gamma + \sum_{M^*}\sum_{\alpha=1}^{8} t_j^{\alpha}\int_{\Delta S_F} U_{ij}N_{\alpha}d\Gamma - \sum_{M'}\sum_{\alpha=1}^{8} u_j^{\alpha}\int_{\Delta S_F} T_{ij}N_{\alpha}d\Gamma \\
&-\sum_{M^*}\sum_{\substack{\alpha'=1 \\ \alpha'\neq\alpha^*}}^{8} u_j^{\alpha'}\int_{\Delta S_F} T_{ij}N_{\alpha'}d\Gamma - \sum_{M^*} u_j^{\alpha^*}\int_{\Delta S_F} T_{ij}N_{\alpha^*}d\Gamma - \sum_{M'}\sum_{\alpha=1}^{3} u_j^{\alpha}\int_{\Delta S_I} T_{ij}M_{\alpha}DD\Gamma \\
&-\sum_{M^*}\sum_{\substack{\alpha'=1 \\ \alpha'\neq\alpha^*}}^{3} u_j^{\alpha'}\int_{\Delta S_I} T_{ij}M_{\alpha'}DD\Gamma - \sum_{M^*} u_j^{\alpha^*}\int_{\Delta S_I} T_{ij}M_{\alpha^*}DD\Gamma
\end{aligned}
\tag{5.8}
$$

in which, ΔS_F and ΔS_I refer to finite and infinite element regions, M refers to elements and α refers to nodes. The prime and the asterisk superscripts refer to non-singular and singular quantities, respectively. It should be noted that for the infinite elements, only the nodes in contact with the finite domain elements are assembled into the system of equations.

5.3.2 Rigid Body Motion Considerations

The two strongly singular integrals, $\int_{\Delta S_F} T_{ij} N_\alpha . d\Gamma$ and $\int_{\Delta S_I} T_{ij} M_\alpha . D d\Gamma$, and the jump term c_{ij} can be determined by indirect means by noting that, for a body undergoing rigid body motion, all of the boundary tractions are zero. However, the method can not be directly applied using equation (5.8) since it contains the decay function D which is incompatible with the rigid body motion constraint. However, the rigid body motion condition can be applied, as usual, to (2.19) from which it follows, for the L-th stratum, that:

$$\begin{aligned} c_{ij} + \sum_{M^*} \int_{\Delta S_F} T_{ij} N_\alpha . d\Gamma + \sum_{M^*} \int_{\Delta S_I} T_{ij} M_\alpha . d\Gamma = -\sum_{M^*} \sum_{\alpha'} \int_{\Delta S_F} T_{ij} N_{\alpha'} d\Gamma - \sum_{M'} \int_{\Delta S_F} T_{ij} d\Gamma \\ - \sum_{M'} \int_{\Delta S_I} T_{ij} d\Gamma - \sum_{M^*} \sum_{\alpha'} \int_{\Delta S_I} T_{ij} M_{\alpha'} d\Gamma - \int_{S_H^L} T_{ij} d\Gamma \end{aligned} \tag{5.9}$$

The last integral (the azimuthal integral) on the right hand side of the above equation can be easily evaluated by making use of spherical polar co-ordinates, which yields:

$$I_{ij}^L = \int_{S_H^L} T_{ij} d\Gamma = \begin{cases} -\frac{1}{2}\delta_{ij} & \text{for the half space} \\ 0 & \text{for other layers} \end{cases} \tag{5.10}$$

The penultimate integral in (5.9) can be evaluated analytically by the method described in the sequel. Meanwhile, substituting (5.9) into (5.8) leads to the regularized form:

$$\begin{aligned} &\{-I_{ij}^L - J_{ij} - \sum_{M'} \sum_{\alpha=1}^{8} \int_{\Delta S_F} T_{ij} N_\alpha d\Gamma - \sum_{M^*} \sum_{\alpha'}^{8} \int_{\Delta S_F} T_{ij} N_{\alpha'} d\Gamma + \sum_{M^*} \int_{\Delta S_I} T_{ij} M_{\alpha^*} (D-1) d\Gamma\} u_i \\ &= \sum_{M'} \sum_{\alpha=1}^{8} t_i^\alpha \int_{\Delta S_F} G_{ij} N_\alpha d\Gamma + \sum_{M^*} \sum_{\alpha=1}^{8} t_i^\alpha \int_{\Delta S_F} G_{ij} N_\alpha d\Gamma - \sum_{M'} \sum_{\alpha=1}^{8} u_i^\alpha \int_{\Delta S_F} T_{ij} N_\alpha d\Gamma \\ &- \sum_{M^*} \sum_{\alpha'}^{8} u_i^{\alpha'} \int_{\Delta S_F} T_{ij} N_{\alpha'} d\Gamma - \sum_{M^*} \sum_{\alpha=1}^{3} u_i^\alpha \int_{\Delta S_I} T_{ij} M_\alpha D d\Gamma - \sum_{M^*} \sum_{\alpha'} u_i^{\alpha'} \int_{\Delta S_I} T_{ij} M_{\alpha'} D d\Gamma \end{aligned} \tag{5.11}$$

where

$$J_{ij} = \int_{S_I} T_{ij} dS \tag{5.12}$$

which arises from the observation that the sum of all shape functions over an element is unity and that the union of all infinite elements constitutes the entire infinite surface. Evidently, all the integrals involved in (5.11) can be computed by means of the standard Gaussian quadrature except for the strongly singular integrals J_{ij} which must be treated separately.

5.4 Analytical Integration over Infinite Elements

The integrals in (5.12) cannot be evaluated numerically by direct means. If the integrals are carried out element-by-element, the sub-integrals are unbounded. Here, this difficulty has been solved analytically by exploiting the anti-symmetry of the traction kernel over the infinite free surface.

5.4.1 Infinite Boundary Integrals in Polar coordinate system

The integral region, i.e. S_I, is shown schematically in Fig.5.3 by the area bounded by the finite region boundary Γ_F and the infinite boundary Γ_∞.

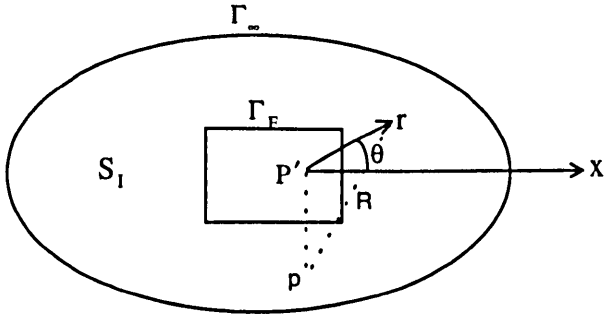

Fig. 5.3 The integral region in the far-field.

We consider a local polar coordinate system (r, θ) with the origin at point P′ in the plane of the half-space surface. P′ has the same co-ordinates x_1 and x_2 as the source point p, which may be inside the body. x_3 is assumed to be in the direction normal to the surface

(Fig.5.3). Noting that $n_1 = n_2 = 0$ and $n_3 = 1$, the components of the traction fundamental solutions (2.14) can be expressed in the form $\int_S f(\theta)\frac{d\Gamma}{R^n}$, where $f(\theta)$ is a function of θ only, and R is the distance between source and field points (see Appendix A). Thus,

$$\begin{aligned}\int_S f(\theta)\frac{d\Gamma}{R^n} &= \int_{\theta_1}^{\theta_2} f(\theta)\left(\int_{R_F}^{R_\infty}\frac{rdr}{R^n}\right)d\theta \\ &= \int_{\theta_1}^{\theta_2} f(\theta)\frac{1}{(2-n)}\left(\frac{1}{\sqrt{R_\infty^{n-2}}}-\frac{1}{\sqrt{R_F^{n-2}}}\right)d\theta\end{aligned} \tag{5.13}$$

for $n\neq 2$, and:

$$\int_S f(\theta)\frac{d\Gamma}{R^2} = \frac{1}{2}\int_{\theta_1}^{\theta_2} f(\theta)(\ln R_\infty - \ln R_F)d\theta \tag{5.14}$$

for n=2.

In (5.13) and (5.14), R_F and R_∞ denote the distances from the source point to the points located on the boundary Γ_F and the infinite boundary Γ_∞, respectively.

5.4.2 Analytical Expressions for Infinite Elements

From (A1-A4) in Appendix A, we observe that only the integrals of T_{11}, T_{22}, T_{33} and T_{12} over Γ_F remain, since the integrals over Γ_∞ tend to zero as R_∞ tends to infinity. The integrals of T_{13}, T_{31}, T_{23} and T_{32} can be easily shown to be zero since $\sin\theta$ and $\cos\theta$ are periodic functions and Γ_∞ is a closed circle.

Consequently, the integrals over the far-field region S_I reduce to line integrals along the boundary Γ_F. To perform these integrations, we discretise the boundary Γ_F into a set of line elements, each formed by two adjacent nodes located on Γ_F. Fig.5.4 shows a typical element.

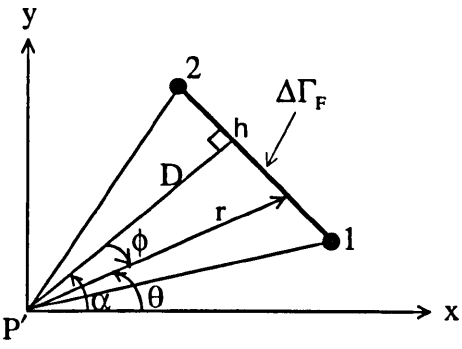

Fig.5.4 Typical line element for nodes 1 and 2.

Thus, (5.12) becomes:

$$J_{ij} = \sum_{M} \int_{\Delta\Gamma_F} T_{ij} dS \tag{5.15}$$

These integrals are evaluated analytically (Appendix B). These results can be readily implemented within a computer code. All that is required is to define the line elements by identifying each pair of adjacent nodes in the contour bounded by the finite boundary elements and infinite elements, ensuring that all of the line elements have the node sequence shown in Fig.5.4.

The co-ordinates of the point H in Fig.5.4 and the distance D from P' to the line element $\Delta\Gamma_F$ are required and can be determined from:

$$\begin{aligned} x^h &= x^1 + k(x^2 - x^1) \\ y^h &= y^1 + k(y^2 - y^1) \end{aligned} \tag{5.16}$$

$$D = \sqrt{(x^h - x^{P'})^2 + (y^h - y^{P'})^2} \tag{5.17}$$

where

$$k = \frac{(x^2 - x^1)(x^{P'} - x^1) + (y^2 - y^1)(y^{P'} - y^1)}{(x^2 - x^1)^2 + (y^2 - y^1)^2}$$

5.4.3 Elimination of Singularities

The terms including $\sin\theta$ or $\cos\theta$ in equations (B5)-(B8) of Appendix B are zero after the assembly of all the infinite elements, since the boundary Γ_F forms a closed contour.

When the source point and the field point are at the same elevation, only the integrals (B9)-(B12) are non-zero. Further, if the source point is a node of the element under consideration, all the integrals become zero since $\phi_1 = \phi_2$ in this particular case. Therefore, all the singularities can be explicitly eliminated.

5.5 Application to Pier Foundations

The infinite element approach has been incorporated into the multi-region computer code (ESMI-3D) and used to analyze various 3D soil-structure interaction problems. All these examples are solved using single precision arithmetic and quadratic quadrilateral parametric elements.

5.5.1 Surface Loads

In the first example, we calculate vertical displacements u on the surface of an elastic half-space (defined by its shear modulus G and Poisson's ratio ν) due to uniformly distributed vertical pressure p acting on a square foundation. Analytical solutions for points beneath the foundation (dimension=2b) have been given by Poulos and Davis (1974). The foundation was discretised using 2×2 finite boundary elements.

Comparison of Two Displacement Decay Functions:

To examine the effect of the near-field size with different decay functions, firstly, the vertical displacement u at the foundation centre was computed using two decay functions ((5.6) and (5.7)) for various ratios of (R/b), where R is the distance from the edge of the loaded area to the inner boundary of the infinite elements (Fig.5.5). In these calculations, the Poisson ratio (ν) was assumed to be 0.2. From symmetry, the geometrical problem can

be reduced to half its original size. Fig.5.5 shows the discretisation employed and Table 5.1 gives the results.

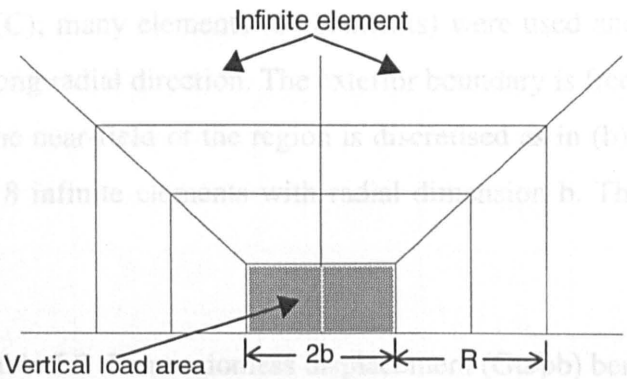

Fig.5.5 Foundation on half-space subjected to vertical load

Table 5.1 Dimensional displacement (Gu_v/pb) beneath centre of square foundation (ν=0.2) (Analytical solution is **0.898**)

R/b / D	0	1	3	5	7	9	12	18
r_0/r	0.902	0.899	0.899	0.899	0.899	0.899	0.899	0.900
e^{1-r/r_0}	0.888	0.889	0.894	0.896	0.897	0.898	0.898	0.899

It can be seen that the first decay function (r_0/r) converges very quickly (as expected from theoretical considerations), and is therefore superior to the alternative.

Displacements Beneath the Foundation:

Displacements beneath *a corner, center of a side, and center of the square* foundation are computed for various Poisson ratios in this example. Results are presented in Tables 5.2 - 5.4 (in which the relative error refers to the difference between the infinite element result and the analytical solution) for five cases:

a) Finite region (A); only the foundation is discretised. (4 elements, see Fig.5.6)

b) Finite region (B); the foundation and a ring of finite-size boundary elements around the foundation are discretised. Eight ring elements were used, with radial dimension b (Fig.5.7).

c) Extended region (C); many elements (84 elements) were used and the far-field region extends to 900b along radial direction. The exterior boundary is free.

d) Infinite element; the near-field of the region is discretised as in (b) above. The far-field is discretised into 8 infinite elements with radial dimension b. There are a total of 20 elements (Fig.5.8).

Table 5.2 Dimensionless displacement (Gu/pb) beneath *corner* of square foundation

ν	Finite region (A)	Finite region (B)	Extended (C)	Infinite element	Analytic solution	Relative error (%)
0.0	0.4351	0.4846	0.5652	0.5606	0.5611	0.089
0.1	0.4159	0.4521	0.5079	0.5047	0.5050	0.059
0.2	0.3929	0.4163	0.4508	0.4488	0.4489	0.022
0.3	0.3645	0.3767	0.3937	0.3928	0.3928	0.0
0.4	0.3285	0.3321	0.3369	0.3367	0.3367	0.0
0.5	0.2806	0.2806	0.2806	0.2806	0.2806	0.0

Table 5.3 Dimensionless displacement (Gu/pb) beneath *center of a side* of square foundation

ν	Finite region (A)	Finite region (B)	Extended (C)	Infinite element	Analytic solution	Relative error (%)
0.0	0.6000	0.6622	0.7654	0.7657	0.7660	0.04
0.1	0.5724	0.6178	0.6891	0.6891	0.6894	0.04
0.2	0.5395	0.5689	0.6127	0.6126	0.6128	0.033
0.3	0.4993	0.5145	0.5362	0.5361	0.5362	0.02
0.4	0.4489	0.4534	0.4595	0.4595	0.4596	0.022
0.5	0.3829	0.3829	0.3829	0.3829	0.3830	0.026

Table 5.4 Dimensionless displacement (Gu/pb) beneath the *center of the square* foundation

ν	Finite region (A)	Finite region (B)	Extended (C)	Infinite element	Analytical solution	Relative error (%)
0.0	0.8805	0.9587	1.1280	1.1253	1.1222	0.28
0.1	0.8397	0.8970	1.0143	1.0121	1.0100	0.21
0.2	0.7911	0.8284	0.9006	0.8990	0.8978	0.13
0.3	0.7319	0.7513	0.7871	0.7862	0.7855	0.09
0.4	0.6578	0.6636	0.6738	0.6735	0.6733	0.03
0.5	0.5611	0.5611	0.5611	0.5611	0.5611	0.0

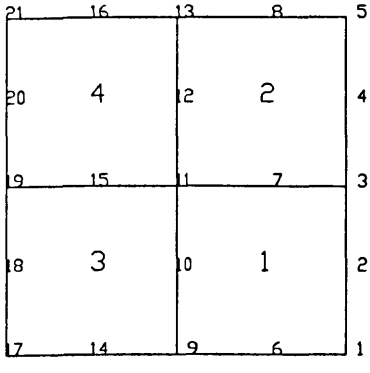

Fig.5.6 Finite region (A) mesh

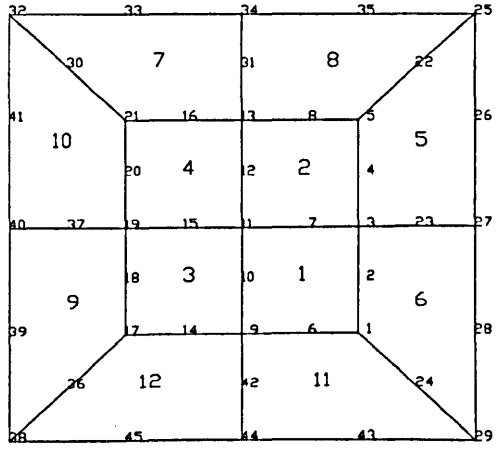

Fig.5.7 Finite region (B) mesh

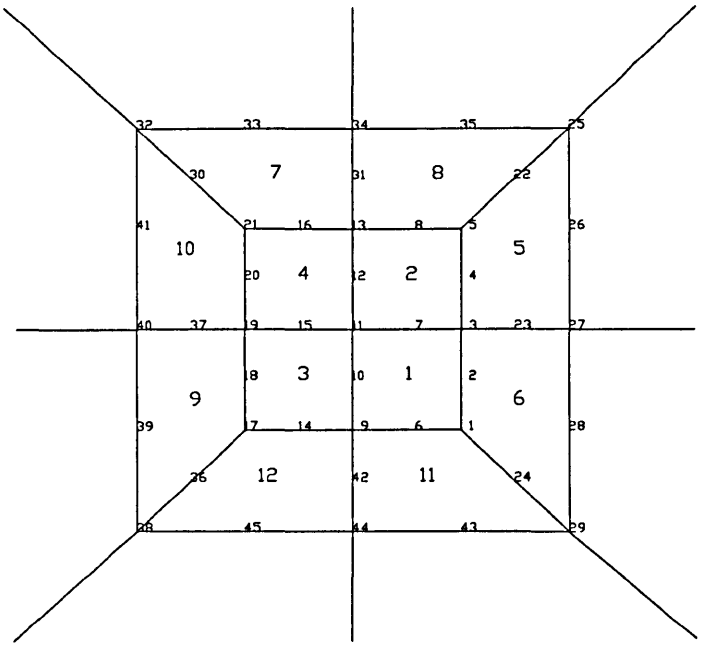

Fig.5.8 Infinite element mesh

From the comparisons between the infinite element results and analytical solutions in Tables 5.1-5.3, we can observe that the infinite boundary element method yields essentially exact results. Of course, one can obtain very good results too with an extended mesh, but at the cost of solving for many degrees of freedom. If one simply uses a local mesh (A or B), then the results are quite poor.

Independence of Near-Field Size:

To examine the convergence of the algorithm, we increased the size of the near-field region and, accordingly, the number of elements in this region, while holding the number (8) of infinite elements constant. The uniformly distributed load acts on the central four elements in each case. Figs.5.9-5.13 show the meshes for five cases and Tables 5.5 and 5.6 show the results for Poisson's ratio ν=0 and ν=0.2.

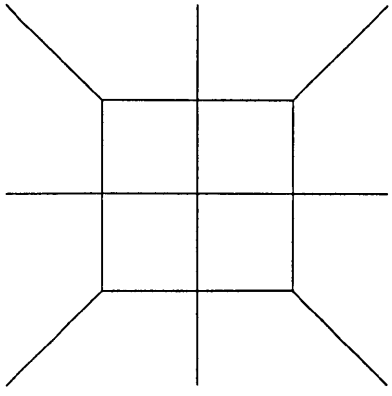

Fig.5.9 Mesh of 12 elements (case 1)

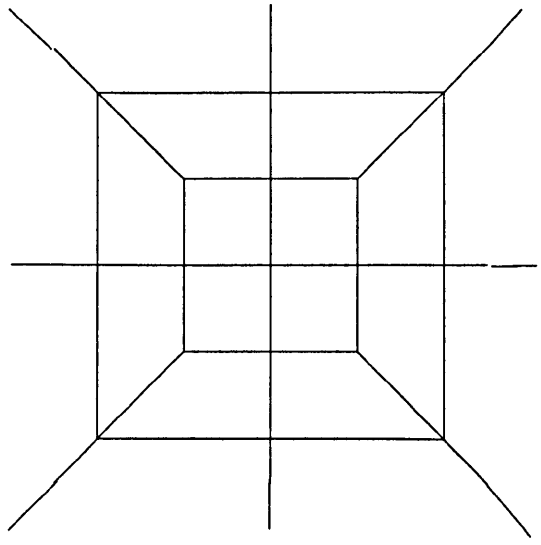

Fig.5.10 Mesh of 20 elements (case 2)

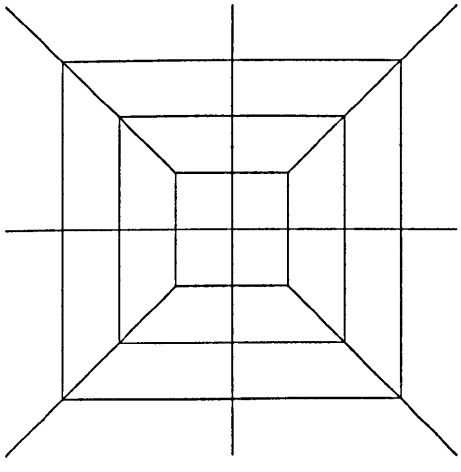

Fig.5.11 Mesh of 28 elements (case 3)

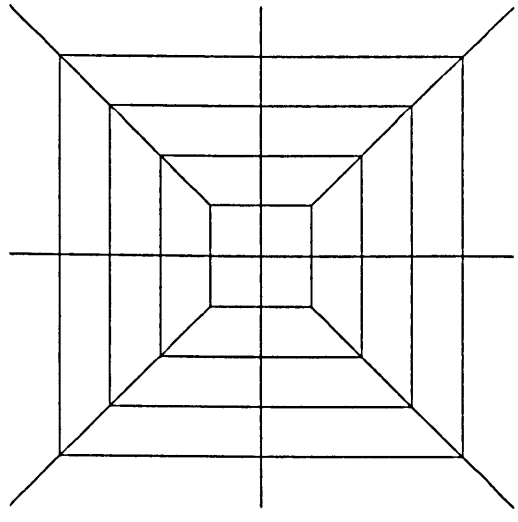

Fig.5.12 Mesh of 36 elements (case 4)

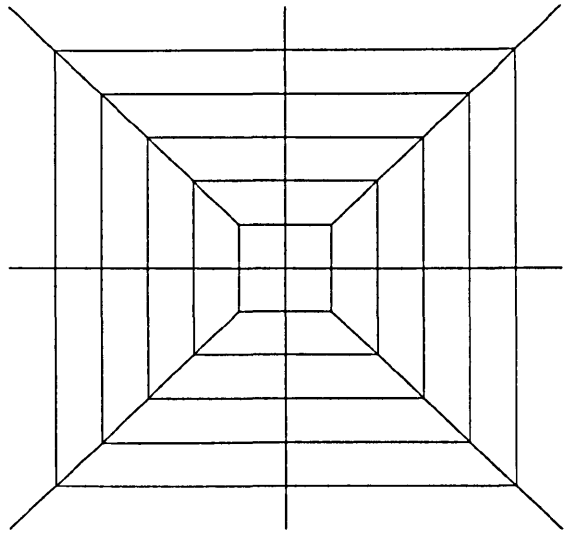

Fig.5.13 Mesh of 44 elements (case 5)

Table 5.5 Dimensionless displacements (Gu/pb) for ν=0

	corner	center of side	center of square
case 1	0.4747	0.7449	1.1356
case 2	0.5606	0.7657	1.1253
case 3	0.5620	0.7617	1.1240
case 4	0.5615	0.7613	1.1238
case 5	0.5617	0.7615	1.1240
Analytical solution	0.5611	0.7660	1.1222

Table 5.6 Dimensionless displacements (Gu/pb) for ν=0.2

	corner	center of side	center of square
case 1	0.4111	0.6054	0.9041
case 2	0.4488	0.6126	0.8990
case 3	0.4491	0.6108	0.8987
case 4	0.4490	0.6108	0.8987
case 5	0.4491	0.6109	0.8988
Analytical solution	0.4489	0.6128	0.8978

From Tables 5.5 and 5.6, we observe that the results converge very rapidly. Only if the infinite elements are located immediately adjacent to the loaded area, are the results significantly different from the analytical solution.

5.5.2 Rigid Piers Subjected to Lateral Loads

A more challenging example is presented here to demonstrate the practical application of this algorithm. This relates to a rigid square-section pier (Fig.5.14), of length L and width D. The relationship between pier head deflections (& rotations) and the applied loads (& moments) is of particular interest. The numerical results obtained here are compared with the analytical results for (hollow) tubular and flat (vertical plate) pier foundations obtained by Abedzadeh and Pak (1995) and Douglas and Davis (1964).

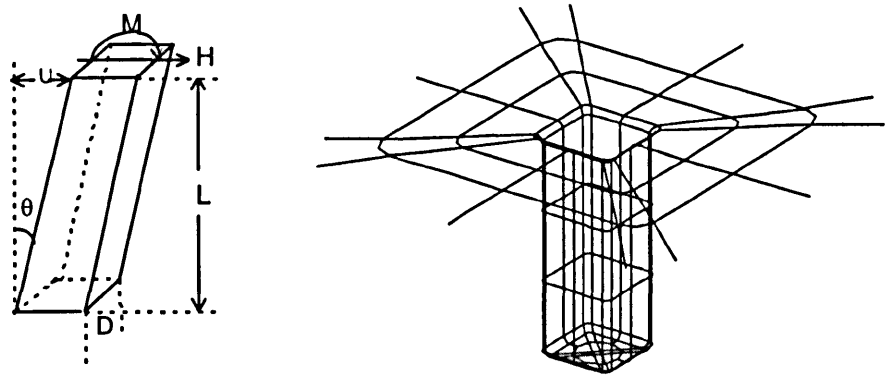

Fig.5.14 (a) Pier subjected to lateral loads; (b) BEM mesh of medium

The relationship between the loads and the deformations for the pier head can be expressed as:

$$\begin{Bmatrix} H \\ M \end{Bmatrix} = \begin{bmatrix} K_{HU} & K_{H\theta} \\ K_{MU} & K_{M\theta} \end{bmatrix} \begin{Bmatrix} u \\ \theta \end{Bmatrix} \tag{5.18}$$

where H and M is the horizontal force and applied moment; u and θ is the lateral displacement and rotation; and $K_{HU}, K_{MU}, K_{H\theta}$ and $K_{M\theta}$ are the stiffness coefficients. From the reciprocal work theorem, $K_{H\theta}$ should be equal to K_{MU}.

The stiffness coefficients in (5.18) are calculated by prescribing unit translation and rotation and then integrating the tractions along the pier surface to obtain the resultant horizontal force H and moment M. Fig.5.14(b) shows the boundary element mesh: typically this consists of 105 finite domain elements and 12 infinite elements. Figs.5.15-5.17 are plots of the stiffness coefficients (normalised with respect to Young's modulus, E) for various values of Poisson's ratio. For comparison, the results by Abedzadeh and Pak (1995) and Douglas and Davis (1964) are also plotted for the case of ν=0.5.

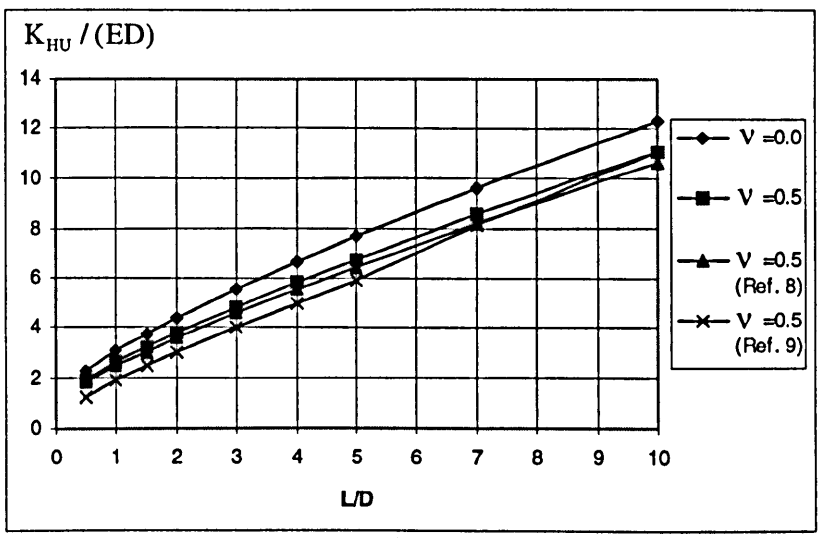

(a)

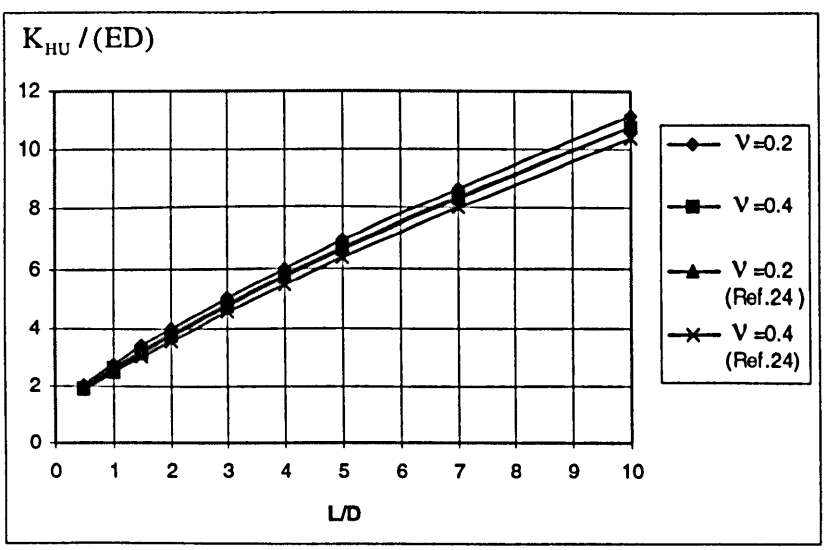

(b)

Fig.5.15 Effect of Slenderness Ratio (L/D) on the Stiffness Coefficient K_{HU}

(a) ν=0 and ν=0.5; (b) ν=0.2 and ν=0.4

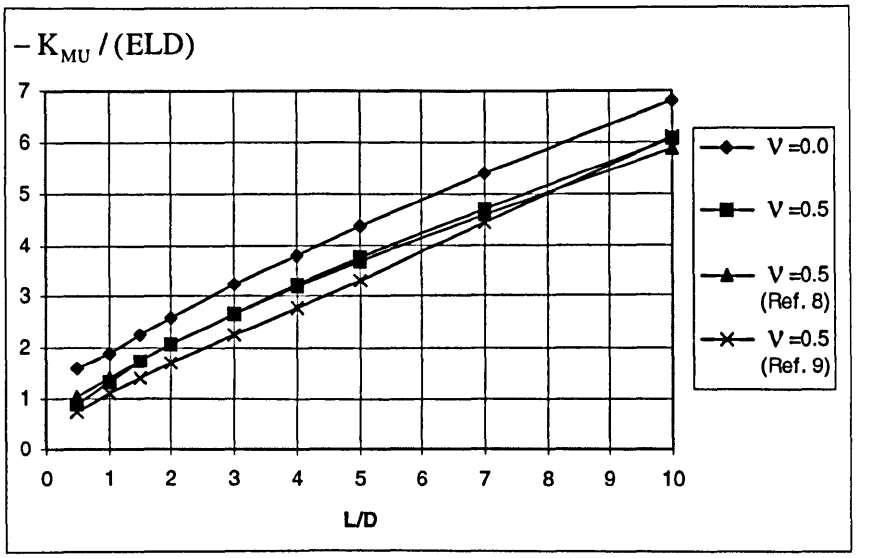

(a)

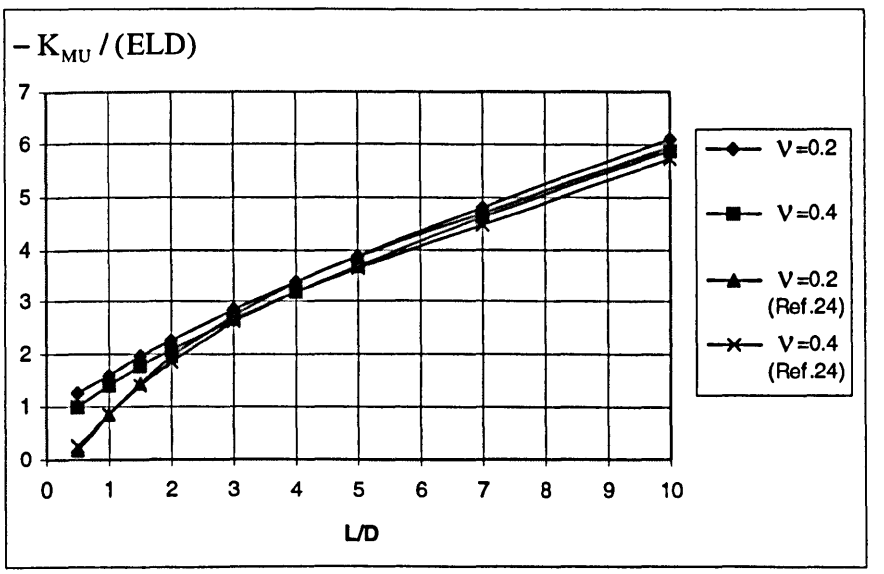

(b)

Fig.5.16 Effect of Slenderness Ratio (L/D) on the Stiffness Coefficient K_{MU}

(a) ν=0 and ν=0.5; (b) ν=0.2 and ν=0.4

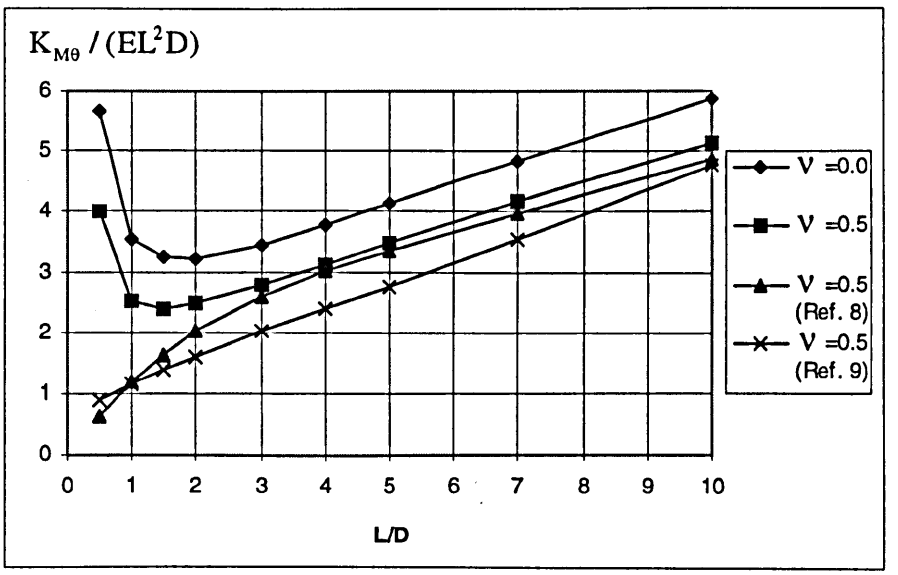

(a)

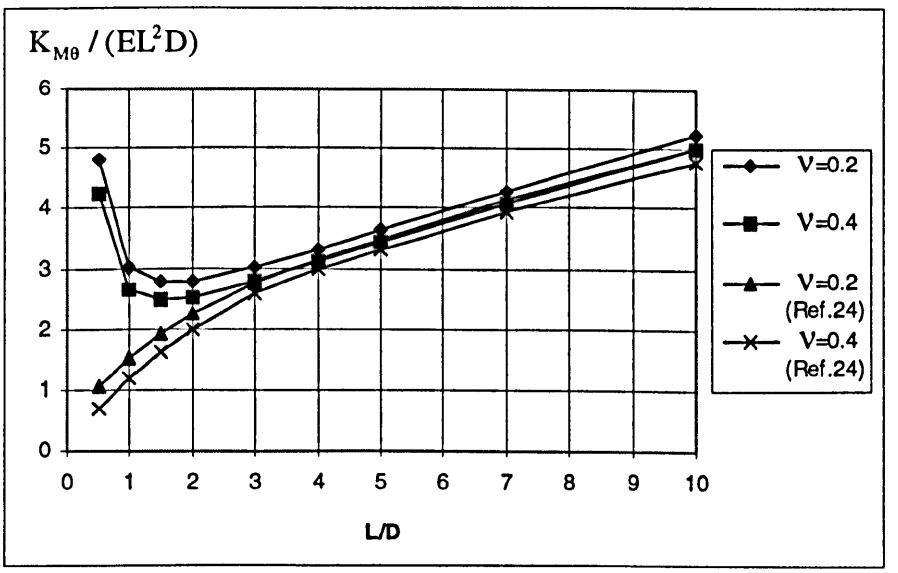

(b)

Fig.5.17 Effect of Slenderness Ratio (L/D) on the Stiffness Coefficient $K_{M\theta}$

(a) ν=0 and ν=0.5; (b) ν=0.2 and ν=0.4

The numerical results appear to be in excellent agreement with the analytical results, since the discrepancies may well be attributable to the shape effect. In particular, as might be expected, the stiffness coefficients for the flat (plate) pier are smaller than those obtained for the cylindrical pier which are in turn smaller than those of the square-section pier. The differences are greatest for the rotational stiffness terms, particularly for "short" piers

(L/D<3), where the contributions of the base tractions for the square-section pier to the $K_{M\theta}$ term becomes dominant. The off-diagonal coefficients K_{MU} and $K_{H\theta}$ were calculated independently, but their values differed by no more than 5%. The discrepancy is least for piers with higher slenderness ratios. The symmetry of these results indirectly demonstrates the validity of the calculation.

5.5.3 Flexible Piers in Half-Space

In this example, a square-section pier (Fig.5.18) embedded in a semi-infinite continuum was analysed to demonstrate the applicability of the infinite element approach in multi-region corner problems .

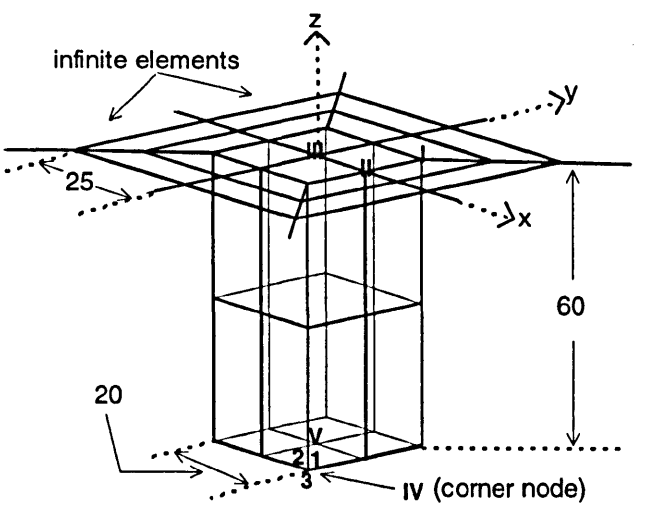

Fig.5.18 Discretisation for a square-section pier in soil

Each surface of the pier was discretised using 2×2 quadratic elements. As for the surrounding medium, in addition to the 10 interface elements, the ground surface was approximated by 24 elements, including 8 infinite elements. The corners at the base of the pier are the corner nodes of three surfaces (elements). The corner IV (for example) is associated with three independent nodes (node 3 on base surface and nodes 1 and 2 on the side surfaces). Other nodes along the sides of the pier are defined by two independent nodes. Two different cases are considered here in order to validate the algorithm.

Case 1:

The vertical displacements u_z of the pier head due to uniformly distributed vertical pressure p_z=1 acting on the pier head (of dimension 2b×2b) are tabulated below (G is the shear modulus of the soil). In this calculation, Young's modulus E and Poisson's ratio ν were assumed to be the same for both the pier and the surrounding medium, i.e., $E_p=E_s=1$; $\nu_p=\nu_s=0$. Because this is actually a half-space surface problem, the numerical results can be compared with analytical solutions. Table 5.7 shows that the computed vertical displacements are in excellent agreement, despite the coarse mesh employed.

Table 5.7 Displacement (Gu_z/p_zb) of the pier head due to vertical load

point	I (corner)	II (centre of side)	III (centre)
computed result	0.5667	0.7673	1.1295
analytical solution	0.5611	0.766	1.1222

Case 2:

In this case, a uniformly distributed lateral load (p_x=1) was assumed to act on the pier head. The material parameters for the two zones were as follows; $E_p=2$; $E_s=1$; $\nu_p=\nu_s=0.3$. Tables 5.8 and 5.9 show the computed displacements and tractions for some selected points on the pier.

Table 5.8 Computed displacements of pier due to lateral load

point	I (top corner)	III (top centre)	V (centre of base)
u_x	11.9965	18.2807	2.8345
u_y	1.0511	2.694E-6	2.997E-6
u_z	-2.1460	4.954E-6	2.026E-5

Table 5.9 Tractions at base corner point IV

node	1	2	3
t_x	1.1212	0.8079	-2.5080
t_y	-0.8079	1.7397	-1.9817
t_z	2.5080	-1.9817	-0.0881

5.5.4 Flexible Piers in Multi-Layered Media

To verify the validity of the program written employing the multi-region BEM algorithm described in Chapter 4 and the infinite boundary element technique presented in this Chapter, one more numerical example is given here. A square-section rod (pier) embedded in a three-dimensional two-layered medium, and subjected to uniformly distributed vertical and lateral loads, P_V and P_H at the surface, as well as a moment, M, is depicted (in cross-section) in Fig.5.19. In this problem, the layer 2 extends to infinity both laterally and vertically. From symmetry, half of the problem is discretised into elements. The discretisation of the infinite surfaces is exactly the same as shown in Fig.5.5. Four elements were used along the rod length (see Fig.5.20(a)).

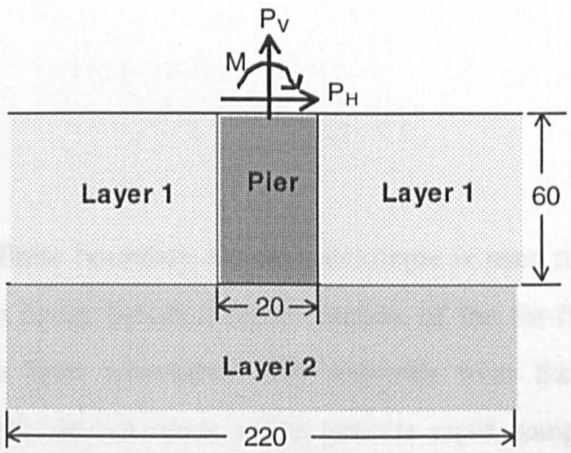

Fig.5.19 A rod (pier) embedded in a two-layered medium

Case 1: To demonstrate the correct implementation of the program for this problem, we assume that $P_H=M=0$, $P_V=1$, and the Young's modulus E and Poisson's ratio ν are taken the same values for each sub-region, i.e., $E_p=E_1=E_2=1$, $\nu_p=\nu_1=\nu_2=0.2$. This reduces the problem to that of the first case in section 5.5.1. The calculated result is $Gu_v/P_Vb=0.8905$ and compares well with the analytical solution (0.8978).

Case 2: This case is intended to simulate a practical situation by assuming: E_p= 10000, E_1=500, E_2=2000; ν_p=0.3, ν_1=0.2, ν_2=0.25; P_V=0, P_H=200, M=33300. Fig.5.20 shows the horizontal displacements along the right side surface of the pier, and the corresponding tractions.

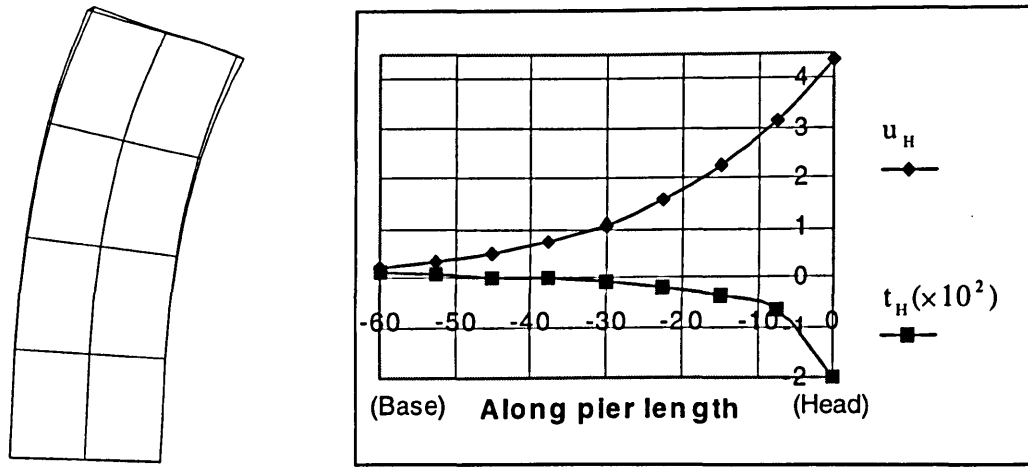

(a) (b)

Fig.5.20 (a) Deformed Mesh; (b) horizontal displacement and traction along pier

5.6 Summary

In this chapter, an infinite boundary element technique is used to model the layered half-space, and employs a decay function representation of the far-field displacements at the free surface and the layer interfaces. The integrals over the far-field are evaluated analytically, resulting in an algorithm which permits rapid computation of the system of equations. Some non-trivial numerical examples are presented to illustrate the application of the algorithm to some typical problems, i.e. pier foundations, in geomechanics. The infinite boundary element approach enjoys the following advantages for half-space problems.

- There is no truncation in the physical domain so that the far-field contribution to the calculations is handled correctly, leading to a highly accurate solution.
- Only the actual surfaces needs to be discretized into elements (instead of all the surfaces of artificially truncated 3D closed bodies), greatly reducing the system size.
- Using the novel analytical formulation described here, no numerical integrations over the entire region is needed, resulting in significant saving in the calculation time, and resulting in improved accuracy.

- Since the technique is computationally efficient, it can be used to attack more complicated problems than has been possible hitherto.

Chapter 6

Rate-Independent Plasticity Theory

6.1 Introduction

In the classical (flow) theory of plasticity, the general elastoplastic constitutive relations are based on Drucker's postulate (e.g., Owen and Hinton, 1980; Chen and Han, 1988; Crisfield, 1997). The origin of this postulate (Drucker, 1959) is based on net work dissipation over a closed stress cycle in stress space and this leads to the result that the plastic strain rate is directed along the normal to the loading surface in stress space. However, Drucker's postulate is only suitable for stable materials under stress control—with perfect plasticity as a limiting case (Naghdi and Trapp, 1975a; Lubliner, 1990). For some geotechnical materials, which exhibit unstable behaviour during deformation, Drucker's postulate is not valid. However, no such limitation applies to theories using strain as an independent variable. Surprisingly, such theories were not proposed until the 1960s, beginning with the pioneering work of Il'iushin (1961), followed by papers by Pipkin and Rivlin (1965), Owen (1968) and Nguyen and Bui (1974). The theory of plasticity in strain space, which is suitable for both stable and unstable behaviour, was extended to finite elastoplastic deformation by Naghdi and Trapp (1975a,b) from a physically plausible assumption concerning the non-negativeness of the work done by external forces acting on the body in a closed cycle of spatially homogeneous deformation. It worth noting that, based on this assumption, they derived an important inequality for restrictions on elastoplastic constitutive relationships from a special deformation cycle path.

In this chapter, we seek to establish general constitutive relations, for a wide range of yield functions, which can be easily implemented in numerical codes. Firstly, the elastoplastic flow rule and loading rule are derived in strain space from Il'iushin's

postulate, following the basic ideas of Naghdi and Trapp (1975b) but develop the formulation for a prescribed (general) closed cyclic strain path. This development is also based on the author's previous published work (Gao et al., 1990; Gao and Zhong, 1992) but we include here more of the underlying mathematical manipulations. Based on these rules, a new set of unified constitutive equations for hardening, softening and perfect plasticity is obtained, which is suitable for a quite wide range of yield functions. This formulation demonstrates that Drucker's normality flow rule does not hold true universally. An expression for the angle of departure between the plastic strain-rate vector and the normal direction to the loading surface in stress space is given, and the normality flow conditions (for zero departure angle) are also derived. In the later part of this Chapter (section 6.6), we further develop the numerical implementation aspects, making use of the work by Simo & Taylor (1985) and Ortiz & Simo (1986) as well as the author's previously published work (Gao and Zhong, 1992), in order to arrive at a practical algorithm. The novel aspects of the present work and, also, notes on the provenance of some of the principal results are indicated, where appropriate.

With respect to the notation employed in this Chapter, the following symbolic operations are implied: $\mathbf{AB}=A_{ik}B_{kj}$, $\mathbf{A}:\mathbf{B}= A_{ik}B_{ki}$, $\mathbf{A}\otimes\mathbf{B}= A_{ij}B_{kl}$ and $(D_{ijkl})^t =D_{klij}$, with proper extension to different order tensors.

6.2 Strain Space Flow Rule and Loading Rule

In general, the total stress-strain relationships may be written in the general form:

$$\sigma = \hat{\sigma}(\varepsilon, \varepsilon^p, h^\alpha) \tag{6.1}$$

in which, the σ denotes the Cauchy stress for infinitesimal deformation problems or the symmetric Piola-Kirchhoff stress for finite deformation problems (Naghdi and Trapp, 1975; Naghdi, 1990). Equation (6.1) implies that the total stress is a function of total strain ε, plastic strain ε^p and some internal variables h^α, α=1,2, ..., which measure the irreversible deformation history. For example, in damage mechanics, the internal variables may be the damage variables, e.g., the void ratio, (Lemaitre, 1992; Gao and Zhong, 1992; Mazars and Cabot, 1996). For linear elasticity, we can interpret the generalised Hooke's law (2.3) as a particular form of (6.1). The phenomenon in which elastic parameters (generally the Young's modulus) in (6.1) vary with plastic deformation is termed an 'elastic-plastic

coupling effect' (Sinha, 1964; Dafalias, 1977; Maier and Hueckel, 1979; Chen, 1994; Zhong and Gao, 1990).

It is assumed that the expression (6.1) is invertible for fixed ε^p and h^α in the form:

$$\varepsilon = \hat{\varepsilon}(\sigma, \varepsilon^p, h^\alpha) \tag{6.2}$$

Furthermore, we assume that the total stress tensor σ is derivable from a potential, such that the partial derivative of σ with respect to ε is symmetric, i.e.

$$\frac{\partial \hat{\sigma}_{ij}}{\partial \varepsilon_{kl}} = \frac{\partial \hat{\sigma}_{kl}}{\partial \varepsilon_{ij}} \quad \text{or} \quad \mathbf{D}^t = \mathbf{D} \tag{6.3}$$

where

$$D_{ijkl} = \frac{\partial \hat{\sigma}_{ij}}{\partial \varepsilon_{kl}} \tag{6.4}$$

We now assume that there is a loading function (yield surface) $g(\varepsilon,\varepsilon^p,h^\alpha)=0$, in strain space which is equivalent to the loading function $f(\sigma,\varepsilon^p,h^\alpha)=0$ in stress space such that:

$$g(\varepsilon,\varepsilon^p,h^\alpha) = f(\hat{\sigma}(\varepsilon,\varepsilon^p,h^\alpha),\varepsilon^p,h^\alpha) = 0 \tag{6.5}$$

The yield surfaces define the boundary of the elastic region. If a strain (or stress) lies inside the surface, we call it an elastic state and only elastic behaviour occurs. On the other hand, the state of strain (or stress) on the yield surface is termed a plastic state, and there elastic-plastic behaviour occurs.

6.2.1 Work Inequality

The Il'iushin postulate states that the work done in a closed strain cycle is non-negative, i.e.,

$$\oint \sigma_{ij} d\varepsilon_{ij} = \int_{t_1}^{t_2} \sigma_{ij} \dot{\varepsilon}_{ij} dt \geq 0 \tag{6.6}$$

in which, t_1 and t_2 represent the beginning and ending times of the strain cycle and the superposed dot denotes the derivative with respect to time.

The inequality (6.6) was also derived by Naghdi and Trapp (1975b) for finite elastoplastic deformation and they state that it is valid for any smooth closed homogeneous deformation cycle. Thus, most relations derived in this chapter are also suitable for finite elastoplastic deformation.

Now let ε^0 be any strain inside the loading surface and consider a strain cycle beginning and ending at ε^0. For this cycle, noting that $\varepsilon(t_1)= \varepsilon(t_2)=\varepsilon^0$, (6.6) can be written (through integration by parts) as:

$$\int_{t_1}^{t_2}(\varepsilon_{ij}-\varepsilon_{ij}^0)\dot{\sigma}_{ij}dt \le 0 \tag{6.7}$$

From (6.7), an important inequality which places constraints on admissible elastoplastic constitutive relationships is derived by Naghdi and Trapp (1975) from consideration of a special strain cycle path. In the following, a more general cycle path is used to deduce a more general inequality.

A typical stress-strain curve for uniaxial tests is shown in Fig.6.1:

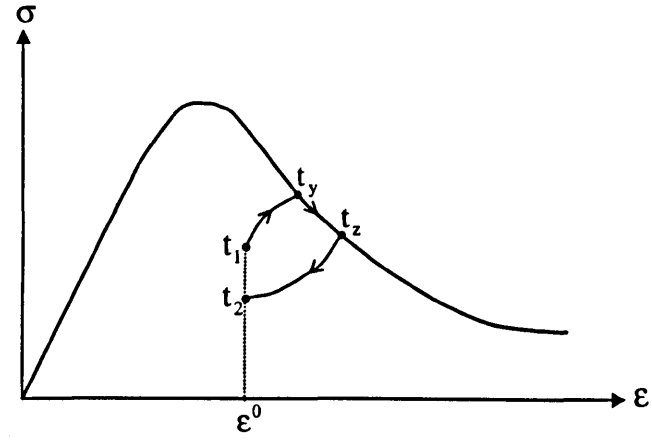

Fig.6.1 Typical stress-strain curve for uniaxial tests

We consider a strain cycle in which the deformation takes place elastically from t_1 to a yield point t_y, then continues elastoplastically to t_z, and finally unloads elastically to point t_2 i.e.,

$$t_1 \rightarrow t_y \rightarrow t_z \rightarrow t_2 \tag{6.8}$$

During this strain cycle, plastic deformation occurs only in the stage $t_y \rightarrow t_z$ and elastic unloading does not (of course) produce irreversible deformation. Incidentally, for non-linear elastic materials, the elastic deformation paths, $t_1 \rightarrow t_y$ and $t_z \rightarrow t_2$ are not straight lines. Now, since t_y and t_z are the turning points between elastic and plastic deformations, we denote t_{y-} and t_{y+} as the left limit and right limit of the point t_y, respectively, and similarly t_{z-} and t_{z+}. Evidently, t_{y+} and t_{z-} are on the loading surface. Differentiating (6.1) with respect to time, leads to:

$$\dot{\sigma} = (\mathbf{D} - \mathbf{D}^e) : \dot{\varepsilon} + \mathbf{D}^e : \dot{\varepsilon} + \dot{\mathbf{G}} \tag{6.9}$$

where

$$\dot{G} = \frac{\partial \hat{\sigma}}{\partial \varepsilon^p} : \dot{\varepsilon}^p + \frac{\partial \hat{\sigma}}{\partial h^\alpha} \dot{h}^\alpha \tag{6.10}$$

$$\mathbf{D}^e = \frac{\partial \hat{\sigma}}{\partial \varepsilon}(t_{y-}) \tag{6.11}$$

Since t_{y-} is located in the elastic region, the fourth order tensor $\mathbf{D}^e$ is called the 'elastic constitutive tensor'. In linear elastic infinitesimal deformation, it has the form of (2.4).

Substituting (6.9) into (6.7), we have (Gao et al., 1990):

$$\int_{t_1}^{t_2} (\varepsilon - \varepsilon^0) : (\mathbf{D} - \mathbf{D}^e) : \dot{\varepsilon}\, dt + \int_{t_1}^{t_2} (\varepsilon - \varepsilon^0) : \mathbf{D}^e : \dot{\varepsilon}\, dt + \int_{t_1}^{t_2} (\varepsilon - \varepsilon^0) : \dot{\mathbf{G}}\, dt \le 0 \tag{6.12}$$

The second integral in (6.12) can be readily integrated to be zero, since $\varepsilon(t_1) = \varepsilon(t_2) = \varepsilon^0$. The last integral can be written in the following form, since only in the interval $t_{y+} \to t_{z-}$ does the plastic strain ε^p and the internal variables h^α alter.

$$\int_{t_1}^{t_2} (\varepsilon - \varepsilon^0) : \dot{\mathbf{G}}\, dt = \int_{t_{y+}}^{t_{z-}} (\varepsilon - \varepsilon^0) : \dot{\mathbf{G}}\, dt \tag{6.13}$$

Expanding (6.13), using Taylor's series about point t_{y+}, yields:

$$\int_{t_1}^{t_2} (\varepsilon - \varepsilon^0) : \dot{\mathbf{G}}\, dt = (\varepsilon - \varepsilon^0) : \dot{\mathbf{G}} \Delta t + [\dot{\varepsilon} : \dot{\mathbf{G}} + (\varepsilon - \varepsilon^0) : \ddot{\mathbf{G}}] \frac{(\Delta t)^2}{2} + \mathbf{O}(\Delta t)^3 \tag{6.14}$$

in which, $\Delta t = t_{z-} - t_{y+} = t_z - t_y$, and $0(\Delta t)^3$ represents the infinitesimal terms of third and higher orders of Δt as $\Delta t \to 0$.

Similarly, the Taylor's series expansion of the first integral in (6.12) about t_{y+}, leads to (see Appendix C):

$$\begin{aligned} \int_{t_1}^{t_2} (\varepsilon - \varepsilon^0) : (\mathbf{D} - \mathbf{D}^e) : \dot{\varepsilon}\, dt &= (\varepsilon - \varepsilon^0) : [(\mathbf{D} - \mathbf{D}^e) : \dot{\varepsilon} + \frac{1}{2} \dot{\mathbf{R}} : (\varepsilon - \varepsilon^0)] \Delta t \\ &+ \left\{ \dot{\varepsilon} : (\mathbf{D} - \mathbf{D}^e) : \dot{\varepsilon} + (\varepsilon - \varepsilon^0) : [(\mathbf{D} - \mathbf{D}^e) : \ddot{\varepsilon} + \dot{\mathbf{R}} : \dot{\varepsilon}] \right\} \frac{(\Delta t)^2}{2} + \mathbf{O}(\Delta t)^3 \end{aligned} \tag{6.15}$$

Substituting (6.15) and (6.14) into (6.12), it follows that:

$$\begin{aligned} &(\varepsilon - \varepsilon^0) : \left\{ \dot{\mathbf{G}} + (\mathbf{D} - \mathbf{D}^e) : \dot{\varepsilon} + \frac{1}{2} \dot{\mathbf{R}} : (\varepsilon - \varepsilon^0) \right\} \Delta t + \\ &\left\{ \dot{\varepsilon} : [\dot{\mathbf{G}} + (\mathbf{D} - \mathbf{D}^e) : \dot{\varepsilon}] + (\varepsilon - \varepsilon^0) : [\ddot{\mathbf{G}} + (\mathbf{D} - \mathbf{D}^e) : \ddot{\varepsilon} + \dot{\mathbf{R}} : \dot{\varepsilon}] \right\} \frac{(\Delta t)^2}{2} \\ &+ \mathbf{O}(\Delta t)^3 \le 0 \end{aligned} \tag{6.16}$$

Inequality (6.16) is an approximate expression of work inequality (6.7), which plays an important role in the establishment of the constitutive relations in this chapter.

6.2.2 Flow Rule and Loading Rule

We now divide (6.16) by Δt, and then let $\Delta t \to 0$, to deduce:

$$(\boldsymbol{\varepsilon}-\boldsymbol{\varepsilon}^0):[\dot{\mathbf{G}}+(\mathbf{D}-\mathbf{D}^e):\dot{\boldsymbol{\varepsilon}}]+\frac{1}{2}(\boldsymbol{\varepsilon}-\boldsymbol{\varepsilon}^0):\dot{\mathbf{R}}:(\boldsymbol{\varepsilon}-\boldsymbol{\varepsilon}^0)\le 0 \tag{6.17}$$

We observe that the first and second terms on the left-hand side of (6.17) are linear and quadratic in $(\varepsilon-\varepsilon^0)$, respectively. Since (6.17) must hold true for any ε^0, we replace $(\varepsilon-\varepsilon^0)$ by $\beta(\varepsilon-\varepsilon^0)$, with β being an arbitrary positive scalar; and then after dividing by β, and then letting $\beta \to 0$, we obtain:

$$(\boldsymbol{\varepsilon}-\boldsymbol{\varepsilon}^0):[\dot{\mathbf{G}}+(\mathbf{D}-\mathbf{D}^e):\dot{\boldsymbol{\varepsilon}}]\le 0 \tag{6.18}$$

We now return to inequality (6.16). Again, we replace $(\varepsilon-\varepsilon^0)$ by $\beta(\varepsilon-\varepsilon^0)$ and let $\beta \to 0$. Then, after dividing by Δt and letting $\Delta t \to 0$, we finally obtain:

$$\dot{\boldsymbol{\varepsilon}}:[\dot{\mathbf{G}}+(\mathbf{D}-\mathbf{D}^e):\dot{\boldsymbol{\varepsilon}}]\le 0 \tag{6.19}$$

With the help of (6.9) and (6.10), inequalities (6.18) and (6.19) can be written as:

$$(\boldsymbol{\varepsilon}-\boldsymbol{\varepsilon}^0):(\dot{\boldsymbol{\sigma}}-\mathbf{D}^e:\dot{\boldsymbol{\varepsilon}})\le 0 \tag{6.20}$$

$$\dot{\boldsymbol{\varepsilon}}:(\dot{\boldsymbol{\sigma}}-\mathbf{D}^e:\dot{\boldsymbol{\varepsilon}})\le 0 \tag{6.21}$$

We note that ε^0 is any strain inside the loading surface $g(\varepsilon,\varepsilon^p,h^\alpha)=0$ and that $\dot{\boldsymbol{\sigma}}-\mathbf{D}^e:\dot{\boldsymbol{\varepsilon}}$ is independent of $\varepsilon-\varepsilon^0$ and varies on the loading surface. Therefore, from (6.20) we can conclude that $\dot{\boldsymbol{\sigma}}-\mathbf{D}^e:\dot{\boldsymbol{\varepsilon}}$ (regarded as a vector in six-dimensional strain space) must be directed along the normal to the loading surface g=0, i.e.,

$$\dot{\boldsymbol{\sigma}}-\mathbf{D}^e:\dot{\boldsymbol{\varepsilon}}=-\dot{\lambda}\frac{\partial g}{\partial \boldsymbol{\varepsilon}}, \qquad \dot{\lambda}\ge 0 \tag{6.22}$$

which can be expressed in an incremental form as:

$$d\sigma_{ij}-D^e_{ijkl}d\varepsilon_{kl}=-d\lambda\frac{\partial g}{\partial \varepsilon_{ij}}, \qquad d\lambda\ge 0 \tag{6.23}$$

where $d\lambda$ is a non-negative scaling factor called the *plastic multiplier*. Substituting (6.22) into (6.21), leads to:

$$\frac{\partial g}{\partial \varepsilon_{kl}} d\varepsilon_{kl} \geq 0 \tag{6.24}$$

Inequality (6.24) must hold when plastic strain occurs. Therefore, we call it the plastic loading rule. Inequality (6.23), which reflects the relationship between the stress increment, strain increments and the loading function, is called the plastic flow rule. From the derivation of (6.23) and (6.24), it can be seen that they are not limited to pure elastoplastic problems. Equations (6.1) and (6.5) might include other variables generated in irreversible process in addition to the plastic strain tensor, such as damage tensors, fabric tensors, crack density tensors, etc. However, we shall not discuss these cases here.

It is noted that equation (6.23) was initially obtained by Gao et al. in 1990, based on linear stress-strain response.

6.3 Constitutive Relations

Equations (6.23) and (6.24) are quite general relations suitable for any rate-independent plasticity deformation. In the following, we assume that the derivatives of stresses with respect to strains are continuous during deformation from elastic state to elastoplastic state, so that:

$$D^{e}_{ijkl} = \frac{\partial \hat{\sigma}_{ij}}{\partial \varepsilon_{kl}} \tag{6.25}$$

Thus, from (6.23), it follows that:

$$\frac{\partial \hat{\sigma}_{ij}}{\partial \varepsilon^{p}_{kl}} d\varepsilon^{p}_{kl} + \frac{\partial \hat{\sigma}_{ij}}{\partial h^{\alpha}} dh^{\alpha} = -d\lambda \frac{\partial g}{\partial \varepsilon_{ij}} \tag{6.26}$$

This equation was obtained by Naghdi and Trapp (1975b) who derived it for a special strain cycle. Although it is based on the continuous assumption, it holds for a wide range of materials. Therefore, in the following, we use (6.26) to develop a new and general elastoplastic constitutive relationship, based on the author's previous published work (Gao et al., 1990; Gao and Zhong, 1992) but we include here more of the underlying mathematical manipulations.

In view of the assumption that the internal variables are only associated with plastic deformation, we assume that:

$$dh^{\alpha} = \mathbf{M}^{\alpha} : d\varepsilon^{p} = M_{ij}^{\alpha} d\varepsilon_{ij}^{p} \tag{6.27}$$

where $\mathbf{M}^{\alpha}$ may be functions of $(\varepsilon,\varepsilon^{p},h^{\alpha})$. For example, if plastic work is taken as an internal variable ($dh^{w}=\sigma:d\varepsilon^{p}$), then $\mathbf{M}^{\alpha}=\sigma$. Substituting the above equation into (6.26), leads to:

$$d\varepsilon^{p}=d\lambda \mathbf{C}:\frac{\partial g}{\partial \varepsilon} \tag{6.28}$$

where

$$\mathbf{C}=-\left(\frac{\partial \hat{\sigma}}{\partial \varepsilon^{p}}+\frac{\partial \hat{\sigma}}{\partial h^{\alpha}}\otimes \mathbf{M}^{\alpha}\right)^{-1} \tag{6.29}$$

From the consistency condition, $d(g(\varepsilon,\varepsilon^{p},h^{\alpha}))=0$, i.e.,

$$\frac{\partial g}{\partial \varepsilon}:d\varepsilon+\frac{\partial g}{\partial \varepsilon^{p}}:d\varepsilon^{p}+\frac{\partial g}{\partial h^{\alpha}}dh^{\alpha}=0 \tag{6.30}$$

and using (6.27) and (6.28), we obtain:

$$d\lambda=\frac{1}{\psi}\frac{\partial g}{\partial \varepsilon}:d\varepsilon \tag{6.31}$$

where

$$\psi=\left(\frac{\partial g}{\partial \varepsilon^{p}}+\frac{\partial g}{\partial h^{\alpha}}\mathbf{M}^{\alpha}\right):\mathbf{C}:\frac{\partial g}{\partial \varepsilon} \tag{6.32}$$

Substituting (6.31) into (6.23) and taking account of unloading cases, we can express the constitutive equations as:

$$d\sigma=\left(\mathbf{D}^{e}-\frac{<\hat{g}>}{\psi}\frac{\partial g}{\partial \varepsilon}\otimes\frac{\partial g}{\partial \varepsilon}\right):d\varepsilon \tag{6.33}$$

where

$$\hat{g}=\frac{\partial g}{\partial \varepsilon}:d\varepsilon \tag{6.34}$$

and according to the loading rule (6.24):

$$<\hat{g}>=\begin{cases}=0 & \text{if } g(\varepsilon,\varepsilon^{p},h^{\alpha})<0 & & \text{(elastic)}\\ =1 & \text{if } g(\varepsilon,\varepsilon^{p},h^{\alpha})=0 & \text{and } \hat{g}\geq 0 & \text{(loading)}\\ =0 & \text{if } g(\varepsilon,\varepsilon^{p},h^{\alpha})=0 & \text{and } \hat{g}<0 & \text{(unloading)}\end{cases} \tag{6.35}$$

Equations (6.28)-(6.35) are expressed in terms of the strain space loading function $g(\varepsilon,\varepsilon^{p},h^{\alpha})=0$. However, almost all loading functions (yielding functions) are established in stress space. Therefore, we employ the relationships (Naghdi and Trapp, 1975):

$$\frac{\partial g}{\partial \varepsilon} = \mathbf{D}^e : \frac{\partial f}{\partial \sigma}, \qquad \frac{\partial g}{\partial \varepsilon^p} = \frac{\partial f}{\partial \varepsilon^p} + \frac{\partial f}{\partial \sigma} : \frac{\partial \hat{\sigma}}{\partial \varepsilon^p}, \qquad \frac{\partial g}{\partial h^\alpha} = \frac{\partial f}{\partial h^\alpha} + \frac{\partial f}{\partial \sigma} : \frac{\partial \hat{\sigma}}{\partial h^\alpha} \tag{6.36}$$

and express them in terms of the stress space loading function $f(\sigma,\varepsilon^p,h^\alpha)=0$ as:

$$d\sigma = \mathbf{D}^{ep} : d\varepsilon \tag{6.37}$$

$$d\varepsilon^p = d\lambda \mathbf{K} : \frac{\partial f}{\partial \sigma} = \frac{\hat{g}}{\psi} \mathbf{K} : \frac{\partial f}{\partial \sigma} \tag{6.38}$$

where

$$\mathbf{D}^{ep} = \mathbf{D}^e - \frac{<\hat{g}>}{\psi} \mathbf{D}^e : \frac{\partial f}{\partial \sigma} \otimes \frac{\partial f}{\partial \sigma} : \mathbf{D}^e \tag{6.39}$$

$$\psi = \frac{\partial f}{\partial \sigma} : \mathbf{D}^e : \frac{\partial f}{\partial \sigma} + \Gamma \tag{6.40a}$$

$$\Gamma = -\left(\frac{\partial f}{\partial \varepsilon^p} + \frac{\partial f}{\partial h^\alpha} \mathbf{M}^\alpha\right) : \mathbf{K} : \frac{\partial f}{\partial \sigma} \tag{6.40b}$$

$$\mathbf{K} = -\left(\frac{\partial \hat{\sigma}}{\partial \varepsilon^p} + \frac{\partial \hat{\sigma}}{\partial h^\alpha} \otimes \mathbf{M}^\alpha\right)^{-1} : \frac{\partial \hat{\sigma}}{\partial \varepsilon} \tag{6.41}$$

$$\hat{g} = \frac{\partial f}{\partial \sigma} : \mathbf{D}^e : d\varepsilon \tag{6.42}$$

The constitutive relations (6.37)-(6.42) are quite general and can be readily implemented in a computer code.

Equations (6.37)-(6.39) are, in form, analogous to the conventional equations derived from the Drucker normality rule (Owen and Hinton, 1980; Chen, 1994; Crisfield, 1997). Close inspection of (6.24), (6.34) and (6.35) shows that one of the differences between the conventional constitutive relations based on Drucker's postulate and the current results is the plastic loading rule. In the former, plastic deformation occurs when $(\partial f/\partial \sigma) : d\dot{\sigma} \geq 0$. However, during the softening stage of the deformation, this value is negative but still plastic deformation occurs. This drawback is overcome in the current formulation, i.e.,

plasticity occurs when $\hat{g}=(\partial f/\partial\sigma):\mathbf{D}^e:d\dot{\varepsilon}\geq 0$, because $\hat{g}$ is always non-negative during plastic loading.

Further inspection of (6.38) reveals that in general the plastic strain increment is not directed along the normal to the yield surface f=0, due to the presence of the fourth order tensor **K** which is termed as 'elastic-plastic coupling tensor', and for small-deformations reduces to the results of Yin and Qu (1982), where **K** was derived from Il'iushin's postulate using a simpler deformation path than used by Naghdi and Trapp (1975) and the similar idea was also demonstrated by Chen and Han (1988). Only in some particular cases, does the normality rule hold, and **K** becomes the identity tensor.

6.4 Coupling Tensor and Normality Conditions

The following work is based on the author's previous work (Gao et al. 1990). From (6.38) it can be observed that the plastic strain increment vector $d\varepsilon^p$ is not orthogonal to the stress space loading surface f=0 in general. Let θ be the angle of departure (coupling angle) between the vector $d\varepsilon^p$ and the normal direction to f=0 (Fig.6.2).

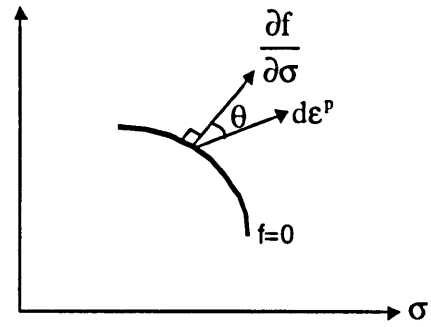

Fig.6.2 Angle between $d\varepsilon^p$ and $\partial f/\partial\sigma$

Then, from (6.38) we have:

$$\cos\theta=\left(\frac{\partial f}{\partial\sigma}:\mathbf{K}:\frac{\partial f}{\partial\sigma}\right)\Big/\sqrt{\left(\frac{\partial f}{\partial\sigma}:\frac{\partial f}{\partial\sigma}\right)\left(\mathbf{K}:\frac{\partial f}{\partial\sigma}\right)^t:\left(\mathbf{K}:\frac{\partial f}{\partial\sigma}\right)} \tag{6.43}$$

Equation (6.43) can be used to calculate the coupling angle θ. Conversely, we can determine some material constants contained in (6.1) and (6.5) using measured values of θ from experiments.

From (6.43), it can be easily seen that if, and only if, the elastic-plastic coupling tensor **K** equals **I** (**I** being the identity tensor), then θ equals zero and the normality rule holds. In this case, from (6.41) it follows that:

$$\frac{\partial\hat{\sigma}}{\partial\varepsilon^{p}}+\frac{\partial\hat{\sigma}}{\partial h^{\alpha}}\otimes\mathbf{M}^{\alpha}=-\frac{\partial\hat{\sigma}}{\partial\varepsilon} \tag{6.44}$$

By multiplying (6.44) with $d\varepsilon^{p}$ and using (6.27), we can write:

$$\frac{\partial\hat{\sigma}}{\partial\varepsilon^{p}}:d\varepsilon^{p}+\frac{\partial\hat{\sigma}}{\partial h^{\alpha}}dh^{\alpha}=-\frac{\partial\hat{\sigma}}{\partial\varepsilon}:d\varepsilon^{p} \tag{6.45}$$

On the other hand, in general from (6.27) we obtain:

$$d\sigma=\frac{\partial\hat{\sigma}}{\partial\varepsilon}:d\varepsilon+\frac{\partial\hat{\sigma}}{\partial\varepsilon^{p}}:d\varepsilon^{p}+\frac{\partial\hat{\sigma}}{\partial h^{\alpha}}dh^{\alpha} \tag{6.46}$$

Thus, substituting (6.45) into (6.46), it follows that:

$$d\sigma=\frac{\partial\hat{\sigma}}{\partial\varepsilon}:d\varepsilon-\frac{\partial\hat{\sigma}}{\partial\varepsilon}:d\varepsilon^{p} \tag{6.47}$$

Contrasting (6.47) with (6.46), yields:

$$\frac{\partial\hat{\sigma}}{\partial\varepsilon^{p}}=-\frac{\partial\hat{\sigma}}{\partial\varepsilon},\qquad\frac{\partial\hat{\sigma}}{\partial h^{\alpha}}=0 \tag{6.48}$$

Evidently, the general solution for (6.48) is that $\hat{\sigma}$ is a function of ε-ε^{p} alone, i.e.,

$$\sigma=\hat{\sigma}(\varepsilon-\varepsilon^{p}) \tag{6.49}$$

Equation (6.49) is a necessary condition for normality. Obviously, as described in the sequel, in elastic-plastic damage mechanics the condition (6.49) can not be satisfied since damage variables (regarded as internal variables) influencing the Young's modulus are included in the stress-strain response (Dafalias, 1977; Lemaitre, 1992; Gao and Zhong, 1992; Chen, 1994), so the normality rule is not applicable.

It may be noted that in this particular case (6.49), expression (6.40b) reduces to the result by Casey and Naghdi (1981).

6.5 Deformation State Function

In general, for a plastic state (f=0), deformation may be unloading ($\hat{g}<0$), neutral ($\hat{g}=0$), and loading ($\hat{g}>0$). Besides, during loading, a material may be in hardening, softening or ideally (perfect) plastic states. Knowledge of these states is helpful in choosing suitable hardening parameters or damage models. Therefore, we need to look for a function which can determine these states (Casey and Naghdi, 1981; Naghdi, 1990). To achieve this purpose, let us examine the following quantity:

$$\hat{f} = \frac{\partial f}{\partial \sigma} : d\sigma = \frac{\partial f}{\partial \sigma_{ij}} : d\sigma_{ij} \tag{6.50}$$

During loading (f=0, $\hat{g}>0$), the value of $\hat{f}$ is positive during hardening, zero for ideally plasticity and negative during softening. Although $\hat{f}$ could be used to discriminate between these three deformation states, it is related to the stress increments, which is inconvenient. In view of the fact that the $\hat{g}$ is always positive during loading, Casey and Naghdi (1981) suggested employing $\hat{f}/\hat{g}$ for this purpose, i.e.,

$$\begin{aligned} &\hat{f}/\hat{g} > 0 && \text{hardening} \\ &\hat{f}/\hat{g} = 0 && \text{ideal plasticity} \\ &\hat{f}/\hat{g} < 0 && \text{softening} \end{aligned} \tag{6.51}$$

where $\hat{f}$ and $\hat{g}$ are determined from (6.50) and (6.42). In this thesis, definition (6.51) is adopted to derive a general function used for these three deformation states.

Differentiating (6.5) and noting (6.27), yields:

$$\hat{f} + \frac{\partial f}{\partial \varepsilon^p} : d\varepsilon^p + \frac{\partial f}{\partial h^\alpha} \mathbf{M}^\alpha : d\varepsilon^p = \hat{g} + \frac{\partial g}{\partial \varepsilon^p} : d\varepsilon^p + \frac{\partial g}{\partial h^\alpha} \mathbf{M}^\alpha : d\varepsilon^p \tag{6.52}$$

Using (6.36), this equation can be written as:

$$\hat{f} = \hat{g} + \frac{\partial f}{\partial \sigma} : \left(\frac{\partial \hat{\sigma}}{\partial \varepsilon^p} + \frac{\partial \hat{\sigma}}{\partial h^\alpha} \otimes \mathbf{M}^\alpha \right) : d\varepsilon^p \tag{6.53}$$

Now substituting (6.41) into (6.38), and the resulting expression into (6.53), leads to:

$$\hat{f} = \hat{g} - \frac{\hat{g}}{\psi}\frac{\partial f}{\partial \sigma} : \mathbf{D}^e : \frac{\partial f}{\partial \sigma} \tag{6.54}$$

Using (6.40a), we obtain:

$$\hat{f} / \hat{g} = \Gamma / \psi \tag{6.55}$$

in which, Γ is determined from (6.40b). Since in plastic loading $d\lambda \geq 0$ (see (6.23)) and $(\partial g / \partial \varepsilon) : d\varepsilon \geq 0$ (see (6.24)), from (6.31) it is observed that:

$$\Psi > 0 \tag{6.56}$$

Therefore, expression (6.51) can be replaced by:

$$\begin{array}{ll} \Gamma > 0 & \text{hardening} \\ \Gamma = 0 & \text{ideal plasticity} \\ \Gamma < 0 & \text{softening} \end{array} \tag{6.57}$$

From (6.40b) we know that Γ is independent of stress (or strain) increments, i.e. it is a function of stress (or strain) states. Hence, this parameter is termed the 'deformation state function'. Although expression (6.57) was obtained by Casey and Naghdi (1981), from (6.49), we can see (from (6.40b)) that it has wider application.

6.6 Numerical Implementation

In the numerical implementation of (6.37) and (6.38), one deals with infinitesimal quantities through increments. Therefore, for given finite strain increments, it is not immediately possible to satisfy exactly the condition f=0 (i.e., equation (6.5)). Consequently, robust algorithms which draw the stresses back to the yield surface must be developed.

6.6.1 Stress-Return Mapping Algorithm

In what follows, the *operator splitting methodology* (Ortiz and Simo, 1986; Simo and Govindjee, 1991) and the *consistent tangent operator* method (Simo and Taylor, 1985) are adopted to develop a stress-return algorithm based on a Newton-Raphson iteration scheme.

Stress Return Using Residual of Global Stress-Strain Response

For a given strain ε, after the i-th iteration in the current increment, equation (6.1) is not, in general, satisfied. The residual tensor of (6.1) can be written as:

$$\mathbf{R}^i = \sigma^i - \hat{\sigma}(\varepsilon, \varepsilon^p, h^\alpha)^i = \sigma^i - \hat{\sigma}(\varepsilon, \lambda^i) \tag{6.58}$$

In order to reduce the residuals to a specified tolerance, the values of σ and λ need to be modified for the (i+1)-th iteration, that is:

$$\begin{aligned} \sigma^{i+1} &= \sigma^i + \dot{\sigma} \\ \lambda^{i+1} &= \lambda^i + \dot{\lambda} \end{aligned} \tag{6.59}$$

where $\dot{\sigma}$ represents a change in σ^i and $\dot{\lambda}$ represents a change in λ^i. Taking a truncated Taylor's series expansion of (6.58) about position i (noting that ε is given), leads to

$$\mathbf{R}^{i+1} = \mathbf{R}^i + \frac{\partial \mathbf{R}}{\partial \sigma^i} : \dot{\sigma} + \frac{\partial \mathbf{R}}{\partial \lambda^i} : \dot{\lambda} = \mathbf{R}^i + \dot{\sigma} - \frac{\partial \hat{\sigma}}{\partial \lambda^i} : \dot{\lambda} \tag{6.60}$$

The flow rule (6.23) can be written, using (6.36) as:

$$d\sigma = d\hat{\sigma} = \mathbf{D}^e : d\varepsilon - \mathbf{D}^e : \frac{\partial f}{\partial \sigma} d\lambda \tag{6.61}$$

The above equations yield:

$$\frac{\partial \hat{\sigma}}{\partial \lambda^i} = -\mathbf{D}^e : \frac{\partial f}{\partial \sigma^i} \tag{6.62}$$

Substituting (6.62) into (6.60) and letting $\mathbf{R}^{i+1}$=0, leads to:

$$\dot{\sigma} = -\mathbf{R}^i - \mathbf{D}^e : \frac{\partial f}{\partial \sigma^i} \dot{\lambda} \tag{6.63}$$

Similarly, the residual of the loading function $f(\sigma, \varepsilon^p, h^\alpha)$, namely:

$$f^i = f(\sigma, \varepsilon^p, h^\alpha)^i \tag{6.64}$$

is given by:

$$f^{i+1} = f^i + \frac{\partial f}{\partial \sigma^i} : \dot{\sigma} + \frac{\partial f}{\partial \varepsilon^p} : \dot{\varepsilon}^p + \frac{\partial f}{\partial h^\alpha} \dot{h}^\alpha \tag{6.65}$$

Substituting (6.27) and (6.38) into (6.65), it follows that:

$$f^{i+1} = f^i + \frac{\partial f}{\partial \sigma^i} : \dot{\sigma} - \Gamma \dot{\lambda} \tag{6.66}$$

where Γ is determined using (6.40b). Using the consistency condition, letting $f^{i+1}=0$ and solving the set of equations formed using (6.63) for $\dot{\lambda}$, one obtains:

$$\dot{\lambda} = \frac{f^i - \frac{\partial f}{\partial \sigma^i} : \mathbf{R}^i}{\frac{\partial f}{\partial \sigma^i} : \mathbf{D}^e : \frac{\partial f}{\partial \sigma^i} + \Gamma} \tag{6.67a}$$

Using (6.40a), this equation can also be written as:

$$\dot{\lambda} = \frac{1}{\psi}(f^i - \frac{\partial f}{\partial \sigma^i} : \mathbf{R}^i) \tag{6.67b}$$

By substituting (6.67) into (6.63), the stress changes can be determined. The stresses and the plastic multiplier are then updated, by an amount equal to the residuals from iteration i to the next, i+1, using (6.59).

Generally, the global stress-strain response (6.1) is easily satisfied in computation. In this case, the residual $\mathbf{R}^i$ can be regarded as zero and, consequently, (6.67) reduces to the results by Ortiz and Simo (1986) and Crisfield (1991) as well as those of Smith and Griffiths (1998) for perfect plasticity, with the difference that ψ is determined here using the more general form (6.40). An alternative approach to this problem is presented in the following section.

Stress Return Using Residual of Incremental Stress-Strain Response

In the following, the elastic constitutive tensor $\mathbf{D}^e$ is assumed constant and the normality rule holds true. We use σ_n and λ_n to denote the stress state and plastic multiplier at the end of the n-th increment, and σ and λ the current stress state and plastic multiplier. Substituting increments:

$$\Delta\sigma = \sigma - \sigma_n, \quad \Delta\lambda = \lambda - \lambda_n \tag{6.68}$$

for differentials in (6.61), one obtains:

$$\sigma = \sigma^t - \Delta\lambda \mathbf{D}^e : \frac{\partial f}{\partial \sigma} \tag{6.69}$$

where

$$\sigma^t = \sigma_n + \mathbf{D}^e : \Delta\varepsilon = \sigma_n + \Delta\sigma^e \tag{6.70}$$

In the above equations, the subscript n refers to the quantities at the end of the previous increment, so for a given strain increment $\Delta\varepsilon$, σ^t is constant. Equation (6.69) is not in

general satisfied and, therefore, the stress state may lie outside the loading surface. Newton-Raphson iteration method is employed to draw the stress back to the loading surface. The residual of (6.69) for the i-th iteration can be written as:

$$\mathbf{R}^i = \sigma^i - \sigma^t + \Delta\lambda^i \mathbf{D}^e : \frac{\partial f}{\partial \sigma^i} \tag{6.71}$$

Now modifying σ^i and λ^i in the next (i+1)-th iteration, as in (6.59) and taking a truncated Taylor's series expansion of (6.71) about position i, leads to:

$$\begin{aligned} \mathbf{R}^{i+1} &= \mathbf{R}^i + \frac{\partial \mathbf{R}}{\partial \sigma} : \dot{\sigma} + \frac{\partial \mathbf{R}}{\partial \lambda} : \dot{\lambda} \\ &= \mathbf{R}^i + (\mathbf{I} + \Delta\lambda^i \mathbf{D}^e : \frac{\partial^2 f}{\partial \sigma^i \otimes \partial \sigma^i}) : \dot{\sigma} + \mathbf{D}^e : \frac{\partial f}{\partial \sigma^i} \dot{\lambda} \end{aligned} \tag{6.72}$$

where $\mathbf{I}$ is the identity tensor. In the above equation, we have assumed that $\mathbf{D}^e$ is a constant tensor, although this is not true in some cases (e.g., in damage mechanics). Setting $\mathbf{R}^{i+1}=0$, we obtain from (6.72):

$$\dot{\sigma} = -\mathbf{G} : \mathbf{R}^i - \mathbf{G} : \mathbf{D}^e : \frac{\partial f}{\partial \sigma} \dot{\lambda} \tag{6.73}$$

where

$$\mathbf{G} = \left(\mathbf{I} + \Delta\lambda^i \mathbf{D}^e : \frac{\partial^2 f}{\partial \sigma^i \otimes \partial \sigma^i} \right)^{-1} \tag{6.74}$$

Solving the set of equations (6.73) and (6.66), we obtain:

$$\dot{\lambda} = \frac{1}{\tilde{\Psi}} (f^i - \frac{\partial f}{\partial \sigma^i} : \mathbf{G} : \mathbf{R}^i) \tag{6.75}$$

where

$$\tilde{\Psi} = \frac{\partial f}{\partial \sigma^i} : \mathbf{G} : \mathbf{D}^e : \frac{\partial f}{\partial \sigma^i} + \Gamma \tag{6.76}$$

The expressions for calculating the second order derivatives of the loading function in (6.74) can be found in Pearce (1996) or Crisfield (1997). Once the value of $\dot{\lambda}$ is obtained, the value of $\dot{\sigma}$ can be determined from (6.73) and the updated stresses and plastic multiplier are calculated using (6.59). An iterative process is needed, until the values of $\dot{\lambda}$ and $\dot{\sigma}$ are within a given tolerance. The Flow Chart 6.1 shows Newton-Raphson iterative processes for the two stress-return algorithm described above.

Flow Chart 6.1 Stress-return iterative process for obtained σ and λ

GSR (Global Stress-Strain Response)	ISR (Incremental Stress-Strain Response)
1. Evaluate total strain $\varepsilon=\varepsilon_n+\Delta\varepsilon$	1. Evaluate elastic trial stress $\sigma^t=\sigma_n+\Delta\sigma^e$
2. Initialise iterative variables $i=0;\ \sigma^i=\sigma;\ \lambda^i=\lambda$	2. Initialise iterative variables $i=0;\ \sigma^i=\sigma;\ \lambda^i=\lambda$
3. Calculate residuals $\mathbf{R}^i=\sigma^i-\hat{\sigma}(\varepsilon,\varepsilon^p,h^\alpha)^i$ $f^i=f(\sigma,\varepsilon^p,h^\alpha)^i$	3. Calculate residuals $\mathbf{R}^i=\sigma^i-\sigma^t+\Delta\lambda^i\mathbf{D}^e:\frac{\partial f}{\partial\sigma^i}$ $f^i=f(\sigma,\varepsilon^p,h^\alpha)^I$
4. Check convergence IF $\lvert\mathbf{R}^i\rvert<\mathrm{TOL}_R$ AND $f^i<\mathrm{TOL}_f$ THEN EXIT	4. Check convergence IF $\lvert\mathbf{R}^i\rvert<\mathrm{TOL}_R$ AND $f^i<\mathrm{TOL}_f$ THEN EXIT
5. Evaluate modification values $\dot{\lambda}=\frac{1}{\psi}(f^i-\frac{\partial f}{\partial\sigma^i}:\mathbf{R}^i)$ $\dot{\sigma}=-\mathbf{R}^i-\mathbf{D}^e:\frac{\partial f}{\partial\sigma^i}\dot{\lambda}$ $\dot{\varepsilon}^p=\dot{\lambda}\mathbf{K}:\partial f/\partial\sigma^i$	5. Evaluate modification values $\dot{\lambda}=\frac{1}{\tilde{\psi}}(f^i-\frac{\partial f}{\partial\sigma^i}:\mathbf{G}:\mathbf{R}^i)$ $\dot{\sigma}=-\mathbf{G}:\mathbf{R}^i-\mathbf{G}:\mathbf{D}^e:\frac{\partial f}{\partial\sigma}\dot{\lambda}$ $\dot{\varepsilon}^p=\dot{\lambda}\partial f/\partial\sigma^i$
6. Update variables $\sigma^{i+1}=\sigma^i+\dot{\sigma};\ \lambda^{i+1}=\lambda^i+\dot{\lambda}$ $\varepsilon^p=\varepsilon^p+\dot{\varepsilon}^p;\ h^\alpha=h^\alpha+\mathbf{M}^\alpha:\dot{\varepsilon}^p$	6. Update variables $\sigma^{i+1}=\sigma^i+\dot{\sigma};\ \lambda^{i+1}=\lambda^i+\dot{\lambda}$ $h^\alpha=h^\alpha+\mathbf{M}^\alpha:\dot{\varepsilon}^p$
7. Perform next iteration i=i+1 and GOTO 3	7. Perform next iteration i=i+1 and GOTO 3

Since the algorithm based on the residual of the incremental stress-strain response involves the second order derivatives of loading functions with respect to stresses, rapid convergence is expected. However, the first algorithm has a wider application range, since it does not have the limitation that $\mathbf{D}^e$ is a constant tensor.

Inspection of (6.77) and (6.67a) shows that in the case of very small increments ($\Delta\lambda^i\rightarrow 0$), the tensor $\mathbf{G}$ in (6.74) degenerates to the identity tensor and (6.75) reduces to (6.67).

Consistent Tangent Operator

The two stress-return algorithms described above are based on local iterative processes using the Newton-Raphson method. Simo and Taylor (1985) proposed a consistent tangent operator which can be incorporated into a global iteration solution algorithm based on the Newton-Raphson method. This operator is *consistent* with the stress integration strategy and is characterised by a *quadratic rate of convergence.*

The flow rule (6.23) can be written, using (6.36), in an incremental form as:

$$\Delta\sigma = \mathbf{D}^e : \Delta\varepsilon - \Delta\lambda \mathbf{D}^e : \frac{\partial f}{\partial \sigma} \tag{6.77}$$

In order to determine the stresses and plastic multiplier in the next iteration from the converged results at the end of the i-th iteration, we substitute the following:

$$\begin{aligned} \Delta\sigma &= \sigma - \sigma^i \\ \Delta\varepsilon &= \varepsilon - \varepsilon^i \\ \Delta\lambda &= \lambda - \lambda^i \end{aligned} \tag{6.78}$$

into (6.77), which leads to:

$$\sigma = \sigma^i + \mathbf{D}^e : \left\{ \varepsilon - \varepsilon^i - (\lambda - \lambda^i) \frac{\partial f}{\partial \sigma} \right\} \tag{6.79}$$

Differentiating (6.79) and noticing that σ^i, ε^i and λ^i are constant, it follows that:

$$\dot{\sigma} = \mathbf{D}^e : \left\{ \dot{\varepsilon} - \dot{\lambda} \frac{\partial f}{\partial \sigma} - (\lambda - \lambda^i) \frac{\partial^2 f}{\partial \sigma \otimes \partial \sigma} : \dot{\sigma} \right\} \tag{6.80}$$

Rearranging the above equation, one can readily obtain:

$$\dot{\sigma} = \tilde{\mathbf{D}} : \left(\dot{\varepsilon} - \dot{\lambda} \frac{\partial f}{\partial \sigma} \right) \tag{6.81}$$

where

$$\tilde{\mathbf{D}} = \mathbf{G} : \mathbf{D}^e \tag{6.82}$$

here, **G** is determined using (6.74). Using (6.27) and (6.38), the consistency condition, df=0, gives:

$$\frac{\partial f}{\partial \sigma} : \dot{\sigma} - \Gamma \dot{\lambda} = 0 \tag{6.83}$$

in which, Γ is determined using (6.40). Substituting (6.81) into (6.83) yields an expression for $\dot{\lambda}$:

$$\dot{\lambda} = \frac{1}{\tilde{\psi}} \frac{\partial f}{\partial \sigma} : \tilde{\mathbf{D}} : \dot{\varepsilon} \tag{6.84}$$

where $\tilde{\psi}$ is determined using (6.76). Substituting (6.84) into (6.81), we obtain:

$$\dot{\sigma} = \mathbf{D}^{ct} : \dot{\varepsilon} \tag{6.85}$$

where

$$\mathbf{D}^{ct} = \tilde{\mathbf{D}} - \frac{<\hat{g}>}{\tilde{\psi}} \tilde{\mathbf{D}} : \frac{\partial f}{\partial \sigma} \otimes \frac{\partial f}{\partial \sigma} : \tilde{\mathbf{D}} \tag{6.86}$$

Comparing (6.85) and (6.86) with (6.37) and (6.40a), respectively, we can see that the consistent tangent operator of (6.86) is analogous with the continuum tangent operator of (6.40a). In the case of very small increments ($\Delta\lambda^i \rightarrow 0$), the tensor **G** in (6.74) degenerates to the identity tensor and (6.86) reduces to (6.40a). It is noted that equation (6.86) was also derived by Pearce (1996) and Crisfield (1997). The difference is that here $\tilde{\psi}$ is determined using (6.76) and the strain space derived quantity $\hat{g}$ is used (which is determined using (6.42)).

In a similar manner, for the cases in which the normality rule holds true (from equation (6.38) with **K** equal to the identity tensor); we have:

$$\Delta\varepsilon^p = \Delta\lambda \frac{\partial f}{\partial \sigma} \tag{6.87}$$

and obtain:

$$\dot{\varepsilon}^p = \dot{\lambda} \frac{\partial f}{\partial \sigma} + \Delta\lambda \frac{\partial^2 f}{\partial \sigma \otimes \partial \sigma} : \dot{\sigma} \tag{6.88}$$

Substituting (6.83) and (6.85) yields:

$$\dot{\varepsilon}^p = \left(\frac{1}{\tilde{\psi}} \frac{\partial f}{\partial \sigma} \otimes \frac{\partial f}{\partial \sigma} : \tilde{\mathbf{D}} + \Delta\lambda \frac{\partial^2 f}{\partial \sigma \otimes \partial \sigma} : \mathbf{D}^{ct} \right) : \dot{\varepsilon} \tag{6.89}$$

For the sake of subsequent use, initial stresses are defined as:

$$\dot{\sigma}^p = \mathbf{D}^e : \dot{\varepsilon}^p \tag{6.90}$$

Thus, using (6.89), we obtain:

$$\dot{\sigma}^p = \mathbf{D}^{cp} : \dot{\varepsilon} \tag{6.91}$$

where

$$\mathbf{D}^{cp} = \mathbf{D}^{p} + \Delta\lambda \mathbf{D}^{e} : \frac{\partial^2 f}{\partial\sigma \otimes \partial\sigma} : \mathbf{D}^{ct} \tag{6.92}$$

and (after using (6.81))

$$\mathbf{D}^{p} = \frac{1}{\tilde{\psi}} \mathbf{D}^{e} : \frac{\partial f}{\partial\sigma} \otimes \frac{\partial f}{\partial\sigma} : \mathbf{G} : \mathbf{D}^{e} \tag{6.93}$$

Using (6.93), the consistent tangent operator $\mathbf{D}^{ct}$ in (6.86) can also be written as:

$$\mathbf{D}^{ct} = \mathbf{G} : (\mathbf{D}^{e} - \mathbf{D}^{p}) \tag{6.94}$$

where $\mathbf{G}$ is determined using (6.74). Moreover, from (6.74), we know that:

$$\Delta\lambda \mathbf{D}^{e} : \frac{\partial^2 f}{\partial\sigma \otimes \partial\sigma} : \mathbf{G} = \mathbf{I} - \mathbf{G}$$

Substituting the above equation and (6.94) into(6.92), it follows that:

$$\mathbf{D}^{cp} = \mathbf{D}^{e} - \mathbf{D}^{ct} \tag{6.95}$$

Since all the above equations involve the second order derivatives of the loading function with respect to stresses, use of these equation leads to a *quadratic rate of convergence* for iteration solution processes based on the Newton-Raphson method.

It is noted that formulations (6.87)-(6.95) are obtained here for the first time.

6.6.2 Constitutive Relations for Infinitesimal Elastoplastic Deformation

The formulations described in the previous sections are applicable to non-linear stress-strain responses and general loading functions in finite elastoplastic deformation. This sub-section gives concrete numerical implementation formulations for infinitesimal elastoplastic deformation. In this case, the strain is decomposed into elastic and plastic parts:

$$\varepsilon = \varepsilon^{e} + \varepsilon^{p} \tag{6.96}$$

The elastic stress-strain response is governed by the generalised Hooke's law:

$$\sigma = \mathbf{D}^{e} : (\varepsilon - \varepsilon^{p}) \tag{6.97}$$

where $\mathbf{D}^e$ is determined from (2.4). In this thesis, the equivalent plastic strain $\bar{\varepsilon}^p$ is taken as the internal variable and the following type of loading function is considered:

$$f(\sigma,\varepsilon^p,h^\alpha)=\bar{f}(\sigma-\rho)-k(\bar{\varepsilon}^p)=0 \tag{6.98}$$

in which ρ is the *back stress*. Here, the modified Melan's kinematic hardening model (Lubliner, 1990) is adopted, which can be written as:

$$d\rho = cd\varepsilon^p - b\rho d\bar{\varepsilon}^p \tag{6.99}$$

where

$$d\bar{\varepsilon}^p = c'\sqrt{d\varepsilon^p : d\varepsilon^p} \tag{6.100}$$

and c and b are material constants. If they are both zero, (6.98) becomes isotropic hardening. Note that the coefficient c' in (6.100) is a constant which makes the equivalent plastic strain $\bar{\varepsilon}^p$ equal to the uniaxial plastic strain under uniaxial yield tests (Chen, 1994). For example, $c'=\sqrt{2/3}$ for the Von Mises loading function.

As described in section 6.4, for materials described by (6.97) and (6.98), the elastoplastic coupling tensor $\mathbf{K}$ reduces to the identity tensor and consequently the constitutive relations (6.37)-(6.40) become:

$$d\sigma=\mathbf{D}^{ep}:d\varepsilon \tag{6.101}$$

$$d\varepsilon^p=d\lambda\frac{\partial\bar{f}}{\partial\sigma}=\frac{\hat{g}}{\psi}\frac{\partial\bar{f}}{\partial\sigma} \tag{6.102}$$

where

$$\mathbf{D}^{ep}=\mathbf{D}^e-\frac{<\hat{g}>}{\psi}\mathbf{D}^e:\frac{\partial\bar{f}}{\partial\sigma}\otimes\frac{\partial\bar{f}}{\partial\sigma}:\mathbf{D}^e \tag{6.103}$$

$$\psi=\frac{\partial\bar{f}}{\partial\sigma}:\mathbf{D}^e:\frac{\partial\bar{f}}{\partial\sigma}+\Gamma \tag{6.104}$$

$$\Gamma=-\frac{\partial\bar{f}}{\partial\varepsilon^p}:\frac{\partial\bar{f}}{\partial\sigma}-(\frac{\partial\bar{f}}{\partial\bar{\varepsilon}^p}-\frac{\partial k}{\partial\bar{\varepsilon}^p})\mathbf{M}:\frac{\partial\bar{f}}{\partial\sigma} \tag{6.105}$$

where

$$<\hat{g}>=\begin{cases}=0 & \text{if } f(\sigma,\varepsilon^p,h^\alpha)<0 & \text{(elastic)}\\ =1 & \text{if } f(\sigma,\varepsilon^p,h^\alpha)=0 \text{ and } \hat{g}\geq 0 & \text{(loading)}\\ =0 & \text{if } f(\sigma,\varepsilon^p,h^\alpha)=0 \text{ and } \hat{g}<0 & \text{(unloading)}\end{cases} \tag{6.106}$$

and

$$\hat{g} = \frac{\partial \bar{f}}{\partial \sigma} : \mathbf{D}^e : d\varepsilon \tag{6.107}$$

From (6.98), we have:

$$\frac{\partial \bar{f}}{\partial \varepsilon^p} = -\frac{\partial \bar{f}}{\partial \sigma} : \frac{\partial \rho}{\partial \varepsilon^p}, \qquad \frac{\partial \bar{f}}{\partial \bar{\varepsilon}^p} = -\frac{\partial \bar{f}}{\partial \sigma} : \frac{\partial \rho}{\partial \bar{\varepsilon}^p} \tag{6.108}$$

and from (6.99), it follows that:

$$\frac{\partial \rho}{\partial \varepsilon^p} = c\mathbf{I}, \qquad \frac{\partial \rho}{\partial \bar{\varepsilon}^p} = -b\rho \tag{6.109}$$

From the definitions (6.27) and (6.100) (and using (6.102)), we can write:

$$d\bar{\varepsilon}^p = \mathbf{M} : d\varepsilon^p = d\lambda \mathbf{M} : \frac{\partial \bar{f}}{\partial \sigma} \quad \text{and} \quad d\bar{\varepsilon}^p = c'\sqrt{d\varepsilon^p : d\varepsilon^p} = d\lambda c'\sqrt{\frac{\partial \bar{f}}{\partial \sigma} : \frac{\partial \bar{f}}{\partial \sigma}} \tag{6.110}$$

Comparing these two equations, we obtain:

$$\mathbf{M} : \frac{\partial \bar{f}}{\partial \sigma} = c'\sqrt{\frac{\partial \bar{f}}{\partial \sigma} : \frac{\partial \bar{f}}{\partial \sigma}} \tag{6.111}$$

Finally, substituting (6.111), (6.109) and (6.108) into (6.105) leads to:

$$\Gamma = (H' - b\frac{\partial \bar{f}}{\partial \sigma} : \rho)c'\sqrt{\frac{\partial \bar{f}}{\partial \sigma} : \frac{\partial \bar{f}}{\partial \sigma}} + c\frac{\partial \bar{f}}{\partial \sigma} : \frac{\partial \bar{f}}{\partial \sigma} \tag{6.112}$$

where $H' = \dfrac{\partial k}{\partial \bar{\varepsilon}^p}$ is the local slope of the uniaxial stress/plastic strain curve, which can be determined experimentally. Expression (6.112) is original to this thesis.

For the Von Mises yield function as described in the sequel, it can be easily shown that:

$$c'\sqrt{\frac{\partial \bar{f}}{\partial \sigma} : \frac{\partial \bar{f}}{\partial \sigma}} = 1, \qquad d\bar{\varepsilon}^p = d\lambda$$

In this case, H' reduces to the parameter "A" of Owen and Hinton (1980) for the following four yield criteria. We note that these two equations do not hold true for other yield criteria.

Four Commonly-Used Yield Functions

Although (6.101)-(6.112) can be applied to quite general loading functions (yield criteria), only four commonly-used yield criteria, i.e., *Tresca, Von Mises, Mohr-Coulomb,* and *Drucker-Prager*, are employed in this thesis. These criteria have been discussed at length

in the literature (e.g., Owen and Hinton, 1980; Crisfield, 1997) and can be outlined as follows. In the following, a rigorous derivation of the constant c' has been followed leading to novel (to the author's knowledge) expressions for the *Mohr-Coulomb* criterion.

Table 6.1 Representation of Four Yield Critera

Yield Criterion	$\bar{f}$	k	c'
Tresca	$2\sqrt{J_2'}\cos\theta$	$\sigma_y + H'\bar{\varepsilon}^p$	$\sqrt{\frac{2}{3}}$
Von Mises	$\sqrt{3J_2'}$	$\sigma_y + H'\bar{\varepsilon}^p$	$\sqrt{\frac{2}{3}}$
Mohr-Coulomb	$J_1 \sin\phi/3 + \sqrt{J_2'}\,(\cos\theta - \sin\theta\sin\phi/\sqrt{3})$	$c\cos\phi + H'\bar{\varepsilon}^p$	$\frac{\sqrt{2}(1+\sin\phi)}{\sqrt{3+2\sin\phi+3\sin^2\phi}}$
Drucker-Prager	$\alpha J_1 + \sqrt{J_2'}$	$k' + H'\bar{\varepsilon}^p$	$\frac{\lvert\alpha + 1/\sqrt{3}\rvert}{\sqrt{3\alpha^2 + 1/2}}$

in which, J_1 is the first invariant of the stresses, J_2' and J_3' are the second and third invariants of the deviatoric stresses, respectively, and θ $(-\pi/6 \le \theta \le \pi/6)$ is the Lode parameter, i.e.,

$$J_1 = \sigma_{ii} - \rho_{ii}, \quad J_2' = \frac{1}{2}\sigma_{ij}'\sigma_{ij}', \quad J_3' = \frac{1}{3}\sigma_{ij}'\sigma_{jk}'\sigma_{ki}'$$

$$\theta = \frac{1}{3}\sin^{-1}\left[-\frac{3\sqrt{3}}{2}\frac{J_3'}{(J_2')^{3/2}}\right] \tag{6.113}$$

$$\sigma_{ij}' = \sigma_{ij} - \rho_{ij} - \frac{1}{3}\delta_{ij}(\sigma_{kk} - \rho_{kk})$$

The parameters c and ϕ in the last two criteria are the cohesion and angle of internal friction, respectively. Further, the parameters α and k' in the fourth (Drucker-Prager) criterion are determined using the equations:

$$\alpha = \frac{2\sin\phi}{\sqrt{3}(3-\sin\phi)}, \quad k' = \frac{6c\cos\phi}{\sqrt{3}(3-\sin\phi)} \tag{6.114}$$

The gradient of the yield functions now can be written as:

$$\frac{\partial \bar{f}}{\partial \sigma} = C_1 \frac{\partial J_1}{\partial \sigma} + C_2 \frac{\partial \sqrt{J_2'}}{\partial \sigma} + C_3 \frac{\partial J_3'}{\partial \sigma} \tag{6,115}$$

where

$$C_1 = \frac{\partial \bar{f}}{\partial J_1}, \quad C_2 = \frac{\partial \bar{f}}{\partial \sqrt{J_2'}}, \quad C_3 = \frac{\partial \bar{f}}{\partial J_3'} \tag{6.116}$$

and from (6.113)

$$\frac{\partial J_1}{\partial \sigma_{ij}} = \delta_{ij}, \quad \frac{\partial \sqrt{J_2'}}{\partial \sigma_{ij}} = \frac{\sigma_{ij}'}{2\sqrt{J_2'}}, \quad \frac{\partial J_3'}{\partial \sigma_{ij}} = \sigma_{ik}'\sigma_{kj}' - \frac{2}{3} J_2' \delta_{ij} \tag{6.117}$$

Table 6.2 gives expressions for C_1- C_3 for the four yield criteria.

Table 6.2 Constants defined in (6.116) ($\theta \neq \pm \pi/6$)

Yield Criterion	C_1	C_2	C_3
Tresca	0	$2\cos\theta(1+\tan\theta\tan 3\theta)$	$\frac{\sqrt{3}}{J_2'}\frac{\sin\theta}{\cos 3\theta}$
Von Mises	0	$\sqrt{3}$	0
Mohr-Coulomb	$\frac{1}{3}\sin\phi$	$\cos\theta[1+\tan\theta\tan 3\theta + \sin\phi(\tan 3\theta - \tan\theta)/\sqrt{3}]$	$\frac{\sqrt{3}\sin\theta + \cos\theta\sin\phi}{2J_2'\cos 3\theta}$
Drucker-Prager	α	1	0

From Table 6.2 it can be seen that when θ approaches $\pm\pi/6$, C_2 and C_3 become indeterminate for Tresca and Mohr-Coulomb criteria. For these particular cases, C_2 and C_3 can be directly derived from Table 6.1 by setting $\theta = \pm\pi/6$, which yields the results shown in Table 6.3.

Table 6.3 Constants defined in (6.116) ($\theta = \pm\pi/6$)

Yield Criteria	C_1	C_2	C_3
Tresca	0	$\sqrt{3}$	0
Mohr-Coulomb	$\frac{1}{3}\sin\phi$	$\frac{\sqrt{3}}{2} - \frac{\sin\theta\sin\phi}{\sqrt{3}}$	0

In numerical implementation, when $|\theta| \leq 29°$, Table 6.2 (otherwise Table 6.3) is used to calculate the values of C_1 to C_3 for the Tresca and Mohr-Coulomb criteria. Physically this artifice corresponds to a 'rounding off' of the yield surface corners.

6.7 Summary

The elastoplastic flow rule and loading rule are derived from the assumption of non-negative work in closed cycles of deformation, from which the unified constitutive relations for hardening, softening, and ideal plasticity behaviour are developed. These relations are applicable to non-linear stress-strain response in finite elastoplastic deformation. It is shown that the Drucker's normality conditions is a particular case of the results derived in this chapter. Furthermore, expressions which are independent of stress (or strain) rates and can be used to evaluate the deformation hardening, softening, or ideal plasticity is presented. Finally, a complete description of small elastoplastic deformation under kinematic hardening is provided for four common yield criteria.

Chapter 7

Boundary Element Formulation for Non-Linear Analysis

7.1 Introduction

The earliest work on non-linear boundary element analysis was done by Swedlow and Cruse (1971), Ricardella (1973), and Mendelson & Albers (1975). Some errors in the earlier formulations were corrected by Mukherjee (1977), Bui (1978) and Telles & Brebbia (1979). However, some inherent difficulties, such as the strongly singular domain integrals and the stability of the system equations, have stymied development of this method.

The crucial task is to remove (or regularise) the strong singularities arising in the domain integrals. The existing methodologies can be categorised as follows:

(1) Interpolation using nodal displacements (differentiating the shape functions):
(Banerjee et al. 1979; Gao and Zheng, 1990a; Wearing and Dimagiba, 1998).

(2) Analytical and semi-analytical techniques:
(Ricardella, 1973; Mendelson and Albers, 1975; Telles and Brebbia, 1979, 1983; Zheng and Gao, 1986; Chandra and Saigal, 1991).

(3) Exclusion of a small sphere (using higher order volume cells):
(Banerjee and Davies, 1984; Banerjee and Raveendra, 1986).

(4) Transformation of domain integrals to surface integrals:
(Huang and Du, 1988; Zhang et al. 1992; Dallner and Kuhn, 1993; Chandra and Mukherjee, 1996; Chen et al., 1996; Dong and Antes, 1998).

(5) Regularization of singular integrals:

(Guiggiani et al. 1992; Huber et al. 1996;

Cisilino et al. 1998; Poon et al. 1998a; Burghardt and Van, 1998).

(6) Indirect approaches:

(Telles and Brebbia, 1979; Brebbia et al. 1984; Lee and Fenner, 1986; Chen and Ji, 1987; Henry and Banerjee, 1988; Banerjee et al. 1989).

In category (1), the internal stresses are calculated using nodal displacements by differentiating the shape functions using methods employed in FEM. Due to the properties of the shape functions and their derivatives, this local procedure is prone to significant errors especially in the case of coarse meshes and low order shape functions. Category (2) is only feasible with "constant" or "linear" cells, in which the singularities of the initial stress (strain) kernels can be eliminated analytically or semi-analytically. For arbitrary cells of more complex geometry and higher order shape functions, more general techniques have to be used. In category (3), the strongly singular domain integrals become bounded, if a small sphere around the singular point is excluded. Although this method can deal with higher order cells, with the help of the volume sub-division technique which was originally proposed by Lachat and Watson (1975) and coded by Mustoe (1984), it may give inaccurate results for cases in which the cells around the singular point are greatly different in shape or size.

In category (4), the singularity is first isolated by subtracting a singular function from the original singular integral. The original strongly singular integral becomes weakly singular, which can then be integrated using standard Gauss quadrature. The singular function is transformed, via Gauss theorem, into a regular surface integral over the boundary of the body or plastic region. A rather different transformation was employed by Dallner and Kuhn (1993) in their initial strain algorithm. In their work, the transformed surface integral is mapped over the boundary of the elements surrounding the source point rather than over the body's surface.

Another approach (category (5)) for direct evaluation of principal value integrals was suggested by Guiggiani and Gigante (1990), based on the regularisation of the singular integral by substracting the truncated Taylor series from the integrand. Although, in principle, this method can also be used for evaluation of singular surface integrals (Guiggiani et al. 1992), it is : robust only for smooth boundary points. All functions must

be expressed in a local spherical co-ordinate system. Then all integrands, including kernels, spatial derivatives, Jacobians and shape functions are expanded in Taylor series form, in terms of the local co-ordinates. As a consequence, the calculations are tedious and complicated, and difficult to implement in a computer code. Another type of regularisation for directly calculating the boundary stresses is developed by Poon et al. (1998a). A simple equation was obtained by the use of three global modes of deformation: rigid-body displacement, linear displacement, and a fully constrained plastic solution. While their approach is relatively straightforward, computation would be prohibitive enormous, since the system equations now involve stresses, displacements and displacement gradients.

In the last category (6), the singularities can be circumvented by employing indirect approaches, based on the application of known reference solutions. The drawback of this approach is that it requires discretisation of the cells through the entire region, which negates to a certain extent the advantage of BEM (namely, that only the yield zone needs to be discretised into cells). To avoid this discretisation, a multi-region BEM technique has been employed (Banerjee et al. 1989) or a second boundary defined (Lee and Fenner, 1986).

In Section 2 of this Chapter, the basic boundary integral equations are reviewed. In Section 3, a new method for efficiently dealing with the strongly singular domain integrals is developed, which, like that of Telles and Brebbia (1979, 1983) for two-dimensional linear cells, should fall into the categories (4) and (2). Two new identities for the initial stress and strain kernels are first derived; a novel transformation technique (from domain integrals to element surface integrals) is then proposed for removing the strongly singularities. The results are suitable for both 2D and 3D problems, linear and higher order cells, and both initial stress and strain approaches. Finally, explicit formulations for calculating boundary stresses using stress recovery method are derived in Section 4.

7.2 Basic Non-Linear BEM Formulations

In this section, the conventional elasto-plastic boundary integral equations are established, mainly based on the work of Swedlow and Cruse (1971), Telles and Brebbia (1979, 1983), and Banerjee (1994).

7.2.1 Boundary Integral Equations

In non-linear problems, the physical quantities are usually formulated in terms of their incremental forms. The relationship between elastic stress increments and total strain increments can be defined as:

$$\dot{\sigma}^e_{ij} = D^e_{ijkl}\dot{\varepsilon}_{kl} \tag{7.1}$$

where the subscript dot denotes increment, and

$$D^e_{ijkl} = \lambda\delta_{ij}\delta_{kl} + G(\delta_{ik}\delta_{jl} + \delta_{il}\delta_{jk}) \tag{2.4) bis.}$$

We consider two elastic equilibrium states in the domain Ω, with boundary Γ, characterized by ($\dot{\sigma}^e_{ij}$, $\dot{\varepsilon}_{ij}$) and (σ^*_{ij}, ε^*_{ij}). Thus, using (7.1), we have:

$$\begin{aligned}\dot{\sigma}^e_{ij}\varepsilon^*_{ij} &= \lambda\delta_{ij}\dot{\varepsilon}_{kk}\varepsilon^*_{ij} + 2G\dot{\varepsilon}_{ij}\varepsilon^*_{ij}\\ &= \lambda\dot{\varepsilon}_{kk}\varepsilon^*_{ll} + 2G\dot{\varepsilon}_{ij}\varepsilon^*_{ij}\\ &= (\lambda\delta_{ij}\varepsilon^*_{ll} + 2G\varepsilon^*_{ij})\dot{\varepsilon}_{ij}\\ &= \sigma^*_{ij}\dot{\varepsilon}_{ij}\end{aligned} \tag{7.2}$$

Hence, the following integral statement holds:

$$\int_\Omega \dot{\sigma}^e_{ij}\varepsilon^*_{ij}d\Omega = \int_\Omega \sigma^*_{ij}\dot{\varepsilon}_{ij}d\Omega \tag{7.3}$$

In the following, small elastoplastic deformations are assumed. Thus, the total strain increments can be decomposed into elastic and plastic parts (e.g. Lubliner, 1990), i.e.,

$$\dot{\varepsilon}_{ij} = \dot{\varepsilon}^e_{ij} + \dot{\varepsilon}^p_{ij} \tag{7.4}$$

where the elastic strain increments $\dot{\varepsilon}^e_{ij}$ are related to stress increments (e.g. Lubliner, 1990) by:

$$\dot{\sigma}_{ij} = D^e_{ijkl}\dot{\varepsilon}^e_{kl} = D^e_{ijkl}(\dot{\varepsilon}_{kl} - \dot{\varepsilon}^p_{kl}) \tag{7.5}$$

Using (7.1), equation (7.5) gives:

$$\dot{\sigma}_{ij} = \dot{\sigma}^e_{ij} - \dot{\sigma}^p_{ij} \tag{7.6}$$

where

$$\dot{\sigma}^p_{ij} = D^e_{ijkl}\dot{\varepsilon}^p_{kl} \tag{7.7}$$

Now, equations (2.1), (2.2) and (2.6) can be written for the two equilibrium states as:

$$\frac{\partial \dot{\sigma}_{ij}}{\partial x_j} + \dot{b}_i = 0, \qquad \frac{\partial \sigma^*_{ij}}{\partial x_j} + b^*_i = 0$$

$$\dot{t}_i = \dot{\sigma}_{ij} n_j, \qquad t^*_i = \sigma^*_{ij} n_j$$

$$\dot{\varepsilon}_{ij} = \frac{1}{2}\left(\frac{\partial \dot{u}_i}{\partial x_j} + \frac{\partial \dot{u}_j}{\partial x_i}\right), \quad \varepsilon^*_{ij} = \frac{1}{2}\left(\frac{\partial u^*_i}{\partial x_j} + \frac{\partial u^*_j}{\partial x_i}\right)$$

Substituting (7.6) into (7.3) and using the above equations, the left-hand side of (7.3) can be manipulated as:

$$\int_\Omega \dot{\sigma}^e_{ij}\varepsilon^*_{ij} d\Omega = \int_\Omega \dot{\sigma}_{ij}\varepsilon^*_{ij} d\Omega + \int_\Omega \dot{\sigma}^p_{ij}\varepsilon^*_{ij} d\Omega = \int_\Omega \dot{\sigma}_{ij}\frac{\partial u^*_i}{\partial x_j} d\Omega + \int_\Omega \dot{\sigma}^p_{ij}\varepsilon^*_{ij} d\Omega$$

$$= \int_\Omega \frac{\partial \dot{\sigma}_{ij} u^*_i}{\partial x_j} d\Omega - \int_\Omega u^*_i \frac{\partial \dot{\sigma}_{ij}}{\partial x_j} d\Omega + \int_\Omega \dot{\sigma}^p_{ij}\varepsilon^*_{ij} d\Omega$$

$$= \int_\Gamma \dot{\sigma}_{ij} u^*_i n_j d\Gamma + \int_\Omega u^*_i \dot{b}_i d\Omega + \int_\Omega \dot{\sigma}^p_{ij}\varepsilon^*_{ij} d\Omega$$

$$= \int_\Gamma u^*_i \dot{t}_i d\Gamma + \int_\Omega u^*_i \dot{b}_i d\Omega + \int_\Omega \varepsilon^*_{ij}\dot{\sigma}^p_{ij} d\Omega$$

and the right-hand side of (7.3) can be manipulated as:

$$\int_\Omega \sigma^*_{ij}\dot{\varepsilon}_{ij} d\Omega = \int_\Omega \sigma^*_{ij}\frac{\partial \dot{u}_i}{\partial x_j} d\Omega = \int_\Omega \frac{\partial \sigma^*_{ij}\dot{u}_i}{\partial x_j} d\Omega - \int_\Omega \dot{u}_i \frac{\partial \sigma^*_{ij}}{\partial x_j} d\Omega$$

$$= \int_\Gamma \sigma^*_{ij}\dot{u}_i n_j d\Gamma + \int_\Omega \dot{u}_i b^*_i d\Omega = \int_\Gamma t^*_i \dot{u}_i d\Gamma + \int_\Omega b^*_i \dot{u}_i d\Omega$$

Substituting the above two equations into (7.3), it follows that:

$$\int_\Gamma u^*_i \dot{t}_i d\Gamma + \int_\Omega u^*_i \dot{b}_i d\Omega + \int_\Omega \varepsilon^*_{ij}\dot{\sigma}^p_{ij} d\Omega = \int_\Gamma t^*_i \dot{u}_i d\Gamma + \int_\Omega b^*_i \dot{u}_i d\Omega \qquad (7.8)$$

Now we take the quantities with the superscript asterisk '*' in (7.8) to be Kelvin's fundamental solutions U_{ij} and T_{ij}, namely:

$$U_{ij}(p,q) = \frac{1}{16\pi(1-\nu)Gr}\{(3-4\nu)\delta_{ij} + r_{,i}r_{,j}\} \qquad (2.10)\text{ bis.}$$

$$T_{ij}(p,q) = \frac{-1}{8\pi(1-\nu)r^2}\{r_{,k}n_k[(1-2\nu)\delta_{ij} + 3r_{,i}r_{,j}] - (1-2\nu)(n_j r_{,i} - n_i r_{,j})\} \qquad (2.14)\text{ bis.}$$

And using the properties:

$$b^*_i(p,q) = \delta(x(q) - x(p))P_i \qquad (2.8)\text{ bis.}$$

$$\int_{\Omega}\delta(x(q)-x(p))f(q)d\Omega(q)=f(p) \qquad (2.9)\text{ bis.}$$

(where P_i is unity in the i direction), from (7.8) it follows that:

$$\begin{aligned}\dot{u}_i(p)=&\int_{\Gamma}U_{ij}(p,Q)\dot{t}_j(Q)d\Gamma(Q)-\int_{\Gamma}T_{ij}(p,Q)\dot{u}_j(Q)d\Gamma(Q)\\&+\int_{\Omega}U_{ij}(p,q)\dot{b}_j(q)d\Omega(q)+\int_{\Omega}E_{ijk}(p,q)\dot{\sigma}^p_{jk}(q)d\Omega(q)\end{aligned} \qquad (7.9)$$

where p and q stand for the source point and field point, respectively, for internal points, and P and Q for boundary points, and

$$\begin{aligned}E_{ijk}(p,q)&=\frac{1}{2}\left(\frac{\partial U_{ij}}{\partial x_k}+\frac{\partial U_{ik}}{\partial x_j}\right)\\&=\frac{-1}{16\pi(1-\nu)Gr^2}\left\{(1-2\nu)(r_{,k}\delta_{ij}+r_{,j}\delta_{ik})-r_{,i}\delta_{jk}+3r_{,i}r_{,j}r_{,k}\right\}\end{aligned} \qquad (7.10)$$

Equation (7.9) is only applicable for internal points. For points which are located on boundary, integral equations can be obtained by allowing the source point p approach a boundary point P, which results in (Swedlow and Cruse, 1971; Telles & Brebbia, 1979; Banerjee,1994):

$$\begin{aligned}c_{ij}(P)\dot{u}_j(P)+&\int_{\Gamma}T_{ij}(P,Q)\dot{u}_j(Q)d\Gamma(Q)=\int_{\Gamma}U_{ij}(P,Q)\dot{t}_j(Q)d\Gamma(Q)\\&+\int_{\Omega}U_{ij}(P,q)\dot{b}_j(q)d\Omega(q)+\int_{\Omega}E_{ijk}(P,q)\dot{\sigma}^p_{jk}(q)d\Omega(q)\end{aligned} \qquad (7.11)$$

where $c_{ij}(P)=\delta_{ij}/2$ for smooth boundary points. Equation (7.11) is expressed in terms of initial stresses. In terms of initial strains, the last integral on the right-hand side is replaced using the equations:

$$\int_{\Omega}E_{ijk}(P,q)\dot{\sigma}^p_{jk}(q)d\Omega(q)=\int_{\Omega}\Sigma_{ijk}(P,q)\dot{\varepsilon}^p_{jk}(q)d\Omega(q) \qquad (7.12)$$

where

$$\Sigma_{ijk}(P,q)=D^e_{jkrs}E_{irs}(P,q) \qquad (7.13)$$

We observe that, apart from the additional domain integrals involving initial stresses (or initial strains), equation (7.11) is the same as that obtained earlier for linear elastic analysis.

7.2.2 Internal Stresses

In order to evaluate the domain integrals involving the initial stresses in (7.9) and (7.11), the yield region (only) must be discretized (usually into internal cells).

Differentiating (7.9) with respect to the source point p leads to:

$$\frac{\partial \dot{u}_i(p)}{\partial x_m^p} = \int_\Gamma \frac{\partial U_{ij}(p,Q)}{\partial x_m^p} \dot{t}_j(Q)d\Gamma(Q) - \int_\Gamma \frac{\partial T_{ij}(p,Q)}{\partial x_m^p} \dot{u}_j(Q)d\Gamma(Q) + \int_\Omega \frac{\partial U_{ij}(p,q)}{\partial x_m^p} \dot{b}_j(q)d\Omega(q) + \frac{\partial}{\partial x_m^p} \int_\Omega E_{ijk}(p,q)\dot{\sigma}_{jk}^p(q)d\Omega(q) \tag{7.14}$$

Considering that the domain integral in the above equation includes the singular point p, this integral can be evaluated by excluding a small sphere D centred at p (Banerjee, 1994). Thus we have:

$$\frac{\partial}{\partial x_m^p} \int_\Omega E_{ijk}(p,q)\dot{\sigma}_{jk}^p(q)d\Omega(q) = \lim_{D\to 0} \int_{\Omega-D} \frac{\partial E_{ijk}(p,q)}{\partial x_m^p} \dot{\sigma}_{jk}^p(q)d\Omega(q) + \dot{\sigma}_{jk}^p(p) \lim_{D\to 0} \int_D \frac{\partial E_{ijk}(p,q)}{\partial x_m^p} d\Omega(q) \tag{7.15}$$

in which, $\lim_{D\to 0} \dot{\sigma}_{jk}^p(q) = \dot{\sigma}_{jk}^p(p)$ has been used. Noticing that $\partial(\cdot)/\partial x_m^p = -\partial(\cdot)/\partial x_m^q$ and using Gauss theorem, the last integral on the right-hand side of (7.15) can be integrated analytically, i.e.,

$$\int_D \frac{\partial E_{ijk}(p,q)}{\partial x_m^p} d\Omega(q) = -\int_D E_{ijk}(p,Q)n_m(Q)d\Gamma(Q) = \frac{-1}{30(1-\nu)G}\{\delta_{im}\delta_{jk} - (4-5\nu)(\delta_{ij}\delta_{mk} + \delta_{ik}\delta_{mj})\} \tag{7.16}$$

Substituting (7.16) into (7.15) and the result into (7.14), and using (2.6), (7.5) and (7.7) we obtain:

$$\dot{\sigma}_{ij}(p) = \int_\Gamma U_{ijk}(p,Q)\dot{t}_k(Q)d\Gamma(Q) - \int_\Gamma T_{ijk}(p,Q)\dot{u}_k(Q)d\Gamma(Q) + \int_\Omega U_{ijk}(p,q)\dot{b}_k(q)d\Omega(q) + \int_\Omega E_{ijkl}(p,q)\dot{\sigma}_{kl}^p(q)d\Omega(q) + F_{ijkl}^\sigma \dot{\sigma}_{kl}^p(p) \tag{7.17}$$

in which, $\partial r/\partial x_m^p = -\partial r/\partial x_m^q = -r_{,m}$ has been used and all integrals are interpreted in the Cauchy principal value sense. The kernels and free term coefficients in (7.17) are given by:

$$U_{ijk} = \frac{1}{8\pi(1-\nu)r^2}\left\{(1-2\nu)(r_{,k}\delta_{ij} + r_{,j}\delta_{ik} - r_{,i}\delta_{jk}) + 3r_{,i}r_{,j}r_{,k}\right\} \tag{7.18}$$

$$\begin{aligned} T_{ijk} = \frac{G}{4\pi(1-\nu)r^3}\Bigg\{ & 3\frac{\partial r}{\partial n}[(1-2\nu)r_{,k}\delta_{ij} + \nu(r_{,j}\delta_{ik} + r_{,i}\delta_{jk}) - 5r_{,i}r_{,j}r_{,k}] \\ & -(1-4\nu)n_k\delta_{ij} + 3\nu(n_i r_{,j}r_{,k} + n_j r_{,i}r_{,k}) \\ & +(1-2\nu)(3n_k r_{,i}r_j + n_j r_{,i}r_{,k} + n_i r_{,j}r_{,k})\Bigg\} \end{aligned} \tag{7.19}$$

$$\begin{aligned} E_{ijkl} &= \frac{1}{2}(U_{ijk,l} + U_{ijl,k}) \\ &= \frac{1}{8\pi(1-\nu)r^3}\Big\{(1-2\nu)\big(\delta_{ik}\delta_{lj} + \delta_{jk}\delta_{li} - \delta_{ij}\delta_{kl} + 3\delta_{ij}r_{,k}r_{,l}\big) \\ &\quad + 3\nu\big(\delta_{li}r_{,j}r_{,k} + \delta_{jk}r_{,l}r_{,i} + \delta_{ik}r_{,l}r_{,j} + \delta_{jl}r_{,i}r_{,k}\big) + 3\delta_{kl}r_{,i}r_{,j} - 15r_{,i}r_{,j}r_{,k}r_{,l}\Big\} \end{aligned} \tag{7.20}$$

$$F_{ijkl}^{\sigma} = \frac{-1}{30(1-\nu)}\left\{(7-5\nu)(\delta_{ik}\delta_{jl} + \delta_{il}\delta_{jk}) + (2-10\nu)\delta_{ij}\delta_{kl}\right\} \tag{7.21}$$

For initial strain approach, (7.17) can be expressed by using (7.7) as:

$$\begin{aligned} \dot{\sigma}_{ij}(p) = & \int_\Gamma U_{ijk}(p,Q)\dot{t}_k(Q)d\Gamma(Q) - \int_\Gamma T_{ijk}(p,Q)\dot{u}_k(Q)d\Gamma(Q) \\ & + \int_\Omega U_{ijk}(p,q)\dot{b}_k(q)d\Omega(q) + \int_\Omega \Sigma_{ijkl}(p,q)\dot{\varepsilon}_{kl}^p(q)d\Omega(q) \\ & + F_{ijkl}^{\varepsilon}\dot{\varepsilon}_{kl}^p(p) \end{aligned} \tag{7.22}$$

where

$$\Sigma_{ijkl} = E_{ijrs}D_{rskl}^e \tag{7.23}$$

$$F_{ijkl}^{\varepsilon} = F_{ijrs}^{\sigma}D_{rskl}^e \tag{7.24}$$

7.3 Accurate Evaluations of Strongly Singular Domain Integrals

Apart from the domain integrals involving initial stresses (or strains), the other integrals are exactly the same as those in linear problems, and of course these can be treated as described in Chapter 2. The domain integrals involving the initial stresses (or strains) are weakly singular, and thus can be accurately evaluated using standard Gauss quadrature (by employing the cell sub-division technique described in Chapter 2). However, the domain integral in (7.17) is strongly singular. Consequently, the standard numerical integration fails. Advanced, and efficient, methods must be employed to evaluate this integral.

The most popular method for treating strongly singular integrals consists of two steps, namely, isolation and transformation of the singularity (e.g., Krishnasamy et al., 1992). Firstly, the singularity is isolated by subtracting a singular function from the original kernel so that the subtracted term becomes a weakly singular one, which can then be evaluated by standard numerical integration procedures. The isolated strongly singular integral is then evaluated by analytical methods or by integral transformation.

7.3.1 Isolation of Strong Singularity

To evaluate domain integrals, the domain is usually discretised into cells. For the cells including the source point p, we re-write equation (7.17) as:

$$\int_{\Omega} E_{ijkl}(p,q)\dot{\sigma}^{p}_{kl}(q)d\Omega(q) = \int_{\Omega} E_{ijkl}(p,q)\left[\dot{\sigma}^{p}_{kl}(q)-\dot{\sigma}^{p}_{kl}(p)\right]d\Omega(q) + \dot{\sigma}^{p}_{kl}(p)\left(\int_{\Omega} E_{ijkl}(p,q)d\Omega(q)\right) \tag{7.25}$$

For convenience, we express the kernel E_{ijkl} in the form:

$$E_{ijkl} = \frac{\Psi_{ijkl}}{r^3} \tag{7.26}$$

where (from (7.20)):

$$\Psi_{ijkl} = \frac{1}{8\pi(1-\nu)}\Big[(1-2\nu)\big(\delta_{ik}\delta_{lj} + \delta_{jk}\delta_{li} - \delta_{ij}\delta_{kl} + 3\delta_{ij}r_{,k}r_{,l}\big) + 3\nu\big(\delta_{li}r_{,j}r_{,k} + \delta_{jk}r_{,l}r_{,i} + \delta_{ik}r_{,l}r_{,j} + \delta_{jl}r_{,i}r_{,k}\big) + 3\delta_{kl}r_{,i}r_{,j} - 15r_{,i}r_{,j}r_{,k}r_{,l}\Big] \tag{7.27}$$

The cell sub-division technique is now employed, i.e., when the source point p is located at a corner node, the cell is sub-divided into 3 tetrahedra; while when p is located at a mid-side node, the cell is sub-divided into 4 tetrahedra (Fig.7.1). These tetrahedra are defined by a vertex at point p and those surfaces of the cell not including p (in Fig.7.1). Then each sub-cell is mapped on to a unit parametric cell (Fig.7.2).

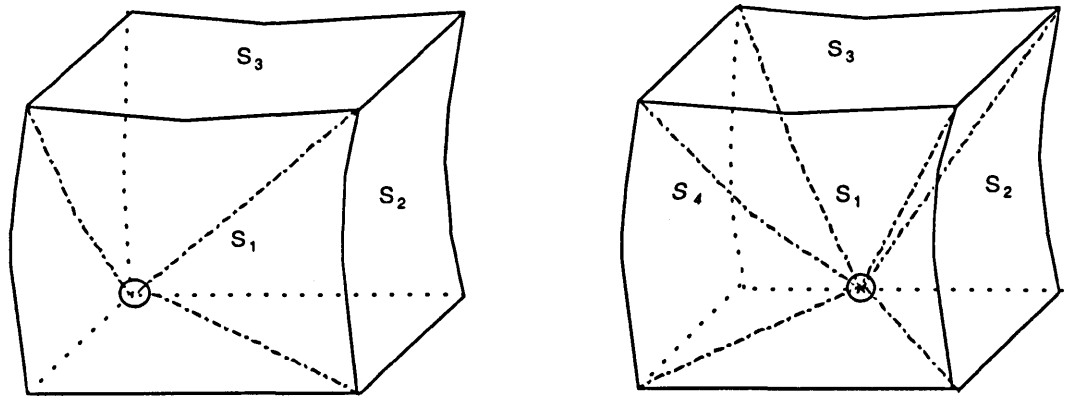

Fig.7.1 Cell sub-division: (a) p at corner; (b) p at mid-side

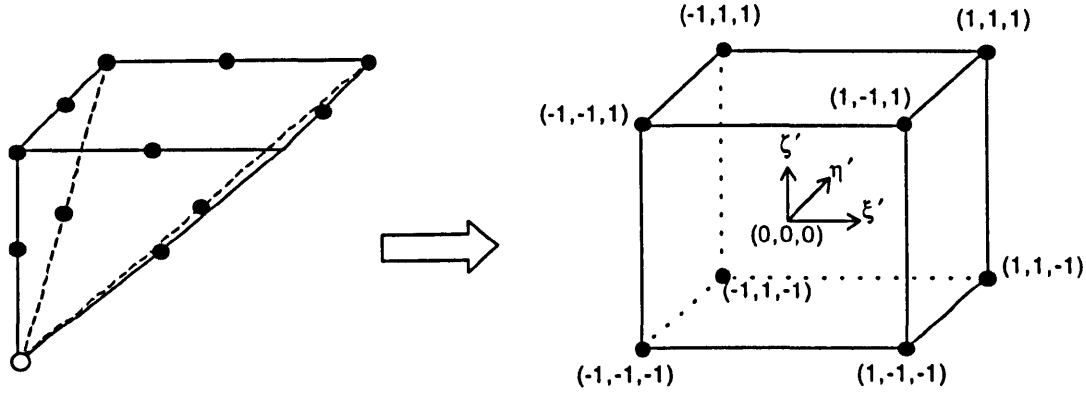

Fig.7.2 Geometrical mapping of a sub-cell on to a unit cube

This mapping scheme results in:

$$d\Omega_s = J_s d\xi' d\eta' d\varsigma', \qquad J_s \to O(r^2) \tag{7.28}$$

Furthermore, when the field point q approaches the source point p, we have:

$$\dot{\sigma}^p_{kl}(q) - \dot{\sigma}^p_{kl}(p) \to O(r)$$

Thus, this cell sub-division technique renders the first integral on the right-hand side of (7.25) well-behaved. And hence its numerical integration presents no difficulty. However, the last integral on the right-hand side of (7.25) is still singular O(1/r) and this must be treated separately. In the following, a new efficient algorithm is developed for this purpose by exploiting the intrinsic properties of the strongly singular kernels, E_{ijkl} and Σ_{ijkl}.

7.3.2 New Identities for Integrations of Strongly Singular Kernels

We examine the integration of the strongly singular kernels, E_{ijkl} and Σ_{ijkl} over a sphere around the source point p with a radius R (Fig.7.3).

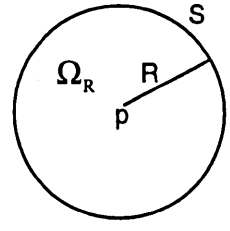

Fig.7.3 A sphere with radius R

First, we define a spherical co-ordinate system with origin at p (Fig.7.4):

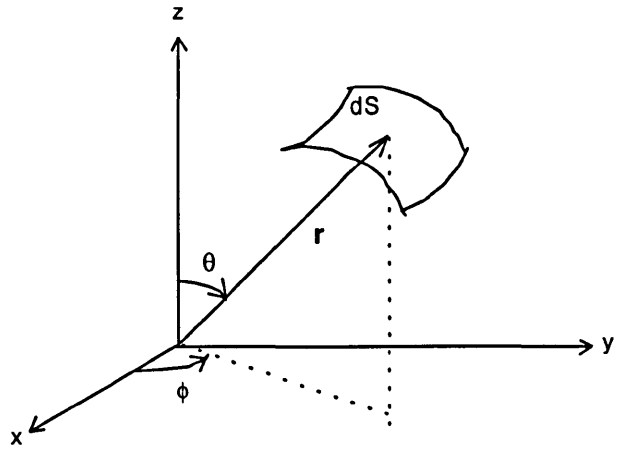

Fig.7.4 Local spherical co-ordinate system

Then relationships between the Cartesian and spherical systems are:

$$\begin{cases} x = r\sin\theta\cos\phi \\ y = r\sin\theta\sin\phi \\ z = r\cos\theta \end{cases} \qquad \begin{matrix} 0 \le \theta \le \pi \\ 0 \le \phi \le 2\pi \end{matrix} \tag{7.29}$$

$$d\Omega = drdS \tag{7.30a}$$

where the differential element on the spherical surface (dS) is:

$$dS = r^2 \sin\theta\, d\theta\, d\phi \tag{7.30b}$$

From (7.29), it follows that:

$$\begin{aligned} r_{,i} &= \frac{\partial r}{\partial x_i} = \frac{\partial r}{\partial x}\frac{\partial x}{\partial x_i} + \frac{\partial r}{\partial y}\frac{\partial y}{\partial x_i} + \frac{\partial r}{\partial z}\frac{\partial z}{\partial x_i} \\ &= \delta_{1i}\sin\theta\cos\phi + \delta_{2i}\sin\theta\sin\phi + \delta_{3i}\cos\theta \end{aligned} \tag{7.31}$$

If we substitute (7.30) and (7.31) into (7.25)-(7.27), we can see that the domain integration over the sphere Ω_R can be separated into a radial part and a spherical surface part, i.e.,

$$\int_{\Omega_R} E_{ijkl}\, d\Omega = \int_0^R \frac{1}{r}\left(\int_{S_I} \Psi_{ijkl}\, dS_I\right) dr \tag{7.32}$$

where S_I is a spherical surface with unit radius and

$$dS_I = \sin\theta\, d\theta\, d\phi \tag{7.33}$$

For such a spherical surface, we can easily show that:

$$\int_{S_I} dS_I = \int_0^{\pi} \int_0^{2\pi} \sin\theta \, d\phi \, d\theta = 4\pi \tag{7.34}$$

From (7.31), and noting that $\delta_{1i}\delta_{1j}+\delta_{2i}\delta_{2j}+\delta_{3i}\delta_{3j}=\delta_{ij}$, it follows that:

$$\int_{S_I} r_{,i} r_{,j} dS_I = \frac{4\pi}{3}\delta_{ij} \tag{7.35}$$

$$\int_{S_I} r_{,i} r_{,j} r_{,k} r_{,l} dS_I = \frac{4\pi}{15}(\delta_{ij}\delta_{kl} + \delta_{ik}\delta_{jl} + \delta_{il}\delta_{jk}) \tag{7.36}$$

Substituting (7.31) into (7.27) and using (7.34)-(7.36), we obtain:

$$\int_{S_I} \Psi_{ijkl} dS_I = 0 \tag{7.37}$$

So from (7.32), it follows that:

$$\int_{\Omega_R} E_{ijkl} d\Omega = 0 \tag{7.38}$$

For the initial strain approach, from (7.23), it is obvious that:

$$\int_{\Omega_R} \Sigma_{ijkl} d\Omega = 0 \tag{7.39}$$

These identities are independent of the sphere radius and provide the basis of accurately evaluating the strongly singular domain integrals of the kernels over cells.

7.3.3 Transformation of the Strongly Singular Domain Integrals into Boundary Integrals

Two novel methods of dealing with the strong singularity appearing in the domain integrals can be advanced, based on the identities established above.

Spherical Exclusion Technique

In this method, we employ the exclusion technique with arbitrary radius to accurately evaluate the strongly singular kernel arising in the last term of (7.25). Fig.7.5 shows the

exclusion pattern for a cross-section, where the cell Ω_c has been divided into two sub-cells, Ω_c^1 and Ω_c^2.

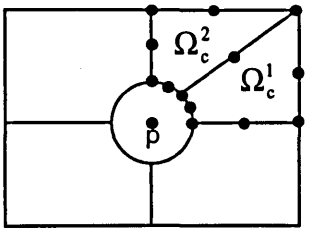

Fig.7.5 Exclusion of a small sphere

If the cells around p are identical in shape and size, the exclusion radius can be taken to be zero. For this particular case, we can directly evaluate the last integral on the right-hand side of (7.17) or (7.22) using only the cell sub-division technique (as described by Banerjee and Davies, 1984), since the shape functions used to approximate the initial stress increment $\dot{\sigma}_{kl}^p$ have the same values for all Gauss points symmetrically disposed about p. Consequently, (7.38) or (7.39) is implicitly satisfied after considering the contributions from all cells. However, if the cells around p are different in shape or size, direct application of the exclusion technique to the evaluation of the strong integral appearing in (7.17) or (7.22) will lead to inaccurate results.

Full Numerical Formulation

Although the exclusion technique together with the element sub-division technique can be used to accurately evaluate the strongly singular domain integrals, this process is cumbersome. An improved formulation can be derived by considering the following integration transformation.

The cell sub-division technique is also needed herein and let us consider the integral of E_{ijkl} over a sub-cell Ω_c^s. Because the integration is carried out in the Cauchy principal value sense, we can cut off a small sphere with radius ε around the singular point p (Fig.7.6).

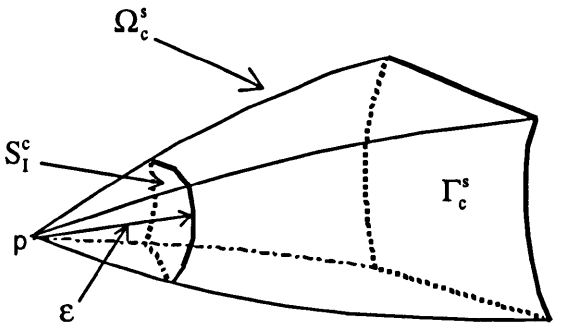

Fig.7.6 Small exclusion cut off from a sub-cell Ω_c^s

Thus from (7.26), we have:

$$\int_{\Omega_c^s} E_{ijkl}\,d\Omega = \int_{S_I^c} \Psi_{ijkl} \left(\lim_{\varepsilon\to 0} \int_{\varepsilon}^{r(\Gamma_c^s)} \frac{1}{r} dr\right) dS_I$$

$$= \int_{S_I^r} \Psi_{ijkl} \ln r(\Gamma_c^s)\,dS_I - \lim_{\varepsilon\to 0} \ln\varepsilon \int_{S_I^c} \Psi_{ijkl}\,dS_I \qquad (7.40)$$

Summing for all cells, the result $\sum_c S_I^c$ forms a closed spherical surface, so according to identity (7.37) the last integral in (7.40) is zero. Furthermore, with the help of Fig.7.7,

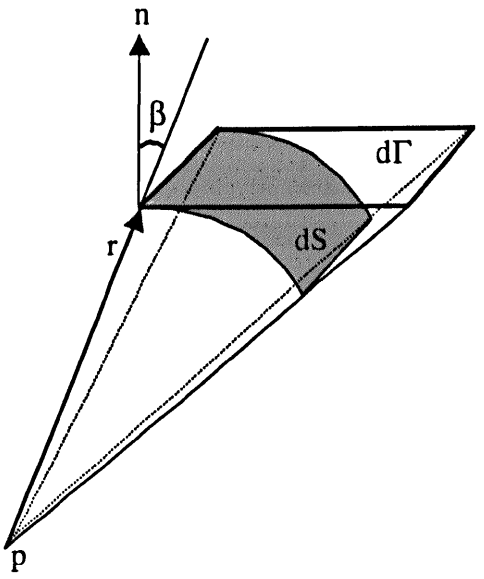

Fig.7.7 Relation between spherical surface (dS) and cell boundary (dΓ)

we have:

$$dS = r^2 \sin\theta \, d\theta \, d\phi = d\Gamma \cos\beta = d\Gamma \frac{r_i n_i}{r} \tag{7.41}$$

where β is the angle between the normal of the differential elements of the spherical surface dS directed along the r direction and the cell boundary surface $d\Gamma$ with normal n.

From (7.33) and (7.41), it follows that:

$$dS_I = \frac{r_i n_i}{r^3} d\Gamma \tag{7.42}$$

Eventually, substituting the above equation into (7.40) and using (7.26), we obtain

$$\int_{\Omega_c^s} E_{ijkl} d\Omega = \int_{\Gamma_c^s} E_{ijkl} r_m n_m \ln r \, d\Gamma \tag{7.43}$$

Similarly, for the initial strain approach, we can derive

$$\int_{\Omega_c^s} \Sigma_{ijkl} d\Omega = \int_{\Gamma_c^s} \Sigma_{ijkl} r_m n_m \ln r \, d\Gamma \tag{7.44}$$

Now that the domain integrals have been transformed into non-singular cell boundary integrals, they can be calculated using standard Gaussian quadrature formulae. It should mentioned that for 2D problems, we can derive exactly the same results as (7.43) and (7.44) with the understanding that the integrals are carried out over line elements (Gao and Davies, 1998b).

Equations (7.43) and (7.44) are very easy to use. The kernels of the transformed boundary integrals are simply formed by multiplying the original kernels, E_{ijkl} and Σ_{ijkl}, by the terms, $r_m n_m \ln r$. The boundary integrals need to be carried out only over the outer surfaces of the volume cells around the source point p. Moreover, they have the same forms for 2D and 3D problems, so simplifying the task of developing unified code.

Weakly Singular Domain Integrals

The transformation method described in this section can also be used to evaluate the domain integrals (in (7.9) and (7.11)) involving the initial stress (or strain) when the source point is located at any node of the cell under consideration. It is, of course, not necessary to evaluate these weakly singular domain integrals in this way: they can be evaluated using

the cell sub-division technique. However, in order to improve computational efficiency, this transformation method is also useful for treating this type of integral.

The isolated form of the domain integrals in (7.9) and (7.11) can be written as:

$$\int_{\Omega} E_{ijk}(p,q)\dot{\sigma}^{p}_{jk}(q)d\Omega(q) = \int_{\Omega} E_{ijk}(p,q)\left[\dot{\sigma}^{p}_{jk}(q) - \dot{\sigma}^{p}_{jk}(p)\right]d\Omega(q) + \dot{\sigma}^{p}_{jk}(p)\left(\int_{\Omega} E_{ijk}(p,q)d\Omega(q)\right) \tag{7.45}$$

where the kernel E_{ijk} can be expressed as:

$$E_{ijk} = \frac{\hat{\Psi}_{ijk}}{r^2} \tag{7.46}$$

in which, $\hat{\Psi}_{ijk}$ is only a function of θ and ϕ (see (7.10)). In a similar manner to (7.40), the last integral in (7.45) can be written as:

$$\int_{\Omega^{*}_{c}} E_{ijk}d\Omega = \int_{\Omega^{*}_{c}} \frac{1}{r^2}\hat{\Psi}_{ijk}d\Omega = \int_{S^{c}_{I}} \hat{\Psi}_{ijk}\left(\lim_{\varepsilon\to 0}\int_{\varepsilon}^{r(\Gamma^{s}_{c})} dr\right)dS_I = \int_{S^{\Gamma}_{I}} \hat{\Psi}_{ijk}\, r(\Gamma^{s}_{c})dS_I \tag{7.47}$$

Using (7.42) and (7.46), we obtain:

$$\int_{\Omega^{*}_{c}} E_{ijk}d\Omega = \int_{\Gamma^{*}_{c}} E_{ijk} r_m n_m \, d\Gamma \tag{7.48}$$

Similarly, for the initial strain approach, we can obtain:

$$\int_{\Omega^{*}_{c}} \Sigma_{ijk}d\Omega = \int_{\Gamma^{*}_{c}} \Sigma_{ijk} r_m n_m \, d\Gamma \tag{7.49}$$

7.4 Evaluation of Boundary Stresses

The formulations described above are only suitable for evaluation of internal stresses. When a source point is located on the boundary, equations (7.17) and (7.22) become hypersingular. The existing methods for evaluating these integrals may be roughly divided into two types, i.e., the direct method and the traction recovery method. The former is based on the 'regularization' of the hypersingular boundary integral equation by expanding the kernel in a Laurent series (Guiggiani et al, 1992; Huber et al, 1996) or by employing deformation modes (Poon et al, 1998a), while the latter evaluates the boundary stresses

using specified traction values and tangential derivatives of the displacements (Telles and Brebbia, 1979; Banerjee and Davies, 1984). In this section, the regularization method based on the global modes and the stress recovery method are reviewed and developed.

7.4.1 Regularization Based on Deformation Modes

We begin the derivation with the equations for stresses at internal points (7.17). Then we let the internal point p approach a boundary point P to obtain the equations for the boundary stresses. For simplicity, body forces are not considered herein.

Rigid-Body Mode:

The Rigid-Body Mode (translation) condition yields:

$$\begin{cases} \dot{u}_i(Q) = \dot{u}_i(p) \\ \dot{t}_i(Q) = \dot{t}_i(p) = 0 \\ \dot{\sigma}_{ij}(p) = \dot{\sigma}^p_{ij}(q) = 0 \end{cases} \tag{7.50}$$

Using this condition, it follows from (7.17) that:

$$\int_\Gamma T_{ijk}(p,Q)\dot{u}_k(p)d\Gamma(Q) = 0 \tag{7.51}$$

Subtracting (7.51) from (7.17), we obtain:

$$\begin{aligned} \dot{\sigma}_{ij}(p) = &\int_\Gamma U_{ijk}(p,Q)\dot{t}_k(Q)d\Gamma(Q) - \int_\Gamma T_{ijk}(p,Q)[\dot{u}_k(Q) - \dot{u}_k(p)]d\Gamma(Q) \\ &+ \int_\Omega E_{ijkl}(p,q)\dot{\sigma}^p_{kl}(q)d\Omega(q) + F^\sigma_{ijkl}\dot{\sigma}^p_{kl}(p) \end{aligned} \tag{7.52}$$

The first and second integrands on the right-hand side of equation (7.52) are $O(1/r^2)$ while the domain integrand is $O(1/r^3)$. After using element (cell) sub-division technique, a singularity of order O(1/r) remains for each integral. Thus, further regularization must be carried out.

Linear Displacement Mode:

This mode, used by Krishnasamy et al. (1992) and Lutz et al. (1992) for applications in potential theory and linear elasticity, yields:

$$\begin{cases} \dot{u}_i(Q) = \dot{u}_i(p) + \dot{u}_{i,n}(p) r_n \\ \dot{u}_{i,n}(Q) = \dot{u}_{i,n}(p) \\ \dot{t}_i(Q) = \dot{\sigma}_{ij}(Q) n_j(Q) = \dot{\sigma}_{ij}(p) n_j(Q) \\ \dot{\sigma}^p_{ij}(q) = 0 \end{cases} \tag{7.53}$$

where $\dot{u}_{i,n}$ stands for the derivative of the displacement increment $\dot{u}_i$ with respect to the co-ordinate x_n. Using this mode, it follows from (7.52) that:

$$\dot{\sigma}_{ij}(p) = \int_\Gamma U_{ijk}(p,Q)\dot{\sigma}_{kl}(p) n_l(Q) d\Gamma(Q) - \int_\Gamma T_{ijk}(p,Q)\dot{u}_{k,n}(p) r_n d\Gamma(Q) \tag{7.54}$$

Subtracting (7.54) from (7.52) and using (2.2), leads to:

$$\begin{aligned} 0 = & \int_\Gamma U_{ijk}(p,Q)[\dot{\sigma}_{kl}(Q) - \dot{\sigma}_{kl}(p)] n_l(Q) d\Gamma(Q) \\ & - \int_\Gamma T_{ijk}(p,Q)[\dot{u}_k(Q) - \dot{u}_k(p) - \dot{u}_{k,n}(p) r_n] d\Gamma(Q) \\ & + \int_\Omega E_{ijkl}(p,q)\dot{\sigma}^p_{kl}(q) d\Omega(q) + F^\sigma_{ijkl}\dot{\sigma}^p_{kl}(p) \end{aligned} \tag{7.55}$$

In equation (7.55), noting that term $\dot{u}_k(Q) - \dot{u}_k(p) - \dot{u}_{k,n}(p) r_n$ results in $O(r^2)$ (e.g., Krishnasamy et al. 1992), the first and second integrands in (7.55) are weakly singular. However, the domain integral is still strongly singular, and again regularization must be carried out.

Constrained Plastic Mode:

This mode was suggested by Poon et al. (1998a). In this mode, the boundary of the body has zero displacement but the body undergoes plastic deformation, i.e.,

$$\begin{cases} \dot{u}_i(Q) = 0 \\ \dot{u}_{i,n}(p) = 0 \\ \dot{\sigma}^p_{ij}(q) = \dot{\sigma}^p_{ij}(p) \\ \dot{\sigma}_{ij}(Q) = \dot{\sigma}_{ij}(p) = -\dot{\sigma}^p_{ij}(p) \\ \dot{t}_i(Q) = \dot{\sigma}_{ij}(Q) n_j(Q) = -\dot{\sigma}^p_{ij}(p) n_j(Q) \end{cases} \tag{7.56}$$

Using this mode, it follows from (7.55) that:

$$0 = \int_{\Omega} E_{ijkl}(p,q)\dot{\sigma}^{p}_{kl}(p)d\Omega(q) + F^{\sigma}_{ijkl}\dot{\sigma}^{p}_{kl}(p) \tag{7.57}$$

Subtracting (7.57) from (7.55), finally we obtain:

$$\begin{aligned} 0 = & \int_{\Gamma} U_{ijk}(p,Q)[\dot{\sigma}_{kl}(Q) - \dot{\sigma}_{kl}(p)]n_{l}(Q)d\Gamma(Q) \\ & - \int_{\Gamma} T_{ijk}(p,Q)[\dot{u}_{k}(Q) - \dot{u}_{k}(p) - \dot{u}_{k,n}(p)r_{n}]d\Gamma(Q) \\ & + \int_{\Omega} E_{ijkl}(p,q)[\dot{\sigma}^{p}_{kl}(q) - \dot{\sigma}^{p}_{kl}(p)]d\Omega(q) \end{aligned} \tag{7.58}$$

When the source point p approaches the field point Q (or q), the terms in (7.58) exhibit the following singularities:

$$\begin{cases} U_{ijk}(p,Q) \rightarrow O(r^{-2}) \\ T_{ijk}(p,Q) \rightarrow O(r^{-3}) \\ E_{ijkl}(p,q) \rightarrow O(r^{-3}) \\ \dot{\sigma}_{kl}(Q) - \dot{\sigma}_{kl}(p) \rightarrow O(r) \\ \dot{u}_{k}(Q) - \dot{u}_{k}(p) - \dot{u}_{k,n}(p)r_{n} \rightarrow O(r^{2}) \\ \dot{\sigma}^{p}_{kl}(q) - \dot{\sigma}^{p}_{kl}(p) \rightarrow O(r) \end{cases} \tag{7.59}$$

and after using boundary element and volume cell sub-division technique, we have from (2.31) and (7.28) that:

$$\begin{aligned} d\Gamma(Q) &\rightarrow O(r) \\ d\Omega(q) &\rightarrow O(r^{2}) \end{aligned} \tag{7.60}$$

Thus, from (7.59) and (7.60) it can be seen that all the integrals in (7.58) are regular. It is therefore possible to take the limit of (7.58) as an internal source point approaches a boundary point. In other words, equation (7.58) can be used to evaluate boundary stresses. Following Cruse and Richardson (1996, for the elastic case) and Poon et al. (1998a), equation (7.58) is valid at any point (including edges and corners), provided that the stress, displacement gradient, and initial stress are continuous there. The drawback of using (7.58) is that the stress, displacement and displacement derivatives appear in the system equations, so computation is prodigious.

Another method using the fully regularized direct boundary formulation uses the displacement gradients (as unknowns) in the boundary integrals. Details of this method can be found, for example, in Burghardt and Van (1998).

7.4.2 Traction Recovery with Initial Stresses

The most popular method for evaluation of the boundary stress is the traction recovery method (Cruse, 1974; Telles and Brebbia, 1979; Banerjee and Davies, 1984; Kane, 1994). In this section, the detailed formulation for this method is derived. To date, no such detailed and rigorous formulation exists in literature, to our knowledge.

First, we calculate the tangential strains over a boundary element. This requires the introduction of a local Cartesian co-ordinate system x_i' with the axes x_1' and x_2' tangential to the surface and x_3' in the **n** direction (Fig. 7.8).

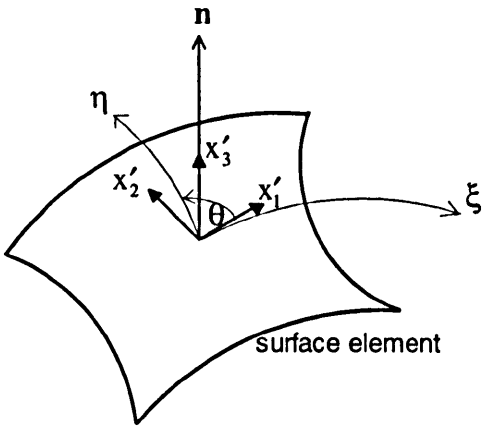

Fig.7.8 Local orthogonal set of axes over a boundary element

The local tangential strains can be expressed in terms of the differentials of the displacements as follows:

$$\dot{\varepsilon}'_{IJ} = \frac{1}{2}\left(\frac{\partial \dot{u}'_I}{\partial x'_J} + \frac{\partial \dot{u}'_J}{\partial x'_I}\right) \tag{7.61}$$

where, I=1, 2; J=1, 2; and

$$\frac{\partial \dot{u}'_I}{\partial x'_J} = \frac{\partial \dot{u}'_I}{\partial \xi_K}\frac{\partial \xi_K}{\partial x'_J} \tag{7.62}$$

in which, K=1, 2 and $\xi_1 = \xi$, $\xi_2 = \eta$. The derivatives of the intrinsic co-ordinates with respect to the local co-ordinates are (Lachat, 1975; Becker, 1992):

$$\frac{\partial \xi}{\partial x_1'} = \frac{1}{|m_1|}; \quad \frac{\partial \xi}{\partial x_2'} = \frac{-\cos\theta}{|m_1|\sin\theta};$$
$$\frac{\partial \eta}{\partial x_1'} = 0; \quad \frac{\partial \eta}{\partial x_2'} = \frac{1}{|m_2|\sin\theta} \tag{7.63}$$

where

$$|m_K| = \sqrt{\left(\frac{\partial x_1}{\partial \xi_k}\right)^2 + \left(\frac{\partial x_2}{\partial \xi_k}\right)^2 + \left(\frac{\partial x_3}{\partial \xi_k}\right)^2} \tag{7.64}$$

$$\cos\theta = \frac{1}{|m_1||m_2|}\frac{\partial x_i}{\partial \xi_1}\frac{\partial x_i}{\partial \xi_2} \tag{7.65}$$

The local displacement components in (7.62) can be expressed in terms of the global ones, i.e.,

$$\dot{u}_I' = l_{Ij}\dot{u}_j = l_{Ij}N_\alpha \dot{u}_j^\alpha \tag{7.66}$$

where

$$u_i(\xi,\eta) = \sum_{\alpha=1}^{8} N_\alpha(\xi,\eta)\, u_i^\alpha$$
$$t_i(\xi,\eta) = \sum_{\alpha=1}^{8} N_\alpha(\xi,\eta)\, t_i^\alpha \tag{2.22 bis}$$

and l_{Ij} are the direction cosines of the local co-ordinate system with respect to the global co-ordinate system:

$$l_{1i} = \frac{1}{|m_1|}\frac{\partial x_i}{\partial \xi_1}, \quad i = 1,2,3 \tag{7.67}$$

$$l_{21} = n_2 l_{13} - n_3 l_{12}$$
$$l_{22} = n_3 l_{11} - n_1 l_{13} \tag{7.68}$$
$$l_{23} = n_1 l_{12} - n_2 l_{11}$$

Using (7.61)-(7.68), we can calculate the local tangential strain components. To obtain the local stresses, the local elastic stresses $\dot{\sigma}_{ij}'^{e}$ and strains $\dot{\varepsilon}_{ij}'$ are substituted in Hooke's law (2.3) and then after eliminating $\dot{\varepsilon}_{33}'$, we obtain (see also Becker, 1992, for elastic problems):

$$\begin{aligned}
\dot{\sigma}'^{e}_{11} &= \frac{2G}{1-\nu}(\dot{\varepsilon}'_{11} + \nu\dot{\varepsilon}'_{22}) + \frac{\nu}{1-\nu}\dot{\sigma}'^{e}_{33} \\
\dot{\sigma}'^{e}_{22} &= \frac{2G}{1-\nu}(\dot{\varepsilon}'_{22} + \nu\dot{\varepsilon}'_{11}) + \frac{\nu}{1-\nu}\dot{\sigma}'^{e}_{33} \\
\dot{\sigma}'^{e}_{12} &= 2G\,\dot{\varepsilon}'_{12}
\end{aligned} \tag{7.69}$$

where $\dot{\varepsilon}'_{11}$, $\dot{\varepsilon}'_{22}$ and $\dot{\varepsilon}'_{12}$ are determined using (7.61), and

$$\begin{aligned}
\dot{\sigma}'^{e}_{11} &= \dot{\sigma}'_{11} + \dot{\sigma}'^{p}_{11} \\
\dot{\sigma}'^{e}_{22} &= \dot{\sigma}'_{22} + \dot{\sigma}'^{p}_{22} \\
\dot{\sigma}'^{e}_{33} &= \dot{\sigma}'_{33} + \dot{\sigma}'^{p}_{33} \\
\dot{\sigma}'^{e}_{12} &= \dot{\sigma}'_{12} + \dot{\sigma}'^{p}_{12}
\end{aligned} \tag{7.70}$$

In (7.70), the local initial stresses $\dot{\sigma}'^{p}_{ij}$ can be expressed in terms of global ones by

$$\dot{\sigma}'^{p}_{ij} = l_{ik} l_{jl} \dot{\sigma}^{p}_{kl} \tag{7.71}$$

Considering the equilibrium of the boundary segment gives:

$$\begin{aligned}
\dot{\sigma}'_{33} &= \dot{t}'_3 = l_{3j}\dot{t}_j \\
\dot{\sigma}'_{23} &= \dot{\sigma}'_{32} = \dot{t}'_2 = l_{2j}\dot{t}_j \\
\dot{\sigma}'_{13} &= \dot{\sigma}'_{31} = \dot{t}'_1 = l_{1j}\dot{t}_j
\end{aligned} \tag{7.72}$$

where

$$l_{31} = n_1,\ l_{32} = n_2,\ l_{33} = n_3 \tag{7.73}$$

Substituting (7.66) and (7.62) into (7.61), and the results together with (7.70)-(7.72) into (7.69), one can obtain:

$$\begin{aligned}
\dot{\sigma}'_{11} &= \frac{2G}{1-\nu}\left(\frac{\partial\xi_K}{\partial x'_1} l_{1j} + \nu\frac{\partial\xi_K}{\partial x'_2} l_{2j}\right)\frac{\partial\dot{u}_j}{\partial\xi_K} + \frac{\nu}{1-\nu} l_{3j}\dot{t}_j - \left(l_{1k}l_{1l} - \frac{\nu}{1-\nu} l_{3k}l_{3l}\right)\dot{\sigma}^{p}_{kl} \\
\dot{\sigma}'_{22} &= \frac{2G}{1-\nu}\left(\frac{\partial\xi_K}{\partial x'_2} l_{2j} + \nu\frac{\partial\xi_K}{\partial x'_1} l_{1j}\right)\frac{\partial\dot{u}_j}{\partial\xi_K} + \frac{\nu}{1-\nu} l_{3j}\dot{t}_j - \left(l_{2k}l_{2l} - \frac{\nu}{1-\nu} l_{3k}l_{3l}\right)\dot{\sigma}^{p}_{kl} \\
\dot{\sigma}'_{12} &= G\left(\frac{\partial\xi_K}{\partial x'_1} l_{2j} + \frac{\partial\xi_K}{\partial x'_2} l_{1j}\right)\frac{\partial\dot{u}_j}{\partial\xi_K} - l_{1k}l_{2l}\dot{\sigma}^{p}_{kl}
\end{aligned} \tag{7.74}$$

Finally, we can employ the transformation relation:

$$\dot{\sigma}_{mn} = l_{km} l_{ln} \dot{\sigma}'_{kl} \tag{7.75}$$

to transform these local stresses (7.74) into global Cartesian stresses as follows:

$$\dot{\sigma}_{mn} = A_{mnj\alpha}\dot{u}_j^{\alpha} + B_{mnj}\dot{t}_j + C_{mnkl}\dot{\sigma}_{kl}^{p} \tag{7.76}$$

where

$$\begin{aligned} A_{mnj\alpha} = 2G\Bigg\{ & \frac{\nu}{1-\nu}\Bigg[l_{1m}l_{1n}\left(\frac{\partial\xi_K}{\partial x_1'}l_{1j} + \nu\frac{\partial\xi_K}{\partial x_2'}l_{2j}\right) + l_{2m}l_{2n}\left(\frac{\partial\xi_K}{\partial x_2'}l_{2j} + \nu\frac{\partial\xi_K}{\partial x_1'}l_{1j}\right)\Bigg] \\ & + \frac{1}{2}(l_{1m}l_{2n} + l_{2m}l_{1n})\left(\frac{\partial\xi_K}{\partial x_1'}l_{2j} + \frac{\partial\xi_K}{\partial x_2'}l_{1j}\right)\Bigg\}\frac{\partial N_\alpha}{\partial\xi_K} \end{aligned} \tag{7.77}$$

$$B_{mnj} = (l_{3m}l_{1n} + l_{1m}l_{3n})l_{1j} + (l_{2m}l_{3n} + l_{3m}l_{2n})l_{2j} + \left(\frac{\nu}{1-\nu}\delta_{mn} + \frac{1-2\nu}{1-\nu}l_{3m}l_{3n}\right)l_{3j} \tag{7.78}$$

$$\begin{aligned} C_{mnkl} = & -\sum_{i=1}^{3} l_{im}l_{in}l_{ik}l_{il} + \left(\frac{\nu}{1-\nu}\delta_{mn} + \frac{1-2\nu}{1-\nu}l_{3m}l_{3n}\right)l_{3k}l_{3l} \\ & - \frac{1}{2}(l_{1m}l_{2n} + l_{2m}l_{1n})(l_{1k}l_{2l} + l_{2k}l_{1l}) \end{aligned} \tag{7.79}$$

The explicit relationship (7.76) allows us to compute the stresses at a boundary node as an algebraic function of the nodal displacements of the element associated with that node and the tractions and initial stresses at that node. If the coefficients in (7.76) are assembled in the global stress computing matrices (for internal points, which is formed from (7.17)), the matrices corresponding to the boundary points are extremely sparse. For those nodes which are shared by several elements, two further operations are necessary:

(a) Averaging

Since equation (7.76) is performed over an element, the contributions from all adjacent elements to a common boundary node should be averaged, provided that tractions are continuous across the boundary node over these elements.

(b) Traction Discontinuities

For a boundary node where the tractions are discontinuous (Fig.7.9), multiple nodes should be defined. The number of nodes at this common point should be equal to the number of different traction values (including zero traction) at this point. For example, three nodes (N_1,N_2, N_3) are defined for the central point in Fig.7.9, in which node N_1 is shared by boundary elements E_1 and E_2. Stresses at N_1 should be the average of the values

obtained by applying (7.76) to E_1 and E_2, while the stresses at node N_2 is calculated from element E_3 alone.

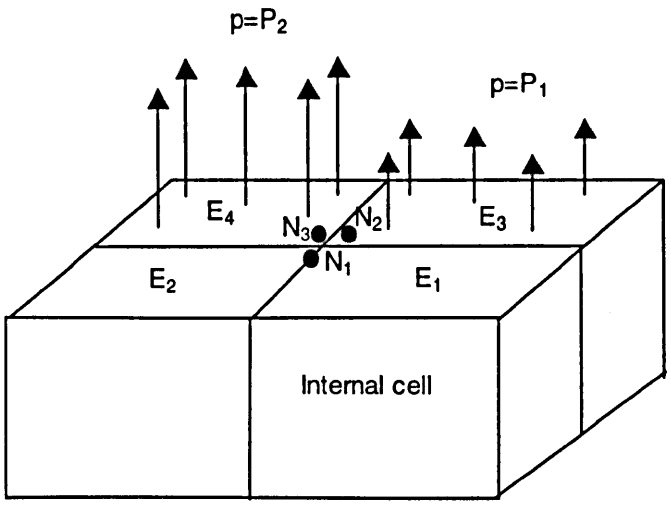

Fig.7.9 Multiple nodes at a traction discontinuity

Multiple nodes are necessary for a traction-discontinuous boundary node in non-linear BEM analysis, even if all tractions are specified for the boundary elements sharing this node. This is because some internal cells will share the nodes of these elements. Accordingly discontinuous stresses should be distinguished for these cells.

An alternative method for calculation of the boundary stresses using the traction recovery method is the implicit method (Mukherjee, 1982; Iwasaki and Ishizaki, 1986; Raveendra, 1984; Kane, 1994). In this method, a 9×9 square matrix for solving displacement gradients is formed from (2.2)-(2.6) and a chain relation between derivatives of displacements with respect to the intrinsic co-ordinates and to the global co-ordinates. After inverting this matrix, boundary stresses can be calculated through the displacement gradients. Apparently, this method requires more computation time.

7.5 Summary

In this Chapter, boundary integral equations are developed based on conventional non-linear boundary element theory. New identities (7.39) and (7.38) for initial stress and strain

kernels are derived, which provide the basis for a novel method of transforming the strongly singular domain integrals into surface ones. The resulting equations (7.43) and (7.44) can accurately evaluate the strongly singular domain integrals. Since the transformed surface integrals in (7.43) and (7.44) are performed only over cells' boundaries surrounding the source point, substantial computational effort is saved, comparing to the conventional transformed integrals over the whole boundary of the problem (category (4) methods in the Introduction). Moreover, these results are suitable for any isoparametric (linear or higher order) cells in 2D and 3D problems, for both initial stress and strain approaches.

Two methods for computing boundary stresses are described. In particular, a complete explicit numerical implementation formulation is given, based on the traction recovery method. This is particularly efficient and easy to use.

Chapter 8

Solution Schemes for Non-Linear BEM Equations

8.1 Introduction

Algorithms for solving non-linear BEM equations using the domain discretization methods have been developed by several workers. More often than not the algorithms are "explicit" as described in detail by Telles (1983) and Banerjee (1994). These solution algorithms can be roughly divided into two groups, i.e., the initial strain approach (Riccardella, 1973; Mendelson and Albers, 1975; Kumar and Mukherjee, 1977; Mukherjee and Kumar, 1978; Telles and Brebbia, 1979, 1980; Lee and Fenner, 1986; Kane, 1994; Cisilino et al., 1998;) and the initial stress approach (Banerjee et al., 1979; Banerjee and Davies, 1979; Raveendra, 1984; Zheng and Gao, 1986; Henry, 1987).

The choice between the use of initial stress or initial strain approaches is not critical. The initial stress approach, however, is capable of handling perfectly plastic materials, whereas the initial strain approach is more suitable for strongly strain-hardening materials (Becker, 1992). However, the initial strain approach has two distinctly different forms for plane stress and plane strain problems, while the initial stress approach takes the same form for both cases.

A different type of solution strategy (*incremental variable stiffness*) has been successfully demonstrated by Banerjee and co-workers (Raveendra, 1984; Banerjee et al., 1989; Banerjee, 1994). In this scheme, the internal variables are eliminated, by expressing

them in terms of boundary variables, and consequently no iteration is needed. Since the unknowns at internal nodes are eliminated, less computer memory is required.

Recently, many workers have investigated implicit solution schemes on account of their unconditional stability (Telles and Carrer, 1991; Bonnet and Mukherjee, 1996; Poon et al., 1998b; Burghardt and Van, 1998). Among these works, Bonnet and Mukherjee (1996) first applied the *consistent tangent operator* method. This method, which was first proposed by Simo and Taylor (1985) in the finite element method context, exploits the quadratic rate of convergence by utilising the consistent elastoplastic constitutive relations in the Newton-Raphson iterative process.

In this Chapter, the *consistent tangent operator* and the *incremental variable stiffness* solution schemes are developed for the initial stress method described earlier. In principle, the former is similar to that by Bonnet and Mukherjee (1996), but derived differently and expressed in a different form. In the latter, a new variable stiffness solution scheme is proposed, in which the system equations are expressed in terms of the *plastic multiplier*. Moreover, two iterative processes are presented for the first time for both the existing variable stiffness method (expressed in terms of boundary unknowns) and the new one. These iterative schemes enable us to use larger load increments.

8.2 Domain Discretisation and System Equations

The solution procedure can be summarized thus:

- The boundary and (expected) yield region of the body are discretized into boundary elements and internal volume cells, respectively, over which geometry and field variables are approximated by nodal values via shape functions.
- Source terms (7.11) are collocated at each boundary node, resulting in algebraic system equations, in terms of boundary values.
- Algebraic equations are established for the stresses by using (7.76) for boundary nodes and (7.17) for internal nodes.
- These equations are solved for the boundary unknowns, internal stresses and displacements, as well as other quantities such as equivalent plastic strains/stresses.

The discretization procedure for the boundary integrals appearing in (7.11) and (7.17) is similar to that described in Chapter 2. The discretization of the yield region into internal cells is elaborated below.

We assume that the yield region is divided into N_c internal volume cells, each of which forms a piecewise continuous approximation to the yield region. Over each cell, the positional co-ordinates and initial stresses are interpolated using 20-noded quadratic shape functions, i.e.,

$$\begin{aligned} x_i &= \sum_{\alpha=1}^{20} N_\alpha(\xi,\eta,\zeta)x_i^\alpha \\ \dot{\sigma}_{ij}^p &= \sum_{\alpha=1}^{20} N_\alpha(\xi,\eta,\zeta)\dot{\sigma}_{ij}^{p\alpha} \end{aligned} \tag{8.1}$$

where $\dot{\sigma}_{ij}^{p\alpha}$ is the ij-th component of the initial stress at node α and $N_\alpha(\xi,\eta,\zeta)$ are:

$$N_\alpha(\xi,\eta,\zeta) = \frac{1}{8}(1+\xi_\alpha\xi)(1+\eta_\alpha\eta)(1+\zeta_\alpha\zeta)(\xi_\alpha\xi+\eta_\alpha\eta+\zeta_\alpha\zeta-2) \tag{8.2a}$$

for corner nodes; and

$$\begin{aligned} N_\alpha(\xi,\eta,\zeta) = \frac{1}{4}(1+\xi_\alpha\xi)(1+\eta_\alpha\eta)(1+\zeta_\alpha\zeta)\{1+(\xi_\alpha^2-1)\xi^2 \\ +(\eta_\alpha^2-1)\eta^2+(\zeta_\alpha^2-1)\zeta^2\} \end{aligned} \tag{8.2b}$$

for mid-side nodes. Fig.8.1 shows the values of the local co-ordinates $(\xi_\alpha,\eta_\alpha,\zeta_\alpha)$ at nodes over a cell.

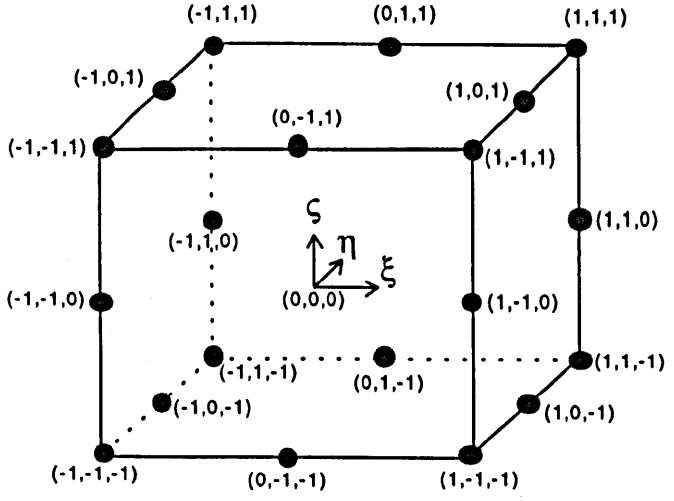

Fig.8.1 20-noded iso-parametric cell

8.2.1 Discretization of Weakly Singular Domain Integrals

Discretizing the yield region into N_c cells and using (8.1), the domain integrals in the boundary integral equation (7.11) can be written as:

$$\int_{\Omega} E_{ijk}(P,q)\dot{\sigma}^{p}_{jk}(q)d\Omega(q) = \sum_{c=1}^{N_c}\sum_{\alpha=1}^{20} E^{c\alpha}_{ijk}\dot{\sigma}^{p\alpha}_{jk} \tag{8.3}$$

where

$$E^{c\alpha}_{ijk} = \int_{-1}^{1}\int_{-1}^{1}\int_{-1}^{1} E_{ijk}(x^P, x(\xi,\eta,\zeta))N_\alpha(\xi,\eta,\zeta)J(\xi,\eta,\zeta)d\xi d\eta d\zeta \tag{8.4}$$

for cells not including the collocation point P, and,

$$J(\xi,\eta,\zeta) = \left|\frac{\partial(x,y,z)}{\partial(\xi,\eta,\zeta)}\right| = \begin{vmatrix} \frac{\partial x}{\partial\xi} & \frac{\partial y}{\partial\xi} & \frac{\partial z}{\partial\xi} \\ \frac{\partial x}{\partial\eta} & \frac{\partial y}{\partial\eta} & \frac{\partial z}{\partial\eta} \\ \frac{\partial x}{\partial\zeta} & \frac{\partial y}{\partial\zeta} & \frac{\partial z}{\partial\zeta} \end{vmatrix} \tag{8.5}$$

For cells including the collocation point P, (8.4) is replaced by:

$$E^{c\alpha}_{ijk} = \sum_{s=1}^{N_s}\int_{-1}^{1}\int_{-1}^{1}\int_{-1}^{1} E_{ijk}(x^P, x(\xi,\eta,\zeta))N_\alpha(\xi,\eta,\zeta)J(\xi,\eta,\zeta)J_s(\xi',\eta',\zeta')d\xi' d\eta' d\zeta' \tag{8.6}$$

where N_s is the number of the sub-cells over the cell under consideration (see Figs.7.1 and 7.2)

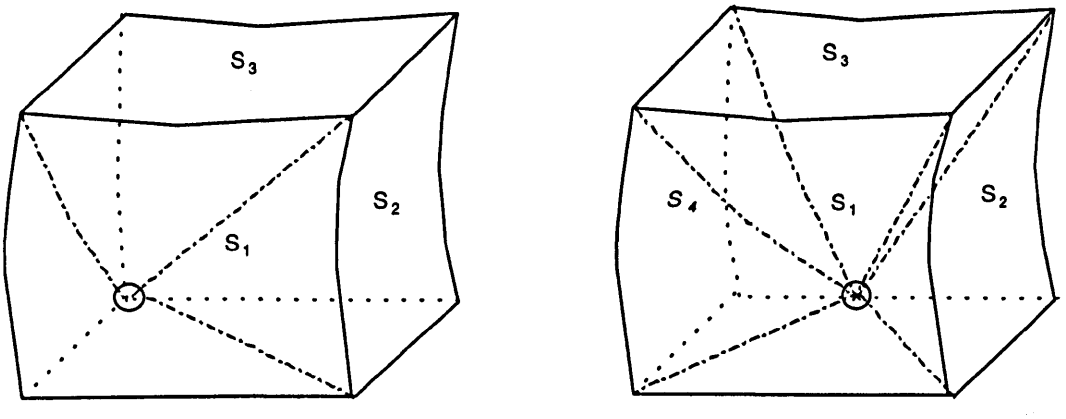

(a) (b)

Fig.7.1 Cell sub-division: (a) p at corner; (b) p at mid-side

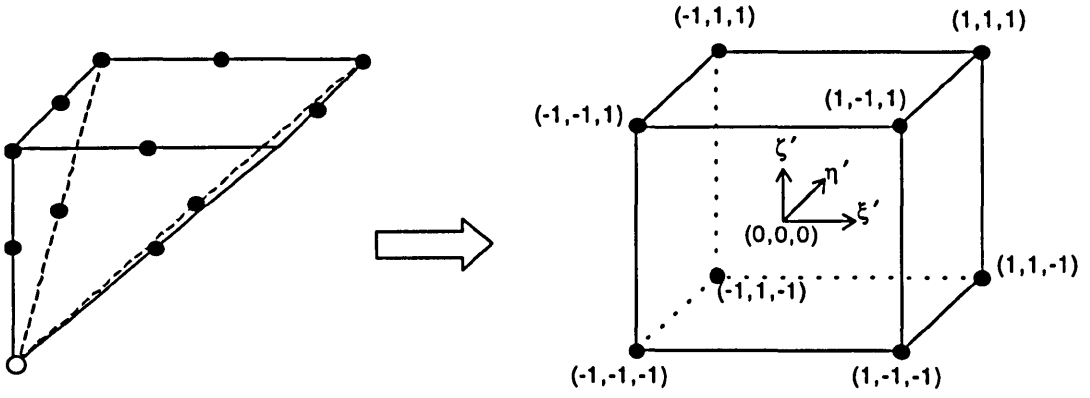

Fig.7.2 Geometrical mapping of a sub-cell on to a unit cube

and J_s is the Jacobian of the transformation from the original local co-ordinates to the new sub-cell intrinsic co-ordinate system, i.e.,

$$J_s(\xi',\eta',\zeta') = \left| \frac{\partial(\xi,\eta,\zeta)}{\partial(\xi',\eta',\zeta')} \right| \tag{8.7}$$

in which, the original local co-ordinates are calculated using:

$$\begin{aligned} \xi &= \sum_{\alpha=1}^{8} N'_\alpha(\xi',\eta',\zeta')\xi_\alpha \\ \eta &= \sum_{\alpha=1}^{8} N'_\alpha(\xi',\eta',\zeta')\eta_\alpha \\ \zeta &= \sum_{\alpha=1}^{8} N'_\alpha(\xi',\eta',\zeta')\zeta_\alpha \end{aligned} \tag{8.8}$$

In (8.8), N'_α, α=1, ...,8, are the 8-noded shape functions:

$$N'_\alpha(\xi',\eta',\zeta') = \frac{1}{8}(1+\xi'_\alpha\xi')(1+\eta'_\alpha\eta')(1+\zeta'_\alpha\zeta') \tag{8.9}$$

in which, the values of $(\xi'_\alpha,\eta'_\alpha,\zeta'_\alpha)$ are shown in Fig.7.2. Apparently, the linear mapping has been used here, since the variation of the local co-ordinates are linear in a cell. At the singularity, the sub-cell nodes degenerate to a single point. As a consequence, the Jacobian J_s tends to zero as $O(r^2)$ as $r\rightarrow 0$, nullifying the weak singularity.

8.2.2 Discretization of Strongly Singular Domain Integrals

After discretizing the yield region into N_c cells, using (8.1) the domain integrals appearing in the internal stress integral equation (7.17) (without consideration of body forces) can be approximated by:

$$\int_{\Omega} E_{ijkl}(p,q)\dot{\sigma}^{p}_{kl}(q)d\Omega(q) = \sum_{c=1}^{N_c}\sum_{\alpha=1}^{20} E^{c\alpha}_{ijkl}\dot{\sigma}^{p\alpha}_{kl} \tag{8.10}$$

where

$$E^{c\alpha}_{ijkl} = \int_{\Omega_c} E_{ijkl}(p,q)N_{\alpha}(q)d\Omega(q) \tag{8.11}$$

in which, Ω_c is the domain of the cell c.

For cells not including the point p, (8.11) can be calculated in the usual way, i.e.,

$$E^{c\alpha}_{ijkl} = \int_{-1}^{1}\int_{-1}^{1}\int_{-1}^{1} E_{ijkl}(x^{P}, x(\xi,\eta,\zeta))N_{\alpha}(\xi,\eta,\zeta)J(\xi,\eta,\zeta)d\xi d\eta d\zeta \tag{8.12}$$

However, for the cells which include the source point p, we can not directly employ the cell sub-division technique, since the kernel E_{ijkl} is strongly singular. Instead, as described in Chapter 7, we first isolate the singularity in (8.11) as follows:

$$E^{c\alpha}_{ijkl} = \int_{\Omega_c} E_{ijkl}(p,q)\{N_{\alpha}(q) - \delta_{\alpha p}\}d\Omega(q) + \delta_{\alpha p}\int_{\Omega_c} E_{ijkl}(p,q)d\Omega(q) \tag{8.13}$$

where

$$\delta_{\alpha p} = \begin{cases} 1 & \text{when } \alpha = p \\ 0 & \text{when } \alpha \neq p \end{cases} \tag{8.14}$$

Now the first integral on the right-hand side of (8.13) is weakly singular and can be evaluated by using the cell sub-division technique as:

$$E^{c\alpha}_{ijkl} = \sum_{s=1}^{N_s}\int_{-1}^{1}\int_{-1}^{1}\int_{-1}^{1} E_{ijkl}(x^{P}, x(\xi,\eta,\zeta))\{N_{\alpha}(\xi,\eta,\zeta) - \delta_{\alpha p}\}J(\xi,\eta,\zeta)J_s(\xi',\eta',\zeta')d\xi' d\eta' d\zeta' \tag{8.15}$$

in which, J_s and ξ',η',ζ' are determined using (8.7)-(8.9). The last integral on the right-hand side of (8.13) can be evaluated using (7.43); thus:

$$\int_{\Omega_c} E_{ijkl}\,d\Omega = \sum_{s=1}^{N_s} \int_{\Omega_c^s} E_{ijkl}\,d\Omega = \sum_{s=1}^{N_s} \int_{\Gamma_c^s} E_{ijkl} r_m n_m \ln r\, d\Gamma =$$

$$\sum_{s=1}^{N_s} \int_{-1}^{1}\int_{-1}^{1} E_{ijkl}(x^p, x(\xi,\eta)) r_m(x^p, x(\xi,\eta)) n_m(\xi,\eta) \ln r(x^p, x(\xi,\eta))\, N_\alpha(\xi,\eta) J(\xi,\eta) d\xi d\eta \tag{8.16}$$

The last integration on the right-hand side of (8.16) is performed over the outer surface of the sub-cells (see Fig.7.6). And $N_\alpha(\xi,\eta)$ and $J(\xi,\eta)$ are determined using (2.21) and (2.24).

8.2.3 Algebraic System Equations of Non-Linear BEM

Collocating the source point P for each boundary node in turn using (8.3) and assembling these coefficients into a global system matrix, the following incremental matrix system equation can be formed from (7,11):

$$[H]\{\Delta u\} = [G]\{\Delta t\} + [E^b]\{\Delta\sigma^p\} \tag{8.17}$$

After applying the boundary conditions to (8.17), transferring all the boundary unknowns to the left-hand side and transferring the known matrix products to the right-hand side, we obtain:

$$[A^b]\{\Delta X\} = \{\Delta Y^b\} + [E^b]\{\Delta\sigma^p\} \tag{8.18}$$

where $\{\Delta X\}$ are the boundary unknowns.

Similarly, applying (7.76) to all boundary nodes, resulting in the following matrix equation:

$$\{\Delta\sigma^b\} = [H^b]\{\Delta u\} + [G^b]\{\Delta t\} + [\tilde{E}^b]\{\Delta\sigma^p\} \tag{7.76b}$$

where $\{\Delta\sigma^b\}$ are stresses at boundary nodes. Since (7.76) is from the traction recovery method, the coefficient matrices $[H^b]$, $[G^b]$ and $[\tilde{E}^b]$ are extremely sparse. And for internal nodes, using (8.10), equation (7.17) yields:

$$\{\Delta\sigma^I\} = [H^I]\{\Delta u\} + [G^I]\{\Delta t\} + [E^I]\{\Delta\sigma^p\} \tag{7.17b}$$

where $\{\Delta\sigma^I\}$ are stresses at internal nodes.

Incorporating (7.76b) and (7.17b) into a unified global equation and using the prescribed boundary conditions, we can obtain the following equation:

$$\{\Delta\sigma\} = [A^{\sigma}]\{\Delta X\} + \{\Delta Y^{\sigma}\} + [E^{\sigma}]\{\Delta\sigma^{p}\} \tag{8.19}$$

where $\{\Delta\sigma\}$ is a global stress vector, consisting of stresses at both boundary nodes and internal nodes.

In a similar manner, the following matrix equation can be written, using (7.9), for internal displacements:

$$\{\Delta u\} = [A^{u}]\{\Delta X\} + \{\Delta Y^{u}\} + [E^{u}]\{\Delta\sigma^{p}\} \tag{8.20}$$

Only (8.18) and (8.19) are necessary for the solution process, while equation (8.20) serves to compute (if required) the internal nodal displacements. In the following, two solution strategies are developed for solving the system equations.

8.3 Newton-Raphson Iterative Method with Consistent Tangent Operators

Eliminating $\{\Delta X\}$ from (8.18) and (8.19), leads to:

$$\{\Delta\sigma\} = \{\Delta Y^{e}\} + [E]\{\Delta\sigma^{p}\} \tag{8.21}$$

where

$$\{\Delta Y^{e}\} = \{\Delta Y^{\sigma}\} + [A^{\sigma}][A^{b}]^{-1}\{\Delta Y^{b}\} \tag{8.22}$$

$$[E] = [E^{\sigma}] + [A^{\sigma}][A^{b}]^{-1}[E^{b}] \tag{8.23}$$

Since the initial stress appears in (8.21), which is loading-path dependent, an incremental iterative process is needed. We use $\{\sigma\}_n$ and $\{\sigma^{p}\}_n$ to denote the stress and initial stress, respectively, at the end of the n-th increment. Now the new stress and initial stress $\{\sigma\}$ and $\{\sigma^{p}\}$ need to be determined from the imposed (n+1)-th load increment $\{\Delta Y^{e}\}$.

Substituting:

$$\begin{aligned} \{\Delta\sigma\} &= \{\sigma\} - \{\sigma\}_n \\ \{\Delta\sigma^{p}\} &= \{\sigma^{p}\} - \{\sigma^{p}\}_n \end{aligned} \tag{8.24}$$

into (8.21), yields:

$$\{\sigma\}-\{\sigma\}_n=\{\Delta Y^e\}+[E]\left(\{\sigma^p\}-\{\sigma^p\}_n\right) \tag{8.25}$$

For the imposed new load increment $\{\Delta Y^e\}$, (8.25) is not, in general, satisfied. The residual of (8.25) can be written as:

$$\{R\}=\{\sigma\}-\{\sigma\}_n-\{\Delta Y^e\}-[E]\left(\{\sigma^p\}-\{\sigma^p\}_n\right) \tag{8.26}$$

It is noted that now the $\{\Delta Y^e\},\{\sigma\}_n$ and $\{\sigma^p\}_n$ in (8.26) are constants. To reduce the residual to a specified tolerance, the values of stress and initial stress need to be modified through iteration. We assume that, after the i-th iteration, the stress and initial stress are $\{\sigma\}^i$ and $\{\sigma^p\}^i$, respectively, and, for the (i+1)-th iteration, they are modified as:

$$\begin{aligned}\{\sigma\}^{i+1}&=\{\sigma\}^i+\{\dot\sigma\}\\ \{\sigma^p\}^{i+1}&=\{\sigma^p\}^i+\{\dot\sigma^p\}\end{aligned} \tag{8.27}$$

where the $\{\dot\sigma\}$ and $\{\dot\sigma^p\}$ are determined in such a way that the residual shown in (8.26) is forced to be zero for the new stress and initial stress, i.e.,

$$\begin{aligned}0=\{R\}^{i+1}&=\{R\}^i+\frac{\partial\{R\}}{\partial\{\sigma\}}\{\dot\sigma\}+\frac{\partial\{R\}}{\partial\{\sigma^p\}}\{\dot\sigma^p\}\\ &=\{R\}^i+\{\dot\sigma\}-[E]\{\dot\sigma^p\}\end{aligned} \tag{8.28}$$

Now the relations (6.85) and (6.91) are used, i.e.,

$$\{\dot\sigma\}=[D^{ct}]\{\dot\varepsilon\} \tag{6.85bis}$$

$$\{\dot\sigma^p\}=[D^{cp}]\{\dot\varepsilon\} \tag{6.91bis}$$

which are characterized by the *consistent tangent operators* $\mathbf{D}^{ct}$ and $\mathbf{D}^{cp}$:

$$[D^{ct}]=[G]([D^e]-[D^p]) \tag{6.94bis}$$

$$[D^{cp}]=[D^e]-[D^{ct}] \tag{6.95bis}$$

Thus, writing (6.85) and (6.91) in matrix forms and substituting them into (8.28), yields:

$$[K]^i\{\dot\varepsilon\}=\{R\}^i \tag{8.29}$$

where

$$[K]^i=[E]\left([D^e]-[D^{ct}]^i\right)-[D^{ct}]^i \tag{8.30a}$$

In the case of very small increments ($\Delta\lambda^i\to 0$), the tensor [G] degenerates to the identity matrix (see (6.74)) and (8.30a) reduces to:

$$[K]^i = ([I]+[E])[D^p]^i - [D^e] \tag{8.30b}$$

and in terms of (6.82) and (6.93), $[D^p]^i$ reduces to:

$$[D^p]^i = \frac{1}{\psi}[D^e]\{\frac{\partial f}{\partial \sigma}\}^i \left(\{\frac{\partial f}{\partial \sigma}\}^i \right)^t [D^e] \tag{8.31}$$

Once the non-linear equation (8.29) is solved for $\{\dot{\varepsilon}\}$, all the variables for (i+1)-the iteration can be computed. The Flow Chart 8.1 shows the detailed computational process.

Flow Chart 8.1 Iterative process with consistent tangent operators

Computational Process	Equation Index and notation
1. Impose load increment	
$\{\Delta Y^e\} = \{\Delta Y^\sigma\} + [A^\sigma][A^b]^{-1}\{\Delta Y^b\}$	(8.22)
2. Scale stresses for each node	
$\{\sigma^t\} = \{\sigma\}_n + \{\Delta Y^e\}$	Trial stress (constant in iteration).
IF $f(\sigma^t) < TOL_f$ THEN	
$\{\sigma\}_n = \{\sigma^t\}$ and next node	Elastic state.
ELSE IF $f(\sigma_n) < 0$ THEN	
$\alpha = \frac{-f(\sigma)}{f(\sigma^t) - f(\sigma)}$	Cross yield surface.
$\{\sigma\}_n = \{\sigma\}_n + \alpha\{\Delta Y^e\}$	
$\{\Delta Y^e\} = (1-\alpha)\{\Delta Y^e\}$	Scale to surface.
END IF	
3. Initialise iterative variables for each node	
$i=0;\ \{\sigma\}^i = \{\sigma\}_n;\ \{\sigma^p\}^i = \{\sigma^p\}_n;\ \lambda^i = \lambda_n$	
4. Calculate residual of the system equations	
$\{R\}^i = \{\sigma\}^i - \{\sigma\}_n - \{\Delta Y^e\} - [E](\{\sigma^p\}^i - \{\sigma^p\}_n)$	(8.62)
5. Check convergence	
IF $\lvert\{R\}^i\rvert < TOL_R$ THEN	
ISR method in Flow Chart 6.1 for each node	Local stress-return

GOTO 1	iteration.
END IF	Go to next increment.
6. Evaluate non-linear matrices	
$[G]^i = \left([I] + \Delta\lambda^i [D^e] [\frac{\partial^2 f}{\partial\sigma \otimes \partial\sigma}]^i \right)^{-1}$	
$[D^p]^i = [D^e]\{\partial f/\partial\sigma\}^i (\{\partial f/\partial\sigma\}^i)^t [G]^i [D^e] / \tilde{\psi}$	(6.74)
$[D^{ct}]^i = [G]^i ([D^e] - [D^p]^i)$	(6.93)
$[K]^i = [E]\left([D^e] - [D^{ct}]^i\right) - [D^{ct}]^i$	(6.94)
7. Solve system equations for $\{\dot{\varepsilon}\}$	(8.30)
$[K]^i\{\dot{\varepsilon}\} = \{R\}^i$	
8. Evaluate changes in variables for each node	(8.29)
$\{\dot{\sigma}\} = [D^{ct}]\{\dot{\varepsilon}\}$; $\{\dot{\sigma}^p\} = [D^{cp}]\{\dot{\varepsilon}\}$	
$\dot{\lambda} = \{\partial f/\partial\sigma\}^i [G]^i [D^e]\{\dot{\varepsilon}\} / \tilde{\psi}$	(6.85); (6.91)
$\{\dot{\varepsilon}^p\} = [D^e]^{-1}\{\dot{\sigma}^p\}$; $\dot{\bar{\varepsilon}}^p = c'\sqrt{\{\dot{\varepsilon}^p\}^t\{\dot{\varepsilon}^p\}}$	(6.84)
9. Update variables for each node	(6.90); (6.100)
$\{\sigma\}^{i+1} = \{\sigma\}^i + \{\dot{\sigma}\}$; $\{\sigma^p\}^{i+1} = \{\sigma^p\}^i + \{\dot{\sigma}^p\}$;	
$\lambda^{i+1} = \lambda^i + \dot{\lambda}$; $k(\bar{\varepsilon}^p) = k(\bar{\varepsilon}^p) + k(\dot{\bar{\varepsilon}}^p)$	
10. i=i+1; GOTO 4	
	Perform next iteration

In principle, the method described above is similar to that by Bonnet and Mukherjee (1996), but it has been derived differently and expressed in a different form.

Although this iterative method is relatively easy to code, it requires large computer memory. This is because the system equations are formulated in terms of strain increments, which have 6 degrees of freedom at each node. Even if the block decomposition technique is employed for the coefficient matrix, as described by Bonnet and Mukherjee (1996), the computer memory requirement is substantial. Thus, this method is impractical in real engineering applications.

8.4 Incremental Variable Stiffness Solution Schemes

In this section, robust solution schemes are developed based on the variable stiffness approach (Raveendra, 1984; Banerjee et al., 1989; Banerjee, 1994). This approach requires less computer memory: for large problems, the number of degrees of freedom is equal to the number of nodes. Moreover, if small increments are applied, this method can give satisfactory results without iteration.

8.4.1 Boundary Unknown Representation

In this sub-section, the variable stiffness approach proposed by Raveendra (1984) and Banerjee et al. (1989) is described.

The total number of nodes is denoted by N. For each node, say node n, the flow rule and the plastic multiplier can be written (see Chapter 6) in incremental matrix forms, as:

$$\{\Delta\sigma\}_{(n)} = [D^e]\{\Delta\varepsilon\}_{(n)} - \Delta\lambda_{(n)}[D^e]\{\frac{\partial f}{\partial\sigma}\}_{(n)} \tag{8.32}$$

$$\Delta\lambda_{(n)} = \frac{1}{\psi}\{\frac{\partial f}{\partial\sigma}\}_{(n)}^t[D^e]\{\Delta\varepsilon\}_{(n)} = \{\nabla f_\psi\}_{(n)}^t\{\Delta\sigma^e\}_{(n)} \tag{8.33}$$

where

$$\{\nabla f_\psi\}_{(n)} = \frac{1}{\psi}\{\frac{\partial f}{\partial\sigma}\}_{(n)} \tag{8.34}$$

$$\{\Delta\sigma^e\}_{(n)} = [D^e]\{\Delta\varepsilon\}_{(n)} \tag{8.35}$$

and ψ is determined using (6.40a). From equation (7.6), i.e.,

$$\dot{\sigma}_{ij} = \dot{\sigma}^e_{ij} - \dot{\sigma}^p_{ij} \tag{7.6bis}$$

we have:

$$\{\Delta\sigma^e\}_{(n)} = \{\Delta\sigma\}_{(n)} + \{\Delta\sigma^p\}_{(n)} \tag{8.36}$$

Using equation (8.35) and (8.36), equation (8.32) leads to:

$$\{\Delta\sigma^p\}_{(n)} = \{d^f\}_{(n)}\Delta\lambda_{(n)} \tag{8.37a}$$

where

$$\{d^f\}_{(n)} = [D^e]\{\frac{\partial f}{\partial\sigma}\}_{(n)} \tag{8.38}$$

A global initial stress vector can be formed from (8.37) for each node as:

$$\{\Delta\sigma^p\} = [d^f]\{\Delta\lambda\} \tag{8.37b}$$

where $[d^f]$ is a 6N×N sparse matrix, formed from (8.38).

Substituting (8.37b) into (8.18) and (8.19), yields:

$$[A^b]\{\Delta X\} = \{\Delta Y^b\} + [E^{b\lambda}]\{\Delta\lambda\} \tag{8.39}$$

$$\{\Delta\sigma\} = [A^\sigma]\{\Delta X\} + \{\Delta Y^\sigma\} + [E^\sigma][d^f]\{\Delta\lambda\} \tag{8.40}$$

where

$$[E^{b\lambda}] = [E^b][d^f] \tag{8.41}$$

Substituting (8.40) into (8.36), and the result into (8.33), then written in global form, we obtain:

$$\{\Delta\lambda\} = [\nabla f_\psi]\left([A^\sigma]\{\Delta X\} + \{\Delta Y^\sigma\} + [E^\sigma][d^f]\{\Delta\lambda\} + [d^f]\{\Delta\lambda\}\right) \tag{8.42}$$

where $[\nabla f_\psi]$ is a N×6N diagonally dominated strip sparse matrix, formed by $\{\nabla f_\psi\}^t_{(n)}$ in (8.34). Rearranging (8.42) gives:

$$[H^\lambda]\{\Delta\lambda\} = [A^\lambda]\{\Delta X\} + \{\Delta Y^\lambda\} \tag{8.43}$$

where

$$[H^\lambda] = [I] - [\nabla f_\psi]\left([E^\sigma] + [I]\right)[d^f] \tag{8.44}$$

$$[A^\lambda] = [\nabla f_\psi][A^\sigma] \tag{8.45}$$

$$\{\Delta Y^\lambda\} = [\nabla f_\psi]\{\Delta Y^\sigma\} \tag{8.46}$$

Inverting (8.43) gives:

$$\{\Delta\lambda\} = [H^\lambda]^{-1}[A^\lambda]\{\Delta X\} + [H^\lambda]^{-1}\{\Delta Y^\lambda\} \tag{8.47}$$

Finally, substituting (8.47) into (8.39), we obtain:

$$[A]\{\Delta X\} = \{\Delta Y\} \tag{8.48}$$

where

$$[A] = [A^b] - [E^{b\lambda}][H^\lambda]^{-1}[A^\lambda] \tag{8.49}$$

$$\{\Delta Y\} = \{\Delta Y^b\} - [E^{b\lambda}][H^\lambda]^{-1}\{\Delta Y^\lambda\} \tag{8.50}$$

Equation (8.48) is constructed and solved for the boundary unknowns $\{\Delta X\}$ for every increment of loading. Once these unknowns are obtained, we can obtain $\{\Delta\lambda\}$ from

equation (8.47). Then, we can obtain the stress increment $\{\Delta\sigma\}$ from (8.40). The detailed solution process can be found in Banerjee (1994).

In this solution scheme, the largest matrix is either $[H^{\lambda}]$ of size N×N or [A] of size $3N_b \times 3N_b$, where N_b is the number of boundary nodes. In any case, this is much less than the size (6N×6N) of the stiffness matrix [K] described in the preceding section. Therefore, much larger problems can be solved, other things being equal, using this scheme.

Since both the square matrices $[H^{\lambda}]$ and [A] are functions of stresses, in every increment they must be reformed. However, most of the computational time is spent in the evaluation of the inverse of the matrix $[H^{\lambda}]$ in (8.47) and in the solution of equation (8.48). To save computational time, a more effective assembly process is needed: this is described in the following section.

8.4.2 Plastic Multiplier Representation

In this sub-section, a new, more efficient, assembly process for the variable stiffness approach is proposed.

Inverting (8.18) and using (8.37b), it follows that:

$$\{\Delta X\} = \{\Delta Y^c\} + [A^c][d^f]\{\Delta\lambda\} \tag{8.51}$$

where

$$\{\Delta Y^c\} = [A^b]^{-1}\{\Delta Y^b\} \tag{8.52}$$

$$[A^c] = [A^b]^{-1}[E^b] \tag{8.53}$$

Substituting equations (8.51) and (8.37b) into (8.19), leads to:

$$\{\Delta\sigma\} = \{\Delta Y^e\} + [E][d^f]\{\Delta\lambda\} \tag{8.54}$$

where

$$\{\Delta Y^e\} = \{\Delta Y^\sigma\} + [A^\sigma]\{\Delta Y^c\} \tag{8.55}$$

$$[E] = [E^\sigma] + [A^\sigma][A^c] \tag{8.56}$$

Substituting (8.54) and (8.37b) into (8.36), and the result into (8.33), written in matrix form, we obtain:

$$\{\Delta\lambda\} = [\nabla f_\psi]\left(\{\Delta Y^e\} + [E][d^f]\{\Delta\lambda\} + [d^f]\{\Delta\lambda\}\right) \tag{8.57}$$

where $[\nabla f_\psi]$ is a N×6N sparse matrix, formed from $\{\nabla f_\psi\}^t_{(n)}$ in (8.34).

Rearranging (8.57), we obtain the system equations:

$$[H]\{\Delta\lambda\} = \{\Delta Y^f\} \tag{8.58}$$

where

$$[H] = [I] - [\nabla f_\psi][C][d^f] \tag{8.59}$$

$$\{\Delta Y^f\} = [\nabla f_\psi]\{\Delta Y^e\} \tag{8.60}$$

In (8.59), [C] is a constant matrix:

$$[C] = [I] + [E] \tag{8.61}$$

Once the $\{\Delta\lambda\}$ is solved from (8.58), the increments of the boundary unknowns and stresses can be computed using (8.51) and (8.54), respectively. In all the equations, only $[\nabla f_\psi]$ and $[d^f]$, which explicitly appear in equations and are determined using (8.34) and (8.38), respectively, involve stresses. Therefore, (8.58) is an explicit method for evaluation of the plastic multiplier increment $\{\Delta\lambda\}$. Moreover, in computation, only the square matrix [H] with size N×N needs to be reformed for each increment. Hence, this solution scheme needs less computational time than the previous one.

8.4.3 Iteration Schemes for Variable Stiffness Algorithms

For small increments, no iteration is needed in the variable stiffness approach. However, what is meant by "small" in this context is difficult to quantify. In this sub-section, novel iterative procedures are proposed for the two variable stiffness approaches described earlier, in order to improve their accuracy in practice.

The essential idea is to minimize the residuals of the system equations through an iterative process. These operations are described in what follows:

Iteration Scheme for Boundary Unknown Representation

In this approach, equations (8.39) and (8.40) are the system equations. The notation $\{\sigma\}_n$, $\{X\}_n$ and $\{\lambda\}_n$ is used to denote the stress, boundary unknown and plastic multiplier

matrices, respectively, at the end of the n-th increment. For the new increments $\{\Delta Y^b\}$ and $\{\Delta Y^\sigma\}$, we use $\{\sigma\}^i$, $\{X\}^i$ and $\{\lambda\}^i$ to denote the results after the i-th iteration. The residuals of equations (8.39) and (8.40) can be written as:

$$\{R_x\}^i = \{\Delta Y^b\} + [E^{b\lambda}]^i\left(\{\lambda\}^i - \{\lambda_n\}\right) - [A^b]\left(\{X\}^i - \{X\}_n\right) \tag{8.62}$$

$$\{R_\sigma\}^i = [A^\sigma]\left(\{X\}^i - \{X\}_n\right) + \{\Delta Y^\sigma\} + [E^\sigma][d^f]^i\left(\{\lambda\}^i - \{\lambda_n\}\right) - \left(\{\sigma\}^i - \{\sigma\}_n\right) \tag{8.63}$$

If one or both of the norms of $\{R_x\}^i$ and $\{R_\sigma\}^i$ are greater than a given tolerance, then we replace $\{\Delta Y^b\}$ and $\{\Delta Y^\sigma\}$ with $\{R_x\}^i$ and $\{R_\sigma\}^i$ in (8.39) and (8.40), and repeat the process. Flow Chart 8.2 shows the details.

Flow Chart 8.2 Iterative process for *Boundary Unknown Representation*

1. Impose load increment $\{\Delta Y^b\}$ and $\{\Delta Y^\sigma\}$ and
   the corresponding elastic stress increment $\{\Delta Y^e\}$
2. Scale stresses for each node
   $\{\sigma^t\} = \{\sigma\}_n + \{\Delta Y^e\}$
   IF $f(\sigma^t) < TOL_f$ THEN $\{\sigma\}_n = \{\sigma^t\}$ and next node
   ELSE IF $f(\sigma_n) < 0$ THEN
   $$\alpha = \frac{-f(\sigma)}{f(\sigma^t) - f(\sigma)}; \quad \{\sigma\}_n = \{\sigma\}_n + \alpha\{\Delta Y^e\}; \quad \{\Delta Y^e\} = (1-\alpha)\{\Delta Y^e\}$$
3. Initialise iterative variables for each node
   $i=0$; $\{\sigma\}^i = \{\sigma\}_n$; $\{X\}^i = \{X\}_n$; $\{\lambda\}^i = \{\lambda\}_n$
4. Calculate residual of the elementary equations
   $$\{R_b\}^i = \{\Delta Y^b\} + [E^{b\lambda}]^i\left(\{\lambda\}^i - \{\lambda_n\}\right) - [A^b]\left(\{X\}^i - \{X\}_n\right)$$
   $$\{R_\sigma\}^i = [A^\sigma]\left(\{X\}^i - \{X\}_n\right) + \{\Delta Y^\sigma\} + [E^\sigma][d^f]^i\left(\{\lambda\}^i - \{\lambda_n\}\right) - \left(\{\sigma\}^i - \{\sigma\}_n\right)$$
5. Check convergence
   IF $\left|\{R_b\}^i\right| < TOL_b$ AND $\left|\{R_\sigma\}^i\right| < TOL_\sigma$ THEN
   Local stress-return iteration for each node (GSR method in Flow Chart 6.1)
   GOTO 1 for next increment

6. Evaluate non-linear matrices

$$[H^{\lambda}]^i = [I] - [\nabla f_{\psi}]^i \left([E^{\sigma}] + [I]\right)[d^f]^i; \quad [A^{\lambda}]^i = [\nabla f_{\psi}]^i [A^{\sigma}]$$

$$\{\Delta Y^{\lambda}\}^i = [\nabla f_{\psi}]^i \{R_{\sigma}\}^i$$

$$[A]^i = [A^b] - [E^{b\lambda}]^i ([H^{\lambda}]^i)^{-1} [A^{\lambda}]^i; \quad \{\Delta Y\}^i = \{R_b\}^i - [E^{b\lambda}]^i ([H^{\lambda}]^i)^{-1} \{\Delta Y^{\lambda}\}^i$$

7. Solve system equations for $\{\Delta X\}$ by

$$[A]^i \{\Delta X\} = \{\Delta Y\}^i$$

8. Evaluate change in plastic multiplier using $\{\Delta X\}$

$$\{\Delta\lambda\} = ([H^{\lambda}]^i)^{-1} [A^{\lambda}]^i \{\Delta X\} + ([H^{\lambda}]^i)^{-1} \{\Delta Y^{\lambda}\}^i$$

9. Evaluate change in stress using $\{\Delta X\}$ and $\{\Delta\lambda\}$

$$\{\Delta\sigma\} = [A^{\sigma}]\{\Delta X\} + \{R_{\sigma}\}^i + [E^{\sigma}][d^f]^i \{\Delta\lambda\}$$

10. Evaluate changes in internal variables

$$\{\Delta\varepsilon^p\} = [\partial f/\partial\sigma]\{\Delta\lambda\}; \quad \{\Delta\bar{\varepsilon}^p\} = c'\sqrt{\{\Delta\varepsilon^p\}^t \{\Delta\varepsilon^p\}}$$

11. Update variables for each node

$$\{\sigma\}^{i+1} = \{\sigma\}^i + \{\Delta\sigma\}; \quad \{X\}^{i+1} = \{X\}^i + \{\Delta X\};$$

$$\{\lambda\}^{i+1} = \{\lambda\}^i + \{\Delta\lambda\}; \quad k(\bar{\varepsilon}^p) = k(\bar{\varepsilon}^p) + k(\Delta\bar{\varepsilon}^p)$$

12. i=i+1; GOTO 4 for next iteration

It is noted that in the above process, the matrices $[\nabla f_{\psi}]$ and $[d^f]$ are zero for elastic nodes.

Iteration Scheme for Plastic Multiplier Representation

In this approach, equation (8.58) is the system equations. After the i-th iteration in the (n+1)-th increment, the residuals of equations (8.58) can be written as:

$$\{R_{\lambda}\}^i = \{\Delta Y^f\}^i - [H]^i \left(\{\lambda\}^i - \{\lambda_n\}\right) \tag{8.64}$$

If the norm of $\{R_{\lambda}\}^i$ is greater than a given tolerance, then we replace $\{\Delta Y^f\}$ with $\{R_{\lambda}\}^i$ and solve equation (8.58) for a new $\{\Delta\lambda\}$. Then, new changes in boundary unknowns and stresses can be computed using the terms involving $\{\Delta\lambda\}$ in (8.51) and (8.54). Flow Chart 8.3 shows the details.

Flow Chart 8.3 Iterative process for *Plastic Multiplier Representation*

1. Impose load increment $\{\Delta Y^b\}$ and $\{\Delta Y^\sigma\}$ and corresponding elastic stress increment $\{\Delta Y^e\}$ using $\{\Delta Y^e\}=\{\Delta Y^\sigma\}+[A^\sigma]\{\Delta Y^c\}$; $\{\Delta Y^c\}=[A^b]^{-1}\{\Delta Y^b\}$
2. Scale stresses for each node

   $\{\sigma^t\}=\{\sigma\}_n+\{\Delta Y^e\}$

   IF $f(\sigma^t)<TOL_f$ THEN $\{\sigma\}_n=\{\sigma^t\}$ and next node

   ELSE IF $f(\sigma_n)<0$ THEN

   $$\alpha=\frac{-f(\sigma)}{f(\sigma^t)-f(\sigma)};\quad \{\sigma\}_n=\{\sigma\}_n+\alpha\{\Delta Y^e\};\quad \{\Delta Y^e\}=(1-\alpha)\{\Delta Y^e\}$$

3. Initialise iterative variables for each node

   $i=0;\ \{\sigma\}^i=\{\sigma\}_n+\{\Delta Y^e\};\ \{X\}^i=\{X\}_n+\{\Delta Y^c\};\ \{\lambda\}^i=\{\lambda\}_n$

4. Evaluate non-linear matrices using stress $\{\sigma\}^i$

   $[H]^i=[I]-[\nabla f_\psi]^i[C][d^f]^i;\quad \{\Delta Y^f\}^i=[\nabla f_\psi]^i\{\Delta Y^e\}$

5. Calculate residual of the elementary equation

   $\{R_\lambda\}^i=\{\Delta Y^f\}^i-[H]^i\left(\{\lambda\}^i-\{\lambda_n\}\right)$

6. Check convergence

   IF $\left|\{R_\lambda\}^i\right|<TOL_\lambda$ THEN

   Local stress-return iteration for each node (GSR method in Flow Chart 6.1)

   GOTO 1 for next increment

7. Solve system equations for $\{\Delta\lambda\}$ by

   $[H]^i\{\Delta\lambda\}=\{R_\lambda\}^i$

8. Evaluate change in boundary unknowns using $\{\Delta\lambda\}$

   $\{\Delta X\}=[A^c][d^f]^i\{\Delta\lambda\}$

9. Evaluate change in stress using $\{\Delta\lambda\}$

   $\{\Delta\sigma\}=[E][d^f]^i\{\Delta\lambda\}$

10. Evaluate changes in internal variables

    $\{\Delta\varepsilon^p\}=[\partial f/\partial\sigma]\{\Delta\lambda\};\quad \{\Delta\bar{\varepsilon}^p\}=c'\sqrt{\{\Delta\varepsilon^p\}^t\{\Delta\varepsilon^p\}}$

11. Update variables for each node

$\{\sigma\}^{i+1} = \{\sigma\}^{i} + \{\Delta\sigma\}$; $\{X\}^{i+1} = \{X\}^{i} + \{\Delta X\}$;

$\{\lambda\}^{i+1} = \{\lambda\}^{i} + \{\Delta\lambda\}$; $k(\bar{\varepsilon}^{p}) = k(\bar{\varepsilon}^{p}) + k(\Delta\bar{\varepsilon}^{p})$

12. i=i+1; GOTO 4 for next iteration

It is noted that stress scaling (step 2, above) is necessary to determine the stress state in the current increment. Since in every increment the sum of the stresses at end of the previous increment and the elastic stress increment calculated for the current increment may cross the yield surface, determination of the stresses right at the yield point is critical in the calculation of correct non-linear matrices. On the other hand, the local stress-return iteration described in Flow Chart 6.1 to draw stress to the yield surface in step 6 is not essential.

8.5 Summary

In this Chapter, solution schemes for the Newton-Raphson iteration and variable stiffness algorithms are described. The former incorporates the *consistent tangent operator* method in the iterative process, so quadratic rate of convergence can be achieved. However, since the system equations are expressed in terms of strain increments, this scheme requires considerable computer memory. In the latter, apart from the existing variable stiffness solution scheme (i.e., the *boundary unknown presentation* method), a novel *plastic multiplier presentation* method is proposed, which has greater computational efficiency. To improve computational accuracy, two iterative schemes for these two variable stiffness methods are proposed for the first time, which enable us to use larger increments.

These solution scheme are coded in a computer program, which is described in the following Chapter, together with a number of numerical examples.

Chapter 9

Applications of Non-Linear BEM

The boundary element solution of three-dimensional problems of elastoplasticity is evidently complex and should be thoroughly validated. This chapter describes some work carried out for this purpose using the computer code (***BEAN3D***) which was developed during this research study. In addition to the 3D analyses described in the last three chapters, plane strain and plane stress analyses are also incorporated in the program. The program has the following features:

- Boundary elements:
  2D: 2 noded Linear and 3 noded quadratic isoparametric elements
  3D: 4 noded Linear and 8 noded quadratic isoparametric elements
- Volume cells:
  2D: 4 noded linear and 20 noded quadratic isoparametric cells
  3D: 8 noded linear and 20 noded quadratic isoparametric cells
- Material models: Tresca, Von Mises, Mohr-Coulomb and Drucker-Prager. All with hardening, softening and perfect plasticity.
- Solver of system equations:
  Newton-Raphson iterative scheme.
  Incremental variable stiffness technique.
- Traction-discontinuous problems are solved using multiple-node technique.
- Consideration of 7 symmetry conditions (about the axes):
  x, y, z, x-y, y-z, z-x, x-y-z.

- Self-adaptive algorithm in the evaluation of non-singular integrals (including automatically sub-dividing boundary elements and internal cells and choosing Gauss order).

A number of 2D and 3D benchmark tests have been analysed using this program and some of these are described here. Apart from the first example, which was analysed using both the Newton-Raphson iterative scheme and the variable stiffness solution scheme, all other examples were analysed using the variable stiffness solution scheme. The Gauss-Jordan partial pivoting method (with single precision arithmetic) was used to solve the algebraic matrix equations in all cases.

9.1 3D Cube Under Uniaxial Tension

This first example deals with a cube subjected to tensile displacement (Fig.9.1). The material satisfies the *Von Mises criterion*, and this example is intended to illustrate hardening, perfect plasticity, and softening phenomena under uniaxial loading.

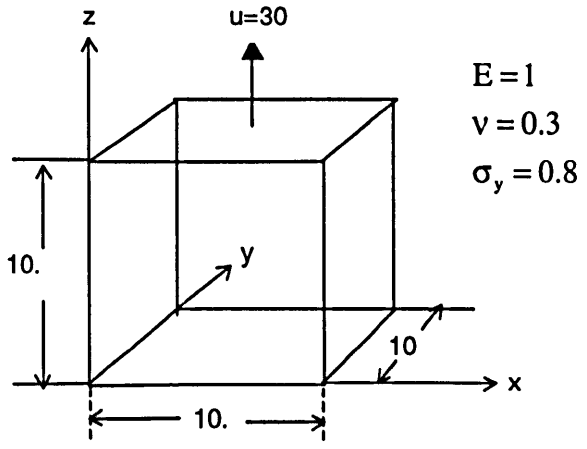

Fig.9.1 A cube under tension

The cube was discretized by four boundary elements per surface and eight volume cells and the "roller" condition was imposed on the three planes x=0, y=0 and z=0. The computation is displacement-controlled. Table 9.1 gives some values of selected components of the initial stress coefficients which are calculated, in the *current* method, using the equation:

$$E^{c\alpha}_{ijkl} = \int_{\Omega_c} E_{ijkl}(p,q)\{N_\alpha(q) - \delta_{\alpha p}\}d\Omega(q) + \delta_{\alpha p}\sum_{s=1}^{N_s}\int_{\Gamma_c^s} E_{ijkl}(p,Q)\, r_m n_m \ln r\, d\Gamma(Q) \qquad (8.13)\text{bis}$$

and calculated, in the *direct* technique (Banerjee and Davies, 1984), using the equation, $E^{c\alpha}_{ijkl} = \int_{\Omega_c} E_{ijkl}(p,q)N_\alpha(q)d\Omega(q)$. There is a marked difference (15-50%) between the two sets of coefficients which, in the light of the results obtained later, suggests that the error lies with the direct method. There appears to be no significant difference in the disparity between the two sets of coefficients whether one considers linear or quadratic cells.

Table 9.1 Selected initial stress coefficients $E^{c\alpha}_{ijkl}$ ($\times 10^{-2}$)

		$E^{c\alpha}_{1111}$	$E^{c\alpha}_{1122}$	$E^{c\alpha}_{2211}$	$E^{c\alpha}_{1212}$
Linear cell and Element	*Current*	-50.778	6.3413	6.3413	-49.222
	Direct	-57.983	9.9438	9.9438	-42.017
Quadratic cell and Element	*Current*	-57.115	9.5101	9.5101	-42.885
	Direct	-64.320	13.113	13.113	-35.680

Table 9.2 gives the computed results at the cube centre for a linear hardening case ($H' = 0.1$), using linear and quadratic elements and cells. From Table 9.2 it is observed that the results calculated by the current method are in excellent agreement with the analytical solutions. The results obtained using the direct technique are poor, although they are distinctly better for the quadratic cells and elements.

Table 9.2 Calculated results for the cube centre ($H' = 0.1$)

		σ_{zz}	ε^p_{zz}	u_z	u_x
Linear cell and Element	*Current*	1.0000	2.0000	15.000	-6.500
	Direct	0.9675	1.5552	13.948	-5.972
Quadratic cell and Element	*Current*	0.9999	1.997	14.992	-6.498
	Direct	1.0776	2.0473	15.479	-6.742
Analytical	Solution	1.0	2.0	15.0	-6.5

Fig.9.2 shows computed results for hardening ($H'=0.1$), perfect plasticity ($H'=0$), and softening ($H'=-0.1$). All of these results are, essentially, exact and illustrate the capacity of the program to cope with the spectrum of hardening rules.

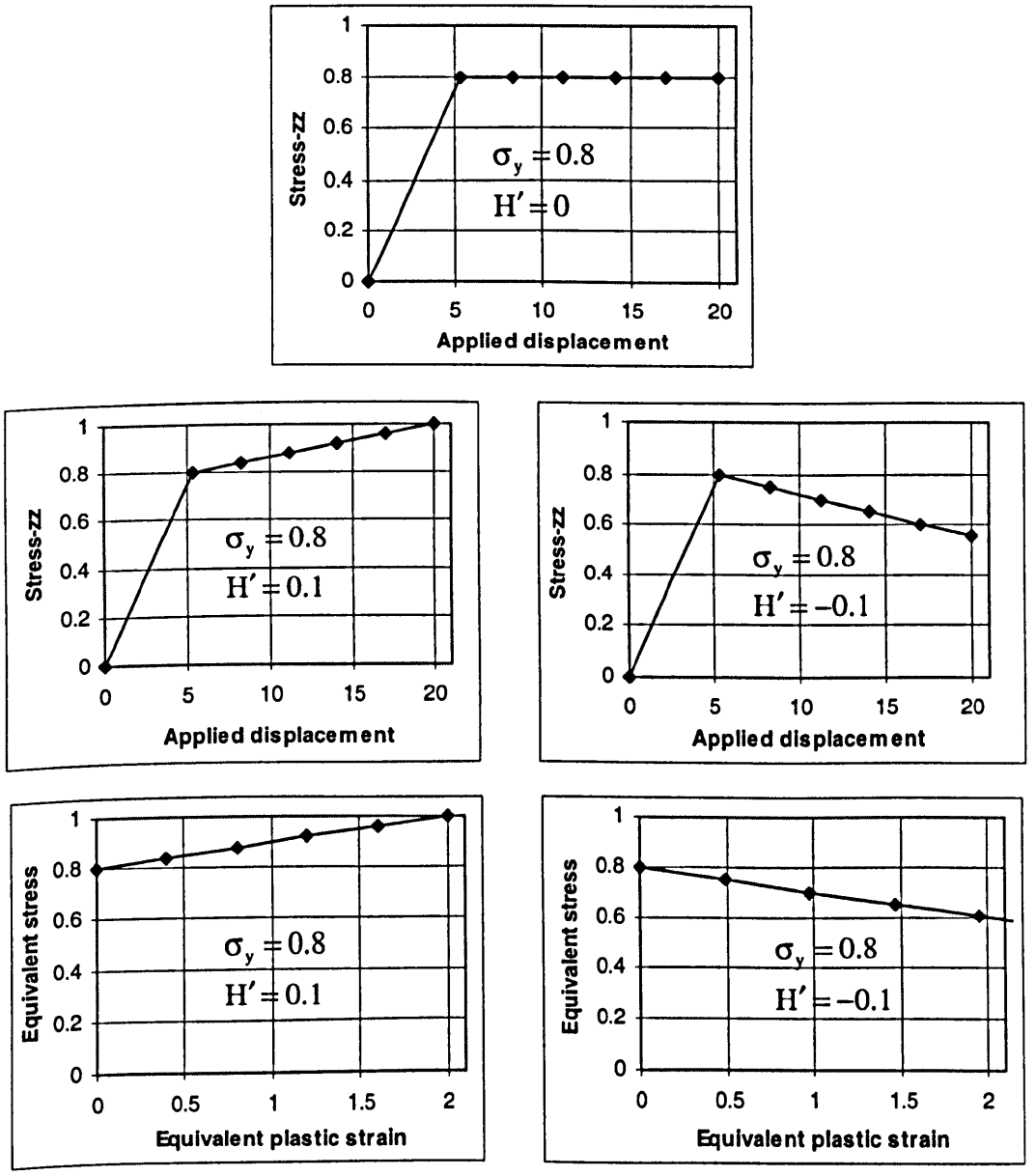

Fig.9.2 Hardening, perfect plasticity, and softening performance

This problem was analysed using both the Newton-Raphson iterative method and the variable stiffness method: both methods gave the same results. In this problem, the results

are essentially independent of increment size, provided that stress-scaling is carried out when the trial stresses $\{\sigma^t\}$ cross the yield surface.

9.2 2D Thick-Wall Cylinder Under Internal Pressure

The second numerical example considered is a thick cylinder subjected to internal pressures (Fig.9.3), under plane strain conditions. The Tresca yield criterion is assumed and the numerical solutions obtained are compared with the theoretical results of Lubliner (1990). The pressure/radial displacement characteristics are shown in Fig.9.4 and radial and circumferential (hoop) stress distributions for specified pressure values, p=20 and p=18, are plotted in Fig.9.5. To examine the dependence of the results on load increment size, plots of radial and hoop stress against the number of the increments (for radius r=100 (inner surface) and r=150 (middle surface)), are reproduced in Fig.9.6.

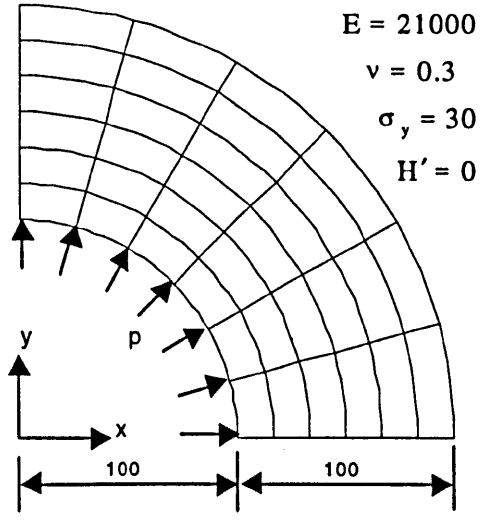

Fig.9.3 Mesh and material properties of an internally pressurised thick cylinder

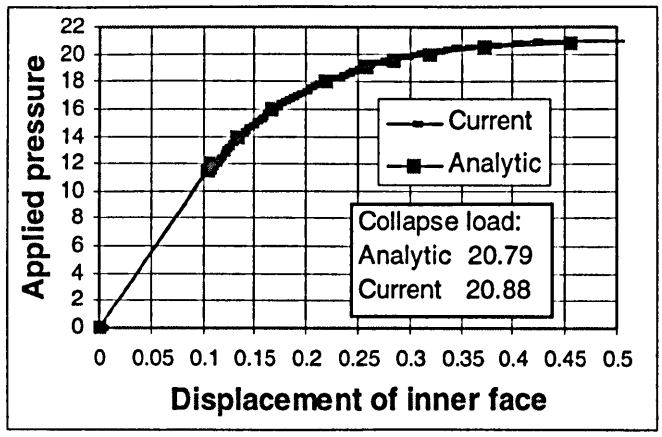

Fig.9.4 Displacement of the inner surface with increasing pressure

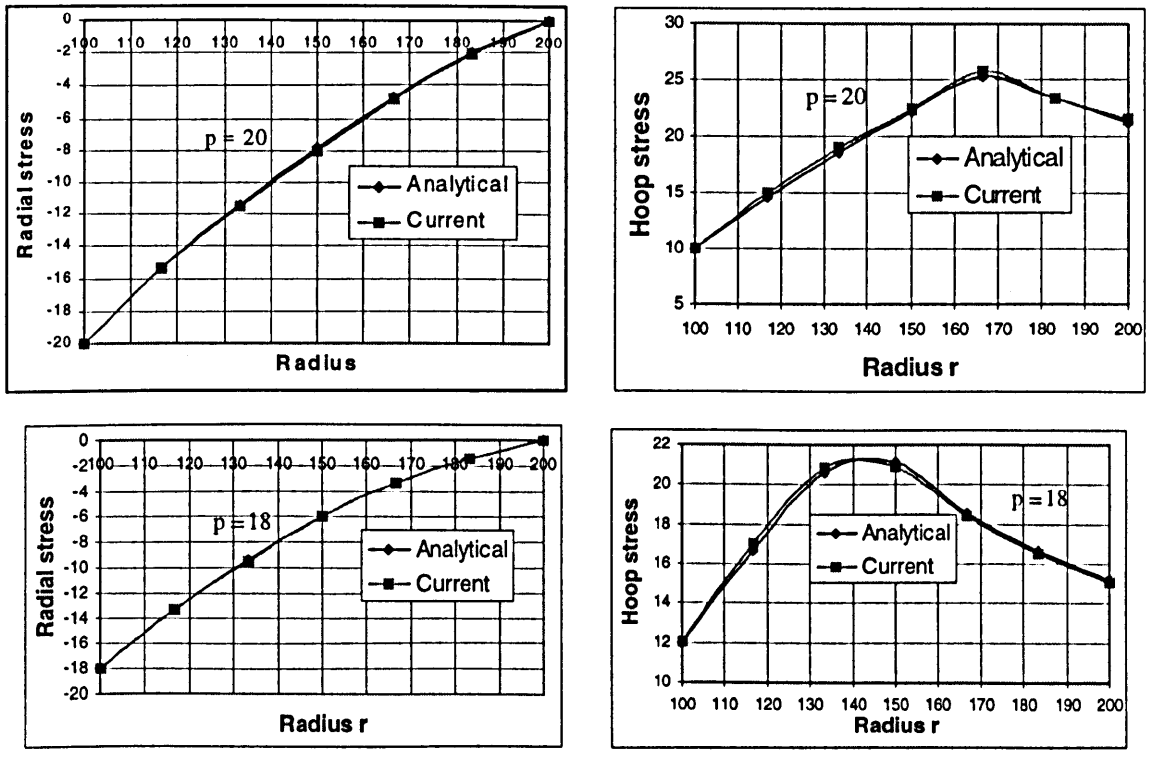

Fig.9.5 Radial and hoop stresses distributions along radius

On the scale of Fig.9.4, the theoretical and numerical results are indistinguishable. Similarly, the radial stresses (Fig.9.5) are also essentially exact. Some discrepancies (2-3%) are apparent however in the hoop stresses at the higher load levels (in the interior), although the hoop stresses at the outer boundary are well-captured. The reason for these

discrepancies have not been fully investigated, but may be due to direct or consequential effects of the geometrical discretisation.

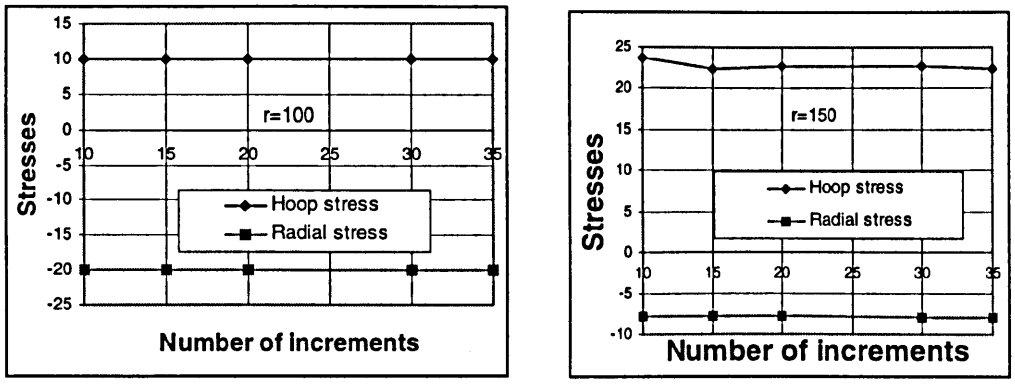

Fig.9.6 Stresses versus number of increments (p = 20)

Fig.9.6 shows that, at the inner surface, a stable solution is obtained using very few increments of loading. However, the internal solution is more sensitive to the number of increments employed, presumably because the plastic front must be tracked quite accurately in order to determine these stresses accurately, especially given the fairly coarse mesh employed in the radial direction.

9.3 2D Rigid Punch

In this example, a rigid punch is impressed into a finite continuum under plane-strain conditions. Since the punch is rigid and the contact conditions are assumed to be frictionless, it is possible to simulate the contact by gradually increasing the vertical displacements at the nodes. Hence, this plasticity test is displacement-controlled. Fig.9.7 summarises the model, in which only half of the punch is discretized into cells. The assembly consists of 528 nodes including 120 boundary nodes, 60 boundary elements, and 143 internal cells. Computations were carried out using the Von Mises criterion for perfect plasticity ($H'=0$) and isotropic hardening ($H'=0.111E$).

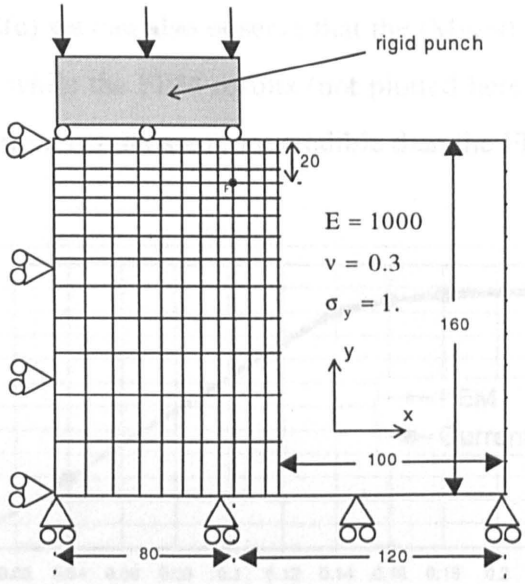

Fig.9.7 Computation model of a 2D punch problem

Figs.9.8 and 9.9 show the computed results for these two cases, with stresses for the point F, at coordinates (80,20). The FEM results are from the benchmarks by Linkens (1993), where the stress values (at the point F) were obtained by extrapolation from the Gauss points of the element at the upper left of the point F. Fig.9.8(a) depicts the load-displacement response of the punch: there is very good agreement between the FEM (Reference) and current results. The reasons for the small discrepancy is unknown. Fig.9.8(b) is a plot of the vertical stress beneath the edge of the punch, as a function of punch displacement. The stress gradients are high here so the extrapolation (employed only in the FEM analysis) may not be entirely satisfactory. Two FEM results are shown: the ''target'' results were obtained using a mesh not unlike the BEM cell configuration, while the ''reference'' results were obtained using an undefined (but presumably finer) mesh. The ''target'' results do not appear to be entirely convincing (two inflection points). There is excellent qualitative agreement between the ''reference' results and our ''current'' results, and fair quantative agreement. Certainly, the difference between the BEM and ''reference'' results is far less than between the two sets of FEM results. Further convergence studies would establish a definitive answer to this demanding test of accuracy. Fig.9.8(c) shows the convergence characteristics of our current method, in terms of various stress and strain components at the point F, where different increments are used for the same input displacement 0.24. Satisfactory convergence is achieved with about 40

increments. From Fig.9.8(c) we can also observe that the (Mises) equivalent stress value of unity is reached quickly, while the FEM results (not plotted here) deviate from this value. This indicates that the current results are more credible than the FEM results.

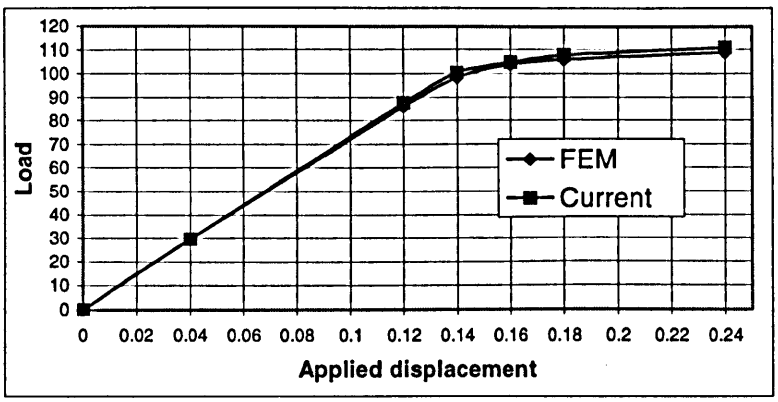

(a)

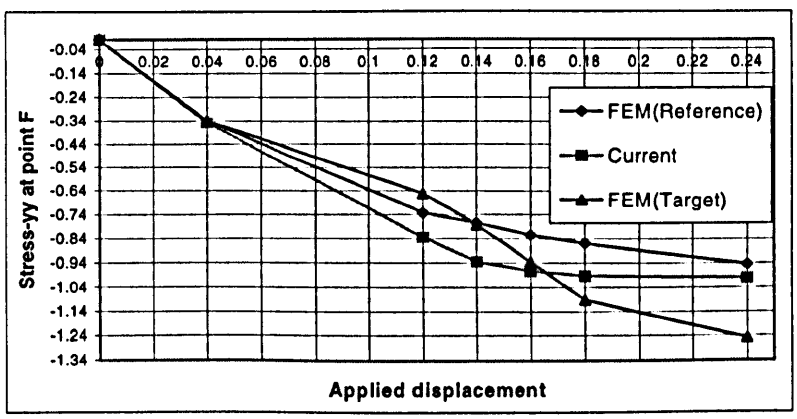

(b)

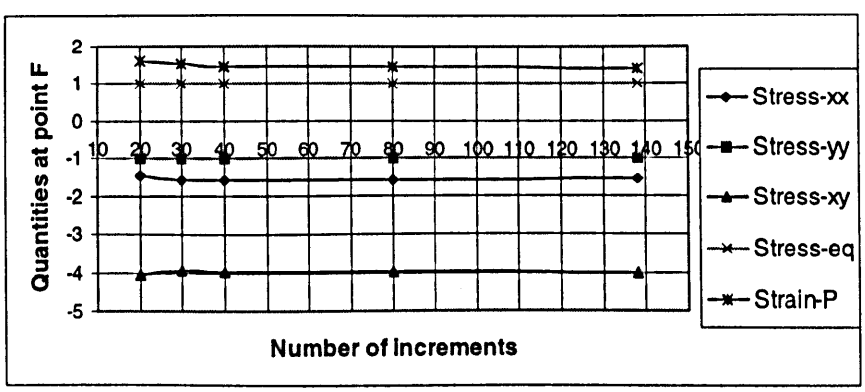

(c)

Fig.9.8 Computed results for perfect plasticity (H′=0)

Fig.9.9(a)/(b) are illustrative results for hardening plasticity and again agree very well with the finite element (Reference) solutions.

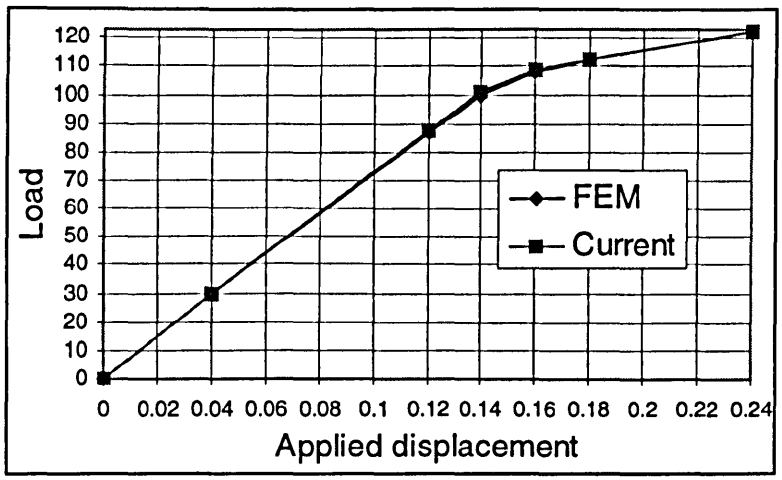

(a)

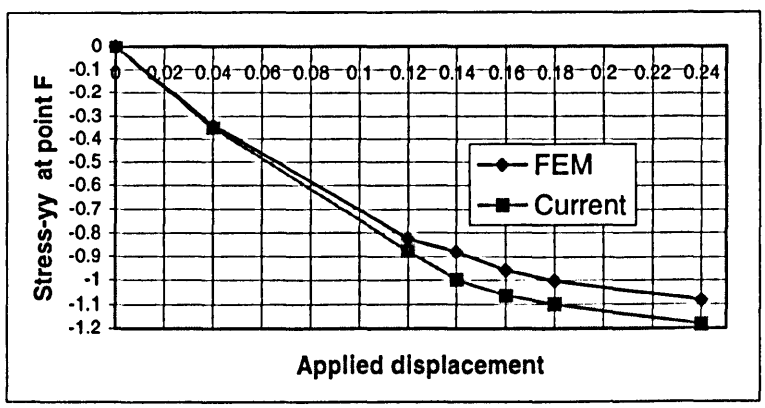

(b)

Fig.9.9 Computed results for hardening material (H'=0.111E)

9.4 Half-Space Under Vertical Loading

This example pertains to the collapse behaviour of a square footing (with dimension B = 1) on the surface of a half-space. It is conventional practice to express the collapse load in terms of the undrained shear strength (C_u) of the soil. From the definition of the equivalent stress σ_y (uniaxial tension yield limit) which characterises the von Mises yield criterion, it

can be easily shown that $\sigma_y = 2C_u$. The computation was carried out for flexible and rigid footings, using quadratic boundary elements and internal cells. The far-field ground surface was discretised using progressively larger boundary elements. At each node shared by the footing and ground surface, two nodes were used to model the traction-discontinuity. Young's modulus E=1000 and Poison's ratio ν=0.3 are assumed through out. The displacements in the following figures should be divided by 10^3 to recover the actual displacements.

9.4.1 3D Flexible Footing

In this case, uniform vertical pressure is applied on the footing and quadrantal symmetry is utilised. To examine the convergence characteristics, three analyses were performed: (a) 155 nodes (including 48 boundary nodes), 11 boundary elements and 15 cells; (b) 476 nodes (including 119 boundary nodes), 32 boundary elements and 64 cells; and (c) 1197 nodes (including 200 boundary nodes), 57 boundary elements and 198 cells. The number of elements over (the quadrant of) the footing is one, four and nine, respectively. Fig.9.10 shows the meshes for each case (over the expected yield region only), depicting both the boundary elements and the corresponding cells. Figs.9.11-9.13 are load-displacement plots for the corner and the centre of the footing, as well as the "mean" displacement. The latter is approximated using the equation (Fox, 1948) $u_M = \frac{1}{3}(u_{corner} + 2u_{centre})_{flexible}$. This should yield approximately the same displacement as a rigid footing.

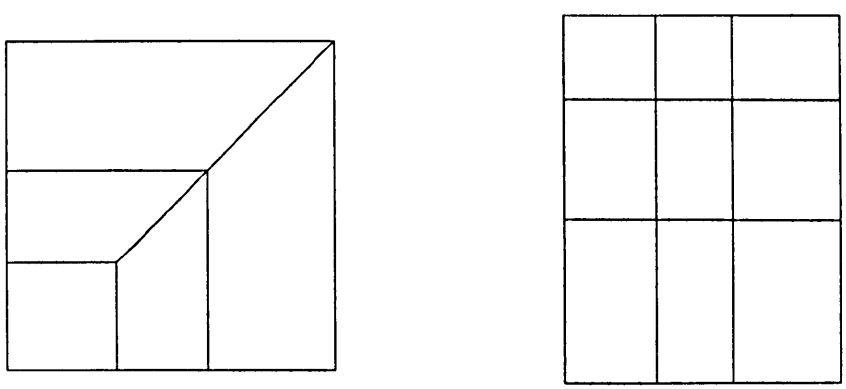

1 element over footing

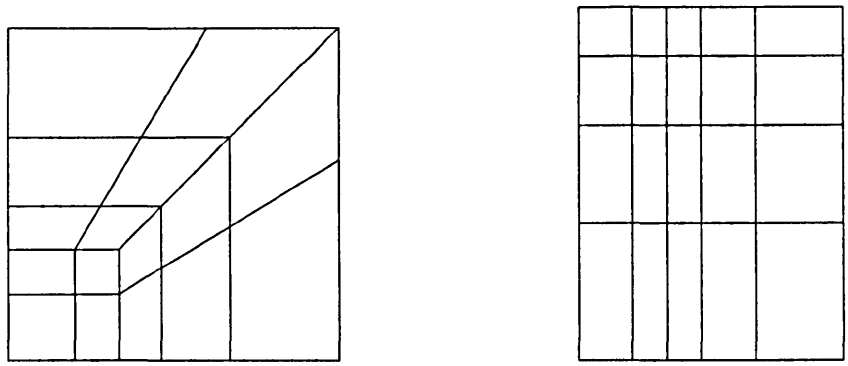

4 elements over footing

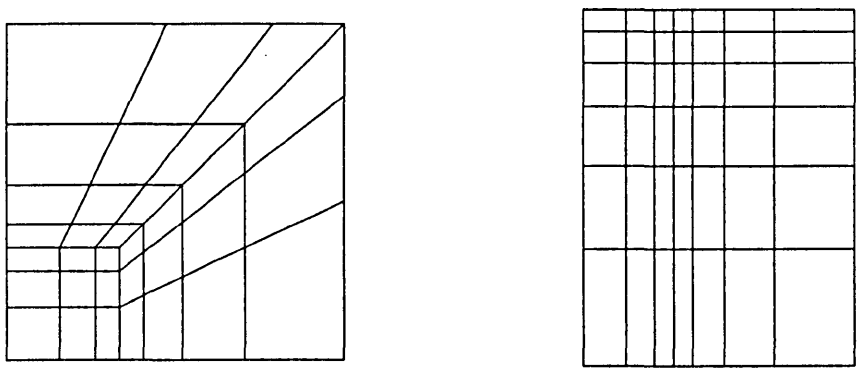

9 elements over footing

Fig.9.10 Boundary elements and internal cells for footing problem

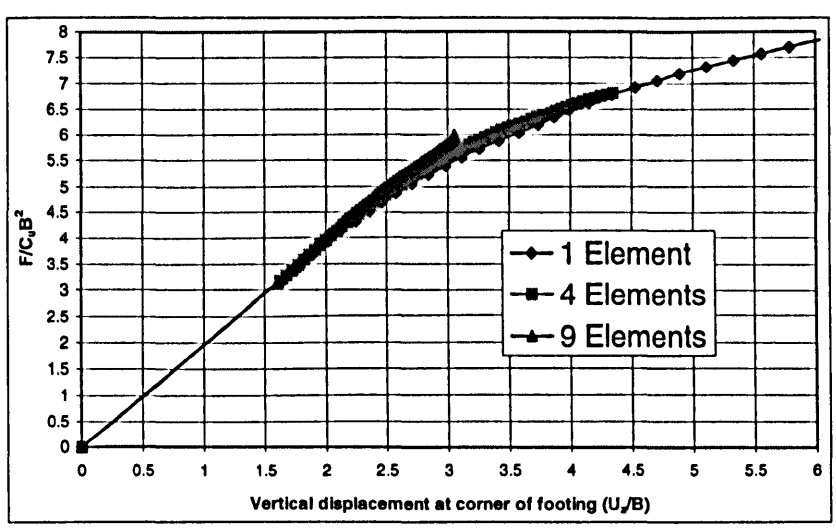

Fig.9.11 Load versus corner settlement, for a square flexible footing

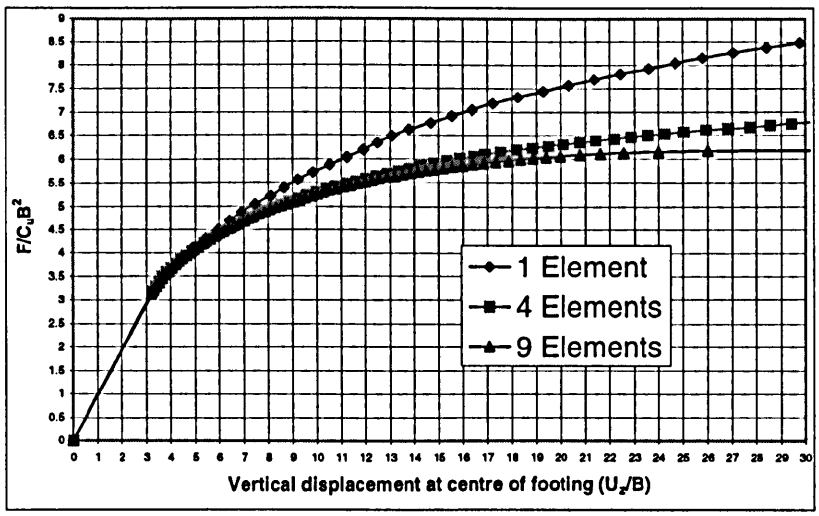

Fig.9.12 Load versus central settlement, for a square flexible footing

Fig.9.11 shows that there is little difference between the results up to a load level of $5C_uB^2$. The coarse discretisations however fail to capture the collapse (at about $6C_uB^2$) and instead return a monotonically increasing function to higher load levels. The convergence characteristics are more clearly illustrated in Fig.9.12. Here, one can see the departure between the three levels of discretisation, and the marked non-linearity of the load-displacement response, at load levels of $4C_uB^2$ and above. Also, the relatively small difference between the results for four elements (over the footing quadrant) with respect to results for nine elements suggests that convergence is very nearly achieved at the latter level. The horizontal asympotote, indicating collapse, is also apparent in this case. Fig.9.13 combines the data obtained from the previous two figures, using the equation given previously. This figure may be interpreted as an approximation to the load-displacement plot for a rigid footing.

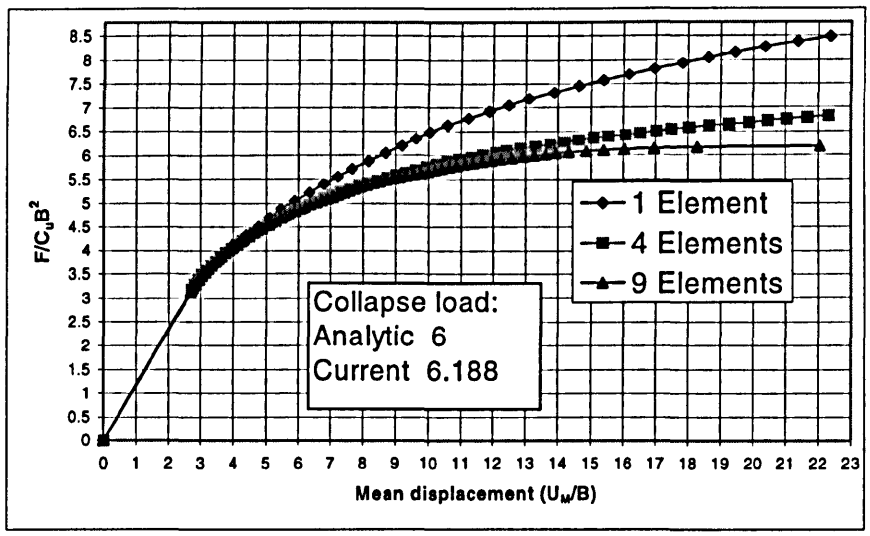

Fig.9.13 Load versus mean settlement, for a square flexible footing

To highlight the convergence, the loads corresponding to a normalised displacement of 22.0 (in Fig.9.13) are replotted in Fig.9.14. This suggests that the true collapse load is about 6.0.

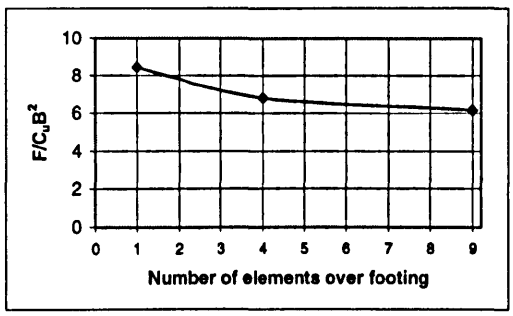

Fig.9.14 Convergence of footing collapse load solutions

Fig.9.15 identifies which nodes yield (near to collapse) in plan and in transverse section. The yield region extends laterally to encompass an area equal to at least four times the footing area and to a depth rather greater than the footing width.

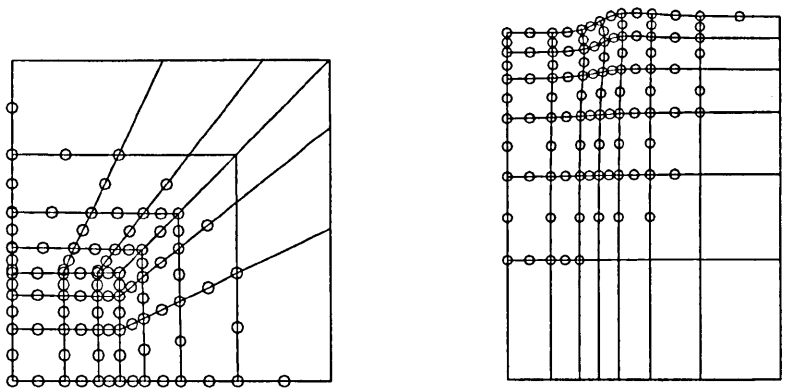

Fig.9.15 Deformed mesh and yield nodes for 9 element case (near collapse)

The exact solution to this problem is not known. However, the collapse load for a rigid circular footing under the same condition is given by $F_c=6A_cC_u$ where A_c is the area of the footing, and it is probable that the collapse load for a square footing will not be much greater.

9.4.2 3D Rigid Footing

A rigid square footing with the same geometry as above is now analysed. As demonstrated in Chapter 2, a very fine mesh is necessary to capture the stress concentration at the edges reasonably accurately. Therefore, as well as using the 9 element mesh (over the footing), a finer mesh is also used here (2462 nodes, including 325 boundary nodes, 96 boundary elements and 448 cells). This mesh uses 16 elements to model one quadrant of the footing. Fig.9.16 depicts the boundary elements over the ground surface and a transverse section view of the cells (both within the expected yield region).

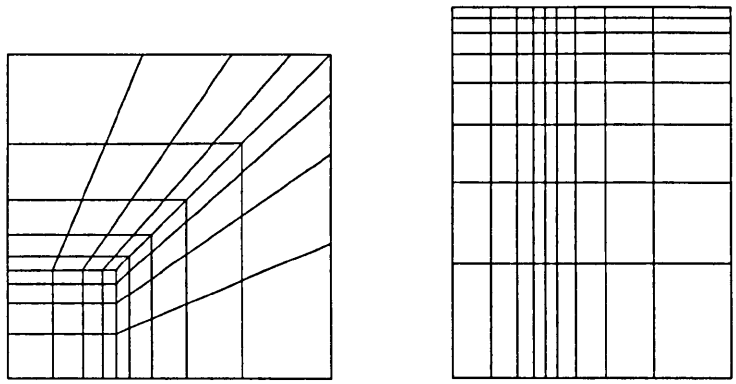

(a) (b)

Fig.9.16 Boundary element discretisation (within expected yield region)
(a) plan view (quadrant), (b) transverse section view

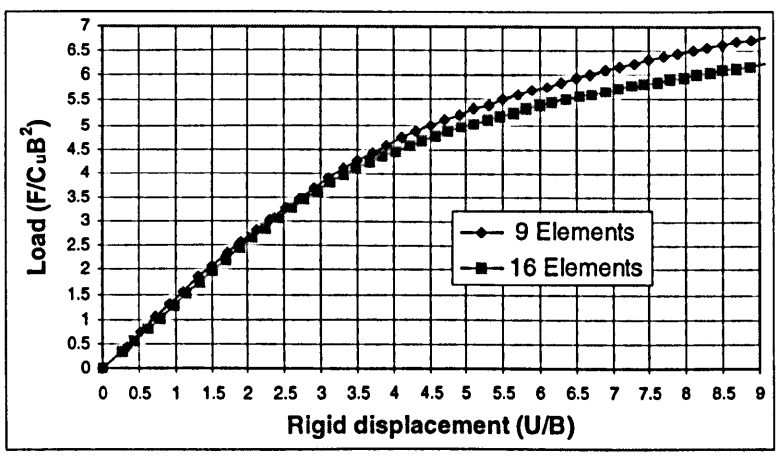

Fig.9.17 Load-settlement response for a square rigid footing

Fig.9.17 is a plot of the load-settlement response for the 9- and 16-element meshes. There is a significant difference between the two sets of results, which means that convergence has not yet been attained. This is also evident from the fact that the horizontal asymptote has not been approached either. One might speculate that about thirty elements might be necessary to achieve satisfactory convergence. However, this level of discretisation is impractical with our current computing resources and this suggestion must therefore remain conjectural. Further, as the numbers of degree of freedom increases, the stability of the Gauss-Jordan solver used here must come into question. More stable and efficient solvers (see Leung & Walker, 1997) will certainly be required in this case.

9.4.3 2D Rigid Footing

In this section, we analyse some two-dimensional (plane strain) rigid footing problems, using fine meshes. Fig.9.18 shows the computational model for a rigid footing (with dimension B=1) and, in particular, the internal cells, which is subjected to an eccentric vertical force F. The discretization consists of 623 nodes, 30 boundary elements and 180 cells.

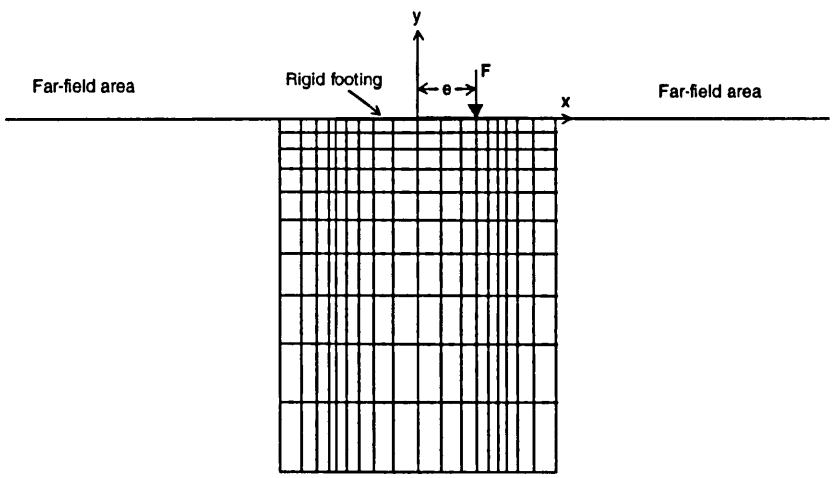

Fig.9.18 Mesh for rigid strip footing subjected to eccentric vertical load

The boundary conditions are conveniently imposed by incrementing the centroidal displacement u_c and the rotation θ, in such a way that the ratio of moment to vertical force is maintained constant (e) (Davies and Gao, 1999). Fig.9.19 is a plot of the load-displacement response for centric loading (e=0) and Fig.9.20 depicts the evolution of the yielded zone. As expected, yielding begins beneath the edges of the footing (Fig.9.20) and then the plastic enclave grows progressively, while always enclosing an elastic region centred underneath the footing centroid. Collapse occurs only when the plastic enclave reaches a depth in excess of 1.5B. In Fig.9.19, we observe that collapse (indicated by solution instability) occurs at a load level of $5.11BC_u$ (i.e., within 1% of the theoretical collapse load of $(\pi+2)BC_u$). It is believed that a better equation solver might eliminate the spurious data generated at the collapse load level.

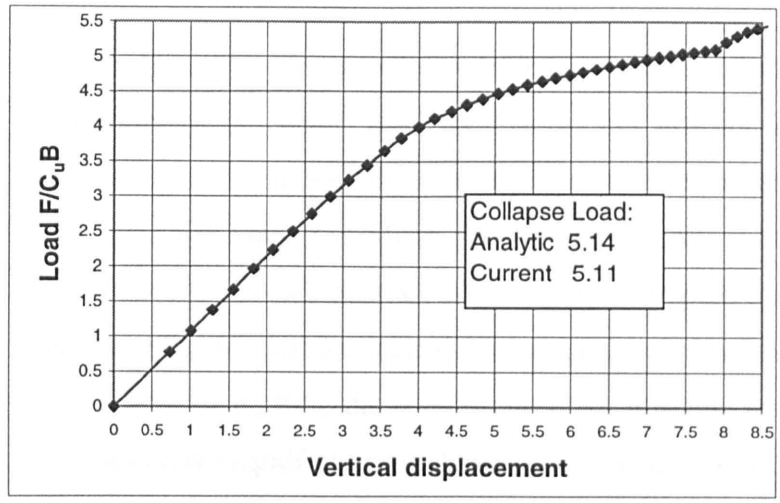

Fig.9.19 Load versus vertical centric displacement (e=0)

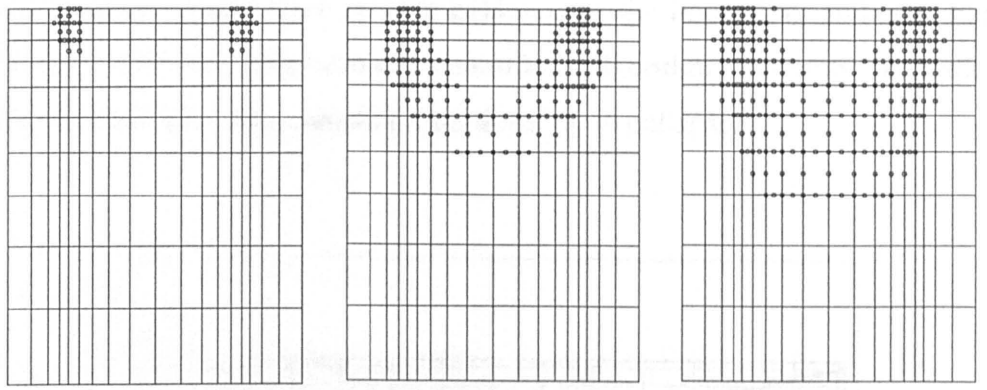

(u=3.08, **F**=3.23) (u=4.21, **F**=4.11) (u=5.24, **F**=4.53)

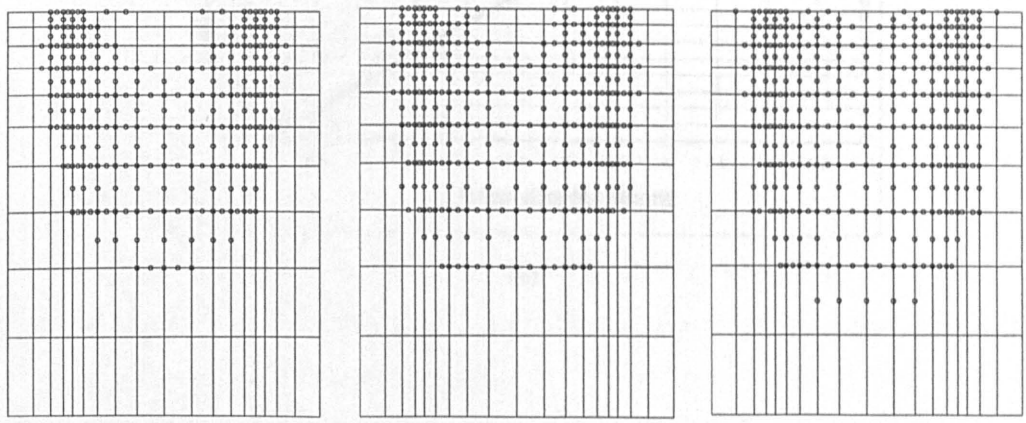

(u=6.16, **F**=4.78) (u=7.00, **F**=4.96) u=(7.75, **F**=5.08)

Fig.9.20 Growth of plastic yield zone under centric loading (e=0)

Figs.9.21 and 9.22 are the principal results obtained for one case of eccentric loading (e/B = 0.2). This is a severe test of the model since the loading lies just outside the "middle-third". Hence, the vertical stresses at one edge are expected to be near zero, if not tensile. (The material model employed here, Von Mises does not incorporate a "tension cut-off" and therefore a "real" soil mechanics analysis is not being attempted here). Fig.9.21 (a) shoes how the edge displacement (on the load side) increases with increasing load. With little warning, at a load level of $3.2BC_u$, the solution becomes unstable which we interpret as the collapse load. From limit equilibrium conditions, we would expect collapse at about 60% of the centric collapse load (i.e. $3.07BC_u$), so this result seems reasonable. Indeed, from a physical point of view, it does seem likely that collapse would be very sudden under such eccentric loading. Rotations of the footing (Fig.9.21(b)) also increases steadily with increasing load and again there is little evidence of the impending collapse. Fig.9.21(c) demonstrates that the displacement-controlled algorithm correctly increments the moment/load condition: they remain proportional up to collapse.

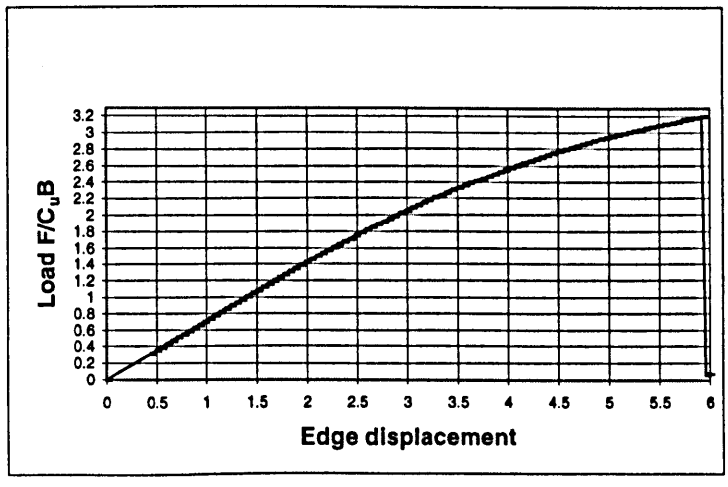

(a)

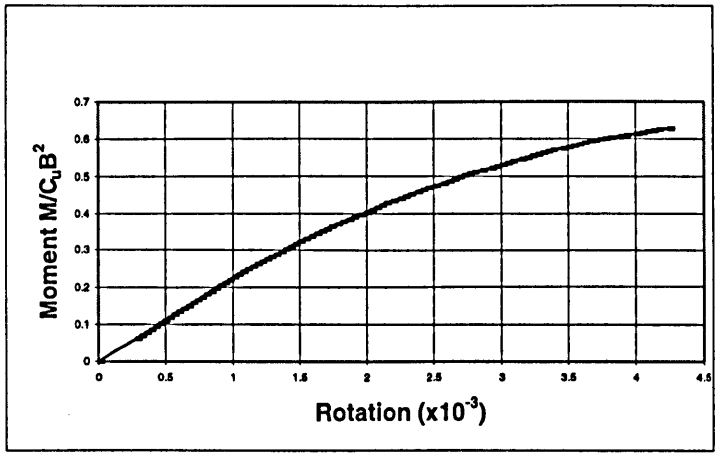

(b)

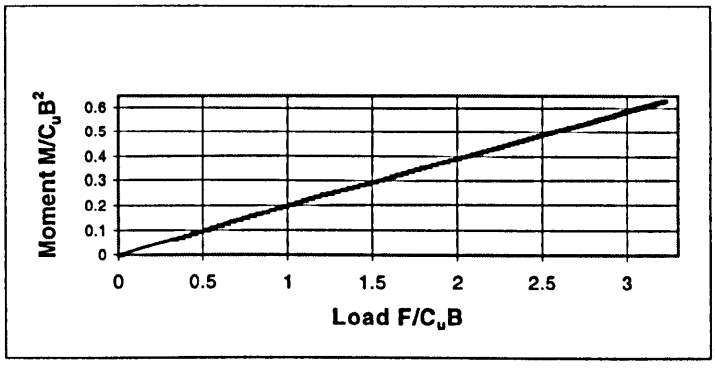

(c)

Fig.9.21 Computed results (e=0.2B)

Fig.9.22 depicts the growth of the plastic enclave with increasing load. This spreads out from beneath one edge steadily increasing in area until, very near to collapse, rapid expansion occurs. This, of course, reflects the sudden collapse noted earlier. It is also observed that at these higher load levels, a separate plastic enclave begins to develop under the opposite edge. When the two coalesce, rotational failure surely follows. Finally, it may be remarked that the maximum depth of the plastic enclave is less than the footing width (much less than in the case of centric loading).

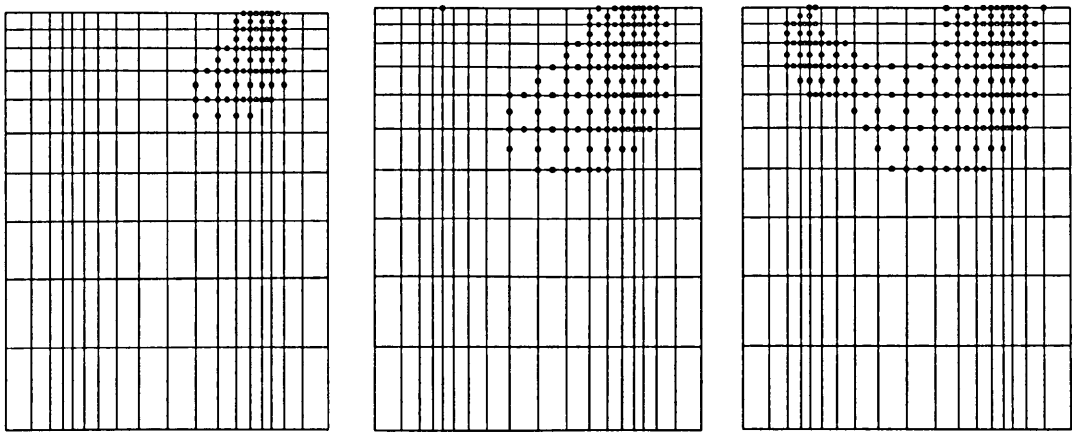

Fig.9.22 Growth of plastic yield zone under eccentric loading (e=0.2B)

9.5 Summary

In this Chapter, we have demonstrated the numerical performance of the elasto-plastic boundary element method described in this thesis. The comparisons with various benchmarks show that this method can give very satisfactory numerical solutions. Where (theoretical) stress singularities occur, as in rigid footing problems, it is necessary to use very fine meshes to achieve high accuracy. For such problems, it would probably be advantageous to use "non-conforming" elements (or multiple nodes) to isolate the singularity, but this has not been explored here. In the variable stiffness scheme, the number of degrees of freedom is equal to the total number of nodes (boundary elements and cells). This means that large matrices must be solved, yet these are still tractable for 3D problems of practical interest, even with quite modest computing resources. Nevertheless, it is evident (for reasons of solution stability as well as efficiency) that adoption of state-of-the-art matrix reduction algorithms (i.e. GMRES) is desirable in demanding applications of the method. In the final Chapter of this thesis, these observations are drawn together to compile a list of desirable refinements of the current program.

Chapter 10

Conclusions and Recommendations

10.1 Summary and Conclusions

This thesis was aimed at resolving some important issues in boundary element analysis in solid mechanics. Particular emphasis has been placed on the treatment of corners and edges arising in traction-discontinuity problems, especially in multi-region problems; development of the infinite boundary element technique for multi-layered media; the evaluation of strongly singular domain integrals in calculating interior stresses, and the solution techniques in non-linear BEM. The following conclusions can be made:

- A multiple-node technique was employed to solve the corner problem, where displacements are uniquely defined but tractions are multi-valued. Novel auxiliary equations, which are required to supplement the fundamental boundary integral equations, are derived from the symmetric property and the equilibrium equations of the stress tensor. These equations are very simple and can be used to deal with the corners and edges of single region and multi-region problems in elastostatics, plasticity and dynamics. For 2D problems, these auxiliary equations do not invoke the assumption of a continuous stress field, but this more restrictive assumption may be required for some 3D problems.

- A sub-structure algorithm has been developed for solving multi-region problems with corners and edges, using the auxiliary equations. This algorithm can deal with arbitrarily many zones. We show that the conventional approach fails where more than two zones intersect.

- A novel infinite element formulation was developed, in which the strongly singular surface integrals over the infinite surface are evaluated analytically. Using these analytical formulation, no numerical integrations over the far field are needed, resulting in significant saving in the calculation time, and resulting in improved accuracy.

- A new effective algorithm was proposed for accurate evaluation of the strongly singular domain integrals in calculating interior stresses. The results derived here provide a basis for removing the strong singularities in both initial stress and initial strain approaches. The resulting transformed integrals, which have the same simple forms for both 2D and 3D problems and suitable for any isoparametric (linear or higher order) cells, are fully numerical and are performed only over cells' boundaries surrounding the source point rather than over the whole boundary of the body under consideration. This results in significant economics in computational time.

- Two type of solution techniques for the non-linear system of equations have been advanced. The *consistent tangent operator* has been incorporated in the Newton-Raphson iterative process which leads to a quadratic rate of convergence. However, since the system equations are formulated in terms of the strain increments, it is impracticable for solving large-scale problems. In the second solution technique (i.e., the incremental variable stiffness technique), a new assembly process was proposed, in which the system equations are expressed in terms of *plastic multipliers*. This assembly process results in an explicit system equations and greater computational speed than the existing variable stiffness method. Since the number of the degrees of freedom is equal to the number of the nodes, larger problems can be solved using this technique. Further, iterative processes were proposed for both the existing variable stiffness method and the new one, so larger load increments can be used. In both solution techniques, since strain space constitutive relations are used, hardening, perfect-plasticity and softening behaviour are treated in a unified way.

10.2 Recommendations for Further Work

The work described in this thesis provides an important basis for some further work in boundary element analysis. The suggestions that are considered most relevant are as follows:

- Multi-region non-linear boundary element analysis: the non-linear formulations and the infinite boundary element technique described in this thesis should be combined with the multi-region boundary element algorithm described in the earlier part of the thesis, to deal with more complicated engineering problems.

- Isotropic elastoplastic damage analysis: the strain-space elastoplastic constitutive relationships can be readily developed to solve damage mechanics problems. Damage variables can be regarded as internal variables in the loading functions. Softening is a major feature in the damage analysis.

- Direct evaluation of the boundary stresses: the stress-recovery method employed in the current program gives unsatisfactory results for coarse meshes. To overcome this deficiency, the direct method based on the regularization using deformation modes (described in Chapter 7) could be developed to evaluate the boundary stresses.

- Use of the discontinuous elements: the continuous elements used in current program requires use of fine meshes for solving some displacement-specified problems, such as the rigid foundation problems, where the stresses are singular at the edges. Discontinuous elements could obviate this problem, although perhaps at the loss of some rigour.

In addition, pre- and post-processors need to be developed. Software such as Auto CAD may be useful for this purpose. More efficient equation solution techniques (e.g. GMRES) should also be incorporated.

References

[1] Abedzadeh, F. and Pak, R.Y.S. (1995) Horizontal translation and rocking rotation of a rigid tubular foundation. *Geotechnique*, **45**, No.1, 83-94.

[2] Alarcon, A., Martin, A. and Paris, F. (1979) Boundary elements in potential and elasticity theory. *Comput. Struct.*, **10**, 351-362.

[3] Aliabadi, M. H. and Rooke, D.P. (1991) *Numerical Fracture Mechanics*, Kluwer Academic Publishers, Dordrecht, and, Computational Mechanics Publications, Southampton.

[4] Aliabadi, M. H. (1997) Boundary element formulations in fracture mechanics. *Appl. Mech. Rev.*, **50**, 83-96.

[5] Bailecki, R. and Nahlik, R. (1987) Linear equations solver for large block matrices arising in boundary element methods. *Boundary Elements IX*, Vol.1, Computational Mechanics Publications, Springer-Verlag, Southampton and Boston.

[6] Bailecki, R. (1987) Nonlinear equations solver for large equation sets arising when using BEM in homogenous regions of nonlinear material. *Boundary Elements IX*, Vol.1, Computational Mechanics Publications, Springer-Verlag, Southampton and Boston.

[7] Banerjee, P. K. and Butterfield, R. (1981) *Boundary element methods in engineering science*, McGRAW-HILL Book Company (UK) Limited, pp.168-176.

[8] Banerjee, P.K. and Cathie, D.N. (1980) A direct formulation and numerical implementation of the boundary element method for two-dimensional problems of elasto-plasticity, *Int. J. Mech. Sci.*, **22**, pp. 233-245.

[9] Banerjee, P.K., Cathie, D.N. and Davies, T.G. (1979) Two and three-dimensional problems of elasto-plasticity. In *Developments in Boundary Element Methods*, Elsevier Applied Science Publishers, London.

[10] Banerjee, P.K., and Davies, T.G. (1979) Analysis of some case histories of laterally loaded pile groups. In: *Proc. of Int. Conf. On Numerical Methods in Offshore Piling*, Institution of Civil Engineers, London.

[11] Banerjee, P.K., and Davies, T.G. (1984) Advanced implementation of the boundary element methods for three-dimensional problems of elasto-plasticity, in:*Developments in Boundary Element Methods*, Elsevier, London.

[12] Banerjee, P.K. and Raveendra, S.T. (1986) Advanced boundary element analysis of two- and three-dimensional problems of elasto-plasticity, *Int. J. Num. Meth. Engng.*, **23**, pp. 985-1002.

[13] Banerjee, P.K., Ahmad, S. and Manolis, G.D. (1986) Advanced boundary element method for two and three-dimensional problems of elastodynamics. *Int. J. Earthqu. Engng. Struct. Dynam.*, **14**, 933-949.

[14] Banerjee, P.K., Henry, D.P. and Raveendra, S.T. (1989) Advanced inelastic analysis of solids by the boundary element method. *Int. J. Mech. Sci.*, **31**, 309-322.

[15] Banerjee, P.K., Israil, A.S.M. and Wang, H.C. (1992) Time-domain formulations of BEM for two-dimensional, axisymmetric and three-dimensional transient elastodynamics. In *Advanced Dynamic Analysis by Boundary Element Methods*, Elsevier Applied Science, London and New York, pp.115-153.

[16] Banerjee, P. K. (1994) *The Boundary Element Methods in Engineering*, McGRAW-HILL BOOK COMPANY, pp.73-75.

[17] Becker, A.A. (1992) *The Boundary Element Method in Engineering*, McGRAW-HILL BOOK COMPANY, London.

[18] Beer, G., Watson, J.O. and Swoboda, G. (1987) Three-dimensional analysis of tunnels using infinite boundary elements', *Computers and Geotechnics*, **3**, 37-58.

[19] Beer, G. and Watson, J.O. (1989) Infinite boundary elements. *Int. J. Numer. Methods Eng.*, **28**, 1233-1247.

[20] Beer, G. (1993) An efficient numerical method for modelling initiation and propagation of cracks along material interfaces. *Int. J. Numer. Methods Eng.*, **36**, 3579-3594.

[21] Betti, E. (1872) Teoria dell elastica. *Il Nuovo Ciemento*, **1872**, 7-10.

[22] Blandford, G.E., Ingraffea, A.R. and Liggett, J.A. (1981) Two-dimensional stress intensity factor computations using the boundary element method. *Int. J. Num. Meth. Eng.*, **17**, 387-404.

[23] Bonnet, M. (1989) Regular boundary integral equations for three-dimensional finite or infinite bodies with and without curved cracks in elastodynamics. In: *Boundary Element Techniques: Applications in Engineering*, Eds C. A. Brebbia and N. Zamani, Computational Mechanics Publications, Southampton, UK.

[24] Bonnet, M. and Mukherjee, S. (1996) Implicit BEM formulations for usual and sensitivity problems in elasto-plasticity using the consistent tangent operator concept. *Int. J. Solids Structures*, **33**, 4461-4480.

[25] Brebbia, C.A. (1978) *The boundary element method for engineers*. Pentech Press, London.

[26] Brebbia, C.A. and Dominguez, J. (1977) Boundary element methods for potential problems. *Applied Mathematical Modelling*, **1**, 7.

[27] Brebbia, C.A. and Dominguez, J. (1992) *Boundary elements: an introductory course*, Computational Mechanics Publications, McGraw-Hill Book Company.

[28] Brebbia, C. A., Telles, J. C. F. and Wrobel, L. C. (1984) *Boundary Element Techniques*, Springer, Berlin and New York.

[29] Brebbia, C. A. and Walker, S. (1980) *Boundary element techniques in engineering*, Newnes-Butterworths, London and Boston.

[30] Bu, S. and Davies, T.G. (1995) Effective evaluation of non-singular integrals in 3D BEM. *Advances in Engng. Software*, **23**, 121-128.

[31] Bui, H.D. (1978) Some remarks about the formulation of three-dimensional thermoelastoplastic problems by integral equations, *Int. J. Solids and Structures*, **14**, pp. 935-939.

[32] Burghardt, B. and Van, A.L. (1998) A fully regularized direct boundary formulation for three-dimensional elastoplastic problems. In: *Boundary Element XX*, Eds. by A. Kassab, C.A. Brebbia and M. Chopra, Computational Mechanics Publications.

[33] Butenschon, H. J., Mohrmann, W. and Bauer, W. (1989) Advanced stress analysis by a commercial BEM code. In: *Industrial Applications of Boundary Element Methods* (Edited by P. K. Banerjee and R. B. Wilson), pp. 239.

[34] Butterfield, R. and Tomlin, G. R. (1971) Integral techniques for solving zoned anisotropic continuum problems. *Proc. Int. Conf. On Variational Methods in Engineering*, Southampton University, pp. 9/31-9/51.

[35] Casey, J. and Naghdi, P.M. (1981) On the characterization of strain hardening in plasticity. *J. Appl. Mech.*, **48**, 285-296.

[36] Cathie, D.N. (1980) On the implementation of elastoplastic boundary element analysis, Proc. 2nd Int. Seminar on Recent Advances in Boundary Element Methods (Brebbia ed.), Southampton, pp.318-334.

[37] Chandra, A. and Saigal, S. (1991) A boundary element analysis of the axisymmetric extrusion process. *In. J. Nonlinear Mech.*, **26**, 1-13.

[38] Chandra, A. and Mukherjee, S. (1996) *Boundary Element Methods in Manufacturing*. Oxford University Press, Oxford, UK.

[39] Chaudonneret, M. (1978) On the discontinuity of the stress vector in the boundary integral equation method for elastic analysis, in *Recent Advances in Boundary Element Methods*, ed C. A. Brebbia, Pentech Press, London.

[40] Chen, W. F. and Han, D.J. (1988) *Plasticity for Structural Engineers.* Springer-Verlag, London.

[41] Chen, W. F. (1994) *Constitutive Equations for Engineering Materials.* Volume 2: Plasticity and Modeling. Elsevier, London.

[42] Chen, Z.Q. and Ji, X. (1987) Boundary element analysis of finite deformation problems of elasto-plasticity. In M. Tanaka and Q. Du, eds., *Theory and Application of Boundary Element Methods*, Proc. 1st Japan-China Symp. On Boundary Element Methods, Pergamon, Oxford, pp. 261-270.

[43] Chen, H., Wang, Y.C. and Lu, P. (1996) Stress rate integral equations of elastoplasticity. *ACTA Mechanica Sinica* (English Series), **12**, 55-64.

[44] Cisilino, A.P., Aliabadi, M.H. and Otegui, J.L. (1998) A three-dimension boundary element formulation for the elastoplastic analysis for cracked bodies. *Int. J. Numer. Meth. Engng.*, **42**, 237-256.

[45] Crisfield, M.A. (1991) *Non-linear Finite Element Analysis of Solids and Structures.* John Wiley & Sons, Chichester.

[46] Crisfield, M.A. (1997) *Non-linear Finite Element Analysis of Solids and Structures.* John Wiley & Sons, Chichester.

[47] Crotty, J. M. (1982) A block equation solver for large unsymmetric matrices arising in the boundary element method. *Int. J. Num. Meth. Engng.*, **18**, 997-1017.

[48] Crotty, J. M. and Wardle, L.J. (1985) Boundary integral analysis of piecewise homogeneous media with structural discontinuities. *Int. J. Roch Mech. Min. Sci. Geomech. Abstr.*, **22**, 419-427.

[49] Crouch, S.L. and Starfield, A.M. (1983) *Boundary element methods in solid mechanics*. George Allen & Unwin, London.

[50] Cruse, T.A. and Rizzo, F.J. (1968) A direct formulation and numerical solution of the general transient elastodynamic problem I. *Journal of Math. Analysis and Applications*, **22**, 244.

[51] Cruse, T.A. (1968) A direct formulation and numerical solution of the general transient elastodynamic problem II. *Journal of Math. Analysis and Applications*, **22**, 341.

[52] Cruse, T.A. (1969) Numerical solutions in three dimensional elastostatics. *Int. J. Solids and Structures*, **5**, 1259-1274.

[53] Cruse, T. A. (1974) An improved boundary-integral equation method for three dimensional elastic stress analysis. *Comput. Struct.*, **4**, 741-754.

[54] Cruse, T.A. and Myers, G.J. (1977) Three-dimensional fracture mechanics analysis. *J. Struct. Div. (ASCE)*, **103**, 309-320.

[55] Cruse, T.A. (1978) Two-dimensional BIE fracture mechanics analysis. *Appl. Math. Modell.*, **2**, 287-293.

[56] Cruse, T.A. (1988) *Boundary element analysis in computational fracture mechanics*. Kluwer Academic Publishers, Boston, MA.

[57] Cruse, T.A. and Novati, G. (1992) Traction BIE formulations and applications to nonplanar and multiple cracks. Fracture Mechanics: *Twenty-Second Symposium*, II, ASTM STP 1131. Ed. S.N. Atluri et al., American Society for Testing and Materials, Philadelphia, 314-332.

[58] Cruse, T.A. and Richardson, J.D. (1996) Non-singular Somigliana stress identities in elasticity. *Int. J. Num. Meth. Engng.*, **39**, 3273-3304.

[59] Dafalias,Y.F.(1977) Elastoplastic coupling within a thermodynamic strain space formulation of plasticity. *Int. J. Non-Linear Mech.*, **12**,327-337.

[60] Dallner, R. and Kuhn, G. (1993) Efficient evaluation of volume integrals in boundary element method, *Comp. Methods in Appl. Mech. and Engng.*, **109**, 95-109.

[61] Davies, T. G. and Bu, S. (1996) Infinite boundary elements for the analysis of halfspace problems. *Computers and Geotechnics*, **19**, 137-151.

[62] Davies, T. G. and Gao, X. W. (1999) A 3D non-linear BEM algorithm for solving rigid foundations. (In preparation)

[63] Dominguez, J. and Alarcon, E. (1981) Elastodynamics, in *Progress in Boundary Element Methods*, Vol. 1 (C.A. Brebbia, Ed.), Pentech Press, London.

[64] Dong, C.Y. and Antes, H. (1998) An improved inner point stress integral equation and its application in 2-D elastoplastic problems. *Engineering Analysis with Boundary Elements*, **22**, 133-139.

[65] Douglas, D. J. and Davies, E. H. (1964) The movement of buried footings due to moment and horizontal load and the movement of anchor plates. *Geotechnique*, **14**, No.2, 115-132.

[66] Drucker, D.C. (1959) A definition of stable inelastic material. *J. Appl. Mech.*, **26**, Trans. ASME 81, Series E, 101.

[67] Fox, E.N. (1948) The mean elastic settlement of a uniformly loaded area at a depth below the ground surface. *Proc. 2nd Int. Conf. Soil Mechs. Fndn. Eng.*, Vol. 1, pp.129.

[68] **Gao, X. W.** and Davies, T. G. (1997) 3D Boundary Element Analysis of Soil-Pier Interaction, In: *Boundary Elements XIX* (C.A.Brebbia et al. Eds.), pp.45-54, Computational Mechanics Publication.

[69] **Gao, X. W.** and Davies, T. G. (1998a) 3-D infinite boundary elements for half-space problems. *Engineering Analysis with Boundary Elements*, **21**, 207-213.

[70] **Gao, X. W.** and Davies, T. G. (1998b) Accurate Evaluations of Strongly Singular Domain Integrals in Non-Linear BEM, In: *Boundary Elements XX* (C.A.Brebbia et al. Eds.), pp.85-94, Computational Mechanics Publication, Southampton.

[71] **Gao, X. W.** and Davies, T. G. (1998c) 3D BEM Analysis of Flexible Inclusions in Multi-Layered Media, In: *Boundary Element Research in Europe* (C.A.Brebbia Ed.), pp.43-52, Computational Mechanics Publication, Southampton.

[72] **Gao, X. W.** and Davies, T. G. (1999a) 3D Multi-Region BEM with Corners and Edges, *International Journal of Solids and Structures,* (In press).

[73] **Gao, X. W.** and Davies, T. G. (1999b) Adaptive algorithm in elasto-plastic boundary element analysis. *Journal of the Chinese Institute of Engineers,* (submitted).

[74] **Gao, X. W.** and Zheng, Y. R. (1990a) Elastoplastic boundary element method formulated in displacement. *The Combination of Analytic and Numerical Solutions in Engineering*, Ed. by Li Jiabao et al., Hunan University Press, P. R. China.

[75] **Gao, X. W.** and Zheng, Y. R. (1990b) An Accelerating Convergence Method for Elastoplastic Iterative Computation in Strain Space, *Proc. of Third Int. Conf. on EPMESC*, MACAU.

[76] **Gao, X. W.**, Liu, J. and Zheng, Y. R. (1991) On Treatment of Measured Displacement and Back Analysis in Underground Excavation, *Tunnel and Underground Engineering*, No.1.

[77] **Gao**, X. W., Zhang, D. C. and Y. R. Zheng (1990) The general relationship of elasto-plastic constitutive equations. *Journal of NingXia University*, **11**, 28-37.

[78] **Gao, X. W.** and Zhong, Z. Q. (1992) Elastoplastic Damage Theory in Isotropic Medium, Chinese *Journal of Theoretical and Applied Mechanics*, No.4.

[79] **Gao, X. W.** and Lu, J. T. (1992) A Combination Method of FEM and BEM for Elastoplastic Problems, *Proc. of Forth Int. Conf. on EPMESC*, Dalian, China, Aug.

[80] Giroud, J.P. (1968) Settlement of a linearly loaded rectangular area. Jnl. Soil Mechs. Fndns. Divn., ASCE, **94**, No.SM4, 813-831.

[81] Gray, L.J. and Lutz, E. (1990) On the treatment of corners in the boundary element method. *J. Comp. Appl. Math.*, **32**, 369-86.

[82] Gray, L.J., Martha, L.F. and Ingraffea, A.R. (1990) Hypersingular integrals in boundary element fracture analysis. *Int. J. Num. Meth. Engng*, **29**, 1135-58.

[83] Guiggiani, M. and Gigante, A. (1990) A general algorithm for multidimensional Cauchy principal value integrals in the boundary element method. *J. Appl. Mech.*, **57**, 906-915.

[84] Guiggiani, M., Krishnasamy, G., Rudolphi, T.J. and Rizzo, F.J. (1992) General algorithm for the numerical solution of hyper-singular boundary integral equations, *ASME J. Appl. Mech.*, **59**,604-614.

[85] Hartmann, F. (1983) Computing the C-matrix in non-smooth boundary point, in new developments. In *Boundary Element Methods*, ed. C.A. Brebbia. Butterworths, Southampton.

[86] Hartmann, F. (1989) *Introduction to boundary element theory and applications.* Springer-Verlag, New York.

[87] Henry, D.P. (1987) Advanced development of the boundary element method for elastic and inelastic thermal stress analysis. *PhD Dissertation*, State University of New York at Buffalo.

[88] Henry, D.P. and Banerjee, P.K. (1988) A variable stiffness type boundary element formulation for axisymmetric elastoplastic media. *Int. J. Num. Meth. Engng.*, **26**, 1005-1027.

[89] Huber, O., Lang, A. and Kuhn, G. (1993) Evaluation of the stress tensor in 3D elastostatics by direct solving of hypersingular integrals. *Computational Mechanics*, **12**, 39-50.

[90] Huber, O., Dallner, R., Partheymuller, P. and Kuhn, G. (1996) Evaluation of the stress tensor in 3-D elastoplasticity direct solving of hypersingular integrals, *Int. J. Num. Meth. Engng.*, **39**, 2555-73.

[91] Huang, Q. and Du, Q. (1988) An improved formulation for domain stress evaluation by boundary element methods in elastoplastic problems. *Proc. China-U.S. Seminar on Boundary Integral Equations and Finite Element Methods in Physics and Engineering*, Xian, China.

[92] Il'iushin, A.A. (1961) On the postulate of plasticity. *Prikl, Mat. Meh.*, **25**, 503-507.

[93] Iwasaki, R. and Ishizaki, T. (1986) Three-dimensional elastoplastic boundary element analysis. In: *Betech 86*, ed. J. J. Connor and C.A. Brebbia, Computational Mechanics Publications.

[94] Jaswon, M.A. and Ponter, A.R. (1963) An integral equation solution of the torsion problem. Proc. Roy. Soc. Lond, A**275**, 237-246.

[95] Jaswon, M. A. and Symm, G.T. (1977) *Integral equation methods in potential theory and elastostatics*, Academic Press, London.

[96] Jiang, Y.S. (1986) Half-plane with body force problem and its uses in geomechanics by BEM. in: J.J.Connor and C.A.Brebbia (eds), *Proc. of the 2nd Boundary Element Technology Conference, Massachusetts Institue of Technology*, USA, pp. 699.

[97] Kane, J. H. and Saigal, S. (1990) An arbitrary condensing , noncondensing solution strategy for large scale, multi-zone boundary element analysis. *Comp. Methods Appl. Mech. Eng.*, **29**, 219.

[98] Kane, J. H., Kumar, B. L. K. and Saigal, S. (1990) An arbitrary multi-zone condensation technique for boundary element design sensitivity analysis, *AIAA Jl*, **28**,1277-84.

[99] Kane, J. H., Keyes, D. E. and Prasad, K. G. (1991) Iterative solution techniques in boundary element analysis. *Int. J. Num. Meth. Engng.*, 31, 1511-36.

[100] Kane, J. H. (1994) *Boundary Element Analysis in Engineering Continuum Mechanics*. Prentice-Hall, Englewood Cliffs, New Jersey 07632.

[101] Krishnasamy, G., Rizzo, F.J. and Rudolphi, T.J. (1992) Hypersingular boundary integral equations: Their occurrence, interpretation, regularization and computation. In: *Advanced dynamic analysis by boundary element methods* (Eds by P.K. Banerjee and S. Kobayashi), Elsevier Applied Science, London and New York, pp.207-252.

[102] Kumar, V. and Mukherjee, S. (1977) A boundary-integral equation formulation for time-dependent inelastic deformation in metals. *Int. J. Mechanical Science*, **19**, 713-724.

[103] Lachat, J. C. (1975) *A Further Development of the Boundary Integral technique for Elastostatics*, Ph.D. Thesis University of Southampton.

[104] Lachat, J. C. and Watson, J. O. (1975) A second generation boundary integral program for three dimensional elastic analysis. In T. A. Cruse and F. J. Rizzo (eds.), *Boundary Integral Equation Method: Computational Applicatins in Applied Mechanics*, AMD Vol.11, ASME, New York.

[105] Lachat, J.C. and Watson, J. O. (1976) Effective numerical treatment of boundary integral equation, *Int. J. Num. Meth. Engng*, **10**, 991-1005.

[106] Lachat, J.C. and Watson, J. O. (1977) Progress in the use of boundary integral equations, illustrated by examples. *Comp. Methods Appl. Mech. Eng.*, **10**, 273-289.

[107] Lee, K.H. and Fenner, R.T. (1986) A quadratic formulation for two-dimensional elastoplastic analysis using the boundary integral equation method, *J. Strain Analysis*, **21**, No.3, pp. 159-175.

[108] Lemaitre, J. (1992) *A course on Damage Mechanics*. Springer-Verlag, Berlin.

[109] Leung, C. Y. and Walker, S. P. (1997) Iterative solution of large three-dimensional BEM elastostatic analyses using the GMRES technique. *Int. J. Num. Meth. Engng.*, **40**, 2227-36.

[110] Linkens, D. (1993) *Selected benchmarks for material non-linearity.* Published by NAFEMS (Ref: R0026).

[111] Liu, M. and Farris, T.N. (1993) Three-dimensional infinite boundary elements for contact problems. *Int. J. Num. Meth. Engng.*, **36**, 3381-3398.

[112] Love, A.E.H. (1944) *A treatise on the mathematical theory of elasticity.* Dover, New York.

[113] Lubliner, J. (1990) *Plasticity theory.* Macmillan Publishing Company, New York; Collier Macmillan Publishers, London.

[114] Lutz, E.D., Ingraffea, A.R. and Gray, L.J. (1992) Use of simple solutions for boundary integral methods in elasticity and fracture analysis. *Int. J. Num. Meth. Engng.*, **35**, 1737-1751.

[115] Maier, G. and Hueckel, T. (1979) Nonassociated and coupled flow rules of elastoplasticity for rock-like materials. *Pergamon press ltd*, 77-91.

[116] Manolis, G.D. and Davies, T.G. (1992) Boundary element techniques in geomechanics, Elsevier Applied Science, London.

[117] Martinez, J. and Dominguez, J. (1985) On the use of Quarter-point boundary elements for stress intensity factor computations. *Int. J. Num. Meth. Eng.*, **20**, 1941-1950.

[118] Mazars, J. and Cabot, G. P. (1996) From damage to fracture mechanics and conversely: A combined approach. *Int. J. Solids Structures*, **33**, 3327-3342.

[119] Mendelson, A. and Albers, L.V. (1975) An application of the boundary integral equation method to elastoplastic problems, *Proc. ASME Conf. On Boundary Integral Equation Methods, AMD 11*(Eds Cruse, T.A. and Rizzo, F.J.), New York.

[120] Mi, Y. and Aliabadi M.H. (1992) Dual boundary element method for three-dimensional fracture analysis. *Engng. Anal. Boundary Elements*, **10**, 161-171.

[121] Mi, Y. and Aliabadi M.H. (1996) A Taylor expansion algorithm for integration of 3D near-singular integrals. *Comm. Num. Meth. In. Engng*, **12**, 51-62.

[122] Mi, Y. (1996) Three-dimensional analysis of crack growth. *Topics in Engineering*, vol.28, ed., C.A. Brebbia and J. Connor, Computational Mechanics Publications, Southampton.

[123] Mindlin, R.D. (1936) Force at a point in the interior of a semi-infinite solid. *Physics*, **7**, 195-202.

[124] Mukherjee, S. (1977) Corrected boundary integral equations in planar thermo-elastoplasticity, *Int. J. Solids Structures*, **13**, 331-335.

[125] Mukherjee, S. and Kumar, V. (1978) Numerical analysis of time dependent inelastic deformation in metallic media using boundary integral equation method, *J. Appl. Mech., ASME*, **45**, 785-790.

[126] Mukherjee, S. (1982) *Boundary element method in creep and fracture.* Applied Science Publishers, New York.

[127] Mustoe, G. G. W. (1980) *A combination of the finite element method and boundary integral procedure for continuum problems*, Ph.D thesis, University of Wales, University College, Swansea.

[128] Mustoe, G.G.W. (1984) Advanced integration schemes over boundary elements and volume cells for two- and three-dimensional non-linear analysis, in:*Developments in Boundary Element Methods*, Elsevier, London.

[129] Naghdi, P.M. and Trapp, J.A. (1975a) The significance of formulating plasticity theory with reference to loading surfaces in strain space. *Int. J. Eng. Scie.*, **13**, 785-797.

[130] Naghdi, P.M. and Trapp, J.A. (1975b) Restrictions on constitutive equations of finite deformed elastic-plastic materials. *Q. JI. Mech. Appl. Math.*, **XXVIII**, 25-46.

[131] Naghdi, P.M. (1990) A critical review of the state of finite plasticity. *J. Appl. Math. and Physics (ZAMP)*, **41**, 315-393.

[132] Nakaguma, R.K. (1979) *Three dimensional elastostatics using the boundary element method.* Ph.D Thesis, University of Southampton.

[133] Nardini, D. and Brebbia, C.A. (1982) A new approach to free vibration analysis using boundary elements. In C.A. Brebbia (ed.), *Proc. 4th International Conference on BEM*, Springer-Verlag, Berlin, pp.313-326.

[134] Nguyen, Q. L. and Bui, H.D. (1974) Sur les materiaux elastoplastiques a ecrouissage positif ou negatif. *J. Mechanique*, **13**, 321.

[135] Ortiz, M. and Simo, J.C. (1986) An analysis of a new class of integration algorithms for elastoplastic constitutive relations. *Int. J. Num. Meth. Eng.*, **23**, 353-366.

[136] Owen, D.R. (1968) *Arch. Ration. Mech. Anal.*, **31**, 91.

[137] Owen, D.R.J. and Hinton, E. (1980) *Finite elements in Plasticity: Theory and Practice.* Pineridge Press Limited, Swansea, U.K.

[138] Patterson, C. and Sheikh, M.A. (1984) Interelement continuity in the boundary element method. In *Topics in Boundary Element Research*, Vol. 1, ed. C.A. Brebbia. Springer-Verlag, Berlin.

[139] Pearce, C.J. (1996) *Computational Plasticity in Concrete Failure Mechanics.* Ph.D Thesis, University of Wales Swansea.

[140] Perucchio, R. and Ingraffea, A.R. (1985) An integrated boundary element analysis system with interactive computer graphics for three-dimensional linear-elastic fracture mechanics. *Comput. Struct.*, **20**, 157-171.

[141] Pipkin, A.C. and Rivlin, R.S. (1965) *Z. Angew. Math. Mech.*, **16**, 313.

[142] Polch, E.Z., Cruse, T.A. and Huang, C.J. (1987) Traction BIE solutions for flat cracks. *Computational Mechanics*, **2**, 253-267.

[143] Poon, H., Mukherjee, S. and Ahmad, M.F. (1998a) Use of ''simple solutions'' in regularizing hypersingular boundary integral equations in elastoplasticity. *ASME, J. Appl. Mech.*, **65**, 39-45.

[144] Poon, H., Mukherjee, S. and Bonnet, M. (1998b) Numerical implementation of a CTO-based implicit approach for the BEM solution of usual and sensitivity problems in elasto-plasticity. *Engineering Analysis with Boundary Elements*, **22**, 257-269.

[145] Poulos, H.G. and Davies, E.H. (1974) Elastic solutions for soil and rock mechanics, John Wiley & Sons, New York.

[146] Prasad, K. G., Kane, J. H., Keyes, D. E. and Balakrishna, C. (1994) Preconditioned KRYLOV solvers for BEA. *Int. J. Num. Meth. Engng.*, **37**, 1651-72.

[147] Press, W. H., Teukolsky, S. A., Vetterling, W. T. and Flannery, B. P. (1992) *Numerical recipes in FORTRAN: The art of scientific computing*, Second Edition, Cambridge University Press.

[148] Raveendra, S. T. (1984) Advanced development of BEM for two and three-dimensional inelastic analysis. *PhD Dissertation*, State University of Neww York at Buffalo.

[149] Raveendra, S. T. and Banerjee, P. K. (1992) Eigenvalue analysis by boundary element method. In: *Advanced dynamic analysis by boundary element methods*, Elsevier Applied Science, London and New York, 283-320.

[150] Raveendra, S. T. and Cruse, T. A. (1989) BEM analysis of problems of fracture mechanics. In *Industrial Applications of Boundary Element Methods* (Ed. P. K. Banerjee and R. B. Wilson), Elsevier Applied Science, London and New York, pp.187-204.

[151] Riccardella, P. (1973) An implementation of the boundary integral technique for planar problems of elasticity and elastoplasticity, *Ph.D Thesis*, Carnegie-Mellon University , Pittsurgh, PA.

[152] Richardson, J.D. and Cruse, T.A. (1998) Nonsingular BEM for fracture modeling. *Computers & Structures*, **66**, 695-703.

[153] Rizzo, F.J. (1967) An integral equation approach to boundary value problems of classical elastostatics, *Quart. Appl. Math.*, **25**, 83-95.

[154] Rudolphi, T. J. (1983) An implementation of the boundary element method for zoned media with stress discontinuities. *Int. J. Num. Meth. Engng.*, **19**, 1-15.

[155] Rudolphi, T. J. , Krishnasamy, G., Schmerr, L.W. and Rizzo, F.J. (1988) On the use of strongly singular integral equations for crack problems. In: *Boundary Elements 10*, Ed. C.A. Brebbia, Spinger-Verlag and Computational Mechanics Publications, Southampton, UK.

[156] Saada, A. S. (1974) *Elasticity: theory and applications*. Pergamon, Oxford.

[157] Saad, Y. and Schultz, M. H. (1986) GMRES: A generalised minimal residual algorithm for solving nonsymmetric linear systems. *SIAM J. Sci. Statist. Comput.*, **7**, 856-869.

[158] Smith, I.M. and Griffiths, D.V. (1998) *Programming the finite element method.* JOHN WILEY & SONS, New York.

[159] Simo, J.C. and Govindjee, S. (1991) Non-linear B-stability and symmetry preserving return mapping algorithms for plasticity and viscoplasticity. *Int. J. Num. Meth. Engng.*, **31**, 151-176.

[160] Simo, J.C. and Tayor, R.L. (1985) Consistent tangent operators for rate-independent elastoplasticity. *Comp. Meth. Appl. Mech. Engng*, **48**, 101-118.

[161] Sinha, B. P., Gerstle, K.H. and Tulin, L.G. (1964) Stress-strain relation for concrete under cyclic loading. *ACI Journal*, **61**, 195-211.

[162] Sladek, V., Sladek, J. and Balas, J. (1986) Boundary integral formulation of crack problems. *ZAMM Z Angew. Math. Mech.*, **66**(2), 83-94.

[163] Snyder, M.D. and Cruse, T.A. (1975) Boundary integral equation analysis of anisotropic cracked plates. *Int. J. Fracture*, **11**, 315-328.

[164] Somigliana, C. (1885) Sopra l'equilibrio di un corpo elastico isotropo. *Il Nuovo Cimento*, **3**, 17-20.

[165] Southwell, R.V. (1946) *Relaxation methods in theoretical physics.* Oxford University Press.

[166] Symm, G.T. (1964) Integral equation methods in elasticity and potential theory. Ph.D. Thesis, London University.

[167] Stern, M., Becker, E.B. and Dunham, R.S. (1976) A contour integral computation of mixed-mode stress intensity factors. *Int. J. Fracture*, **12**, 359-368.

[168] Swedlow, J.L. and Cruse, T.A. (1971) Formulation of boundary integral equations for three-dimensional elasto-plastic flow, *Int. J. Solids and Structures*, **7**, pp. 1673-1683.

[169] Tan, C.L. (1979) *Three-dimensional Boundary Integral Equation Stress Analysis of Cracked Components*, PhD Thesis, Imperial College, University of London.

[170] Telles, J.C.F. (1983) The boundary element method applied to inelastic problems, Springer-Verlag, Berlin.

[171] Telles, J.C.F. and Brebbia, C.A. (1979) On the application of the boundary element method to plasticity, Appl. Math. Modelling, **3**, 466-470.

[172] Telles, J.C.F. and Brebbia, C.A. (1980) The boundary element method in plasticity, *Proc. Second Int. Conf. On Recent Advances in Boundary Element Methods*, Pentech Press, Plymouth, pp. 295-317.

[173] Telles, J.C.F. and Brebbia, C.A. *(1981)* Boundary element solution for half-plane problems. *Int. J. Solids Structures*, **17**, 1149-1158.

[174] Telles, J.C.F. and Carrer, J.A.M. (1991) Implicit procedures for the solution of elastoplastic problems by the boundary element method. *Math. Comput. Modelling*, **15**, 303-311.

[175] Tomlin, G. R. (1972) Numerical analysis of continuum problems in zoned anisotropic media. *Ph.D Thesis*, Southampton University.

[176] Wang, Y. C. and **Gao, X. W.** (1998) Practicable BEM analysis of frictional bolts in underground opening, ASCE *Journal of Structural Engineering*, **124,** 342-346.

[177] Wardle, L. J. and Crotty, J.M. (1978) Two-dimensional boundary integral equation analysis for non-homogeneous mining applications. in *Recent Advances in Boundary Element Methods* (Ed. C.A. Brebbia), Pentech Press, London, pp.233-249.

[178] Watson, J.O. (1979) Advanced implementation of the boundary element method for two-and three-dimensional elastostatics. in: *Developments in Boundary Element Methods-Ed. by P.K.Banerjee and R.Butterfield*, Elsevier Applied Science Publishers, London, 31-63.

[179] Wearing, J.L. and Dimagiba, R.R.M. (1998) The development of the boundary element method for three dimensional elasto-plastic analysis, in: *Boundary Element Research in Europe* (Brebbia ed.), Computational Mechanics Publications, pp.93-102.

[180] Whitman, R.V. and Richart, F.E. (1967) Design procedures for dynamically loaded foundations. *Jnl. Soil Mechs.* Fndns. Divn., ASCE, **93**, No.SM6, 169-193.

[181] Wilde, A.J. (1998) *A Hypersingular Dual Boundary Element Formulation for Three-Dimensional Fracture Analysis.* Ph.D Thesis, Wessex Institute of Technology, University of Wales.

[182] Wilson, R. B., Miller, N. M. and Banerjee, P. K. (1990) Free-vibration analysis of three-dimensional solids by BEM. *Int. J. Num. Meth. Engng*, **29**, 1737-57.

[183] Xu, G. C. and **Gao, X. W.** (1987) The Analytic Expression of Initial Stress Coefficients in Elastoplastic BEM, *Journal of Air Force College*, No.1.

[184] Yan, G. and Lin, F.B. (1994) Treatment of corner node problems and its singularity. *Engineering Analysis with Boundary Elements*, **13**, 75-81.

[185] Yin, Y.Q. and Qu, S.N. (1982), Elastic-plastic coupling and generalized normality rule. *Acta Mechanica Sinica*, No.1., 63-70 (in Chinese).

[186] Zhang, Q. and Mukherjee, S. (1991) Design sensitivity coefficients for linear elastic bodies with zones and corners by the derivative boundary element method, *Int. J. Solids Structures*, **27**, 983-998.

[187] Zhang, Q., Mukherjee, S. and Chandra, A. (1992) Design sensitivity coefficients for elastoviscoplastic problems by boundary element methods, Int. J. Num. Meth. Engng., **34**, 947-966.

[188] Zhang, C., Song, C., Wang, G. and Jin, F. (1989) 3-D infinite boundary elements and simulation of monolithic dam foundations', *Communications in Applied Numerical Methods*, **5**, 389-400.

[189] Zhang, D. C., **Gao, X. W.** and Zheng, Y. R. (1988) Back Analysis Method of Elastoplastic BEM in Strain Space, *Proc. of Int. Conf. on Numerical Method in Geomechanics* (INNSBRUCK), Swoboda(ed.).

[190] Zhang, W. X. and **Gao, X. W.** (1991) A New Iterative Method on Elastoplastic BEM, Chinese *Journal of Theoretical and Applied Mechanics*, No.2.

[191] Zheng, Y.R. and **Gao, X.W.** (1986) Application of Elastoplastic BEM to Back Analysis, *Journal of Underground Technology*, No.2.

[192] Zheng, Y. R., Xu, G. C. and **Gao, X. W.** (1989) The Coupled Computational Method of Elastoplastic BEM and FEM, Chinese *Journal of Engineering Mechanics*, No.1.

[193] Zhong, Z. Q. and **Gao, X. W.** (1990) The Deformation Characteristic of Elastoplastic Coupled Materials, Chinese *Journal of Theoretical and Applied Mechanics*, No.1.

[194] Zienkiewicz, O.C. (1977) *The finite element method.* McGraw-Hill.

Appendix A

Components of the Traction Kernels in in Polar Coordinate System

The coefficients of the traction kernels, using a polar coordinate system, can be written as:

$$T_{11} = \frac{CZ}{R^3}[3\cos^2\theta + (1-2v)] \tag{A1}$$

$$T_{22} = \frac{CZ}{R^3}[3\sin^2\theta + (1-2v)] \tag{A2}$$

$$T_{33} = \frac{CZ}{R^3}[\frac{Z^2}{R^2} + (1-2v)] \tag{A3}$$

$$T_{12} = T_{21} = \frac{3CZ\cos\theta\sin\theta}{R^3} \tag{A4}$$

$$T_{13} = \frac{C}{R^2}[3\cos\theta\frac{Z^2}{R^2} + (1-2v)\cos\theta] \tag{A5}$$

$$T_{31} = \frac{C}{R^2}[3\cos\theta\frac{Z^2}{R^2} - (1-2v)\cos\theta] \tag{A6}$$

$$T_{23} = \frac{C}{R^2}[3\sin\theta\frac{Z^2}{R^2} + (1-2v)\sin\theta] \tag{A7}$$

$$T_{32} = \frac{C}{R^2}[3\sin\theta\frac{Z^2}{R^2} - (1-2v)\sin\theta] \tag{A8}$$

where

$$C = \frac{-1}{8\pi(1-v)}, \quad Z = x_3(Q) - x_3(p), \quad R = \sqrt{Z^2 + r^2} \tag{A9}$$

From equations (A1)-(A4), we can see that for the source points located on the surface of the half-space, the integrals of T_{11}, T_{22}, T_{33} and T_{12} are zero, since Z=0 for those points.

Appendix B

Analytical Expressions for the Integrals of the Traction Kernels

The analytical integrals of the strongly singular integrals are:

$$\int_{\Delta\Gamma_F} T_{11}d\Gamma = \frac{3C}{2}\{[\frac{1}{3}c_1 - d\cos(2\alpha)]\beta + \frac{1}{2}R'\cos(2\alpha)\sin(2\phi) - R'\sin(2\alpha)\cos^2\phi + d\sin(2\alpha)L_R\}\Big|_{\phi_1}^{\phi_2} \tag{B1}$$

$$\int_{\Delta\Gamma_F} T_{22}d\Gamma = \frac{3C}{2}\{[\frac{1}{3}c_1 + d\cos(2\alpha)]\beta - \frac{1}{2}R'\cos(2\alpha)\sin(2\phi) + R'\sin(2\alpha)\cos^2\phi - d\sin(2\alpha)L_R\}\Big|_{\phi_1}^{\phi_2} \tag{B2}$$

$$\int_{\Delta\Gamma_F} T_{33}d\Gamma = \frac{C}{3}\{(4-6\nu)\beta - \frac{ZD^2}{R(D^2+Z^2)}tg\phi\}\Big|_{\phi_1}^{\phi_2} \tag{B3}$$

$$\int_{\Delta\Gamma_F} T_{12}d\Gamma = \frac{3C}{2}\{\sin(2\alpha)[R'\sin\phi\cos\phi - d\beta] + \cos(2\alpha)[R'\cos^2\phi - dL_R]\}\Big|_{\phi_1}^{\phi_2} \tag{B4}$$

$$\int_{\Delta\Gamma_F} T_{13}d\Gamma = \frac{C}{2}\{(\hat{R}-3)\sin\theta + c_2 L_\theta \cos\alpha + c_1\gamma\sin\alpha - (a_1 + c_1 a_2)L_D\cos\alpha\}\Big|_{\phi_1}^{\phi_2} \tag{B5}$$

$$\int_{\Delta\Gamma_F} T_{31}d\Gamma = \frac{C}{2}\{-(\hat{R}+3)\sin\theta - c_2 L_\theta \cos\alpha + c_3\gamma\sin\alpha + (a_1 - c_3 a_2)L_D\cos\alpha\}\Big|_{\phi_1}^{\phi_2} \tag{B6}$$

$$\int_{\Delta\Gamma_F} T_{23}d\Gamma = \frac{C}{2}\{(3-\hat{R})\cos\theta + c_2 L_\theta \sin\alpha - c_1\gamma\cos\alpha - (a_1 + c_1 a_2)L_D\sin\alpha\}\Big|_{\phi_1}^{\phi_2} \tag{B7}$$

$$\int_{\Delta\Gamma_F} T_{32}d\Gamma = \frac{C}{2}\{(3+\hat{R})\cos\theta - c_2 L_\theta \sin\alpha - c_3\gamma\cos\alpha + (a_1 - c_3 a_2)L_D\sin\alpha\}\Big|_{\phi_1}^{\phi_2} \tag{B8}$$

where,

$$c_1 = 5-4\nu, \quad c_2 = 2-4\nu, \quad c_3 = 1+4\nu$$

$$a_1 = \frac{c_2}{\sqrt{1+d}}, \quad a_2 = \frac{d}{\sqrt{1+d}}, \quad d = \left(\frac{D}{Z}\right)^2,$$

$$R = \sqrt{r^2+Z^2} = \sqrt{\frac{D^2}{\cos^2\phi}+Z^2}, \qquad \hat{R} = c_2 \ln R, \quad R' = \frac{R}{Z},$$

$$\beta = \arcsin\left(\sqrt{\frac{1}{1+d}}\,\sin\phi\right), \qquad \gamma = \frac{D}{Z}\,\mathrm{arctg}\left(\frac{Z}{D}\cos\phi\right),$$

$$L_R = \ln[(R+Z)\cos\phi], \quad L_\theta = \ln\left(\frac{1+\sin\phi}{\cos\phi}\right)$$

$$L_D = \frac{1}{2}\ln\left(\frac{\sqrt{1+d}+\sin\phi}{\sqrt{1+d}-\sin\phi}\right)$$

For the case of Z=0, i.e., when the source point and the field point are located at the same elevation, only the integrals, $\int_{\Delta\Gamma_F} T_{13}dS$, $\int_{\Delta\Gamma_F} T_{31}dS$, $\int_{\Delta\Gamma_F} T_{23}dS$, $\int_{\Delta\Gamma_F} T_{32}dS$, are different from zero. They are as follows:

$$\int_{\Delta\Gamma_F} T_{13}dS = (1-2\nu)CL_\theta \cos\alpha\Big|_{\phi_1}^{\phi_2} \tag{B9}$$

$$\int_{\Delta\Gamma_F} T_{31}dS = -(1-2\nu)CL_\theta \cos\alpha\Big|_{\phi_1}^{\phi_2} \tag{B10}$$

$$\int_{\Delta\Gamma_F} T_{23}dS = (1-2\nu)CL_\theta \sin\alpha\Big|_{\phi_1}^{\phi_2} \tag{B11}$$

$$\int_{\Delta\Gamma_F} T_{32}dS = -(1-2\nu)CL_\theta \sin\alpha\Big|_{\phi_1}^{\phi_2} \tag{B12}$$

Appendix C

Approximate Form of $\int_{t_1}^{t_2}(\varepsilon-\varepsilon^0):(\mathbf{D}-\mathbf{D}^e):\dot{\varepsilon}\,dt$

Since t_y and t_z in Fig.6.1 are turning points between elastic and plastic deformations, the above integral can be written as:

$$\int_{t_1}^{t_2}(\varepsilon-\varepsilon^0):(\mathbf{D}-\mathbf{D}^e):\dot{\varepsilon}\,dt=\int_{t_1}^{t_{y-}}+\int_{t_{y-}}^{t_{y+}}+\int_{t_{y+}}^{t_{z-}}+\int_{t_{z-}}^{t_{z+}}+\int_{t_{z+}}^{t_2}(\varepsilon-\varepsilon^0):(\mathbf{D}-\mathbf{D}^e):\dot{\varepsilon}\,dt \qquad (C1)$$

According to the Integral Mean Value Theorem, the second and fourth integrals are zero. Thus (C1) becomes:

$$\int_{t_1}^{t_2}(\varepsilon-\varepsilon^0):(\mathbf{D}-\mathbf{D}^e):\dot{\varepsilon}\,dt=\int_{t_1}^{t_{y-}}+\int_{t_{y+}}^{t_{z-}}+\int_{t_{z+}}^{t_2}(\varepsilon-\varepsilon^0):(\mathbf{D}-\mathbf{D}^e):\dot{\varepsilon}\,dt \qquad (C2)$$

The second integral on the right-hand side of (C2) can be expanded using Taylor's series about point t_{y+} as follows:

$$\begin{aligned}\int_{t_{y+}}^{t_{z-}}(\varepsilon-\varepsilon^0):(\mathbf{D}-\mathbf{D}^e):\dot{\varepsilon}\,dt&=(\varepsilon-\varepsilon^0):(\mathbf{D}-\mathbf{D}^e):\dot{\varepsilon}\,\Delta t+\\&\left\{\dot{\varepsilon}:(\mathbf{D}-\mathbf{D}^e):\dot{\varepsilon}+(\varepsilon-\varepsilon^0):[\dot{\mathbf{D}}:\dot{\varepsilon}+(\mathbf{D}-\mathbf{D}^e):\ddot{\varepsilon}]\right\}\frac{(\Delta t)^2}{2}+\mathbf{O}(\Delta t)^3\end{aligned} \qquad (C3)$$

The first integral on the right-hand side of (C2) can be expressed, through integrating by parts and taking account of (6.3), as:

$$\begin{aligned}\int_{t_1}^{t_{y-}}(\varepsilon-\varepsilon^0):(\mathbf{D}-\mathbf{D}^e):\dot{\varepsilon}\,dt&=\int_{t_1}^{t_{y-}}(\varepsilon-\varepsilon^0):(\mathbf{D}-\mathbf{D}^e):\mathbf{d}(\varepsilon-\varepsilon^0)\\&=\frac{1}{2}(\varepsilon-\varepsilon^0):(\mathbf{D}-\mathbf{D}^e):(\varepsilon-\varepsilon^0)\Big|_{t_1}^{t_{y-}}-\frac{1}{2}c_1\end{aligned} \qquad (C4)$$

where

$$c_1=\int_{t_1}^{t_{y-}}(\varepsilon-\varepsilon^0):\mathbf{dD}:(\varepsilon-\varepsilon^0)=\int_{t_1}^{t_{y-}}(\varepsilon_{ij}-\varepsilon_{ij}^0)(\varepsilon_{kl}-\varepsilon_{kl}^0)dD_{ijkl} \qquad (C5)$$

Noting that $\varepsilon(t_1)=\varepsilon^0$ and $\mathbf{D}(t_{Y-})=\mathbf{D}^e$, (C4) becomes:

$$\int_{t_1}^{t_{y-}} (\varepsilon-\varepsilon^0):(\mathbf{D}-\mathbf{D}^e):\dot{\varepsilon}\,\mathbf{dt} = -\frac{1}{2}c_1 \tag{C6}$$

Since the interval $t_1 \rightarrow t_{y-}$ belongs to the elastic region, then in terms of (6.3), we have:

$$dD_{ijkl} = \frac{\partial^2 \hat{\sigma}_{ij}}{\partial\varepsilon_{kl}\partial\varepsilon_{rs}} d\varepsilon_{rs} = L_{ijklrs} d\varepsilon_{rs} \tag{C7}$$

in which

$$L_{ijklrs} = \frac{\partial^2 \hat{\sigma}_{ij}}{\partial\varepsilon_{kl}\partial\varepsilon_{rs}} = L_{ijrskl} = L_{rsklij} \tag{C8}$$

We assume that the curvatures of the arcs t_1—t_y and t_z—t_2 are not large, so that L_{ijklrs} in (C8) are approximately constants. (This assumption is true for most finite deformation problems. In fact, even if this is not the case, the final results are unaffected, since the higher order terms of Δt in the final results will be ignored).

Substituting (C7) into (C5) and integrating by parts, we obtain:

$$c_1 = \frac{1}{3} L_{ijklrs}[\varepsilon_{ij}(t_{y-})-\varepsilon_{ij}^0][\varepsilon_{kl}(t_{y-})-\varepsilon_{kl}^0][\varepsilon_{rs}(t_{y-})-\varepsilon_{rs}^0] \tag{C9}$$

In a similar manner, the third integral on the right-hand side of (C2) can be derived as:

$$\begin{aligned} &\int_{t_{z+}}^{t_2} (\varepsilon-\varepsilon^0):(\mathbf{D}-\mathbf{D}^e):\dot{\varepsilon}\,\mathbf{dt} \\ &\quad = -\frac{1}{2}[\varepsilon(t_{z+})-\varepsilon^0)]:[\mathbf{D}(t_{z+})-\mathbf{D}^e]:[\varepsilon(t_{z+})-\varepsilon^0] - \frac{1}{2}c_2 \end{aligned} \tag{C10}$$

where

$$c_2 = -\frac{1}{3} L_{ijklrs}[\varepsilon_{ij}(t_{z+})-\varepsilon_{ij}^0][\varepsilon_{kl}(t_{z+})-\varepsilon_{kl}^0][\varepsilon_{rs}(t_{z+})-\varepsilon_{rs}^0] \tag{C11}$$

Furthermore, due to the continuity of strain at t_y, we have:

$$\begin{aligned} \varepsilon_{ij}(t_{z+}) &= \varepsilon_{ij}(t_{y-}) + \dot{\varepsilon}_{ij}\Delta t = \varepsilon_{ij}(t_{y+}) + \dot{\varepsilon}_{ij}\Delta t \\ D_{ijkl}(t_{z+}) &= D_{ijkl}(t_{y-}) + \dot{D}_{ijkl}\Delta t = D^e_{ijkl} + \dot{D}_{ijkl}\Delta t \end{aligned} \tag{C12}$$

Substituting (C12) into (C11), and (C10), it follows that:

$$\int_{t_{z+}}^{t_2} (\varepsilon - \varepsilon^0) : (\mathbf{D} - \mathbf{D}^e) : \dot{\varepsilon}\, dt$$
$$= \frac{1}{2} c_1 + \frac{1}{2} (\varepsilon - \varepsilon^0) : \dot{\mathbf{R}} : (\varepsilon - \varepsilon^0) \Delta t + \frac{1}{2} (\varepsilon - \varepsilon^0) : (\dot{\mathbf{R}} : \dot{\varepsilon} - \dot{\mathbf{D}} : \dot{\varepsilon}) (\Delta t)^2 \qquad \text{(C13)}$$

in which, ε takes the value at t_{y+}, and

$$\dot{R}_{ijkl} = L_{ijklrs} \dot{\varepsilon}_{rs} - \dot{D}_{ijkl} \qquad \text{(C14)}$$

Finally, substituting (C13), (C6) and (C3) into (C2), we obtain:

$$\int_{t_1}^{t_2} (\varepsilon - \varepsilon^0) : (\mathbf{D} - \mathbf{D}^e) : \dot{\varepsilon}\, dt = (\varepsilon - \varepsilon^0) : [(\mathbf{D} - \mathbf{D}^e) : \dot{\varepsilon} + \frac{1}{2} \dot{\mathbf{R}} : (\varepsilon - \varepsilon^0)] \Delta t$$
$$+ \left\{ \dot{\varepsilon} : (\mathbf{D} - \mathbf{D}^e) : \dot{\varepsilon} + (\varepsilon - \varepsilon^0) : [(\mathbf{D} - \mathbf{D}^e) : \ddot{\varepsilon} + \dot{\mathbf{R}} : \dot{\varepsilon}] \right\} \frac{(\Delta t)^2}{2} + \mathbf{O}(\Delta t)^3 \qquad \text{(6.15)}$$